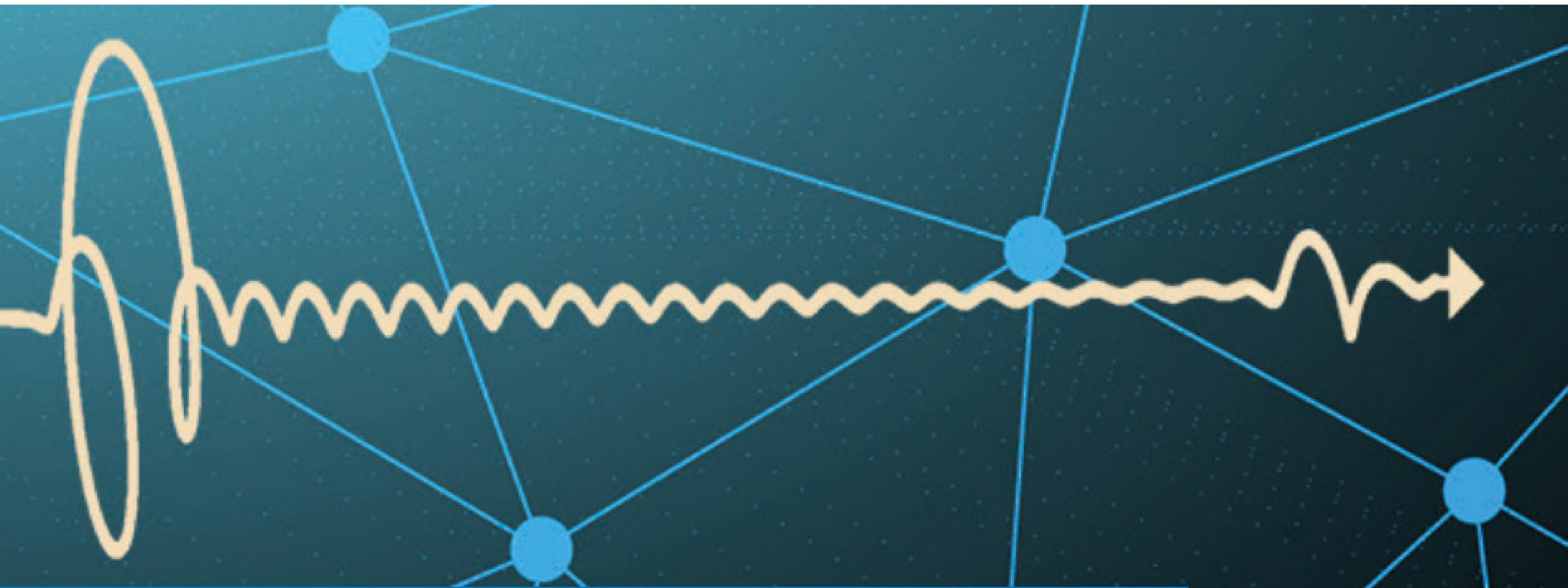

Ultrasonic Evaluation of Layer Parameters in Functionally Graded Materials and Fiber Reinforced Polymers

Xiaoyu Yang

Doctoral dissertation submitted to obtain the academic degrees of
Doctor of Electromechanical Engineering (UGent) and Doctor of Engineering (ZJU)

Supervisors
Prof. Mathias Kersemans, PhD* - Prof. Bing-Feng Ju, PhD**

* Department of Materials, Textiles and Chemical Engineering
Faculty of Engineering and Architecture, Ghent University

** School of Mechanical Engineering
Faculty of Engineering, Zhejiang University, China

January 2022

GHENT UNIVERSITY

ZHEJIANG UNIVERSITY 1897

Ultrasonic Evaluation of Layer Parameters in Functionally Graded Materials and Fiber Reinforced Polymers

Xiaoyu Yang

Doctoral dissertation submitted to obtain the academic degrees of
Doctor of Electromechanical Engineering (UGent) and Doctor of Engineering (ZJU)

Supervisors
Prof. Mathias Kersemans, PhD* - Prof. Bing-Feng Ju, PhD**

* Department of Materials, Textiles and Chemical Engineering
Faculty of Engineering and Architecture, Ghent University

** School of Mechanical Engineering
Faculty of Engineering, Zhejiang University, China

January 2022

GHENT UNIVERSITY

ZHEJIANG UNIVERSITY 1897

ISBN 978-94-6355-563-0
NUR 971, 929
Wettelijk depot: D/2022/10.500/3

Members of the Examination Board

Chairs

Prof. Jian Chen, PhD, Zhejiang University, China
Prof. Em. Luc Taerwe, PhD, Ghent University

Other members entitled to vote

Xiaolong Bai, PhD, Huawei, China
Prof. Roger Groves, PhD, Technische Universiteit Delft, the Netherlands
Prof. Elena Jasiuniene, PhD, Kauno Technologijos Universitetas, Lithuania
Prof. Hua-Xin Peng, PhD, Zhejiang University, China
Prof. Wim Van Paepegem, PhD, Ghent University

Supervisors

Prof. Mathias Kersemans, PhD, Ghent University
Prof. Bing-Feng Ju, PhD, Zhejiang University, China

Acknowledgements

Without the help of my supervisors, colleagues, teachers, classmates, family, and friends, I would not have been able to finish this thesis. Therefore, I would like to express my sincere gratitude to them.

First and foremost, I want to express my gratitude to Prof. Mathias Kersemans, who is my supervisor at Ghent University. He is knowledgeable and has a deep insight into ultrasonic NDT. He patiently went over every academic issue concerning my research with me. Our discussions and questions led to new insights and gave me a lot of inspiration with my research. Mathias always meticulously reviewed and edited my papers, especially this thesis. I appreciate him a lot for his professionalism, kindness, and patience. Besides, he is a nice friend and colleague, who helped me a lot with my living in Ghent. His professionalism and kindness deeply impressed me during my time in Ghent

I solemnly thank my supervisor, Prof. Bing-Feng Ju at Zhejiang University. Prof. Bing-Feng Ju is a rigorous scholar and takes good care of his students like sons. During my PhD research, he provided me with a wonderful platform and a great deal of academic freedom. Therefore I could pursue my goal of becoming a researcher. I deeply benefited from Bing-Feng's care and devoted guidance. From the selection of the topic to the start of the project, he carefully and patiently gave me great support and motivation. My achievements have been marked by the hard work and carefulness of Bing-Feng.

I sincerely thank my colleagues in the MMS group at Ghent University for their help. Dr. Erik Verboven has built the ultrasonic equipment and helped me with the experiments. Dr. Ives De Baere has made the optical microscopy images for me. Dr. Joost Segers produced some samples of composites for me. Of course, I would like to thank all the other colleagues in the MMS group who have provided me with the samples, important information on the materials, and the required experimental equipment. The research on fiber-reinforced polymers in this thesis could not be completed without their help.

I would also like to thank Dr. Chengcheng Zhang and Prof. Qiang Shen at Wuhan University of Technology, who provided the samples of the functionally graded materials to help me complete the research in Part one of this thesis.

I am also grateful to Dr. Anyu Sun and other colleagues at Zhejiang University who built the acoustic microscope and constructed the lab infrastructure. They also did some basic research, which laid a good foundation for the research of this thesis.

Of course, I am also grateful to my friends who are still working in the lab or have graduated, my roommates, and my relatives. During my doctoral research, they helped me with solving problems in both life and work and selflessly shared the latest news and interesting stories, making my doctoral career fun and motivating.

I would like to thank China Scholarship Council and Ghent University for granting me the Preference CSC program, which supported my PhD research and gave me the chance to study at Ghent University.

I want to express my gratitude for all the nice teachers and professors during my bachelor and PhD studies. They taught me the best and useful knowledge. I benefited a lot from what I learned from them.

Last, but not least, I would like to thank my family, especially my father, Wen Pan, and my mother, Qizhen Wu. During my PhD research, we were separated from each other a lot, but they always supported my research work. They are ordinary people, but the greatest mentors for me. They selflessly provided me with support and care and taught me to be a warm person. I would like to express my highest respect to them!

Thanks!

Xiaoyu Yang

January 2022

English Summary

Composites are materials composed of two, or more, constituents in view of exploiting the strengths of the individual constituents. By proper selection of the constituents and structural composition, composite materials can be tailored to meet specific engineering requirements. Current state-of-the-art composites, e.g. Functionally Graded Materials and Fiber Reinforced Polymers, typically have a multi-layer structure and can be found in various industrial applications, including aerospace, construction, automotive, energy, infrastructure, and marine.

Multi-layer composites obtain their high structural performance from both the material constituents and the structural composition. However, due to their layered structure, they are quite susceptible to various internal damage phenomena. Therefore, non-destructive testing procedures are of utmost importance in order to ensure the composition and performance of such composites, as well as to detect the presence of possible damage features. With this in mind, several non-destructive testing methods (X-ray testing, infrared thermography, eddy current testing, terahertz inspection, and ultrasound testing) have been described in the scientific literature for evaluating composite materials. Of particular interest to this thesis is ultrasonic testing, as it has already shown its high sensitivity to various material parameters and its good detectability for a wide range of defect types. The pulse-echo mode is a common ultrasonic approach since it only requires single-sided access to the sample and relaxes the limitation of sample dimension in the scanning scheme. However, the ultrasonic pulse-echo approach faces difficulties in quantifying the multi-layer characteristics of composites due to their heterogeneous and anisotropic properties which lead to overlapping echoes in the time domain, frequency-dependent attenuation, and extremely weak echoes from individual layers.

The overall goal of this dissertation is to develop an efficient non-destructive testing method for the inspection of multi-layer composites in order to assess layer parameters and to detect the presence of possible defects. For this purpose, the ultrasonic pulse-echo scan technique is employed, and several novel advanced processing methods are proposed. For **functionally graded materials**, the focus is put on the determination of the thickness and wave velocity of the various layers via a novel **variable focus technique**. For **fiber reinforced polymers**, the interest lies in the extraction of the thickness, in-plane and out-of-plane fiber angle, and damage area for each individual layer via a novel **planar ultrasound computed tomography** technique.

The physical foundation of ultrasonic testing is acoustic wave propagation in solid media. After the introduction of a theoretical framework to understand ultrasonic wave propagation in multi-layer solid media, this thesis is structured in two main parts:

Part I studies the interaction of ultrasound waves with **isotropic functionally graded materials**, and covers the research performed at **Zhejiang University**, China.

It first introduces a **double focus technique** based on geometric ray acoustics, which is already known to be an effective tool for assessing mechanical parameters of a thin layer without any prior knowledge.

Further, a **multi-mode waves focusing model** is proposed in order to interpret the signal waveforms from depth scanning on a single layer based on the theory of wave mode conversion. By employing the double focus technique coupled to the **multi-mode waves focusing model,** the thickness and the multi-mode wave velocities can be simultaneously determined.

Taking the multi-mode waves focusing mode as a technical basis, a **variable focus technique** is proposed in order to simultaneously determine longitudinal wave velocities and thicknesses of a multi-layer structure. In order to produce more accurate measurement results, a Phase Differentiation theory is additionally presented for robust estimation of the incidence angle. Experimental studies are performed on thin stainless-steel plates, a 5-layer metallic graded material, and a 7-layer density gradient material to validate the variable focus technique.

Part II investigates the interaction of ultrasound waves with **anisotropic carbon fiber reinforced polymer laminates**, and covers the research performed at **Ghent University**, Belgium.

It first introduces the concept of the **analytic-signal technique**, and how it benefits the analysis of the ultrasonic response from carbon fiber reinforced polymer laminates. A one-dimensional wave propagation model is used to simulate the analytic-signal response from an immersed multi-layer structure.

The influence of various parameters on the **interply tracking** in carbon fiber reinforced polymers using the **instantaneous phase** is numerically investigated and analyzed. This parametric study exposes the optimal conditions for which the analytic-signal technology provides good interply tracking results. Furthermore, an additional log-Gabor filter is proposed in order to increase the robustness of the interply tracking. The high performance of the analytic-signal procedure combined with a log-Gabor filter is numerically and experimentally verified on carbon fiber reinforced polymer laminates.

Secondly, a dedicated investigation is done on the performance of various ultrasonic pulse-echo techniques, each operated in a different frequency range, to **reconstruct the multi-layer structure** of fiber reinforced polymers. The comparative analysis of this research provides deeper insights into the performance of the ultrasonic techniques operating in different frequency ranges. The simulation and experimental results indicate the outperformance of the log-Gabor filtered analytic-signal when operated near the fundamental ply-resonance frequency.

A **structure tensor** process is proposed to extract the **local out-of-plane ply angle** of each layer in a carbon fiber reinforced polymer laminate from the measured volumetric ultrasonic dataset. Several experimental cases are analyzed with various levels of out-of-plane wrinkling. The experimental results indicate the excellent performance of the structure tensor process for reconstructing local out-of-plane ply orientations. Further, it is shown that the value of the standard deviations of the Gaussian kernels in the structure tensor method could be optimized in view of balancing the noise resistance with the bias in the out-of-plane ply-angle estimation.

Further, a **Gabor filter-based Information Diagram** method based on multiscale analysis is proposed to reconstruct the **local in-plane fiber architecture** of carbon fiber reinforced polymer laminates. The improved reconstruction result of the Gabor filter-based Information Diagram method, compared to the classical Radon transform method, is demonstrated for both synthetic texture images and experimental datasets with in-plane waviness.

Finally, a **planar ultrasound computed tomography** technique is proposed for the full **3D reconstruction of the fiber architecture in** carbon fiber reinforced polymers. The planar ultrasound computed tomography technique relies on the use of ply-resonances and involves three main analysis steps including interply mapping via a hybrid analytic-signal analysis, out-of-plane ply orientation reconstruction via structure tensor process, and local in-plane fiber direction extraction via Gabor filter-based Information Diagram method. The high performance of the novel planar ultrasound computed tomography technique is demonstrated on an impacted 24-layer carbon fiber reinforced polymer laminate.

Nederlandstalige Samenvatting

Composieten zijn materialen samengesteld uit twee, of meer, bouwstenen met het oog op het benutten van de voordelen van de individuele bouwstenen. Door een goede selectie van de materiaalbouwstenen en de structurele opbouw kan men een composietmateriaal op maat maken voor welbepaalde technische vereisten. Huidige state-of-the-art composietmaterialen, zoals functioneel gegradeerde materialen en vezelversterkte kunststoffen, hebben typisch een meerlaagse structuur en worden gebruikt voor verscheidene industriele toepassingen, zoals lucht- en ruimtevaart, infrastructuur en bouwsector, automobiel industrie, energie en maritieme sector.

Deze meerlaagse composieten behalen hun goede performantie uit de gebruikte materiaalbouwstenen en structurele opbouw. Maar door hun meerlaagse structuur zijn deze materialen vaak ook gevoelig aan verschillende interne schadeverschijnselen. Daarom zijn niet-destructieve testprocedures van het grootste belang om de correcte samenstelling en opbouw van dergelijke composieten te verifiëren, en om de aanwezigheid van mogelijke defecten te detecteren. In de wetenschappelijke literatuur worden verschillende niet-destructieve testmethoden (Röntgen testen, infrarood thermografie, wervelstroomtesten, terahertz inspectie en ultrageluid testen) beschreven voor het evalueren van composietmaterialen. Van bijzonder belang voor dit proefschrift is ultrasoon testen omdat deze methode een hoge gevoeligheid heeft aan verschillende materiaalparameters en een goede detecteerbaarheid van een breed scala defecttypen vertoont. De puls-echo techniek is een veelgebruikte ultrasone methode omdat het slechts enkelzijdige toegang tot het proefstuk vereist, en er geen limitaties zijn in de afmetingen van het te inspecteren proefstuk. De ultrasone puls-echo techniek ondervindt echter moeilijkheden bij het kwantificeren van de meerlaagse eigenschappen van composieten vanwege hun heterogene en anisotrope eigenschappen dewelke leiden tot overlappende echo's in tijdsdomein, frequentieafhankelijke demping en extreem zwakke echo's van individuele lagen.

Het algemene doel van dit proefschrift is het ontwikkelen van een efficiënte niet-destructieve testmethode voor de inspectie van meerlaagse composieten om laagparameters te beoordelen en de aanwezigheid van mogelijke defecten te detecteren. Om dit doel te bereiken wordt de ultrasone puls-echo scantechniek gebruikt en worden verschillende nieuwe geavanceerde analysemethoden ontwikkeld. Voor **functioneel gegradeerde materialen** ligt de focus op de bepaling van de dikte en golfsnelheid van de verschillende lagen via een nieuwe **variabele focustechniek**. Voor **vezelversterkte polymeren** ligt de focus op de extractie van de dikte, de in-het-vlak-ligegnde en uit-het-vlak-liggende vezelhoek, en het schadegebied voor elke individuele laag. Hiertoe wordt een nieuwe **vlakke ultrasone computertomografietechniek** ontwikkeld.

De fysieke basis van ultrasoon testen is de voortplanting van akoestische golven in vaste media. Na een korte introductie van het theoretisch kader om de voortplanting van ultrageluidsgolven in meerlaagse media te begrijpen wordt dit proefschrift gestructureerd in twee delen:

<u>Deel I</u> bestudeert de interactie van ultrageluidsgolven met **isotrope functioneel gegradeerde materialen**, en bestrijkt het onderzoek uitgevoerd in **Zhejiang University**, China.

Dit deel introduceert eerst een **techniek met dubbele focus** op basis van geometrische akoestiek, waarvan reeds geweten is dat het een effectief hulpmiddel is voor het beoordelen van mechanische parameters van een dunne laag zonder enige voorkennis.

Verder wordt een **multi-mode golffocusseringsmodel** voorgesteld om de signaalgolfvormen van dieptescanning op een enkele laag te interpreteren op basis van de theorie van de conversie van golfmodes. Door gebruik te maken van de dubbele focustechniek, gekoppeld aan het multi-mode golffocusseringsmodel, kunnen de dikte en de multi-mode golfsnelheden gelijktijdig worden bepaald.

Uitgaande van het multi-mode golffocusseringsmodel als basis, wordt een **variabele focustechniek** voorgesteld om gelijktijdig de longitudinale golfsnelheden en de diktes van een meerlaagse structuur te bepalen. Om nauwkeurigere meetresultaten te verkrijgen wordt aanvullend een fasedifferentiatietheorie voorgesteld voor een meer robuuste schatting van de invalshoek. Om de variabele focustechniek te valideren, worden experimentele studies uitgevoerd op dunne roestvrijstalen platen, een 5-laags metallisch functioneel gegradeerd materiaal en een 7-laags materiaal met gradaties in de dichtheid.

<u>Deel II</u> onderzoekt de interactie van ultrasone golven met **anisotrope koolstofvezelversterkte polymeerlaminaten**, en bestrijkt het onderzoek uitgevoerd aan de **Universiteit Gent**, België.

Het introduceert eerst het concept van **complexe signalen**, en hoe deze beschrijving een meer diepgaande analyse toelaat van de ultrasone respons van een koolstofvezelversterkte polymeerlaminaat. Een vereenvoudigd 1-

dimensionaal golfvoortplantingsmodel wordt gebruikt om de complexe signaalrespons van een ondergedompelde meerlaagse structuur te simuleren.

De invloed van verschillende parameters op de **bepaling van tussenlagen** in koolstofvezelversterkte polymeren met behulp van de ogenblikkelijke fase wordt numeriek onderzocht en geanalyseerd. Deze parametrische studie legt de optimale omstandigheden bloot waarvoor de analyse van de complexe signalen goede resultaten voor de bepaling van de tussenlagen oplevert. Verder wordt een extra log-Gabor filter voorgesteld om de robuustheid van de dieptebepaling van de tussenlagen te verbeteren. De goede prestatie van de complexe signaalprocedure in combinatie met een log-Gabor filter wordt numeriek en experimenteel geverifieerd op verschillende koolstofvezelversterkte polymeerlaminaten.

Ten tweede wordt een studie uitgevoerd naar de performantie van verschillende ultrasone puls-echo technieken, elk in een ander frequentiebereik, om de **meerlaagse structuur** van vezelversterkte polymeren te **reconstrueren**. De vergelijkende analyse van dit onderzoek geeft diepere inzichten in de prestaties van de verschillende ultrasone technieken. De numerieke en experimentele resultaten tonen de goede performantie wanneer een log-Gabor gefilterd complex signaal, met een frequentie rond de fundamentele laag-resonantie, wordt gebruikt.

Er wordt een **structuurtensorproces** voorgesteld om de **lokale uit-het-vlak-liggende vezelhoek** van elke laag in een koolstofvezelversterkt polymeerlaminaat te reconstrueren uit de gemeten volumetrische ultrasone dataset. Verschillende experimentele gevallen worden geanalyseerd met verschillende gradaties van vezelplooien uit het vlak. De experimentele resultaten wijzen op de uitstekende performantie van het structuurtensorproces voor het reconstrueren van lokale oriëntaties van lagen uit het vlak. Verder wordt aangetoond dat de waarde van de standaarddeviatie van de Gaussische kernel in de structuurtensormethode geoptimaliseerd kan worden met het oog op het balanceren van de ruisgevoeligheid enerzijds en de afwijking in de schatting van de vezelhoek uit het vlak anderzijds.

Voorts wordt een **Gabor-filter gebaseerde informatiediagrammethode**, op basis van een multi-schaal analyse, voorgesteld om de **lokale in-het-vlak-liggende vezelarchitectuur** van koolstofvezelversterkte polymeerlaminaten te reconstrueren. De betere reconstructieresultaten van de voorgestelde Gabor-filter gebaseerde informatiediagrammethode, in vergelijking met de klassieke methode op basis van de Radon transformatie, wordt gedemonstreerd voor zowel synthetische textuurafbeeldingen als experimentele datasets met in-het-vlak-liggende vezelplooien.

Ten slotte wordt een **vlakke ultrasone computertomografietechniek** voorgesteld voor de volledige 3**-dimensionele reconstructie van de vezelarchitectuur** in koolstofvezelversterkte polymeerlaminaten. Deze vlakke ultrasone computertomografietechniek is gebaseerd op het gebruik van laag-resonanties en omvat drie analysestappen, waaronder de bepaling van tussenlagen met behulp van een hybride complexe signaalanalyse, reconstructie van de lokale uit-het-vlak-liggende vezelhoeken via een structuurtensorproces en extractie van de lokale in-het-vlak-liggende vezelhoek door gebruik van een Gabor-filter gebaseerde informatiediagrammethode. De goede performantie van deze nieuwe voorgestelde vlakke ultrasone computertomografietechniek wordt gedemonstreerd op een geïmpacteerd 24-laags koolstofvezelversterkt polymeerlaminaat.

List of Abbreviations

AR	Autoregressive
BVID	Barely visible impact damage
BWE	Back-wall echo
CFRP	Carbon fiber reinforced polymer
DE	Defect echo
ECT	Eddy current testing
FGM	Functionally graded material
FIR	Finite impulse response
FRP	Fiber reinforced polymer
FWE	Front-wall echo
GF-ID	Gabor filter-based Information Diagram
LP	Low-pass
LTI	Linear time-invariant
MMWF	Multi-mode waves focusing
NDT	Non-destructive testing
PE	Pulse-echo
pU-CT	Planar ultrasound computed tomography
RT	Radon transform
SEM	Scanning electron microscopy
SMWF	Single-mode wave focusing
SNR	Signal-to-noise ratio
TOF	Time-of-flight
UT	Ultrasonic testing

List of Symbols

ω	Angular frequency
ρ	Density
β	Refraction angle
α	Incident angle
$y(t)$	Response signal
t	Time vector
$s(t)$	Real part of analytic-signal
$n(t)$	Added noise
$g(t)$	Imaginary part of analytic-signal
d	Thickness of single solid layer
c	Wave velocity
Z	Acoustic impedance
N	Sampling points
$G(\omega)$	Log-Gabor filter
$F(\omega)$	Fourier spectrum
A	Amplitude
$h(x,y)$	2D Gabor filter
$\phi_{inst}(t)$	Instantaneous phase
ε^{i}	Absolute error for interply i
$s_a(t)$	Analytic representation of a signal in its complex form
$n_s(t)$	White Gaussian noise
$\vec{k}$	Wavenumber vector
f_s	Sampling rate
$f_{\mathrm{inst}}(t)$	Instantaneous frequency
d_f	Vertical displacement required to focus on the back surface
c_0	Wave velocity in liquid
G_τ	3D Gaussian smoothing kernel with τ the standard deviation
G_σ	3D Gaussian smoothing kernel with σ the standard deviation
F_l	Focal distance
F_c	Center frequency of the signal
$A_{inst}(t)$	Instantaneous amplitude

List of Figures

List of Tables

Table of Contents

Chapter 1 Introduction

1.1 Background and Problem Statement

Composites are materials which are composed of two, or more, constituents in view of exploiting the strengths of each individual constituent. The first use of composite materials dates back to 1500 BC when early Egyptians and Mesopotamian settlers used a mixture of mud and straw to create strong and durable buildings. Straw is then continuously used to reinforce ancient composite products such as pottery and boats. Later, in 1200 AD, the Mongols invented the first composite bow. Their bows were pressed and wrapped with birch bark using a combination of wood, bone, and "animal glue" [1]. In the modern world, industrial development has expanded the usage of composite materials, promoting the growth of these materials. By proper selection of the constituents and structural composition, composite materials can be tailored to meet specific engineering requirements. Current state-of-the-art composites typically have a multi-layer structure and can be found in various industrial applications, including aerospace, construction, automotive, energy, infrastructure, and marine. To date, the use of composite materials is rapidly increasing (see Figure 1-1), and the current global market value exceeds $100 billion [2].

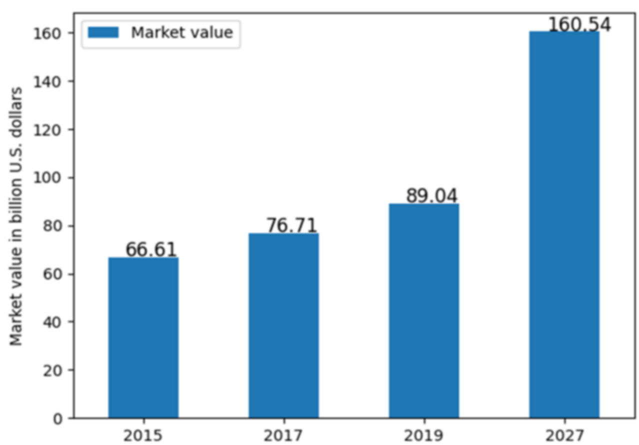

Figure 1-1 Market value of composite materials worldwide from 2015 to 2027 (in billion U.S. dollars) [3].

Of particular interest in this Ph.D. thesis are subclasses of multi-layer composite materials, namely Functional Graded Materials (FGMs) and Carbon Fiber Reinforced Polymers (CFRPs).

The concept of FGM was first proposed in 1984 as a thermal barrier material, and typically consists of a graded material composition pattern or microstructure [4, 5]. Each individual layer in a FGM is often isotropic and homogeneous. By properly designing the composition, structure, and gradients in a FGM, it is able to withstand extreme loading conditions, which makes them interesting for many high-tech applications. Some typical FGMs and their applications are listed here:

- Ceramic/Metal FGMs (see Figure 1-2) are designed to take advantage of the heat and corrosion resistance of ceramics and the mechanical strength, high toughness, good machinability, and bonding capability of metals [6]. Therefore they can be used in space shuttles in order to withstand the extremely high temperature differences (> 1000°C) between the inside and outside [7].

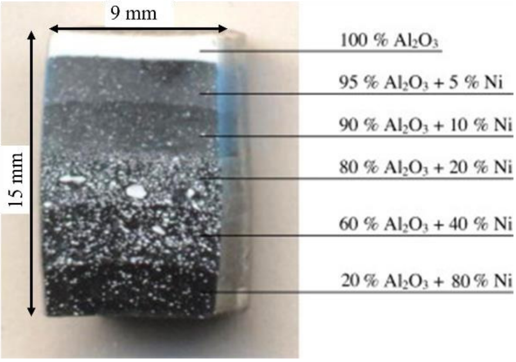

Figure 1-2 A photograph of the polished cross-section of a ceramic/metal FGM. Picture adapted from Reference [8].

- W/Cu FGMs (see Figure 1-3) are designed to combine the features of Tungsten (W), such as high melting point and low coefficient of thermal expansion, and the features of Copper (Cu), such as high heat conductivity and ductility. Therefore, this kind of FGM is a promising material for use as a plasma-facing material for a fusion reactor or a heat sink material for high-power microelectronic devices [9, 10].

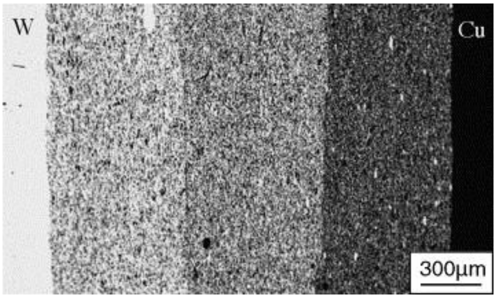

Figure 1-3 SEM micrograph of well-sintered W/Cu FGM. Picture adapted from Reference [11].

- Flier-plate with graded impedance along the thickness direction can be used to generate quasi-isentropic compression energy waves in targets. Therefore, it shows extraordinary potential for application in dynamic high-pressure techniques [12].

The other class of composites studied in this Ph.D. thesis is CFRPs, as they are amongst the most commonly used composites nowadays. Fiber reinforced polymers (FRP) are typically manufactured by adding strong and stiff reinforcement fibers to a low-density polymer matrix (see Figure 1-4).

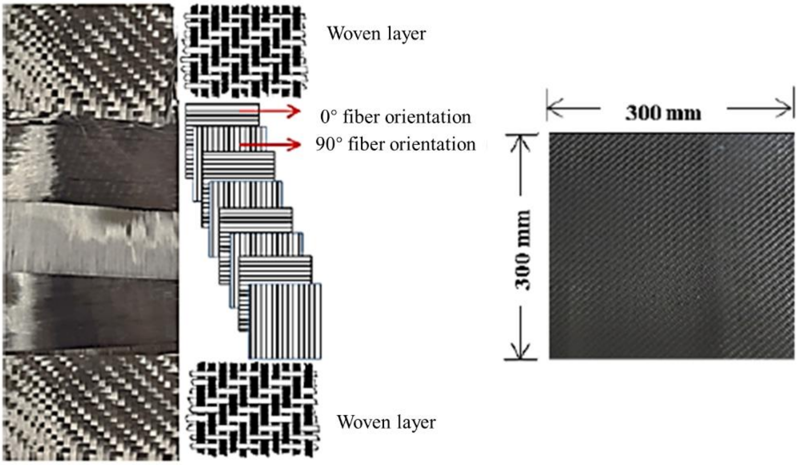

Figure 1-4 Typical structure of FRP. Picture adapted from Reference [14].

As a result, a FRP composite typically has high specific stiffness and strength and excellent chemical resistance. Due to the insertion of the long fibers, the resulting FRP will have anisotropic mechanical properties. The FRP industry as we know it today began in the early 1900s when polymers such as vinyl, polystyrene, phenolic, and polyester have been developed. In those days, reinforcement of the polymer was necessary in order to attain sufficient strength and rigidity. In 1935, Owens Corning introduced the first glass fiber, fiberglass. Fiberglass was on the market since 1939 owing to the joint research efforts of Owen-illinois and Corning Glass works [13].

In the 1970s, better polymers and improved fibers, e.g. carbon fibers, were developed. The modern aircraft industry's requirement for the lowest possible structural weight led to the rapid development of high-performance FRPs [15, 16]. By the usage of FRP, the weight of aircraft components can be reduced by approximately 20%, such as in the case of the 787 Dreamliner in Figure 1-5 [17, 18]. Boeing 787 Dreamliner is the first commercial airplane built from 50% composite materials by weight [19-21]. Recent years have seen a notable increase in the use of FRP composite in the aircraft industry, as shown in Figure 1-6. Apart from the aircraft industry, FRP materials have been the preferred material in various applications nowadays, from automobiles to fishing rods [22].

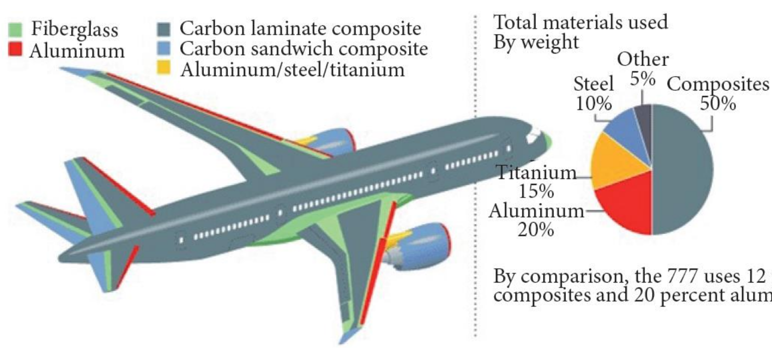

Figure 1-5 Usage of various materials in the Boeing 787 Dreamliner. Picture adapted from Reference [23].

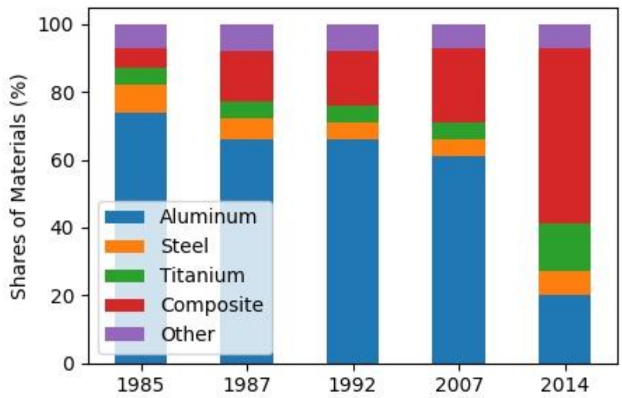

Figure 1-6 Share of materials used in aircraft design 1985–2014 [24]. Note that 'Composite' in this graph stands for fiber reinforced polymer.

Both FGM and FRP composites obtain their high performance from their material constituents and structural composition. Therefore, non-destructive testing (NDT) procedures are of utmost importance in order to ensure the composition and performance of such multi-layer composites. This becomes even more important considering that their multi-layer nature makes them vulnerable to a variety of damage phenomena (e.g., delamination, voids, and cracks). Various NDT techniques have been developed using different physical principles, such as X-ray computed tomography [25], infrared thermography [26], eddy current testing [27], magnetic particle inspection [28], terahertz technique [29], vibration testing [30], and ultrasonic testing (UT) [31]. Each technique has its specific opportunities as well as limitations. For example, X-ray computed tomography provides detailed imaging results but suffers from size limitations, long operation times, and health issues. On the other hand, infrared thermography can be used to scan a large surface area rapidly but suffers from a limited inspection depth (due to thermal diffusion and high attenuation). The established NDT techniques for various types of materials and defects are given in Table 1-1.

Table 1-1 Established NDT techniques for various materials and defects (reproduced from reference [32]). VT=Visual Inspection; RGT=Radiographic testing; ET=Electromagnetic Testing; UT=Ultrasonic Testing; PT=Penetrant testing; MT=Magnetic Particle Test; AE=Acoustic emission testing; IR=Infrared and thermal testing

Materials for testing	Type of defects	VT	RGT	ET	UT	PT	MT	AE	IR
Ferromagnetic metallic	Cracks on the surface	×	×	×	×	×	×	×	
	Internal cracks		×	×	×		×	×	×
Nonferromagnetic metallic	Cracks on the surface	×	×	×	×	×		×	
	Internal Cracks		×	×	×			×	×
Metallic	Pitting		×	×	×				
	Wear corrosion cracking								
	Welding		×	×	×				
Polymer matrix composites	Delamination				×			×	×
	Porosity		×		×				×
	Damages due to impacts	×			×			×	×
Polymers	Curing				×				
	Nonadherence		×		×				×
	Porosity		×		×				×
Ceramic	Density		×		×				
	Porosity		×		×				
	Cracks on the surface	×	×		×	×			
	internal Cracks		×		×	×		×	

Of particular interest is UT, as it has already shown its high sensitivity to a variety of material parameters and a wide range of defect types [33-35]. The merit of inaudible and non-noxious ultrasonic waves has also promoted its industrial application. The pulse-echo (PE) mode is commonly used since it only requires single-sided access to the sample and relaxes the limitation of sample dimension in the scanning scheme. The principle of the ultrasonic PE technique is illustrated in Figure 1-7. An ultrasonic transducer generates an ultrasonic pulse that is partially reflected by the front- and back wall, as well as any defect inside the material. The transducer receives the reflected signal from which different ultrasound metrics can be extracted. Hence the ultrasonic transducer acts as both transmitter (T) and receiver (R). The front-wall echo (FWE), back-wall echo (BWE), and defect echo (DE) can be retrieved in the acquired signal.

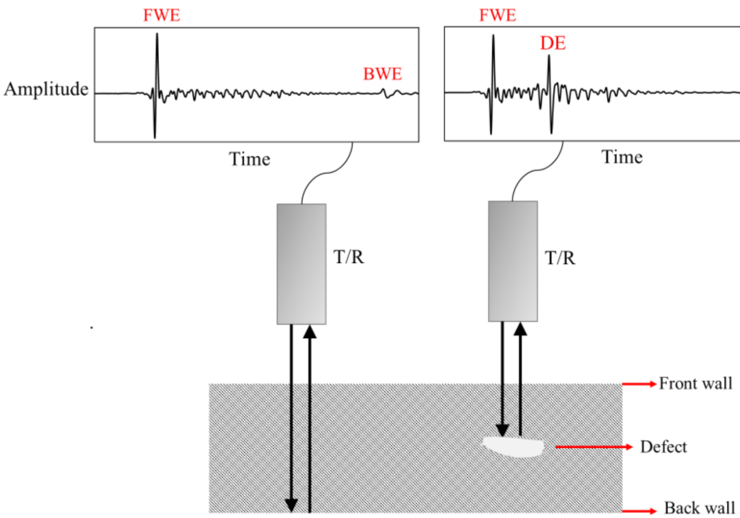

Figure 1-7 Illustration of the ultrasonic PE technique.

Generally, UT results are displayed in the form of A, B, and C-scans. An A-scan is the most straightforward mode. It simply displays the response signal as a function of time (or distance in case the wave velocity is known). An example of an A-scan signal is shown in Figure 1-8, left. For example, one can find defects by searching for echoes which appear between the FWE and BWE. By evaluating the amplitude and the time-of-flight of that echo, the depth position of the defect can be determined. The B-scan mode represents the measured A-scan signals over a linear scan as a 2D map. A color scale is assigned to the signal amplitudes (or other possible metrics), resulting in a 2D plot with the scan distance along the horizontal axis and the time (or depth) along the vertical axis. This is illustrated in Figure 1-8, bottom. The C-scan is a regime where raster scanning is performed over the object's surface, and a specific value, e. g., the maximum amplitude of the A-scan signal, is stored for each scan point. A color scale is assigned to the measured metric, resulting in a 2D plot that visualizes the projected damage area (see Figure 1-8, right).

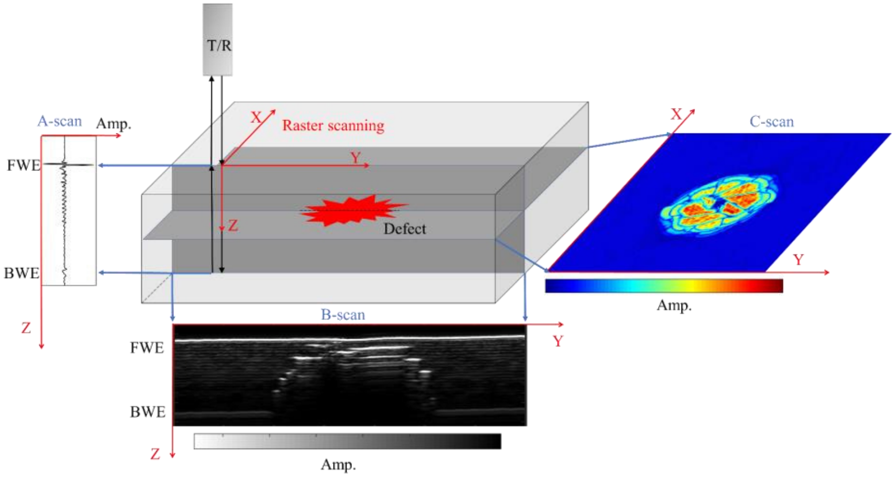

Figure 1-8 Schematic of ultrasonic A (left), B (bottom), and C-scans (right) in PE mode.

Although the ultrasonic PE technique has been established as a routine inspection tool for composites in the industrial field [36], it faces difficulties in quantifying multi-layer characteristics. The challenges involve: [37-43]:

- Overlapping echoes in the time domain and complex wave scattering due to the multi-layer structure of composites
- High and frequency-dependent attenuation due to the heterogeneous nature of composites
- Extremely weak echoes from layers in case of FRP
- Anisotropic properties in the case of FRP

Although many procedures have been proposed over the years to tackle these problems, only a few have shown potential for quantifying the multi-layer characteristics of composites. For example, high-frequency acoustic scanning microscopy was developed to image internal structures with fine resolution [44]. Some have proposed and applied the double focus technique for the characterization of thin layers [45]. Ultrasonic spectrum analysis was applied to characterize the mechanical properties of thin layers [46]. Some have investigated deconvolution techniques to enhance the weak echoes from the interfaces [47].

1.2 Research Objectives

This thesis aims to develop an efficient NDT method for the inspection of multi-layer composites in order to assess layer parameters robustly and to detect the presence of possible defects. For this purpose, the ultrasonic PE technique will be employed, and advanced processing methods are proposed. For FGM composites, the focus is put on the determination of the thickness and wave velocity of the various layers. For the FRP composites, the interest lies in the extraction of the thickness, in-plane fiber angle, out-of-plane fiber angle, and damage area for each layer.

1.3 Outline of the Dissertation

In **Chapter 2,** the **theoretical framework** to understand **wave propagation** in **multi-layer media** is provided. The reflection spectrum of a bi-layer structure is numerically analyzed for a case study. This chapter will be the foundation for the remainder of the dissertation.

Considering that the results leading to this dissertation have been obtained in the framework of a **joint-PhD program** between **Zhejiang University** (China) and **Ghent University** (Belgium), the dissertation is split in 2 parts:

Part I is focused on the ultrasonic evaluation of isotropic **metallic functionally graded materials.** This research has been carried out at **Zhejiang University** in the period 2016-2019.

Part II deals with the ultrasonic assessment of anisotropic **carbon fiber reinforced polymers.** This research was performed at **Ghent University** in the period 2019-2021.

PART I: Isotropic Metallic Functionally Graded Material

This part consists of 2 chapters covering the scientific content for the ultrasonic evaluation of isotropic multi-layer FGM. The focus is to extract the acoustic properties by means of time delay measurements or frequency spectrum analysis.

In 0, the **double focus** technique based on depth scanning is employed for the simultaneous determination of wave velocity and thickness of the thin layer without any prior knowledge. In order to interpret the signal waveforms from the depth scanning on a multi-layer material, a **multi-mode ultrasonic wave focusing theory** is proposed. The experimental results are corroborated with numerical simulation results.

0 proposes a **variable focus technique**, as an extension to the conventional double focus technique, to simultaneously **determine longitudinal wave velocities and thicknesses** of the multi-layer structure. Experimental studies are performed on the FGMs to validate the variable focus technique.

PART II: Anisotropic Carbon Fiber Reinforced Polymer

This part consists of 6 chapters covering the scientific content for evaluating anisotropic multi-layer CFRPs. The focus is on the reconstruction of ply thickness, in-plane and out-of-plane fiber orientation, and damage features by means of advanced signal processing and analysis methods.

0 introduces the concept of the **analytic-signal**. An analytical model is developed for simulating the analytic-signal response from an immersed multi-layer CFRP. This analytical model serves as input for subsequent Chapters.

0 evaluates the **instantaneous phase** of the analytic-signal for **robust interply tracking** in CFRP laminates. The influence of various parameters on interply tracking is numerically investigated and analyzed. Furthermore, a log-Gabor filter is proposed to be coupled to the analytic-signal technology for more robust interply tracking.

In **0**, the performance of various ultrasonic pulse-echo techniques, each operated in a different frequency range (high-mid-low), are investigated for the **reconstruction of the multi-layer structure** of CFRPs. The performance of the different techniques is investigated on synthetic datasets for various levels of added noise. Moreover, an experimental study is performed to validate the performance of the different techniques.

In **0**, a **structure tensor** process is proposed to extract the **out-of-plane ply angle** of CFRP laminates from the measured volumetric ultrasonic dataset. Several experimental cases are presented with various levels of out-of-plane wrinkling.

Chapter 9 proposes a **Gabor filter-based Information Diagram** (GF-ID) method to reconstruct the **in-plane fiber architecture** in multi-layer FRPs. It employs a spatial Gabor Filter method coupled to the concept of Information Diagram in view of obtaining optimal local reconstruction filters associated with the fiber direction. The GF-ID method is compared with the classical Radon transform (RT) method for synthetic texture images and experimental ultrasonic datasets obtained from a CFRP laminate.

0 A **planar ultrasound computed tomography (pU-CT)** technique is developed for **3D reconstruction of the fiber architecture** in (damaged) CFRP laminates.

Finally, **0** lists the **conclusions** of this dissertation and provides prospects and recommendations for future research.

1.4 Innovative Aspects

The most innovative results of this dissertation are briefly listed here.

1.4.1 Part I

- A multi-mode waves focusing (MMWF) theory is established to interpret depth-scanning results.
- A variable focus technique is developed for the simultaneous determination of acoustics properties of isotropic multi-layer structures.

1.4.2 Part II

- Introduction of the log-Gabor filter to the analytic-signal response for more robust interply tracking using the instantaneous phase near the ply resonance frequency.
- Various popular ultrasonic techniques in different frequency scales are comparatively investigated for reconstructing the multi-layer structure of CFRP laminates.
- A structure tensor method is implemented for the reconstruction of the local out-of-plane ply orientations in CFRP laminates.
- The 2D GF-ID method is proposed for the ultrasonic reconstruction of the local in-plane fiber direction of CFRP laminates.
- A pU-CT technique is developed by simply employing a PE-scanning modality for tomographic imaging of (damaged) CFRP laminates.

References

[1] Nagavally, R. R., 2017, "Composite materials-history, types, fabrication techniques, advantages, and applications," Int J Mech Prod Eng, 5(9), pp. 82-87.
[2] Clyne, T. W., and Hull, D., 2019, An introduction to composite materials, Cambridge university press.
[3] Garside, M., 2020, "Market value of composite materials worldwide from 2015 to 2027,"https://www.statista.com/statistics/944471/global-market-value-of-composites/.
[4] Bhavar, V., Kattire, P., Thakare, S., Patil, S., and Singh, R. K. P., 2017, "A Review on Functionally Gradient Materials (FGMs) and Their Applications," Iop Conf Ser-Mat Sci, 229.
[5] Li, Y., Feng, Z. Y., Hao, L., Huang, L. J., Xin, C. X., Wang, Y. S., Bilotti, E., Essa, K., Zhang, H., Li, Z., Yan, F. F., and Peijs, T., 2020, "A Review on Functionally Graded Materials and Structures via Additive Manufacturing: From Multi-Scale Design to Versatile Functional Properties," Adv Mater Technol-Us, 5(6).
[6] El-Wazery, M., and El-Desouky, A., 2015, "A review on functionally graded ceramic-metal materials," Journal of Materials and Environmental Science, 6(5), pp. 1369-1376.
[7] Koizumi, M., 1997, "FGM activities in Japan," Compos Part B-Eng, 28(1-2), pp. 1-4.
[8] Bykov, Y. V., Egorov, S. V., Eremeev, A. G., Holoptsev, V. V., Plotnikov, I. V., Rybakov, K. I., Semenov, V. E., and Sorokin, A. A., 2014, "Temperature profile optimization for microwave sintering of bulk Ni–Al2O3 functionally graded materials," Journal of Materials Processing Technology, 214(2), pp. 210-216.
[9] Chapa, J., and Reimanis, I., 2002, "Modeling of thermal stresses in a graded Cu/W joint," J Nucl Mater, 303(2-3), pp. 131-136.
[10] Pintsuk, G., Brunings, S. E., Doring, J. E., Linke, J., Smid, I., and Xue, L., 2003, "Development of W/Cu - functionally graded materials," Fusion Eng Des, 66-68, pp. 237-240.
[11] Zhou, Z. J., Du, J., Song, S. X., Zhong, Z. H., and Ge, C. C., 2007, "Microstructural characterization of W/Cu functionally graded materials produced by a one-step resistance sintering method," J Alloy Compd, 428(1-2), pp. 146-150.
[12] Wang, C. B., Zhang, L. M., Shen, Q., Tan, H., and Hua, J. S., 2003, "Preparation of flier-plate materials with graded impedance used for hypervelocity launching," Materials Science Forum, 423-4, pp. 77-80.

[13] Vaughan, D. J., 1998, "Fiberglass reinforcement," Handbook of composites, Springer, pp. 131-155.
[14] Moustafa, E. B., and Almitani, K. H., 2021, "Detecting Damage in Carbon Fibre Composites using Numerical Analysis and Vibration Measurements," Lat Am J Solids Stru, 18(3).
[15] Soutis, C., 2005, "Carbon fiber reinforced plastics in aircraft construction," Mat Sci Eng a-Struct, 412(1-2), pp. 171-176.
[16] Mangalgiri, P. D., 1999, "Composite materials for aerospace applications," B Mater Sci, 22(3), pp. 657-664.
[17] Lubin, G., 2013, Handbook of composites, Springer Science & Business Media.
[18] Gay, D., 2014, Composite materials: design and applications, CRC press.
[19] Campbell Jr, F. C., 2011, Manufacturing technology for aerospace structural materials, Elsevier.
[20] Kumar, P. A., Rohatgi, P., and Weiss, D., 2019, "50 Years of Foundry-Produced Metal Matrix Composites and Future Opportunities," International Journal of Metalcasting, 14, pp. 291-317.
[21] Alhammad, M., Fragonara, L. Z., and Avdelidis, N. P., 2020, "Diagnosis of Composite Materials in Aircraft Applications–Brief Survey of Recent Literature."
[22] Bunsell, A. R., Joannès, S., and Thionnet, A., 2021, Fundamentals of fibre reinforced composite materials, CRC Press.
[23] Alemour, B., Badran, O., and Hassan, M. R., 2019, "A Review of Using Conductive Composite Materials in Solving Lightening Strike and Ice Accumulation Problems in Aviation," J Aerosp Technol Man, 11.
[24] Garside, M., 2020, "Share of materials used in aircraft design 1985-2014,"https://www.statista.com/statistics/954913/share-composites-in-aircraft-design/.
[25] Carmignato, S., Dewulf, W., and Leach, R., 2018, Industrial X-ray computed tomography, Springer.
[26] Osornio-Rios, R. A., Antonino-Daviu, J. A., and Romero-Troncoso, R. D., 2019, "Recent Industrial Applications of Infrared Thermography: A Review," Ieee T Ind Inform, 15(2), pp. 615-625.
[27] Garcia-Martin, J., Gomez-Gil, J., and Vazquez-Sanchez, E., 2011, "Non-Destructive Techniques Based on Eddy Current Testing," Sensors-Basel, 11(3), pp. 2525-2565.
[28] Lovejoy, M., 2012, Magnetic particle inspection: a practical guide, Springer Science & Business Media.
[29] Zhong, S. C., 2019, "Progress in terahertz nondestructive testing: A review," Front Mech Eng-Prc, 14(3), pp. 273-281.

[30] Doebling, S. W., Farrar, C. R., and Prime, M. B., 1998, "A summary review of vibration-based damage identification methods," Shock and vibration digest, 30(2), pp. 91-105.
[31] Wang, B., Zhong, S., Lee, T.-L., Fancey, K. S., and Mi, J., 2020, "Non-destructive testing and evaluation of composite materials/structures: A state-of-the-art review," Advances in Mechanical Engineering, 12(4).
[32] Roa-Rodriguez, G., Aperador, W., and Delgado, A., 2013, "Simulation of non-destructive testing methods of ultrasound in concrete columns," Int. J. Electrochem. Sci, 8, pp. 12226-12237.
[33] Hsu, D., 2013, "Non-destructive evaluation (NDE) of aerospace composites: ultrasonic techniques," Non-destructive evaluation (NDE) of polymer matrix composites, Elsevier, pp. 397-422.
[34] Smith, R., 2009, "Composite defects and their detection," Materials science and engineering, 3(1), pp. 103-143.
[35] Wronkowicz, A., Dragan, K., and Lis, K., 2018, "Assessment of uncertainty in damage evaluation by ultrasonic testing of composite structures," Compos Struct, 203, pp. 71-84.
[36] Caminero, M. A., Garcia-Moreno, I., Rodriguez, G. P., and Chacon, J. M., 2019, "Internal damage evaluation of composite structures using phased array ultrasonic technique: Impact damage assessment in CFRP and 3D printed reinforced composites," Compos Part B-Eng, 165, pp. 131-142.
[37] Hung, B., and Goldstein, A., 1983, "Acoustic parameters of commercial plastics," IEEE Transactions on Sonics and Ultrasonics, 30(4), pp. 249-254.
[38] Selfridge, A. R., 1985, "Approximate material properties in isotropic materials," IEEE transactions on sonics and ultrasonics, 32(3), pp. 381-394.
[39] Wang, H., Ritter, T., Cao, W., and Shung, K. K., 2001, "High frequency properties of passive materials for ultrasonic transducers," IEEE transactions on ultrasonics, ferroelectrics, and frequency control, 48(1), pp. 78-84.
[40] Wooh, S.-C., and Wei, C., 1999, "A high-fidelity ultrasonic pulse-echo scheme for detecting delaminations in composite laminates," Composites Part B: Engineering, 30(5), pp. 433-441.
[41] Rokhlin, S., Lewis, D., Graff, K., and Adler, L., 1986, "Real‐time study of frequency dependence of attenuation and velocity of ultrasonic waves during the curing reaction of epoxy resin," The Journal of the Acoustical Society of America, 79(6), pp. 1786-1793.
[42] Sehgal, C. M., and Greenleaf, J. F., 1982, "Ultrasonic absorption and dispersion in biological media: A postulated model," The Journal of the Acoustical Society of America, 72(6), pp. 1711-1718.

[43] Ginzel, E., Ginzel, R., and Brothers, G., 1994, "Ultrasonic properties of a new low attenuation dry couplant elastomer," Ginzel brothers & associates Ltd.
[44] Morokov, E., Levin, V., Chernov, A., and Shanygin, A., 2021, "High resolution ply-by-ply ultrasound imaging of impact damage in thick CFRP laminates by high-frequency acoustic microscopy," Compos Struct, 256, p. 113102.
[45] Haenel, V., and Kleffner, B., 1999, "Double focus technique for quantitative measurements in time - resolved acoustic microscopy," The Journal of the Acoustical Society of America, 105(2), pp. 1015-1015.
[46] Agrawal, M., Prasad, A., Bellare, J. R., and Seshia, A. A., 2016, "Characterization of mechanical properties of materials using ultrasound broadband spectroscopy," Ultrasonics, 64, pp. 186-195.
[47] Shakibi, B., Honarvar, F., Moles, M., Caldwell, J., and Sinclair, A. N., 2012, "Resolution enhancement of ultrasonic defect signals for crack sizing," Ndt&E Int, 52, pp. 37-50.

Chapter 2 Acoustic Wave Propagation in Multi-layer Solids

Acoustic wave propagation in media is the physical foundation of ultrasonic testing. In view of this, this chapter introduces the physics of wave propagation in multi-layer solids. A more thorough description can be found in several textbooks [1, 2].

2.1 Wave equation

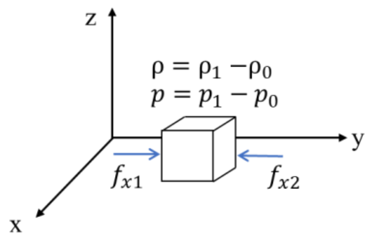

Figure 2-1 Schematic for the derivation of the wave equation for small-amplitude acoustic wave.

Acoustic wave propagation refers to the process of vibration and energy transfer in a medium, resulting in pressure changes at each point, as shown in Figure 2-1. Such a change of pressure can be expressed by acoustic pressure. The acoustic pressure p at a point can be described by the difference between the pressure p_1 in presence of a wave and the constant pressure p_0 in absence of a wave, i.e.,

$$p = p_1 - p_0. \tag{2.1}$$

In general, the effective value of the sound pressure is used, whose unit is Pascal.

During the wave propagation, p is different in various volume elements at a specific time. For a specific volume element, the acoustic pressure p also changes with time. Hence the acoustic pressure p is generally a function of space and time, i.e., $p = p(x, y, z, t) = p(\vec{r}, t)$. The measurement of acoustic pressure is relatively simple. As a result, acoustic pressure has become the most commonly used physical quantity to describe acoustic waves.

Under the assumption of small-amplitude acoustic waves, the wave propagation satisfies three basic laws of physics on the macroscale. They are Newton's second law of motion, the law of conservation of mass, and the law of state equation. By the use of these laws, we can derive the motion equation (i.e., relation between p and particle velocity v), the continuity equation (i.e., relation between v and density ρ), and the state equation (i.e., relation between p and ρ) of the medium.

(1) By the use of Newton's second law of motion, we can obtain the motion equation of the medium as a description of the relation between p and v as follows

$$\rho_0 \frac{\mathrm{d}v}{\mathrm{d}t} = -\frac{\partial p}{\partial x}, \tag{2.2}$$

where ρ_0 is the density without any acoustic disturbance.

(2) By the use of the law of conservation of mass, we can obtain the continuity equation of the medium as a description of the relation between v and ρ as follows

$$-\rho_0 \frac{\partial v}{\partial x} = \frac{\partial \rho}{\partial t}. \tag{2.3}$$

(3) By the use of the law of state equation, we can obtain the state equation of the medium as a description of the relation between p and ρ as follows

$$p = {c_{\mathrm{cons}}}^2 \rho, \tag{2.4}$$

where c_{cons} is the constant wave velocity.

Combining Eqs. (2.2), (2.3), and (2.4), the one-dimensional wave equation of small-amplitude acoustic wave propagation is found

$$\frac{\partial^2 p}{\partial x^2} = \frac{1}{{c_{\mathrm{cons}}}^2} \frac{\partial^2 p}{\partial t^2}. \tag{2.5}$$

Extending to the three-dimensional case, the wave equation of small-amplitude acoustic wave propagation in an ideal medium becomes

$$\nabla^2 \vec{p} = \frac{1}{{c_{\mathrm{cons}}}^2} \frac{\partial^2 \vec{p}}{\partial t^2}, \tag{2.6}$$

where $\vec{p}$ is the acoustic pressure vector, ∇^2 is the Laplace operator, which is represented in the Cartesian coordinate system as:

$$\nabla^2 = \frac{\partial^2}{\partial x^2} + \frac{\partial^2}{\partial y^2} + \frac{\partial^2}{\partial z^2}. \tag{2.7}$$

In an infinite medium, a general solution of the wave equation can be obtained as

$$p(\vec{r}, t) = A\mathrm{e}^{[\mathrm{i}(\omega t - \vec{k}\vec{r})]}, \tag{2.8}$$

where A is the amplitude, $\vec{k}$ is the wavenumber vector, $\vec{r}$ is the coordinate vector, and ω is the angular frequency of the acoustic wave. There is a straightforward generalization of the expression of the plane harmonic wave for inhomogeneous media by assuming a complex wave vector $\vec{k}$:

$$\vec{k} = \vec{k}' + \mathrm{i}\vec{k}''. \tag{2.9}$$

By substituting Eq. (2.9) into Eq. (2.8), we obtain

$$p(t, \vec{r}) = A\mathrm{e}^{[\mathrm{i}(\vec{k}'\vec{r} - \omega t) - \vec{k}''\vec{r}]}. \tag{2.10}$$

The latter term of the exponential function expresses a wave with varying amplitude, describing frequency-dependent attenuation.

2.2 Reflection and Refraction from a Liquid Interface

Now we consider a boundary in the medium in which the wave propagates. Let the plane wave be incident on the plane boundary at $z = 0$ separating two liquid or gaseous media (see Figure 2-2). Note that for brevity in writing, we shall omit the factor $e^{-i\omega t}$ in the remainder. The plane of incidence of the wave is coincident with the xz plane. θ_{up} and θ_{low} are the incidence and refraction angles, respectively. The densities of the upper and the lower media are denoted by ρ_{up} and ρ_{low} respectively. The wave velocities in them are denoted by c_{up} and c_{low} respectively. The wavenumbers in them are denoted by k_{up} and k_{low} respectively. As a result, the wavenumber in the upper media k_{up} is

$$k_{up} = \frac{\omega}{c_{up}}, k_{low} = \frac{\omega}{c_{low}}. \tag{2.11}$$

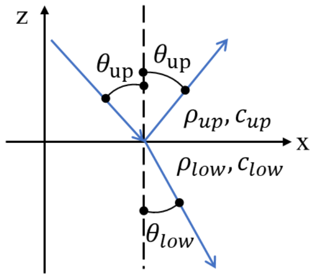

Figure 2-2 Schematic diagram of the reflection and the refraction from an Interface.

Now let us take the amplitude of the incident wave to be unity and denote the reflection coefficient of the wave by V. In this way, the acoustic pressures of the incident and reflected waves are

$$\begin{gathered} p_{\mathrm{inc}} = \mathrm{e}^{\mathrm{i}k_{up}(x\sin\theta_{up} - z\cos\theta_{up})}, \\ p_{\mathrm{refl}} = V\mathrm{e}^{\mathrm{i}k_{up}(x\sin\theta_{up} + z\cos\theta_{up})}. \end{gathered} \tag{2.12}$$

Then the total acoustic pressure in the upper media is

$$p_{up} = p_{inc} + p_{refl} = (\mathrm{e}^{-\mathrm{i}k_{up}z\cos\theta_{up}} + V\mathrm{e}^{\mathrm{i}k_{up}z\cos\theta_{up}})\mathrm{e}^{\mathrm{i}k_{up}x\sin\theta_{up}}. \tag{2.13}$$

The total acoustic pressure in the lower media could be written as

$$p_{low} = W_T\mathrm{e}^{\mathrm{i}k_{low}(x\sin\theta_{low} - z\cos\theta_{low})}, \tag{2.14}$$

where W_T is the transmission coefficient.

Importantly, there is continuity of p and v_z at the boundary, where v_z denotes the component of the particle velocity normal to the boundary. The concept of impedance is defined as

$$Z = -\frac{p}{v_z}, \tag{2.15}$$

which should also be continuous in the transition through the boundary due to the fact that p and v_z are continue. Consequently, the boundary conditions are concluded as

$$\begin{gathered} z = 0, \\ [p] = 0, \end{gathered} \tag{2.16}$$

$$[Z] = 0,$$

where [·] denotes the difference in the values of corresponding quantity on the two sides of the boundary. By substituting Eqs. (2.13) and (2.14) into Eq. (2.16), we obtain

$$1 + V = W_T e^{i(k_{low}\sin\theta_{low} - k_{up}\sin\theta_{up})x}. \tag{2.17}$$

Since the left side of Eq. (2.17) is independent on x, the right side should be also independent on x. From this, we obtain the well-known Snell's law as follows:

$$k_{up}\sin\theta_{up} = k_{low}\sin\theta_{low}, \tag{2.18}$$

which expresses the equality of the phase velocities of wave propagation along the boundary in the upper and lower media. It can be rewritten as

$$\frac{\sin\theta_{up}}{\sin\theta_{low}} = \frac{k_{\mathrm{low}}}{k_{\mathrm{up}}} = \frac{c_{\mathrm{up}}}{c_{\mathrm{low}}} = \mathrm{n}, \tag{2.19}$$

Therefore, Eq. (2.17) takes the form

$$1 + V = W_T. \tag{2.20}$$

The reflection coefficient could also be defined as follows [1]:

$$V = \frac{Z_{low} - Z_{up}}{Z_{low} + Z_{up}}, \tag{2.21}$$

$$Z_{low} = \frac{\rho_{low}c_{low}}{\cos\theta_{low}}, \tag{2.22}$$

$$Z_{up} = \frac{\rho_{up}c_{up}}{\cos\theta_{up}}. \tag{2.23}$$

Now, we should consider some extreme cases. E.g., for the normal incidence of the wave on the boundary, we can obtain

$$V = \frac{\rho_{low}c_{low} - \rho_{up}c_{up}}{\rho_{low}c_{low} + \rho_{up}c_{up}}. \tag{2.24}$$

For grazing incidence in the limit as $\theta_{up} \to \pi/2$, we can obtain $V = -1$. We denote ρ_{low}/ρ_{up} by m and then obtain

$$m\cos\theta_{up} = \sqrt{n^2 - \sin^2\theta_{up}},\ 1 < n \le m \text{ or } 1 > n \ge m. \tag{2.25}$$

The reflection coefficient vanishes in this case, which represents complete transmission at the boundary. In the case of equality of the velocities ($n = 1$), the reflection coefficient proves to be even independent of the angle:

$$V = \frac{\rho_{low} - \rho_{up}}{\rho_{low} + \rho_{up}}. \tag{2.26}$$

In the case $n < 1$ and for angles of incidence that exceed the critical angle $\theta_0 = \sin^{-1} n$, total internal reflection takes place. When the angle of incidence reaches the critical angle, the refracted wave propagates along the boundary with an angle of refraction of 90°. In other words, it gives rise to surface wave phenomena. Note however that surface waves are not explicitly introduced since they are not a focus of this thesis. More thorough descriptions about surface waves can be found in the textbook [3].

2.3 Reflection and Refraction from a Multi-layer Liquid System

Consider a plane wave incident on a plane layer of thickness d at an arbitrary angle (see Figure 2-3). The medium from which the wave arrives, the layer, and the medium into which the wave penetrates are denoted by Medium 3, 2, and 1, respectively. The angles relative to the wave direction in each medium and the normal to the boundary are denoted by θ_n, with n =1,2,3. Z_n, ρ_n, d_n, and c_n represent the impedance, density, thickness, and wave velocity of Medium n, respectively. The plane of incidence of the wave is here assumed as the xz plane. For a multi-layer liquid system, only longitudinal waves should be considered in the analysis.

The equivalent “input impedance” at the Boundary 23 of the layer is denoted by Z_{in}. According to Eq. (2.21), V is given by

$$V = \frac{Z_{in} - Z_3}{Z_{in} + Z_3}, \tag{2.27}$$

where the impedance for the plane wave in Medium 3 is

$$Z_3 = \frac{\rho_3 c_3}{cos\,\theta_3}. \tag{2.28}$$

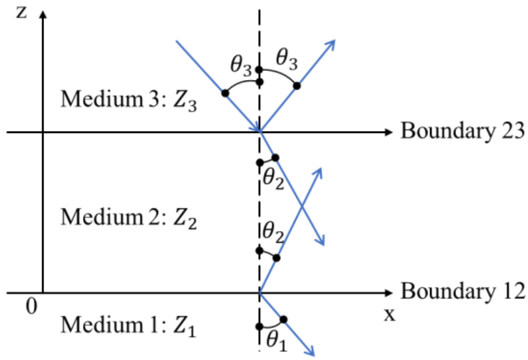

Figure 2-3 Schematic diagram of the reflection and the refraction of a plane wave off a layer. The incident wave is in medium 3.

The equivalent "input impedance" at the Boundary 23 of the layer is denoted by Z_{in}. According to Eq. (2.21), V is given by

$$V = \frac{Z_{in} - Z_3}{Z_{in} + Z_3}, \tag{2.29}$$

where the impedance for the plane wave in Medium 3 is

$$Z_3 = \frac{\rho_3 c_3}{cos\,\theta_3}. \tag{2.30}$$

Now we need to derive Z_{in}. It can be seen in Figure 2-3 that there exist multiple reflections from the boundaries of the liquid layers. Consequently, two resulting waves inside Medium 2, with different propagation directions, are symmetric relative to the plane $z = const$. Thus, the acoustic pressure in Medium 2 can be expressed in the form as follows

$$\begin{gathered} p_2 = \left(A\mathrm{e}^{-\mathrm{i}k_{2z}z} + Be^{\mathrm{i}k_{2z}z}\right)e^{\mathrm{i}k_{2z}x}, \\ k_{2x}^2 + k_{2z}^2 = k_2^2, \\ k_2 = \frac{\omega}{c_2}, \end{gathered} \tag{2.31}$$

where k_{nz} and k_{nx} are z and x-direction components of wavenumber k_n in nth layer media, A and B are two constants to be determined in the following. The z direction component of the velocity v_2 in the Medium 2 can be obtained by

$$v_{2z} = \left(\frac{1}{\mathrm{i}\omega\rho_2}\right)\left(\frac{\partial p_2}{\partial z}\right) = \left(\frac{k_{2z}}{\omega\rho_2}\right)\left(B\mathrm{e}^{\mathrm{i}k_{2z}z} - A\mathrm{e}^{-\mathrm{i}k_{2z}z}\right)\mathrm{e}^{\mathrm{i}k_{2x}x}, \tag{2.32}$$

By considering Eq. (2.15) and the continuity of the impedance on the boundary $z = 0$, we have

$$-\left(\frac{p_2}{v_{2z}}\right)_{z=0} = Z_1. \tag{2.33}$$

By considering Eqs. (2.31), (2.32), and (2.33), we obtain

$$\frac{B}{A} = \frac{(Z_1 - Z_2)}{(Z_1 + Z_2)}, \tag{2.34}$$

where $Z_1 \equiv \omega\rho_1/k_{1z} = \rho_1 c_1/cos\theta_1$ and $Z_2 \equiv \omega\rho_2/k_{2z} = \rho_2 c_2/cos\theta_2$. Then the input impedance at Boundary 23 ($z = d$) is defined as

$$Z_{in} = -\left(\frac{p_2}{v_{2z}}\right)_{z=d}. \tag{2.35}$$

By substituting Eqs. (2.31), (2.32), and (2.34) into Eq. (2.35) here, we obtain

$$Z_{in} = \frac{(Z_1 - \mathrm{i}Z_2\, tan\, k_{2z}d)}{(Z_2 - \mathrm{i}Z_1\, tan\, k_{2z}d)} Z_2, \tag{2.36}$$

which is a crucial formula allowing for calculating the impedance layer by layer recursively. Finally, by substituting Eq. (2.36) in Eq. (2.29), we find that

$$V = \frac{(Z_1 + Z_2)(Z_2 - Z_3)\mathrm{e}^{-\mathrm{i}k_{2z}d} + (Z_1 - Z_2)(Z_2 + Z_3)\mathrm{e}^{\mathrm{i}k_{2z}d}}{(Z_1 + Z_2)(Z_2 + Z_3)\mathrm{e}^{-\mathrm{i}k_{2z}d} + (Z_1 - Z_2)(Z_2 - Z_3)\mathrm{e}^{\mathrm{i}k_{2z}d}}. \tag{2.37}$$

Similar to (2.19), the angles are connected by Snell's law as follows

$$k_1 \sin\theta_1 = k_2 \sin\theta_2 = k_3 \sin\theta_3. \tag{2.38}$$

Note that the presence of absorption in the media can be considered purely formally by having a complex wavenumber k_1, k_2 and k_3 in each media, similar to Section 2.1.

We now consider that there are $n - 1$ layers between two semi-infinite media, which are enumerated by 1 and $n + 1$ (see Figure 2-4). As described above, it suffices to find the input impedance of the set of layers $Z_{in}^{(n)}$. Practically, setting $Z_{in}^{(1)} = Z_1$, $d = d_2$, we obtain the input impedance $Z_{in}^{(2)}$ at the upper boundary of the lower layer according to Eq. (2.36)

$$Z_{\text{in}}^{(2)} = \frac{\left(Z_{\text{in}}^{(1)} - \mathrm{i}Z_2 \tan k_{2z} d_2\right)}{\left(Z_2 - \mathrm{i}Z_{\text{in}}^{(1)} \tan k_{2z} d_2\right)} Z_2. \tag{2.39}$$

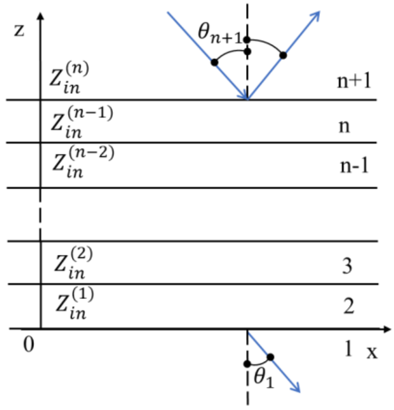

Figure 2-4 Schematic diagram of the reflection and the refraction of a plane wave of a set of layers.

Further, making the substitution $Z_{in}^{(1)} \to Z_{in}^{(2)}$, $Z_2 \to Z_3$, $k_{2z} \to k_{3z}$, $d_2 \to d_3$ on the right side of Eq. (2.39), we obtain the expression for $Z_{in}^{(3)}$ representing the input impedance of the second layer below. Then, $Z_{in}^{(n-1)}$ would be found in a recursive manner, and the required input impedance of the system is determined by [1]

$$Z_{in}^{(n)} = \frac{\left(Z_{in}^{(n-1)} - \mathrm{i}Z_n \tan k_{nz} d_n\right)}{\left(Z_n - \mathrm{i}Z_{in}^{(n-1)} \tan k_{nz} d_n\right)} Z_n. \tag{2.40}$$

Finally, we have the reflection coefficient

$$V = \frac{\left(Z_{in}^{(n)} - Z_{n+1}\right)}{\left(Z_{in}^{(n)} + Z_{n+1}\right)}. \tag{2.41}$$

As above, we also obtain

$$\begin{gathered} Z_j = \frac{\rho_j c_j}{\cos\theta_j}, j = 1,2,\dots,n+1. \\ k_j \sin\theta_j = k_{n+1} \sin\theta_{n+1}, j = 1,2,\dots,n+1. \end{gathered} \tag{2.42}$$

2.4 Reflection and Refraction from an Interface between Solid Media

Now we consider the interface between solid (elastic) media. There are transverse (shear) and longitudinal waves in solid media (see Figure 2-5). The reflection and refraction factors for a perfect solid-solid boundary can be derived by considering boundary conditions [2], which account for the continuity of particle velocity and stress. The reflection and refraction equations are as follows.

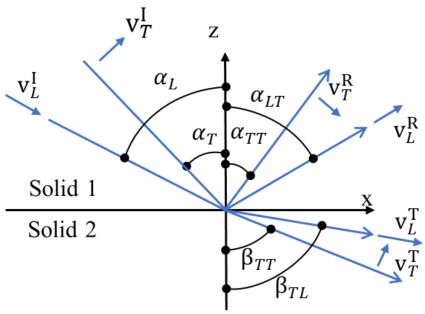

Figure 2-5 Schematic diagram of the reflection and the refraction of a plane wave from an Interface between Solid Media.

$$M\begin{bmatrix} RTL \\ RTT \\ DTL \\ DTT \end{bmatrix} = a_M, \tag{2.43}$$

where

$$M = \begin{bmatrix} -\cos\alpha_{LT} & \sin\alpha_{TT} & -\cos\beta_{TL} & \sin\beta_{TT} \\ -\sin\alpha_{LT} & -\cos\alpha_{TT} & \sin\beta_{TL} & \cos\beta_{TT} \\ -k_{L1}(\boldsymbol{\lambda_1}+2\boldsymbol{\mu_1})\cos 2\alpha_{TT} & k_{T1}\boldsymbol{\mu_1}\sin 2\alpha_{TT} & k_{L2}(\boldsymbol{\lambda_2}+2\boldsymbol{\mu_2})\cos 2\beta_{TT} & -k_{T2}\boldsymbol{\mu_2}\sin 2\beta \\ -k_{L1}\boldsymbol{\mu_1}\sin 2\alpha_{LT} & -k_{T1}\boldsymbol{\mu_1}\cos 2\alpha_{TT} & -k_{L2}\boldsymbol{\mu_2}\sin 2\beta_{TL} & -k_{T2}\boldsymbol{\mu_2}\cos 2\beta \end{bmatrix} \tag{2.44}$$

where $\boldsymbol{\lambda_1}$ and $\boldsymbol{\mu_1}$ are the Lamé constant in Solid 1, $\boldsymbol{\lambda_2}$ and $\boldsymbol{\mu_2}$ are the Lamé constant in Solid 2, α_{ij} represents the reflection angle for longitudinal (i = L) or transverse (i = T) reflection wave, and for longitudinal (j = L) or transverse (j = T) incident wave, β_{ij} represents the refraction angle for longitudinal (i = L) or transverse (i = T) incident wave, and for longitudinal (j = L) or transverse (j =

T) refraction wave, and k_{ij} represents longitudinal (i = L) or transverse (i = T) wavenumber in Solid j. We define each amplitude ratio as follows:

$$RTL = \frac{B_{RL}}{A_T}, RTT = \frac{B_{RT}}{A_T}, DTL = \frac{B_{TL}}{A_T}, DTT = \frac{B_{TT}}{A_T}. \tag{2.45}$$

For each left side in Eq. (2.45), the uppercase letters represent the reflection and transmission coefficients as follows. The first letter R or D represents reflection or transmission. The second letter L or T represents the longitudinal or transverse incident wave. Similarly, the third letter L or T represents longitudinal or transverse reflected/transmitted waves. For instance, RLL represents the amplitude ratio between reflected longitudinal wave and incident longitudinal wave.

For the right side in Eq. (2.45), A_j represents the amplitude of longitudinal (j = L) or transverse (j = T) incident wave, and B_{ij} represents the amplitude of reflection (i = R) or refraction (i = T) wave for longitudinal (j = L) or transverse (j = T) wave.

In the case of transverse wave incidence, we have

$$a_M = \begin{bmatrix} \sin\alpha_T \\ \cos\alpha_T \\ -k_T\boldsymbol{\mu_1}\sin 2\alpha_T \\ -k_{T1}\boldsymbol{\mu_1}\cos 2\alpha_T \end{bmatrix}. \tag{2.46}$$

In the case of longitudinal wave incidence, we have

$$a_M = \begin{bmatrix} -\cos\alpha_L \\ \sin\alpha_L \\ k_{L1}(\boldsymbol{\lambda_1} + 2\boldsymbol{\mu_1})\cos 2\alpha_L \\ -k_{L1}\boldsymbol{\mu_1}\sin 2\alpha_L \end{bmatrix}. \tag{2.47}$$

And the definition of the reflection and refraction coefficients becomes

$$RLL = \frac{B_{RL}}{A_L}, RLT = \frac{B_{RT}}{A_L}, DLL = \frac{B_{TL}}{A_L}, DLT = \frac{B_{TT}}{A_L}. \tag{2.48}$$

Similarly, reflection and refraction coefficients from the solid-liquid or liquid-solid boundary can also be obtained [2]. There are few differences concerning these situations: with liquid media, there is only a longitudinal wave. As such, the shear stress becomes zero at the boundary.

References

[1] Brekhovskikh, L., 2012, Waves in layered media, Elsevier.
[2] Rose, J. L., 2000, Ultrasonic waves in solid media, Cambridge University Press.
[3] Rose, J. L., 2014, Ultrasonic guided waves in solid media, Cambridge university press.

PART I: Isotropic Metallic Functionally Graded Material

The research in this Part I focuses on metallic Functionally Graded Materials (FGMs), and has been performed at Zhejiang University.

FGMs are often used in safety-critical applications. To assure its performance in safety-critical applications, the parameters of the various graded layers should be within narrow design bounds. The focus of this part is to extract (acoustic) properties of isotropic FGMs using high-frequency ultrasound. The isotropic functionally graded material is typically composed of metallic layers with sufficiently different gradient properties, and as such provides obvious interface echoes from which relevant information can be extracted in the time domain and/or frequency domain.

Chapter 3 Multi-mode Ultrasonic Wave Focusing in Double Focus Technique

3.1 Introduction

In the case of no prior knowledge about the acoustic properties of layered materials, it is desirable to determine the wave speed and thickness in a single ultrasonic measurement [1]. This simultaneous assessment of mechanical parameters in layered materials could be done by angular waves and geometric acoustics in a non-destructive way. For example, the pitch-catch method has been used to measure the thicknesses and wave velocities of the pristine part and the corrosion layer of the polymeric materials [2]. With regard to these, the application of a spherically focused immersion transducer has been extensively discussed [3, 4]. Since 1998, Hanel et al. [5, 6] have suggested a double focus technique based on geometric acoustics, which has been proved to be an effective tool for assessing mechanical parameters of a thin layer. With this technique, the wave velocity and thickness of a thin layer could be simultaneously determined through a depth scanning of a spherically focused immersion transducer. Some authors have combined this approach with frequency domain analysis to determine the properties of layered materials [7, 8]. Moreover, the researchers have applied this double focus technique to the in-vivo measurement of wave velocity and thickness of the human skull bone [9]. Others have performed this technique using optically resolved optoacoustic transcranial microscopy [10, 11].

However, in the abovementioned cases, only the longitudinal-wave focus is used and discussed. Only one-dimensional signals are evaluated to find the most significant peaks, whereas additional peaks are generally neglected. As a matter of fact, other authors have already described the wave mode conversions at the interface in the layered media composed of the thin film [12, 13]. Thus, the multi-mode waves focusing (MMWF) occurs during depth scanning while the transducer moves vertically. These foci can be seen on the two-dimensional $V(z,t)$ curve, which denotes a two-dimensional amplitude as a function of the displacement of the transducer z and the time t in the time window. The depth scanning and the $V(z,t)$ curve are illustrated in Figure 3-1, where the amplitude changes corresponding to transducer displacement and time. The classic single-mode wave focusing (SMWF) model cannot account for the additional foci in Figure 3-1. Therefore, a novel MMWF model is presented to account for the additional foci in the $V(z,t)$ results correctly.

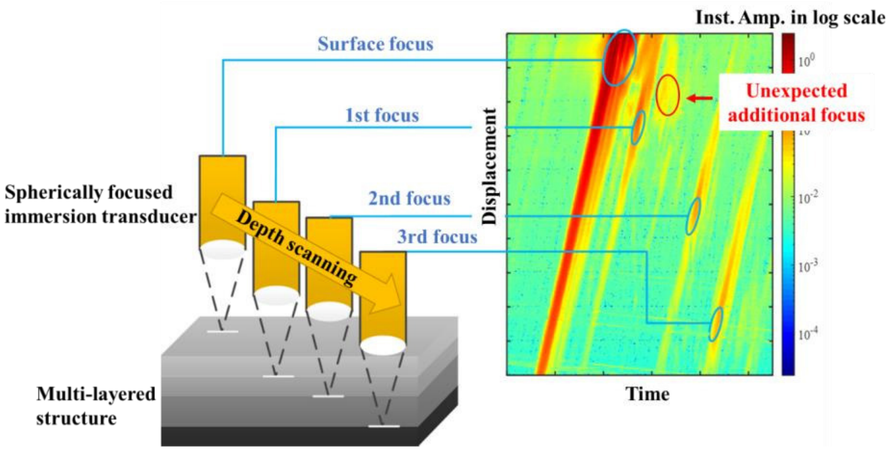

Figure 3-1 Schematic illustration of the variable focus technique and the resulting $V(z,t)$ curve with indications of the foci.

The MMWF ray model is established in Section 3.2. Next, the amplitudes ratios of the reflected focused waves are numerically investigated. The results of the simulation concerning the amplitude and the incident angle are demonstrated in Section 3.3. In Section 3.4, MMWF experiments are performed on thin layers to verify the model. In Section 3.5, the thickness and multi-mode wave velocities are determined based on the MMWF model. The results are discussed in Section 3.6. Finally, a conclusion is given in Section 3.7.

3.2 Theoretical Model

The studies of 0 and 0 are based on two fundamental hypotheses relating to the ultrasonic transducer. First, the wave velocity in the crystals is significantly greater than that of the immersion liquid. Therefore, the aberration in the crystals can be ignored. Secondly, the acoustic lens dimension is significantly greater than the wavelength in the liquid. Therefore, ultrasonic waves can be simplified into rays [14, 15].

3.2.1 Reflection and Transmission Coefficients at the interface

The reflection and transmission coefficients at the interface between a non-viscous liquid and an isotropic solid can be determined according to Chapter 2. Figure 3-2 illustrates the reflection and transmission of ultrasonic waves in a thin layer. The reflection and transmission coefficients are represented as defined in Section 2.4 and derived as follows:

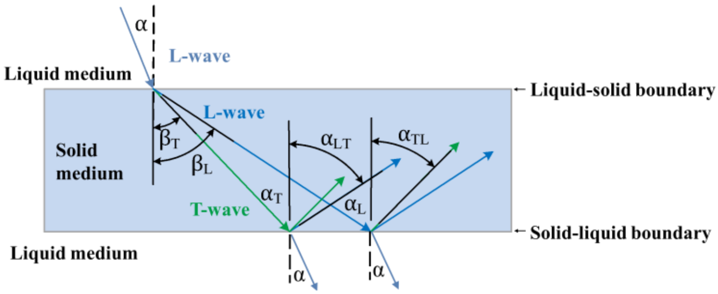

Figure 3-2 Schematic illustration of reflection and transmission of ultrasonic waves in an immersed thin layer.

$$\begin{pmatrix} RLL \\ DLL \\ DLT \end{pmatrix} = M^{-1} \begin{pmatrix} -\cos\alpha \\ k_{L1}\rho c_{l1}^2 \cos 2\alpha \\ 0 \end{pmatrix}, \tag{3.1}$$

$$M = \begin{pmatrix} -\cos\alpha & -\cos\beta_L & \sin\beta_T \\ 0 & k_{L2}(\boldsymbol{\lambda_2} + 2\boldsymbol{\mu_2})\cos 2\beta_T & -k_{T2}\boldsymbol{\mu_2}\sin 2\beta_T \\ 0 & -k_{L2}\boldsymbol{\mu_2}\sin 2\beta_L & -k_{T2}\boldsymbol{\mu_2}\cos 2\beta_T \end{pmatrix}, \tag{3.2}$$

where ρ is the density of the liquid, c_{l1} is the velocity of the wave in the liquid, $\boldsymbol{\lambda_2}$ and $\boldsymbol{\mu_2}$ are Lamé constants of the solid, α is the incident angle in the liquid, β_L and β_T are the refraction angles of longitudinal wave and transverse wave, respectively, k_{L1} is the longitudinal wavenumber in the liquid, $k_{L2} = \frac{\omega}{c_{l2}}(1 + \mathrm{i}\alpha_{l2})$ and $k_{T2} = \frac{\omega}{c_{t2}}(1 + \mathrm{i}\alpha_{t2})$ are longitudinal and transverse wavenumbers in the solid. The refraction angles satisfy Snell's law:

$$\frac{\sin\beta_L}{c_{l2}} = \frac{\sin\beta_T}{c_{t2}} = \frac{\sin\alpha}{c_{l1}}, \tag{3.3}$$

where c_{l2} and c_{t2} are the velocities of the longitudinal and transverse waves in the solid, respectively.

In the event that the wave impinges the interface from the solid medium to the liquid medium, the reflection and transmission coefficients (using the notation system above with an addition of $'$) are:

$$\begin{pmatrix} RLL' \\ RLT' \\ DLL' \end{pmatrix} = N_l^{-1} \begin{pmatrix} -\cos\alpha_L \\ k_{L2}(\boldsymbol{\lambda_2} + 2\boldsymbol{\mu_2})\cos 2\alpha_{TL} \\ -k_{L2}\boldsymbol{\mu_2}\sin 2\alpha_L \end{pmatrix}, \tag{3.4}$$

$$\begin{pmatrix} RTL' \\ RTT' \\ DLT' \end{pmatrix} = N_t^{-1} \begin{pmatrix} \sin\alpha_T \\ -k_{T2}\boldsymbol{\mu_2}\sin 2\alpha_T \\ -k_{T2}\boldsymbol{\mu_2}\cos 2\alpha_T \end{pmatrix}, \tag{3.5}$$

where

$$N_l = \begin{pmatrix} -\cos\alpha_L & \sin 2\alpha_{TL} & -\cos\alpha \\ -k_{L2}(\boldsymbol{\lambda_2} + 2\boldsymbol{\mu_2})\cos 2\alpha_{TL} & k_{T2}\boldsymbol{\mu_2}\sin 2\alpha_{TL} & 0 \\ -k_{L2}\boldsymbol{\mu_2}\sin 2\alpha_L & -k_{T2}\boldsymbol{\mu_2}\cos 2\alpha_{TL} & 0 \end{pmatrix} \quad (3.6)$$

$$N_t = \begin{pmatrix} -\cos\alpha_{LT} & \sin\alpha_T & -\cos\alpha \\ -k_{L2}(\boldsymbol{\lambda_2} + 2\boldsymbol{\mu_2})\cos 2\alpha_T & k_{T2}\boldsymbol{\mu_2}\sin 2\alpha_T & 0 \\ -k_{L2}\boldsymbol{\mu_2}\sin 2\alpha_{LT} & -k_{T2}\boldsymbol{\mu_2}\cos 2\alpha_T & 0 \end{pmatrix}, \quad (3.7)$$

α_L and α_T are the incident angles of longitudinal and transverse waves in the solid media, respectively, α_{TL} and α_{LT} are the reflection angles for longitudinal-to-transverse mode-converted wave and transverse-to-longitudinal mode-converted wave, respectively. The reflection angles satisfy Snell's law:

$$\frac{\sin\alpha_{TL}}{c_{t2}} = \frac{\sin\alpha_L}{c_{l2}}, \quad (3.8)$$

$$\frac{\sin\alpha_{LT}}{c_{l2}} = \frac{\sin\alpha_T}{c_{t2}}. \quad (3.9)$$

3.2.2 Multi-mode waves focusing (MMWF)

If an ultrasonic wave impinges an immersed solid layer, the longitudinal waves reflecting in the liquid have three types of foci. These refer to the transverse-wave, longitudinal-wave, and mode-conversion-wave foci. It is worth pointing out that two mode-conversion-wave foci involve longitudinal-to-transverse and transverse-to-longitudinal reflections on the back surface of the solid, and as such, have identical focusing heights.

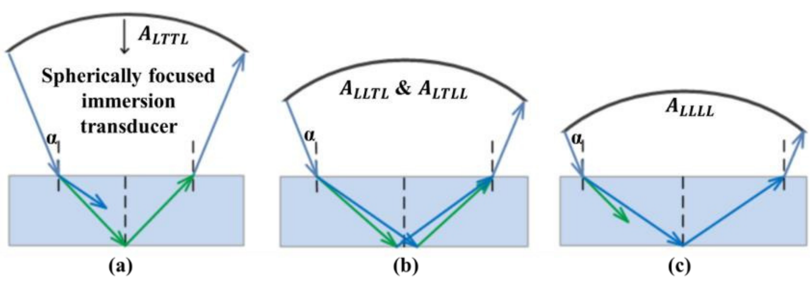

Figure 3-3 Schematic of four types of foci in a solid layer. These are (a) transverse-wave, (b) mode-conversion-wave, and (c) longitudinal-wave foci.

The wave is assumed to reach the solid layer at an incident angle α, and is initially focused on the front surface of the layer. According to the geometric relation and Snell's law, the displacement d_f required to focus on the back surface of the layer is:

$$d_f = \frac{d c_f \cos\alpha}{c_{l1}\sqrt{1-\sin^2\alpha \frac{{c_f}^2}{{c_0}^2}}}, \tag{3.10}$$

where d is the thickness of the single solid layer, and c_f is the equivalent wave velocity within the solid layer.

3.3 Numerical Simulation

First, Table 3-1 lists the nomenclature of amplitude ratios of the focused reflected waves on a solid layer. These amplitude ratios are:

$$A_{LLLL} = DLL \times RLL' \times DLL', \tag{3.11}$$
$$A_{LTTL} = DTL \times RTT' \times DLT', \tag{3.12}$$
$$A_{LTLL} = DTL \times RLT' \times DLL', \tag{3.13}$$
$$A_{LLTL} = DLL \times RTL' \times DLT', \tag{3.14}$$

where DLL, DTL DLL', DLT', RLL', RTT', RLT', RTL' can be derived as described in Section 3.2.1. The properties of the samples used for the simulation are given in

Table 3-2. The measured center frequency of the ultrasonic signal is 57 MHz in the experimental study. The amplitude ratios of the focused reflected waves, corresponding to the incident angle ranging from 0° to the critical angle, are shown in Figure 3-4. With regards to the mode-conversion wave, the mean wave velocity of longitudinal and transverse waves is used.

Table 3-1 Nomenclature of amplitude ratios of the focused reflected waves

Symbol	Incident wave mode		Reflected wave mode	
	Stage 1: liquid	Stage 2: solid	Stage 1: solid	Stage 2: liquid
A_{LLLL}	Longitudinal	Longitudinal	Longitudinal	Longitudinal
A_{LTTL}	Longitudinal	Transverse	Transverse	Longitudinal
A_{LTLL}	Longitudinal	Transverse	Longitudinal	Longitudinal
A_{LLTL}	Longitudinal	Longitudinal	Transverse	Longitudinal

Table 3-2 The reference properties of the samples used for numerical simulation

Sample	Thickness	c_{l2}	c_{t2}	α_{l2}	α_{t2}
Stainless steel	0.5 mm	5950 m/s	3200 m/s	0.029	0.032
Aluminum alloy	0.5 mm	6260 m/s	3080 m/s	0.022	0.024

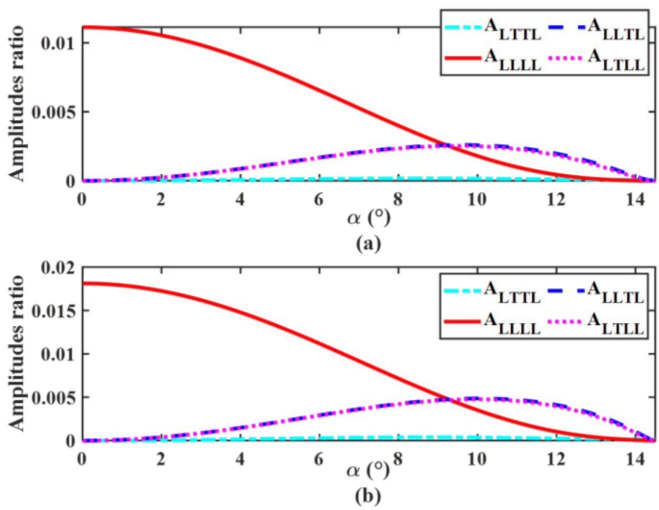

Figure 3-4 Amplitude ratios of the focused reflected waves for (a) stainless steel and (b) aluminum alloy layers.

3.4 Experimental Study

3.4.1 Experimental setup

A 3-axis Cartesian scanner with depth scanning function is used, on which the ultrasonic transducer is mounted. The ultrasonic transducer is a V3346 spherically focused immersion transducer provided by the Olympus Corporation, Japan. The measured center frequency of the signal is 57 MHz, while the -3 dB bandwidth ranges from 37 MHz to 72 MHz. The transducer has a focal distance of 6.35 mm and a half-aperture angle of 13.8°. The signal is acquired at a sampling rate of 400 MS/s. The water temperature T is maintained at 25°. The wave velocity in water is 1497 m/s according to the formula $v_{l1} = 1404.3 + 4.7T - 0.04T^2$, where temperature T in degrees Celsius [16]. The single-layer samples are stainless steel plate and aluminum alloy plate, each 0.5 mm thick. Samples are immersed in water and suspended under the immersion transducer. Then the transducer is initially focused on the front surface of the sample prior to the automatic depth scanning with a vertical position precision is 0.5 μm.

3.4.2 Results

The $V(z,t)$ curve is obtained by depth scanning for each sample. Figure 3-5 shows the $V(z,t)$ curves, on which the peaks of the multi-mode wave foci are indicated.

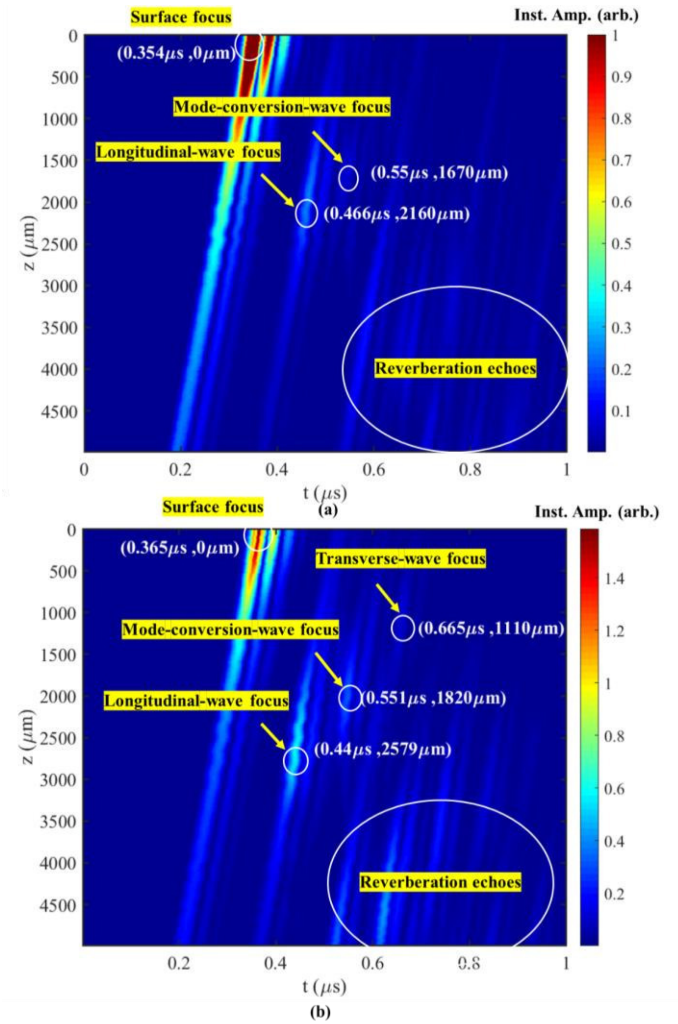

Figure 3-5 $V(z,t)$ curves for (a) the 0.5 mm thick stainless steel layer and (b) the 0.5 mm thick aluminum alloy layer. The peaks of the multi-mode wave foci are indicated.

The z-coordinate is initialized at zero on the curve when the focal point is located on the front surface of the solid layer. The longitudinal-wave, mode-conversion-wave, and transverse-wave foci are identified as the first, second, and third peaks. They all lag behind front-wall echo (FWE) in the time domain. Note that the signal-to-noise ratio (SNR) of transverse-wave foci is considerably low, particularly for the stainless steel (see Figure 3-5a). The vertical displacements of the transducer for moving the focal point from the front surface to the back surface of the layer can be calculated according to Eq. (3.10). The simulation curves illustrating the relation between the vertical displacement and the incident angle α are shown in Figure 3-6.

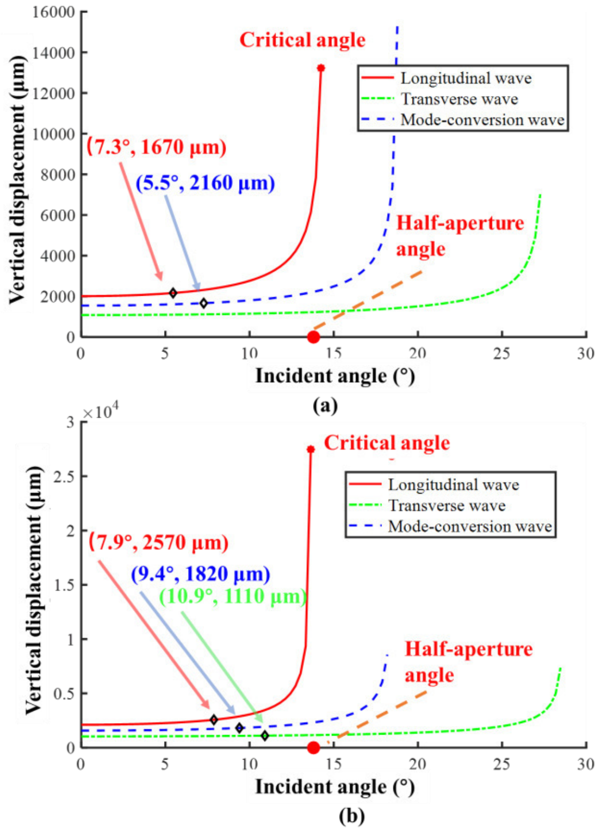

Figure 3-6 Curves illustrating the relation between z and α for different foci on the back surfaces of (a) the 0.5 mm thick stainless steel layer and (b) the 0.5 mm thick aluminum alloy layer respectively. Diamond marks show the corresponding incident angle according to the focal points in Figure 3-5.

In the next step, the incident angle α related to the displacements z from the curves above is obtained (see black diamonds in Figure 3-6). The z and α for the foci are shown in Table 3-3.

Table 3-3 The experimental and simulation parameters for reflected multi-mode wave foci in the $V(z,t)$ curves

Material	Focal wave mode	z (μm)	α (°)	Exp. amp.	Num. amp. ratio
Stainless steel	Longitudinal	2160	5.5	0.133	0.0073
Stainless steel	Mode-conversion	1670	7.4	0.063	0.0022 & 0.0022
Stainless steel	Transverse	-	-	-	-
Aluminum alloy	Longitudinal	2570	7.9	0.508	0.0220
Aluminum alloy	Mode-conversion	1820	9.4	0.258	0.0095 & 0.0095
Aluminum alloy	Transverse	1110	10.9	0.08	0.0001

The multi-mode wave foci are identified by the peaks on the $V(z,t)$ curves in Figure 3-5. The temporal signals for the foci are shown in Figure 3-7 and Figure 3-8. The blue tracks represent the recorded signals and the orange tracks represent the instantaneous amplitude of the recorded signals. The experimental amplitude values for the foci can be read from Figure 3-5 and listed in Table 3-3. Then, using the corresponding incident angle, the simulation amplitude ratios for the foci in the two materials can be calculated based on the curves in Figure 3-4 and listed in Table 3-3. Note that The experimental amplitude is an absolute measured value, while the numerical amplitude ratio is a relative value.

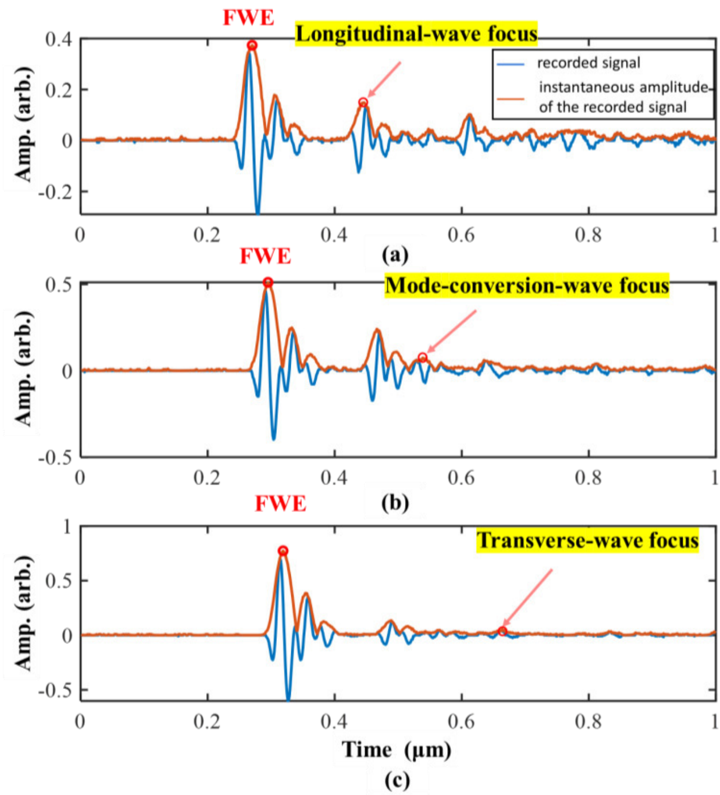

Figure 3-7 Temporal signals for (a) longitudinal, (b) mode-conversion, and (c) transverse wave foci on the 0.5 mm thick stainless-steel layer.

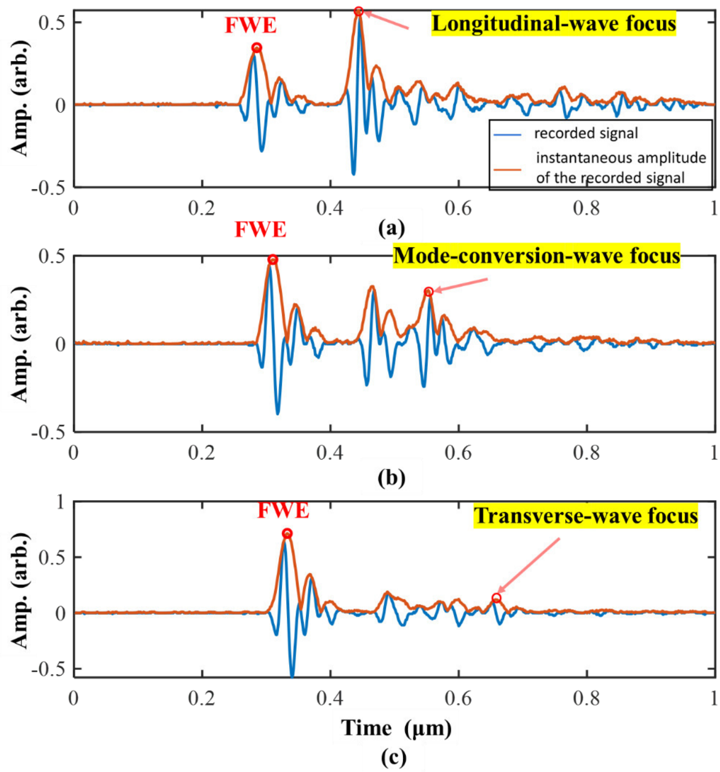

Figure 3-8 Temporal signals for (a) longitudinal, (b) mode-conversion, and (c) transverse wave foci on the 0.5 mm thick aluminum-alloy layer.

3.5 Characterization of thickness and multi-mode wave velocities

By employing the double focus technique, the thickness and the multi-mode wave velocities can be simultaneously determined [5, 7]. The thickness d of the solid layer and the equivalent wave velocity c_f within the solid layer are calculated by

$$c_f = \sqrt{\frac{2d_f {c_{l1}}^2}{\cos\alpha\, \Delta t c_{l1} + 2d_f}}, \tag{3.15}$$

$$d = \frac{d_f c_{l1} \cos\beta}{c_f \cos\alpha}, \tag{3.16}$$

where Δt is the time delay between the FWE and the foci, and β is the refraction angle. Here, the incident angle is assumed to be a constant 8° because the actual incident angle is not pre-known. It is also validated that it does not equal the half-aperture angle. The measured and the reference properties of the stainless-steel and aluminum-alloy layers are listed in Table 3-4. The reference thicknesses are measured by a micrometer with a resolution of 10 μm. Note that a method to estimate the approximate incident angle is given in the following chapter to tackle this issue for thicker multi-layer samples.

Table 3-4 The measured and the reference thickness and multi-mode wave velocities

Material	Focal wave mode	c_f (m/s)	Reference velocity (m/s)	d (mm)	Reference thickness (mm)
Stainless steel	Longitudinal	5472	5950	0.51	0.50
Stainless steel	Mode-conversion	4261	4575	0.54	0.50
Stainless steel	Transverse	-	-	-	-
Aluminum alloy	Longitudinal	6217	6260	0.51	0.50
Aluminum alloy	Mode-conversion	4470	4670	0.56	0.50
Aluminum alloy	Transverse	3077	3080	0.52	0.50

3.6 Discussion

The SMWF model is a handy approach since the numerical and experimental results explicitly indicate that the amplitude of the longitudinal-wave focus is considerably greater than those of other foci. However, the MMWF model interprets the occurrence of multi-mode foci, which allows identifying longitudinal-wave foci in $V(z,t)$ curves. For such a case, it would be hard to recognize the waveforms without an understanding of MMWF. Some discussions in detail are presented as follows.

3.6.1 Incident angles for foci

In earlier work, half-aperture angles were commonly referred to as incident angles [5-8], where a thinner layer and a lower half-aperture angle of 6° were used. However, in this chapter, the simulation and the experimental results indicate that the incident angle does not equal the half-aperture angle. Some studies have also demonstrated that the transducer's effective diameter is less than its nominal size [17], which could partly account for the results. Moreover, the main contribution to the signal amplitude comes from the rays in the central part of the acoustic lens [15]. Therefore, the peaks do not precisely match the foci for the incident wave with a half-aperture angle. There is also evidence that the amplitudes are rising and dropping very slowly around the $V(z,t)$ curve peaks. Thus, considering the prospect of the ray model, an angle between zero and the half-aperture angle should be considered as the incident angle when peaks appear. In a more complex way, a model should be established by integrating the source over the entire emission area of the ultrasonic transducer. In conclusion, we can see the significant effect of the incident angle, which should not be simply referred to as the half-aperture angle.

3.6.2 Amplitudes for multi-mode wave foci

The amplitude ratios for longitudinal-wave focus and mode-conversion-wave focus are much greater than those of the transverse-wave focus in numerical simulation (see Section 3.3). The low SNR of the transverse-wave foci in experiments is thus consistent with the simulation results. The simulation and the experimental amplitudes for the mode-conversion-wave foci are both nearly half of those for the longitudinal-wave foci (see Table 3-3). Furthermore, although two types of mode-conversion-wave foci have similar transition times, they are not located on the center axis of the lens. This fact could be the reason for the complex peak-shapes of the mode-conversion-wave foci in Figure 3-5 and the separated amplitude values in the 3rd and 6th rows in Table 3-3. Also, the results for the mode-conversion wave in Table 3-4 have relatively more significant errors.

3.7 Conclusion

The double focus technique is a practical approach for simultaneous determination of thickness and wave velocity. The one-dimensional signal has been commonly used based on the single-mode wave focusing model. In this chapter, a new MMWF model is presented to interpret the results of depth scanning on thin solid plates. This proposed model fully accounts for the phenomenon of mode conversion. The distribution of energy among multi-mode waves and the transducer displacements during MMWF are numerically analyzed. Experiments are performed on a 0.5 mm thick stainless steel layer and a 0.5 mm thick aluminum alloy layer. The thickness and multi-mode wave velocities are simultaneously extracted from the thin layer. It is pointed out that the transducer displacement and the amplitude for the foci are closely related to the incident angle, which is not precisely the half-aperture angle. The new model is valuable for a comprehensive understanding of the depth-scanning results. It provides a supplementary technical basis for the variable focus technique, presented in the following chapter.

References

[1] Hsu, C.-H., Chang, Y.-W., and Nassif, S. R., 2011, "Simultaneous layout migration and decomposition for double patterning technology," IEEE Transactions on Computer-Aided Design of Integrated Circuits and Systems, 30(2), pp. 284-294.

[2] Kusano, M., Takizawa, S., Sakai, T., Arao, Y., and Kubouchi, M., 2018, "Simultaneous sound velocity and thickness measurement by the ultrasonic pitch-catch method for corrosion-layer-forming polymeric materials," Ultrasonics, 82, pp. 178-187.

[3] Chung, C.-H., and Lee, Y.-C., 2009, "Broadband poly (vinylidene fluoride-trifluoroethylene) ultrasound focusing transducers for determining elastic constants of coating materials," Journal of Nondestructive Evaluation, 28(3-4), p. 101.

[4] Lin, S., Shams, S., Choi, H., and Azari, H., 2018, "Ultrasonic imaging of multi-layer concrete structures," Ndt&E Int, 98, pp. 101-109.

[5] Haenel, V., and Kleffner, B., 1999, "Double focus technique for quantitative measurements in time‐resolved acoustic microscopy," The Journal of the Acoustical Society of America, 105(2), pp. 1015-1015.

[6] Hänel, V., 1998, "Measurement of sound velocity and thickness of thin samples by time-resolved acoustic microscopy," Journal of applied physics, 84(2), pp. 668-670.

[7] Bai, X., Sun, Z., Sun, A., Chen, J., and Ju, B.-F., 2014, "Determination of the multiple local properties of thin layer with high lateral resolution by scanning acoustic microscopy," Review of Scientific Instruments, 85(9), p. 094901.

[8] Chen, J., Bai, X., Yang, K., and Ju, B.-F., 2015, "Simultaneously measuring thickness, density, velocity and attenuation of thin layers using V (z, t) data from time-resolved acoustic microscopy," Ultrasonics, 56, pp. 505-511.

[9] Wydra, A., Malyarenko, E., Shapoori, K., and Maev, R. G., 2013, "Development of a practical ultrasonic approach for simultaneous measurement of the thickness and the sound speed in human skull bones: a laboratory phantom study," Physics in Medicine & Biology, 58(4), p. 1083.
[10] Estrada, H., Rebling, J., Turner, J., and Razansky, D., 2016, "Broadband acoustic properties of a murine skull," Physics in Medicine & Biology, 61(5), p. 1932.
[11] Estrada, H., Huang, X., Rebling, J., Zwack, M., Gottschalk, S., and Razansky, D., 2018, "Virtual craniotomy for high-resolution optoacoustic brain microscopy," Scientific reports, 8(1), pp. 1-9.
[12] Lazri, H., Ogam, E., Amar, B., Fellah, Z., Oduor, A. O., and Baki, P., 2017, "Identification of the mechanical moduli of flexible thermoplastic thin films using reflected ultrasonic waves: Inverse problem," Ultrasonics, 81, pp. 10-22.
[13] Ogam, E., Fellah, Z. E. A., and Ogam, G., 2016, "Identification of the mechanical moduli of closed-cell porous foams using transmitted acoustic waves in air and the transfer matrix method," Compos Struct, 135, pp. 205-216.
[14] Briggs, A., Briggs, G., and Kolosov, O., 2010, Acoustic microscopy, Oxford University Press.
[15] Maev, R. G., 2008, Acoustic microscopy: Fundamentals and applications, John Wiley & Sons.
[16] Lubbers, J., and Graaff, R., 1998, "A simple and accurate formula for the sound velocity in water," Ultrasound in medicine & biology, 24(7), pp. 1065-1068.
[17] Gray, T. A., 1995, "Model-based characterization of planar and focused immersion ultrasonic transducers," Review of Progress in Quantitative Nondestructive Evaluation, Springer, pp. 1021-1028.

Chapter 4 Variable Focus Technique for Multi-layer Functionally Graded Material

4.1 Introduction

With the application of a spherically focused immersion transducer, a thin layer's thickness and wave velocity can be simultaneously measured [1, 2]. As indicated in 0, the depth-scanning results, where multi-mode wave foci occur, must be interpreted more sophisticatedly. Fortunately, the model proposed in 0 has successfully interpreted the depth-scanning results, thus providing the technical basis for the variable focus technique for the multi-layer materials.

The primary work of this chapter is to develop the explanatory framework of the variable focus technique for multi-layer material. First, a 'Bottom Left' principle is proposed using the multi-mode waves focusing (MMWF) model in Chapter 3 to identify the longitudinal-wave foci in the $V(z,t)$ curve. On the merit of this principle, different wave modes are identified, and the most representative longitudinal wave can be used. In addition, the signal composition has been demonstrated to be influenced by the phase differences between waves with different incident angles [3]. In view of this, a phase differentiation theory is also proposed to determine the incident angle for focused waves. Finally, through the new explanatory framework of the variable focus technique, the thickness and wave velocity of the functionally graded material (FGM) are determined from the $V(z,t)$ curve without any prior knowledge.

This chapter is organized as follows. The theoretical model is introduced in Section 4.2. Subsequently, the phase differentiation theory is presented in Section 4.3. The experiments are performed on FGMs to validate the technique in Section 4.4. Finally, the conclusion is given in Section 4.5.

4.2 Theoretical Model

4.2.1 'Bottom Left' principle

The longitudinal wave, mode-conversion wave, and transverse wave (see 0) contribute to the output signal (see Figure 4-1). Thus, three fundamental wave modes could produce the output signal: longitudinal wave, transverse wave, and mode-conversion wave.

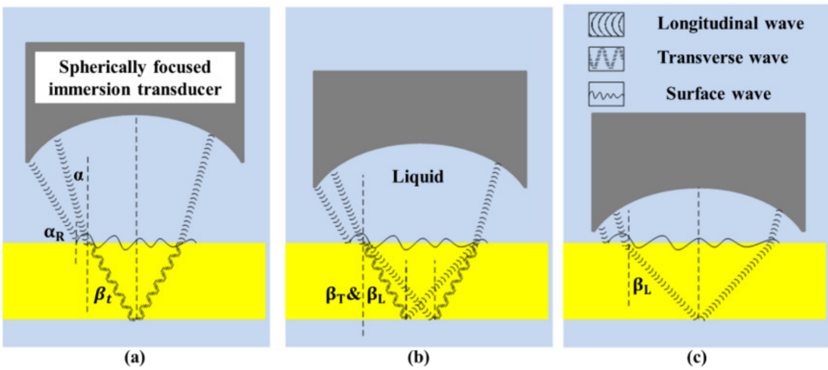

Figure 4-1 Theoretical model of the multi-mode waves propagating in a single layer and the foci of (a) transverse wave, (b) mode-conversion wave, and (c) longitudinal wave.

Due to the fact that the velocity of the transverse wave is significantly lower than the longitudinal wave, focusing on the back surface will happen sequentially. As the transducer moves down, the transverse wave first focuses on the back surface, as shown in Figure 4-1a. The mode-conversion wave focuses secondly, as shown in Figure 4-1b. Finally, the longitudinal wave focuses thirdly, as shown in Figure 4-1c. It is noted that the time-of-flight (TOF) measurements of the three foci instead suggest the opposite order. Thus, there are three types of foci in the $V(z, t)$ curve via depth scanning for the multi-layer material. The longitudinal-wave foci can be clearly identified since it always leads in the time domain but lags in the displacement domain. This principle is here defined as the 'Bottom Left' principle due to the fact that longitudinal-wave foci always appear in the bottom (lags in the displacement z) and left (leads in the time t) positions in the $V(z, t)$ curve.

4.2.2 Multi-layer single-mode wave focusing

In this section, the longitudinal wave focusing for multi-layer materials is studied. As the longitudinal wave with an incident angle of α focuses on the back surface of the multi-layer structure, the geometric relation of the longitudinal wave in the multi-layer structure (see the dotted and solid lines in Figure 4-2) can be written as

$$d_f \tan \alpha = \sum_{i=1}^{n} d_i \tan \beta_i, \tag{4.1}$$

where d_i is the thickness of layer i, β_i is the refraction angle in layer i, d_f is the vertical displacement required to focus on the back surface.

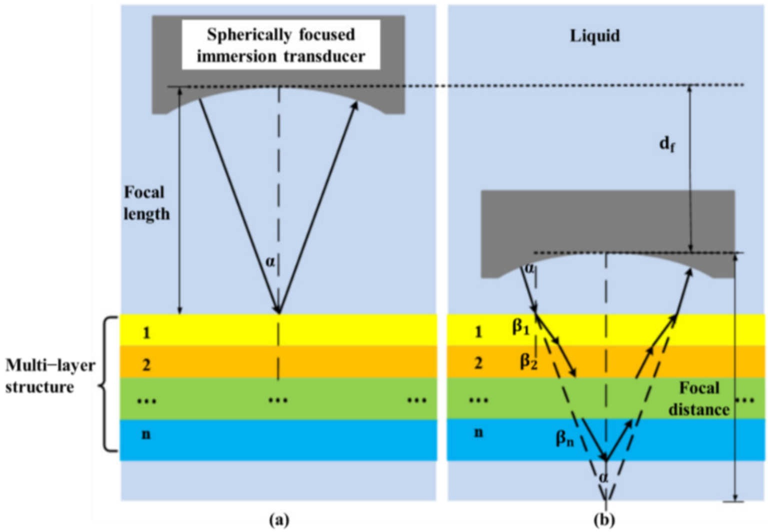

Figure 4-2 Theoretical model of (a) the longitudinal-wave focus in the surface and (b) the focused bulk wave propagating in a multi-layer structure.

Snell's law is here represented as follows:

$$\frac{\sin\alpha}{c_0} = \frac{\sin\beta_n}{c_n}, \tag{4.2}$$

where c_0 is the wave velocity in liquid, and c_i is the wave velocity in layer i. The TOF for the focus on the front surface (Figure 4-2a) and the focus on the back surface of layer n (Figure 4-2b) are

$$T_0 = \frac{2F_l}{c_0}, \tag{4.3}$$

$$T_n = \frac{2F_l}{c_0} - \frac{2d_f}{c_0\cos\alpha} + \sum_{i=1}^{n} \frac{2d_i}{c_i\cos\beta_i}, \tag{4.4}$$

where F_l is the focal distance in the liquid. T_0, T_n, and d_f can be extracted by evaluating the peaks in the $V(z,t)$ curve. As such, based on Eqs. (4.1), (4.2), (4.3), and (4.4), c_n, β_n, and d_n can be formulated as

$$c_n = \sqrt{\frac{\frac{2d_f c_0}{\cos\alpha} - \sum_{i=1}^{n-1}\frac{2h_i c_i}{\cos\beta_i}}{T_n - T_0 + \frac{2d_f}{c_0\cos\alpha} - \sum_{i=1}^{n-1}\frac{2h_i}{c_i\cos\beta_i}}}, \tag{4.5}$$

$$\beta_n = \sin^{-1}\left(\frac{c_n}{c_0}\sin\alpha\right), \tag{4.6}$$

$$d_n = \left(\frac{d_f c_0}{\cos\alpha} - \sum_{i=1}^{n-1}\frac{d_i c_i}{\cos\beta_i}\right)\frac{\cos\beta_n}{c_n}. \tag{4.7}$$

4.3 Phase Differentiation Theory

Now we reconsider Eq. (3.10) with respect to α. It has been demonstrated that rays with different incident angles do not focus simultaneously because of different refraction angles. More specifically, larger incident angles require larger vertical displacements of the transducer. In other words, there is actually not a perfect position where all rays over the entire emission area of the transducer focus on the same point.

It is worth noting that the signal analysis relies on the approximation hypothesis that the main contribution to the signal amplitude comes from the rays arriving from the central part of the lens [4]. For instance, we use the central paraxial ray at normal incidence as a reference (see Figure 4-2b). The TOF of the central paraxial ray (t_c) and the peripheral ray with an incident angle α (t_e) are

$$t_c = 2\left(\frac{F_l - d}{c_0} + \sum_{i=1}^{n}\frac{d_i}{c_i}\right), \tag{4.8}$$

$$t_e = 2\left(\frac{F_l}{c_0} - \frac{d}{c_0\cos\alpha} + \sum_{i=1}^{n}\frac{d_i}{c_i\cos\beta_i}\right). \tag{4.9}$$

The peripheral ray originates from the peripheral region of the lens. It can be seen that there is a time difference between the rays with different incident angles due to the refraction in solid. Note that the signal is not simply the amplitude of the rays since the rays have different phases. Thus, the phase difference between the central paraxial ray and the peripheral rays influences the composition of the signal. A simplification of the actual situation, the rays are considered as sine waves. Therefore, it can be assumed that the peripheral ray could reduce the signal mainly composed of the central paraxial ray when the phase difference β reaches a particular value. Whereas, the incident angle α of the focused wave is not previously known, as indicated in 0. As a result, a solution is to consider all possible angles within the maximum half-aperture angle before computing the β to find an incident angles of the focused wave. The abovementioned assumption is named Phase Differentiation theory in this chapter.

It is here assumed that the peaks in the $V(z,t)$ curve happen where the phase difference β satisfies the condition:

$$\beta = 2\pi F_c(t_c - t_e) < \frac{\pi}{2}, \tag{4.10}$$

where F_c is the center frequency of the signal. Note that this critical phase difference $\frac{\pi}{2}$ is an approximate value on the condition that rays are considered as sine waves.

4.4 Experimental Study

4.4.1 Measurement method

The longitudinal-wave foci are first identified through the $V(z,t)$ curve peaks based on the 'Bottom Left' principle in Section 4.2.1. Both vertical movement z and TOF $\Delta t_i = T_i - T_1$ can be obtained through the positions of the foci in the $V(z,t)$ curve, where T_i represents the actual time-coordinate of peak i and T_1 is the actual time-coordinate of the first peak with $z = 0$. The time-domain curves are aligned (for visualization purposes) by moving the time window. Thus the actual time coordinate of the peak i is

$$T_i = T - \frac{2z_{inc}d_f}{f_s\Delta d}, \tag{4.11}$$

where T is the original time coordinate in the $V(z,t)$ curve, z_{inc} is the increment for the time window, Δd is the step of the vertical displacement, and f_s is the sampling rate. Based on the analysis in Section 4.3, the incident angle and the thickness are measured in order to satisfy the phase-difference condition $\beta = \frac{\pi}{2}$. Then, the wave velocity and thickness of each layer are derived according to the formulas in Section 4.2.2.

4.4.2 Experimental setup

A 3-axis Cartesian scanner with the depth scanning function is used, on which the ultrasonic transducer is mounted. The transducer is a V390 spherically focused immersion transducer provided by the Olympus Corporation, Japan. The measured center frequency of the signal is 48 MHz, while the -3 dB bandwidth ranges from 41 MHz to 57 MHz. The focal distance is 12.7 mm, and the half aperture angle is 14.5°. The sampling rate is 400 MS/s. The $V(z,t)$ curves are obtained by using depth scanning. The vertical position precision is 0.5 μm. The temperature is 27.3℃, for which the wave velocity in water is 1503 m/s. The transducer is initially focused on the front surface of the layer prior to the automatic depth scanning.

The single-layer experiments are performed for simultaneous thickness and multi-mode wave-velocity measurements on two stainless-steel plates with thicknesses of 1.5 mm and 2.0 mm, respectively. Afterward, the thickness and longitudinal-wave-velocity of each layer in graded metallic materials are simultaneously characterized.

4.4.3 Results

4.4.3.1 Stainless-steel plates

The $V(z,t)$ curve for the 2.0 mm stainless-steel plates is shown in Figure 4-3. The phase difference β and calculated thickness corresponding to α are shown in Figure 4-4. The estimated incident angle and measured thickness are determined based on the critical phase difference (see red lines and red circles in Figure 4-4). The measurement is repeated 20 times before the mean and standard deviation are calculated. The same procedures are applied on the 1.5 mm stainless-steel plates to measure the properties. The measured and the reference properties of the stainless-steel plates are listed in Table 4-1 and Table 4-2, wherein Peak 1,2,3 represent longitudinal-wave, mode-conversion-wave, and transverse-wave foci, respectively.

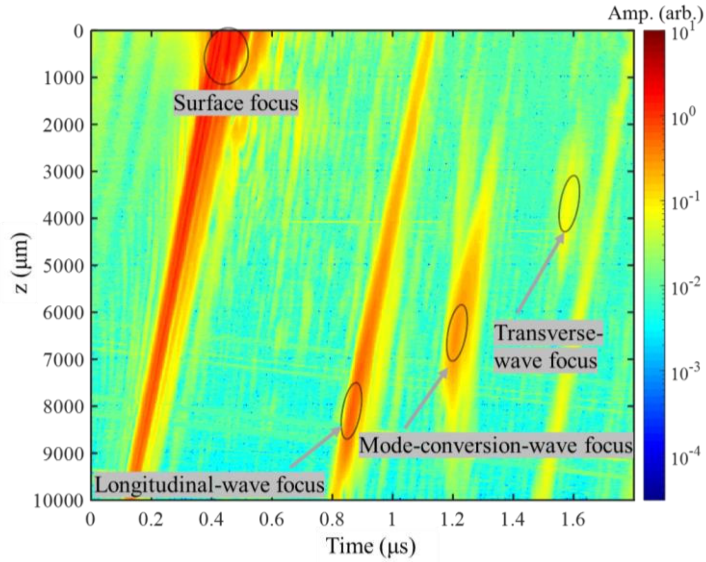

Figure 4-3 $V(z,t)$ curves for the 2.0 mm thick stainless-steel layers respectively, with the indication of multi-mode wave foci.

The measured thicknesses are consistent with the reference thicknesses of the stainless-steel plates. The measured longitudinal and transverse waves velocities (Peak 1 and 3) agree with the reference velocities. Moreover, the measured wave velocity of the mode-conversion wave (Peak 2) is about half of the sum of the longitudinal and transverse wave velocities. The single-layer experiments confirm the occurrence of multi-mode waves, which accords to the study in 0. Furthermore, it can be observed that the transverse-wave and the mode-conversion-wave foci lag in the time domain but lead in the displacement domain, which also verifies the 'Bottom Left' principle for the following multi-layer material experiments.

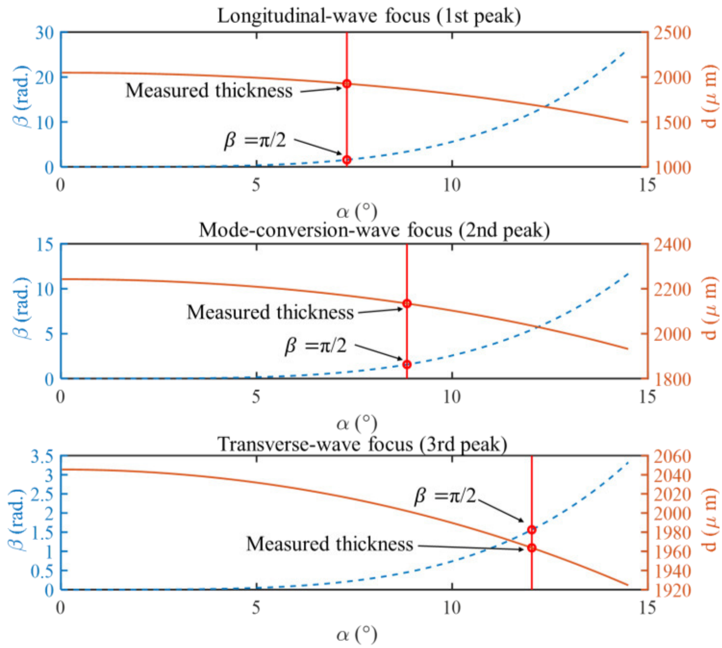

Figure 4-4 Phase difference β and measured thickness d corresponding to α for the stainless steel with a thickness of 2.0 mm.

Table 4-1 The measured and the reference properties of the stainless steel with a thickness of 1.5 mm

Peak	Measured Properties (mean±3σ)			Reference Properties		
	α (°)	$c\ (m/s)$	$d\ (\mu m)$	$c_t\ (m/s)$	$c_l\ (m/s)$	$d\ (\mu m)$
1	7.75±0.19	5584±129	1454±42	3100	5790	1500
2	9.51±0.68	4261±272	1592±122			
3	12.8±1.36	3073±280	1489±132			

Table 4-2 The measured and the reference properties of the stainless steel with a thickness of 2.0 mm

Peak	Measured Properties (mean±3σ)			Reference Properties		
	α (°)	$c\ (m/s)$	$d\ (\mu m)$	$c_t\ (m/s)$	$c_l\ (m/s)$	$d\ (\mu m)$
1	7.17±0.23	5708±298	1933±85	3100	5790	1970
2	8.83±0.24	4315±204	2107±137			
3	11.90±0.71	3114±149	1980±129			

4.4.3.2 5-layer TC4-OFC-Mo-Ta-93W FGM

The studied metallic graded material is a thin TC4-OFC-Mo-Ta-93W 5-layer sheet (see Figure 4-5). The problem of reverberation rises when the wave reaches deep layers due to the multiple reflections. Moreover, the focal distance is not large enough to focus on the back surface of the material. Consequently, two depth scanning have been respectively performed on the two sides of this sample.

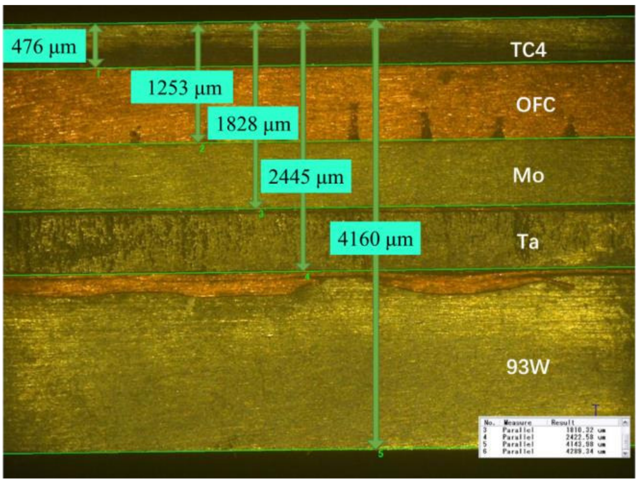

Figure 4-5 Side view under optical microscopy of the 5-layer metallic graded material.

The $V(z,t)$ curve for the TC4-OFC-Mo 3-layers is shown in Figure 4-6. The longitudinal-wave foci are identified by using the 'Bottom Left' principle. The phase difference β and calculated thickness correspond to α are shown in Figure 4-7. The estimated incident angle and measured thickness are determined based on the critical phase difference (see red lines and red circles in Figure 4-7). The measurement is repeated 20 times before the mean and standard deviation are calculated. The measured and the reference thicknesses and velocities of the TC4-OFC-Mo 3-layers are listed in Table 4-3, wherein Peak 1,2,3 represent longitudinal-wave foci of the first layer, second layer, and third layers, respectively.

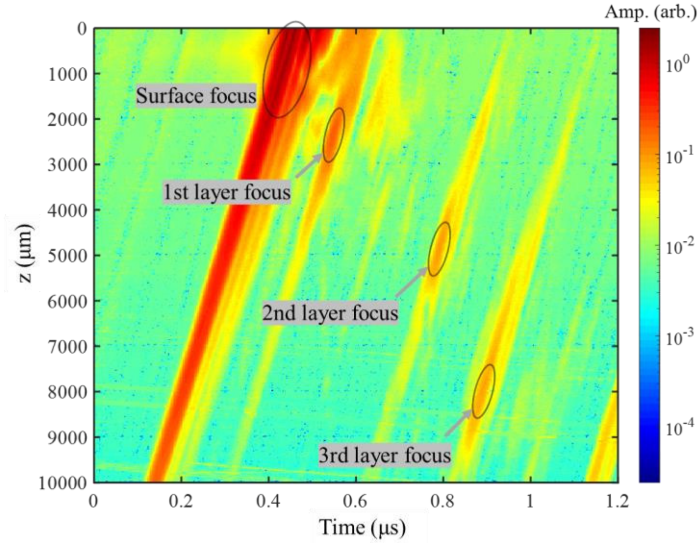

Figure 4-6 $V(z,t)$ curve of the TC4-OFC-Mo 3-layers with the indication of longitudinal-wave foci.

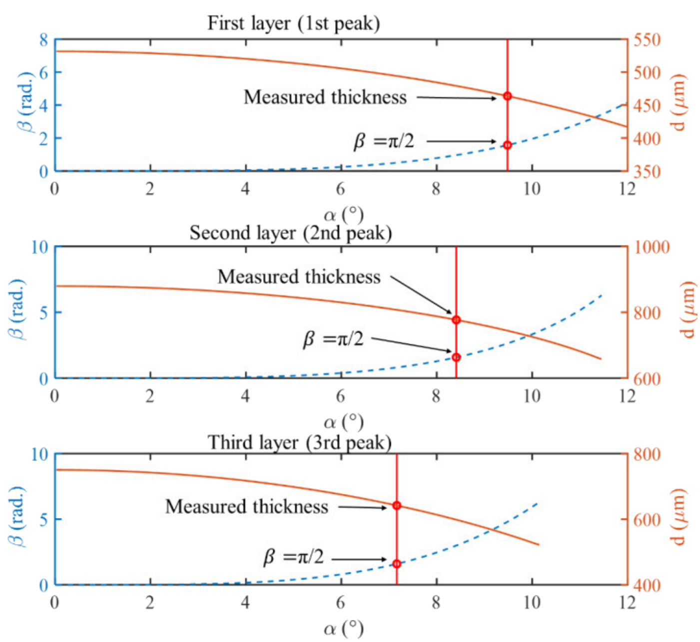

Figure 4-7 Phase difference β and calculated thickness corresponding α for the TC4-OFC-Mo 3-layers.

Table 4-3 The measured and the reference properties of the TC4-OFC-Mo 3-layers

Peak	Measured Properties (mean±3σ)			Reference Properties		
	α (°)	c_n (m/s)	d_n (μm)	Material	c_l (m/s)	d_n (μm)
1	9.08±0.66	6120±428	462±36	TC4	6171	476
2	8.19±0.37	4883±329	760±44	OFC	4763	777
3	7.00±0.36	6616±654	632±62	Mo	6250	575

The same procedure as above is applied to the depth-scanning result ($V(z,t)$ curve) on the other side of the metallic graded material. The measured and the reference thicknesses and velocities of the 93W-Ta 2-layers on the other side are listed in Table 4-4.

Table 4-4 The measured and the reference properties of the 93W-Ta 2-layers

Peak	Measured Properties (mean±3σ)			Reference Properties		
	α (°)	c_n (m/s)	d_n (μm)	Material	c_l (m/s)	d_n (μm)
1	8.01±0.22	5127±129	1721±48	93W	5162	1715
2	7.73±0.19	4125±540	650±93	Ta	4242	617

4.4.3.3 7-layer W-SiCP/Cu FGM

The studied material is a 7-layer W-SiCP/Cu FGM [5, 6]. The SEM image and the designed density gradient are displayed in Figure 4-8.

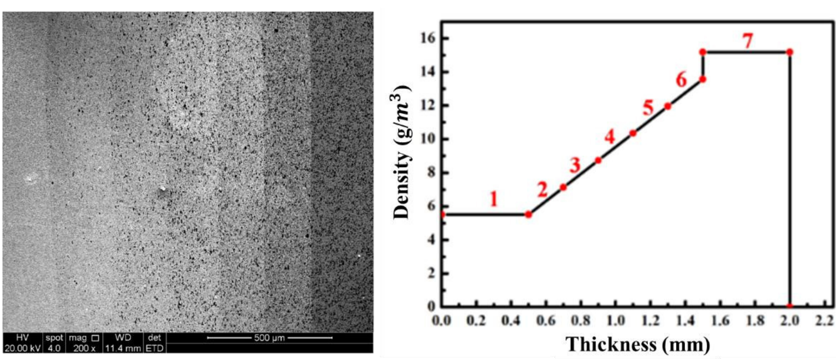

(a) (b)

Figure 4-8 (a) SEM image and (b) designed density-thickness curve of the 7-layer W-SiCP/Cu FGM. Picture adapted from reference [6].

The $V(z,t)$ curve is shown in Figure 4-3. By applying the same procedure used in Section 4.4.3.2, we can measure the properties of each layer in a single depth scanning. The measured and the reference thicknesses and velocities of the 7-layer W-SiCP/Cu FGM are listed in Table 4-5. It can be seen in Table 4-5 that the results have significant errors, which could be attributed to the weak echo from the interface (see the foci in Figure 4-3). The acoustic impedance in the density gradient material gradually changes over the 7 layers, accounting for very low impedance mismatches between the neighboring layers. Although the rays focus on the interfaces, the low impedance mismatches result in weak echoes and unclear foci in the $V(z,t)$ curve (see Figure 4-3).

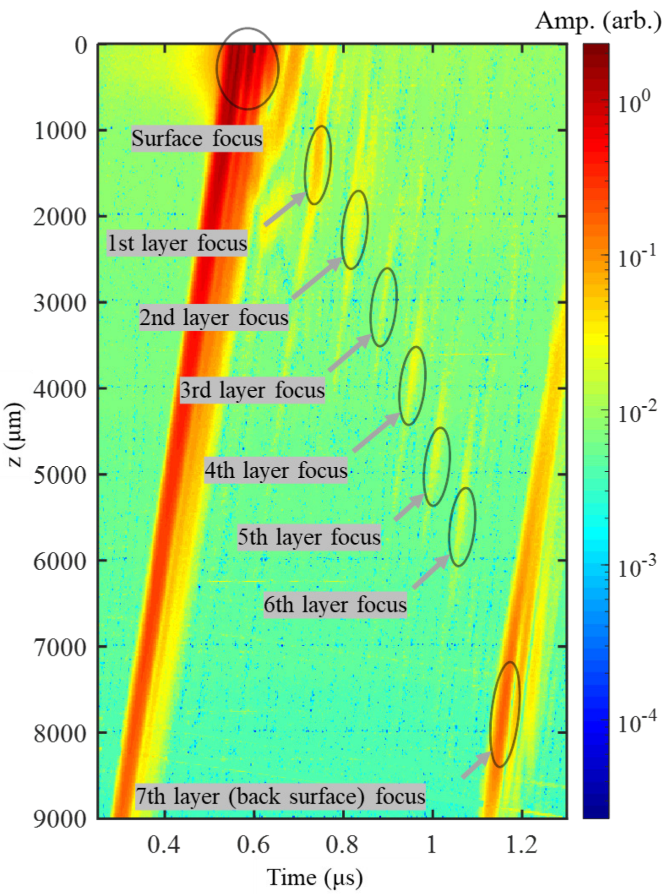

Figure 4-9 $V(z,t)$ curve of the 7-layer W-SiCP/Cu FGM with the indication of longitudinal-wave foci.

Table 4-5 The measured and the reference properties of the 7-layer W-SiCP/Cu FGM

Peak	Measured Properties (mean±3σ)			Reference Properties (Designed)		SEM measured $\boldsymbol{d_n}$ (μm) (mean±3σ)
	α (°)	c_n (m/s)	d_n (μm)	W-SiCP/Cu (vol%) [5]	d_n (μm)	
1	13.35 ±1.63	3947± 448	437±59	0W-60SiC-40Cu	500	-
2	12.06 ±1.34	4125± 1316	216±60	10W-50SiC-40Cu	200	190.65±5.90
3	11.30 ±1.18	4132± 1531	185±81	20W-40SiC-40Cu	200	192.52±11.94
4	9.45± 0.82	5803± 1389	252±64	30W-30SiC-40Cu	200	184.36±2.61
5	8.70± 0.32	5868± 979	215±30	40W-20SiC-40Cu	200	197.62±1.75
6	8.37± 0.38	5268± 1162	201±40	50W-10SiC-40Cu	200	241.57±1.94
7	7.29± 0.23	6578± 443	490±40	60W-0SiC-40Cu	500	-

4.5 Conclusion

This chapter presents the new explanatory frameworks for the variable focus technique to promote its application to multi-layer materials. The longitudinal-wave foci are identified from the depth-scanning results by using the 'Bottom Left' principle. The multi-layer focus model based on geometric acoustics is proposed to interpret positions of the longitudinal-wave foci. In order to produce more accurate measurement results, the Phase Differentiation theory is presented. The measured properties are compared to the reference properties of the FMGs.

By using the variable focus technique, the thicknesses and wave velocities of the FGMs are simultaneously characterized without any prior knowledge. Simultaneous measurement of multi-mode wave velocities demonstrates relatively large errors due to the low signal-to-noise ratio of the multi-mode waves. The very low impedance mismatches in the density gradient material result in weak echoes and unclear foci, thus introducing some errors.

References

[1] Haenel, V., and Kleffner, B., 1999, "Double focus technique for quantitative measurements in time‐resolved acoustic microscopy," The Journal of the Acoustical Society of America, 105(2), pp. 1015-1015.
[2] Hänel, V., 1998, "Measurement of sound velocity and thickness of thin samples by time-resolved acoustic microscopy," Journal of applied physics, 84(2), pp. 668-670.
[3] Gilmore, R., 1996, "Industrial ultrasonic imaging and microscopy," Journal of Physics D: Applied Physics, 29(6), p. 1389.
[4] Maev, R. G., 2008, Acoustic microscopy: Fundamentals and applications, John Wiley & Sons.
[5] Zhang, L. M., Liu, Y., Zhang, C. C., Luo, G. Q., Liu, H., and Shen, Q., "Fabrication and Properties of W-SiCP/Cu Composites by Hot Pressing Sintering," Proc. Key Engineering Materials, Trans Tech Publ, pp. 207-210.
[6] 刘尧, "W-SiC_P/Cu 梯度复合材料的流延法制备及其性能研究," 武汉理工大学.

PART II: Anisotropic Carbon Fiber Reinforced Polymer

The research in this Part II focuses on Carbon Fiber Reinforced Polymers (CFRPs), and has been performed at Ghent University.

CFRPs are increasingly being used for a range of primary structural applications where weight and inertia forces play an important role (e.g. aerospace). Compared to the isotropic functional graded materials (FGMs) investigated in Part I of this thesis, a CFRP laminate is typically composed of more layers which possess mechanical anisotropy and a lower impedance mismatch. To cope with these three additional challenges, a lower frequency approach is considered by making use of the analytic-signal technique coupled to advanced analysis and processing tools.

Chapter 5 Modeling of Analytic-signal Response from an immersed CFRP Laminate

5.1 Introduction

Ultrasonic non-destructive testing (NDT) has been commonly used for the inspection of carbon fiber reinforced polymer (CFRP) laminates based on the evaluation of the instantaneous amplitude (e.g., the variable focus technique in 0 and 0). Commonly, a defect is detected by the conventional ultrasonic frequency (e.g., 5-15 MHz), in which the weak interply reflections are ignored in practice. A higher frequency can be employed to investigate also the interply characteristics between individual layers in a CFRP laminate [1]. It gives detailed results and high spatial and temporal resolution. However, high-frequency ultrasound leads to excessive attenuation of the ultrasonic signal in CFRP due to the high absorption properties of the polymer matrix and scattering at fiber bundles and porosities [2, 3], resulting in a limited effective probing depth [4].

Researchers have tried to couple the conventional ultrasonic signals (e.g., 5-15 MHz) to suitable deconvolution procedures to improve the signal-to-noise ratio (SNR), the effective probing depth, as well as the time resolution. Wiener deconvolution techniques help extract the impulse response from poorly resolved signals for delamination detection [5, 6]. The synthetic aperture focusing technique combined with a variation of Wiener deconvolution has been presented for significantly sharpening the resolution of ultrasonic images [7]. Another deconvolution procedure using a combination of higher-order spectral methods and wavelet analysis has been proposed to improve ultrasonic images' spatial and temporal resolution [8]. Although these efforts have undoubtedly led to better imaging results, it would be interesting if the fundamental limitation, i.e., the low SNR of the response signal in deep layers, could be resolved.

In that regard, it has been recently proposed to employ an ultrasound signal at the ply resonance frequency (around 7.5 MHz for a typical 0.189 mm thick ply in CFRP) coupled with the analytic-signal procedure [9]. The analytic-signal was discovered in 1946 and was predicted as the optimal estimator of interface location in echo signals [10]. This analytic-signal technique utilizes the appearance of ply resonances corresponding to the ply thickness to derive the interply track. As such, it provides a powerful alternative tool for reconstructing fiber structures in CFRP laminate. For instance, it can be used for measuring wrinkling and ply orientation [11], determining in-plane fiber direction [12], tracking individual plies [9], and detecting ply drops [13].

This chapter aims to build the analytic model of the analytic-signal response from the CFRP laminate. The modeling will serve as a theoretical basis for studies in the following chapters. Section 5.2 introduces the theoretical framework underlying the model. Section 5.3 gives details about the CFRR laminates. The signal parameters for the analytical modeling are given in Section 5.4. The simulated response is displayed in Section 5.5. Section 5.6 presents the conclusion.

5.2 Analytical Modeling

5.2.1 Analytic-signal theory

The analytic representation of a recorded signal in its complex form is called the analytic-signal (see Figure 5-1a). It is composed of a real part $s(t)$ (which corresponds to the recorded signal), and an imaginary part $g(t)$:

$$s_a(t) = s(t) + \mathrm{i}g(t). \tag{5.1}$$

The imaginary part $g(t)$ is obtained from $s(t)$ by the Hilbert transform:

$$g(t) = \int_{-\infty}^{+\infty} \frac{s(\tau)}{\pi(t-\tau)} \mathrm{d}\tau. \tag{5.2}$$

The phasor representation of the analytic-signal response indicates the instantaneous amplitude and -phase in the complex-plane. Figure 5-1b and c show the analytic-signal in a 3D representation and phasor representation, respectively. Mathematically the analytic-signal is noted as follows:

$$s_a(t) = A_{inst}(t)\mathrm{e}^{\mathrm{i}\phi_{inst}(t)}, \tag{5.3}$$

where $A_{inst}(t)$ and $\phi_{inst}(t)$ are the instantaneous amplitude and instantaneous phase, respectively. The instantaneous frequency $f_{\mathrm{inst}}(t)$ can be derived from

$$f_{\mathrm{inst}}(t) = \frac{1}{2\pi}\frac{\mathrm{d}\phi_{\mathrm{inst}}(t)}{\mathrm{d}t}. \tag{5.4}$$

In the frequency domain, the relation between a signal and its analytic-signal can be rewritten as [14]

$$F_a(\omega) = (1 + \mathrm{sgn}(\omega))F(\omega), \tag{5.5}$$

where $F_a(\omega)$ is the Fourier spectrum of $s_a(t)$, $F(\omega)$ is the Fourier spectrum of $s(t)$, and $\mathrm{sgn}(\cdot)$ denotes the sign function.

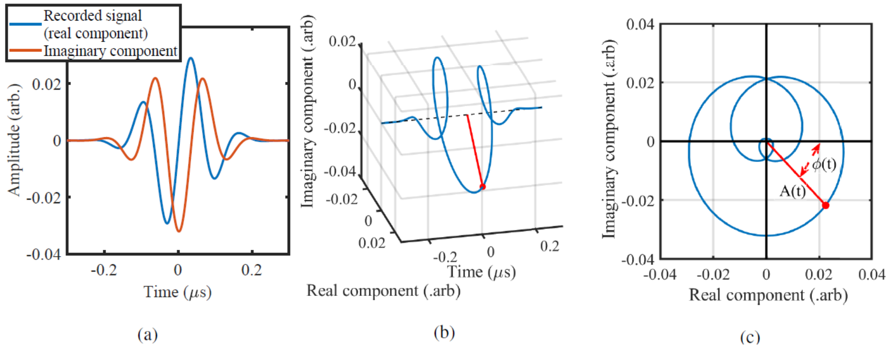

Figure 5-1 Simulation results for an input pulse with a center frequency of 6.5 MHz and a fractional bandwidth (−6 dB) of 0.8. (a) The response signal from one interply layer and the imaginary component of the analytic-signal. The complex analytic-signal is plotted in (b) 3-dimensional representation and (c) phasor representation.

5.2.2 Reflection coefficient from multi-layer structure

The complex reflection spectrum can be obtained for a plane harmonic wave at normal incidence, as introduced in Section 2.3. To account for an arbitrary broadband input signal $y_i(t)$, its complex Fourier representation $Y_i(\omega)$ is multiplied with the complex reflection spectrum $R_t(\omega)$ of the immersed multi-layer structure. The analytic-signal response in the frequency domain can be calculated by

$$F_a^R(\omega) = (1 + \mathrm{sgn}(\omega))Y_i(\omega)R_t(\omega). \tag{5.6}$$

The analytic-signal response of a multi-layer structure to a broadband input signal is represented in the time domain by the application of an inverse Fourier transform:

$$s_a^R(t) = \mathrm{IFT}(F_a^R(\omega)), \tag{5.7}$$

where $\mathrm{IFT}(\cdot)$ denotes the inverse Fourier transform.

To represent experimental conditions, the signal is polluted with white Gaussian noise $n_s(t)$, i.e., noise with uniform power over the considered frequency band and normal distribution in the time domain with zero mean value. The reflected signal $y_s(t)$ finally becomes:

$$y_s(t) = s_a^R(t) + n_s(t). \tag{5.8}$$

The analytical model is implemented in Matlab®. The structure of a multi-layer laminate immersed in water is illustrated in Figure 5-2.

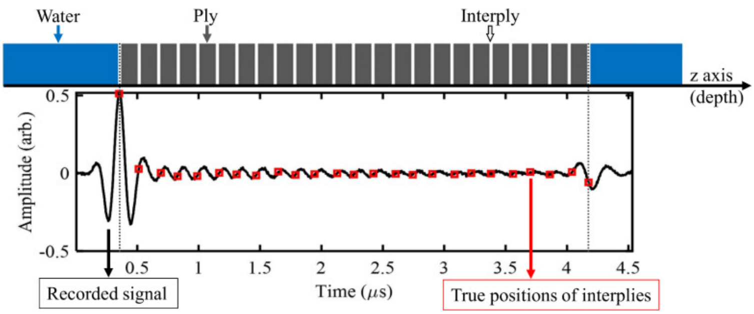

Figure 5-2 Schematic of the CRPP multi-layer structure and the signal response.

5.3 Properties of CFRP Laminate

The simulated CFRP laminate consists of 24 plies with a nominal CFRP ply thickness of 220 µm. These plies are separated by 23 thin polymer interplies with a nominal thickness of 5 µm. Also, on the outer surface of the CFRP laminate, two thin polymer plies are added. The interply should be considered as a pure epoxy layer. Table 5-2 presents the properties of the interply used as a reference in this study. Hence, the total thickness of the laminate equals $(24 \times 0.220 + 23 \times 0.005 + 2 \times 0.005)$ =5.405 mm.

Each CFRP lamina is a mixture of unidirectional fibers and a pure epoxy matrix. The pure fibers and the pure epoxy matrix properties are used to calculate the ply properties (see Table 5-2 for a nominal fiber volume fraction of 60%). The effective mass density for each ply is calculated by the rule of mixture, assuming a density of the carbon fibers of 1800 $\mathrm{kg/m^3}$. The stiffness matrix for each ply is calculated by the Chamis model [15], from which the longitudinal wave velocity propagating in the thickness direction is calculated. The assumed carbon fiber and epoxy matrix properties are listed in Table 5-1.

Table 5-1 The assumed carbon fiber and epoxy matrix properties

Fiber properties [19]	value	Epoxy matrix properties [19]	value
E_1 (GPa)	223.366	E (GPa)	3.7
E_2 (GPa)	18.107	ν (–)	0.4
E_3 (GPa)	18.107	G (GPa)	1.32
ν_{12} (–)	0.006		
ν_{13} (–)	0.006		
ν_{23} (–)	0.599		
G_{12} (GPa)	51.951		
G_{13} (GPa)	51.951		
G_{23} (GPa)	5.661		

The nominal individual ply thickness, together with the longitudinal wave velocity in the ply, indicates a resonance frequency of each ply of approximately 6 MHz. The attenuation in CFRP is directly related to the void content [16, 17]. The experimental results in the literature, conducted on 16-ply quasi-isotropic carbon/epoxy laminates with thicknesses varying from about 2 mm to 2.5 mm and a fiber volume fraction of approximately 60-65%, showed that the attenuation increases almost linearly from 0.09 to 1.8 dB/mm/MHz as the void ratio increases from 0.034% to 4.05% [16]. Therefore, the nominal attenuation coefficient of a ply is selected here as 0.1 dB/mm/MHz.

Table 5-2 The nominal properties of the polymer interply and the CFRP ply

Material	Density $(\mathbf{kg/m^3})$	Thickness (μm)	Wave velocity[1] (m/s)	Attenuation (dB/mm/MHz)
Polymer interply	1270 [18]	5	2499 [19]	0.15 [18]
CFRP ply (60% fiber volume fraction)	1588	220	2906	0.1

The multi-layer structure is assumed to be immersed in water with a density of 1000 $\mathrm{kg/m^3}$ and a wave velocity of 1480 m/s. The material properties are used as the input to calculate the reflection coefficient from the multi-layer structure, as described in Section 5.2.2. The analytic-signal response in the frequency

[1] The direction of the longitudinal wave is along a path perpendicular to the fiber.

domain is obtained by the multiplication of the Fourier representation of the input signal and the reflection coefficient. The input signal is described in Section 5.4 below.

5.4 Input signal

The model is built on the reflection coefficients to process the multi-layer response and to extract the analytic-signal. The input signal $y_i(t)$ is a Gaussian modulated pulse with zero phase at the peak amplitude (see Figure 5-3a):

$$y_i(t) = y_e(t)\cos(2\pi F_c t), \tag{5.9}$$

where F_c is the center frequency, t is time vector, and $y_e(t)$ is the Gaussian pulse envelope defined as follows:

$$y_e(t) = \exp\left(\frac{t^2 W^2 F_c^2 \pi^2}{4\ln\left(10^{\frac{AW_{dB}}{20}}\right)}\right), \tag{5.10}$$

where W is the fractional bandwidth of the pulse, AW_{dB} is the fractional bandwidth reference level expressed in decibels. Table 5-3 lists the nominal parameter values for the input signal. Figure 5-3b and c show the analytic-signal response from the multi-layer structure. White noise with a uniform spectral density and a Gaussian amplitude distribution is added to the response signal. It is related to the measured power of the reflection signal (see Figure 5-3b). This SNR of 35 dB is close to what is achieved in a real ultrasonic experiment without averaging or other noise reduction approaches. The power of the signal P_s is measured by

$$P_s = \frac{\sum_{t=0}^{t_{max}} s_a^R(t)^2}{N_w}, \tag{5.11}$$

where N_w is the number of sampling points within the time window in Figure 5-3b. The power of the added noise P_n is defined by

$$P_n = \frac{P_s}{10^{\frac{SNR}{10}}}, \tag{5.12}$$

where SNR is expressed in decibel. The nominal sampling rate Fs^{nom} for the simulation is taken as 1 GS/s. In real measurement, digital signals also have a natural digital noise due to the vertical bit depth of the acquisition module. A digital signal with a bit depth of 14-bit is simulated as the model output.

Table 5-3 Nominal parameters of the input signal and data acquisition

Pulse-type	F_c^{nom} (MHz)	W^{nom}	AW_{dB}^{nom} (dB)	Media	SNR^{nom} (dB)	Fs^{nom} (GS/s)	Bit depth
In-phase	6	0.8	-6	water	35	1	14 bit

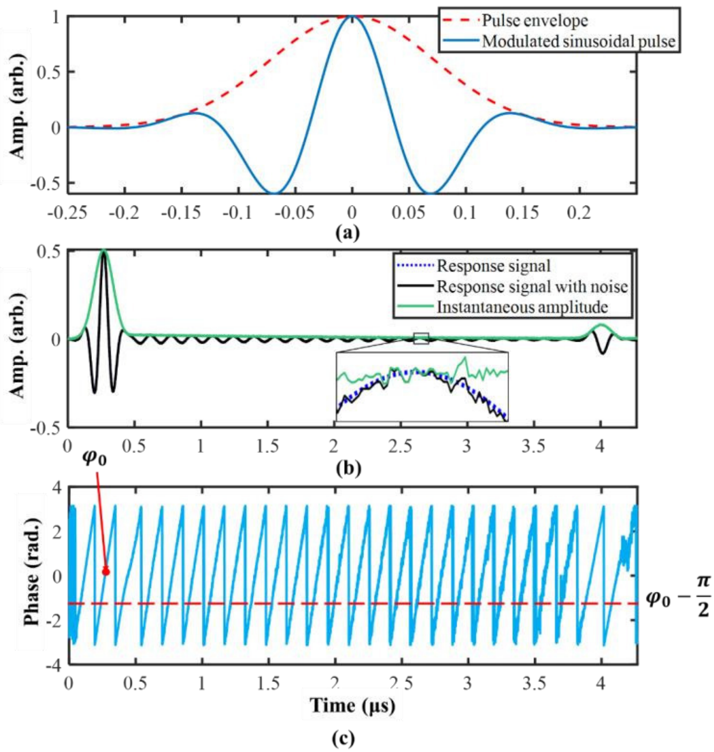

Figure 5-3 (a) In-phase Gaussian pulse as input signal; (b) response signal and its instantaneous amplitude; (c) Instantaneous phase of the response signal.

5.5 Simulation results

The listed values for the multi-layer structure in Section 5.3 are used. Furthermore, the input signal and the data acquisition in Section 5.4 are taken. The analytical modeling is implemented according to Section 5.2. Figure 5-4 displays the instantaneous amplitude, instantaneous phase, and instantaneous frequency of the simulated analytic response without noise (left column) and with noise (right column). It can be observed from Figure 5-4 that the instantaneous frequency is extremely deteriorated by noise. This is expected due to the fact that the derivative process in Eq. (5.4) magnifies noise. Also, the noise dominates the weak echoes from interplies in deep layers where SNR is typically very low.

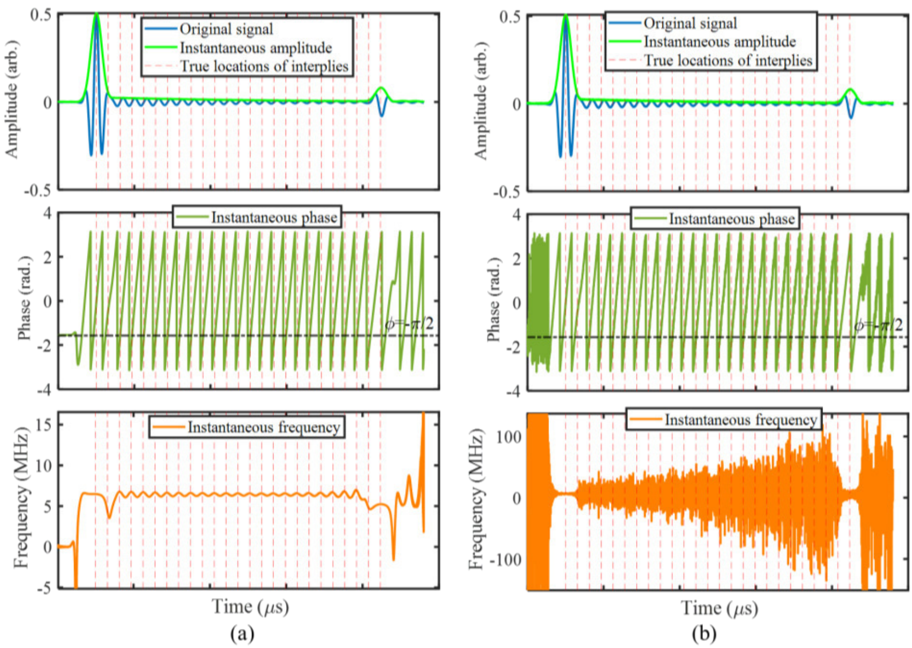

Figure 5-4 Simulated analytic-signal response, together with the instantaneous amplitude (green trace), the instantaneous phase (dark green trace), the instantaneous frequency (orange trace) for the multi-layer CFRP laminate: (a) without noise and (b) with noise.

5.6 Conclusion

The one-dimensional normal wave propagation model has been used to simulate the analytic-signal response from a multi-layer structure. The input parameters for simulation, including the material properties, signal parameters, and acquisition settings, have been introduced. The material properties are derived from previous researches concerning real CFRP. The signal parameters and acquisition settings are selected in accordance with the typical experimental conditions. Based on this modeling approach, the performance of different ultrasonic techniques and processing approaches for reconstructing the multi-layer structure of CFRP will be investigated in the following chapters.

References

[1] Yu, Z., and Boseck, S., 1995, "Scanning acoustic microscopy and its applications to material characterization," Reviews of Modern Physics, 67(4), p. 863.
[2] Garnier, C., Pastor, M.-L., Eyma, F., and Lorrain, B., 2011, "The detection of aeronautical defects in situ on composite structures using Non Destructive Testing," Compos Struct, 93(5), pp. 1328-1336.
[3] Taheri, H., and Hassen, A. A., 2019, "Nondestructive ultrasonic inspection of composite materials: a comparative advantage of phased array ultrasonic," Applied Sciences, 9(8), p. 1628.
[4] Gao, S.-L., and Kim, J.-K., 1999, "Scanning acoustic microscopy as a tool for quantitative characterisation of damage in CFRPs," Compos Sci Technol, 59(3), pp. 345-354.
[5] Honarvar, F., Sheikhzadeh, H., Moles, M., and Sinclair, A. N., 2004, "Improving the time-resolution and signal-to-noise ratio of ultrasonic NDE signals," Ultrasonics, 41(9), pp. 755-763.
[6] Brand, S., Czuratis, P., and Raum, K., 2008, "Signal analysis in acoustic microscopy for nondestructive inspection of varnish layers on metal substrates," Journal of the Acoustical Society of America, 123(5), pp. 3081-3081.
[7] Sinclair, A., Fortin, J., Shakibi, B., Honarvar, F., Jastrzebski, M., and Moles, M., 2010, "Enhancement of ultrasonic images for sizing of defects by time-of-flight diffraction," Ndt&E Int, 43(3), pp. 258-264.
[8] Wan, S., Raju, B. I., and Srinivasan, M. A., 2003, "Robust deconvolution of high-frequency ultrasound images using higher-order spectral analysis and wavelets," IEEE transactions on ultrasonics, ferroelectrics, and frequency control, 50(10), pp. 1286-1295.
[9] Smith, R. A., Nelson, L. J., Mienczakowski, M. J., and Wilcox, P. D., 2017, "Ultrasonic analytic-signal responses from polymer-matrix composite laminates," IEEE transactions on ultrasonics, ferroelectrics, and frequency control, 65(2), pp. 231-243.
[10] Gabor, D., 1946, "Theory of communication. Part 1: The analysis of information," Journal of the Institution of Electrical Engineers-Part III: Radio and Communication Engineering, 93(26), pp. 429-441.
[11] Nelson, L., Smith, R., and Mienczakowski, M., 2018, "Ply-orientation measurements in composites using structure-tensor analysis of volumetric ultrasonic data," Composites Part A: Applied Science and Manufacturing, 104, pp. 108-119.

[12] Nelson, L., and Smith, R., 2019, "Fibre direction and stacking sequence measurement in carbon fibre composites using Radon transforms of ultrasonic data," Composites Part A: Applied Science and Manufacturing, 118, pp. 1-8.
[13] Smith, R. A., Nelson, L. J., Mienczakowski, M. J., and Wilcox, P. D., "Ultrasonic tracking of ply drops in composite laminates," Proc. AIP Conference Proceedings, AIP Publishing LLC, p. 050006.
[14] Bridge, C. P., 2017, "Introduction to the monogenic signal," arXiv preprint arXiv:1703.09199.
[15] Hallal, A., Younes, R., Fardoun, F., and Nehme, S., 2012, "Improved analytical model to predict the effective elastic properties of 2.5 D interlock woven fabrics composite," Compos Struct, 94(10), pp. 3009-3028.
[16] Jeong, H., and Hsu, D. K., 1995, "Experimental analysis of porosity-induced ultrasonic attenuation and velocity change in carbon composites," Ultrasonics, 33(3), pp. 195-203.
[17] Hale, J., and Ashton, J., 1988, "Ultrasonic attenuation in voided fibre-reinforced plastics," NDT international, 21(5), pp. 321-326.
[18] Smith, R. A., 2010, "Use of 3D ultrasound data sets to map the localised properties of fibre-reinforced composites," University of Nottingham, Nottingham.
[19] Sevenois, R., Garoz, D., Verboven, E., Spronk, S., Gilabert, F., Kersemans, M., Pyl, L., and Van Paepegem, W., 2018, "Multiscale approach for identification of transverse isotropic carbon fibre properties and prediction of woven elastic properties using ultrasonic identification," Compos Sci Technol, 168, pp. 160-169.

Chapter 6 Parametric study of Instantaneous Phase-derived Interply Tracking

6.1 Introduction

The analytic-signal procedure is a powerful tool to obtain an in-depth view of the internal structure of the multi-layer carbon fiber reinforced polymer (CFRP). The impedance mismatch between the CFRP ply (fiber + matrix) and interply (matrix) will induce weak echoes when the input signal interacts with the multi-layer structure. The ply-interply interface causes a phase reversal $-\pi$, resulting in a negative reflection coefficient. The interply-ply interface, on the other hand, induces no phase reversal, resulting in a positive reflection coefficient. Both interfaces induce weak echoes with the same amplitude level and with little time difference, thus producing a very weak signal with an instantaneous phase of $\phi_0 - \pi/2$, where ϕ_0 is the phase of the input pulse [1, 2]. Another important aspect is that the instantaneous phase traverses exactly 2π radians for each ply when the center frequency is close to the ply resonance frequency. Hence, by extracting the instantaneous phase from the analytic-signal, it is possible to derive the depth positions of the polymer interplies ($\phi_0 - \pi/2$) as well as of the back surface ($\phi_0 - \pi$). The instantaneous amplitude, on the other hand, can be used to detect the strong front-wall echo (FWE) and back-wall echo (BWE), and as such, to roughly extract the position of the front and back surface. The solid-water interface on the back surface also has a negative reflection coefficient, thus producing an instantaneous phase of $-\pi$. The instantaneous phase information is then used to derive the location of the back surface with higher precision and robustness [3]. The time interval between the FWE and BWE represents the time-of-flight (TOF) of the ultrasonic signal to traverse the structure twice. However, several experimental conditions should be satisfied to properly implement this procedure, which is not always evident in reality. Further, the phase-derived interply tracking accuracy is sensitive to the variation of setup parameters and material properties.

This chapter analytically investigates the performance of the analytic-signal procedure, coupled to the ply resonance condition, in order to extract ply parameters in a CFRP laminate for a wide range of experimental conditions. The theoretical framework underlying the simulation model and the analytical modeling of the analytic-signal response from the multi-layer structure has been given in 0. It is further demonstrated that the analytic-signal procedure combined with a suitable log-Gabor filter can significantly improve the quality of the ply parameters extraction. Also, an experimental demonstration is presented in which the ply parameter are extracted for a 24-layer CFRP laminate.

6.2 Phase-derived Interply Tracking

The modeling approach, and the nominal parameters, presented in 0 are employed. The true ply thickness is approximately 225 µm (CFRP ply thickness plus interply thickness), which indicates an actual ply resonance frequency of approximately 6.5 MHz. In case the ply thickness is not known a priori, we can simply estimate the ply resonance frequency from the instantaneous frequency (see Figure 5-4a). The instantaneous phase associated with the FWE is used to determine the ϕ_0 as a reference to track the physical depth positions of the interplies. More specifically, the interpolated $\phi_0 - \pi/2$ position in each 2π phase cycle is tracked in Figure 5-3c, and the corresponding time value then indicates the TOF (or the depth position) of the interply. The interpolated $\phi_0 - \pi$ position around the BWE is tracked to derive a more accurate depth position of the back surface. A phase increment of 2π in the unwrapped phases is an indicator of the interply at the next layer.

Once the TOF of the interplies are estimated, the absolute error ε^i is calculated as (see Figure 6-1):

$$\varepsilon^i = TOF_{est}^i - TOF_{true}^i, \tag{6.1}$$

where TOF_{est}^i and TOF_{true}^i are the estimated and the true TOF of the ith interply, respectively. The front-surface interply is set as $i = 0$. The measurement error E^i for interply i is defined as the ratio:

$$E^i = \frac{\varepsilon^i}{TOF^{ply}} \times 100[\%], \tag{6.2}$$

where TOF^{ply} is the true TOF of a single ply.

Hence an error $E^i = 0\%$ indicates perfect estimation of the depth position for interply i, while an $E^i = +100\%$ (or $E^i = -100\%$) indicates that the estimated depth position of interply i coincides with the true depth position of layer $i+1$ (or layer $i-1$). Sometimes, the observed phase increment in the unwrapped phases is less than 2π (or more than 4π) in one ply. Consequently, the extracted interplies are occasionally less than (or more than) the actual number of interplies.

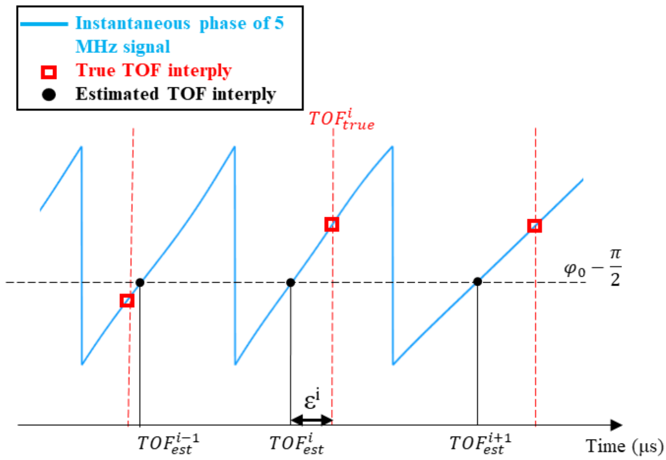

Figure 6-1 Schematic illustration of TOF estimation of the interplies based on the instantaneous phase of a 5 MHz signal. Note: the graphs are only for illustration purposes and do not correspond to real signals.

6.3 Parametric Analysis of interply tracking

This section studies the influence of a wide range of parameters on the extracted interply tracking results.

6.3.1 Front- and back-wall echoes

Figure 6-2a demonstrates the errors of the phase-derived interply tracking for the nominal parameters listed in Table 6-1. Close to the front and back surfaces of the multi-layer structure, the interply tracking has a significant deviation due to the dominating FWE and BWE. The tracking error of the interply between the first and second ply is approximate −25%, while the tracking error of the last interply is almost 15% due to the fact that they are dominated by the echoes from the surfaces [2, 4]. To understand the influence of the FWE and the BWE, these echoes have been subtracted from the original response signal. The FWE was obtained by simulating a single thick interply embedded in the water (upper medium) and the CFRP ply (underlying medium). Similarly, the BWE was obtained by simulating a single thick interply embedded in the CFRP ply (upper medium) and the water (underlying medium). By removal of the surface echoes, it was found that the errors of the first and the last extracted interply reach a comparable level with that of the other interplies (E^{i} < 5%), see orange stars in Figure 6-2. However, this FWE and BWE subtraction procedure becomes challenging to be applied in an actual experimental case.

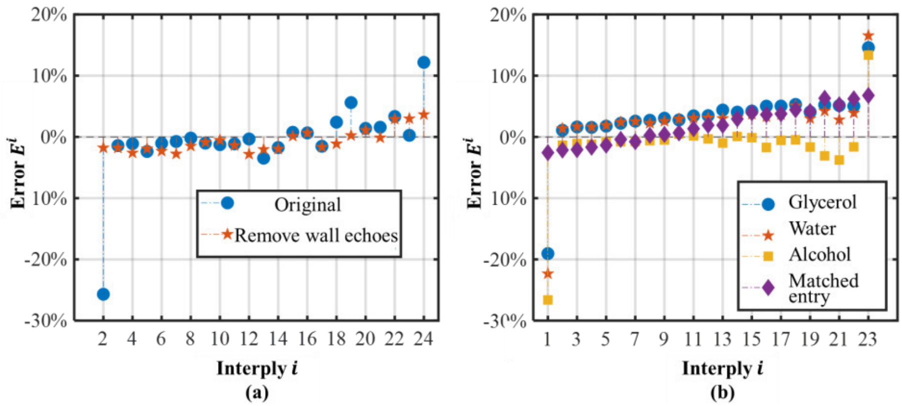

Figure 6-2 (a) Errors E^i (TOF of deviation / TOF of ply) of the phase-derived interply tracking with and without the FWE and BWE; (b) Errors E^i of the phase-derived interply tracking corresponding to different bounding media.

An option to partially alleviate the strong influence of FWE and BWE is the use of a matching medium that has a lower impedance mismatch. Table 6-1 gives the properties of different bounding media. The errors of the interply tracking corresponding to different bounding media are presented in Figure 6-2b. The noise's power is considered constant to avoid dramatic changes in the power of the noise caused by changing FWE and BWE. A lower impedance mismatch between the liquid bounding medium and the structure results in a slight reduction in the relative errors of the first and the last extracted interplies. When the structure is embedded in a matched entry, i.e., bounding medium with the same acoustical impedance as the CFRP ply, the errors of the first and the last extracted interplies reach a comparable level with that of the other interplies.

Table 6-1 The properties of different bounding media

Media	Density (kg/m^3)	Wave velocity (m/s)
Glycerol	1250	1900
Water	1000	1500
Alcohol	800	1100
Matched entry (CFRP ply)	1588	2641

6.3.2 Signal-to-noise ratio SNR

Considering that the interply tracking procedure relies on the analysis of the instantaneous phase of the analytic-signal response, it is expected that both the electronic and ultrasonic noise could degrade the results significantly. Therefore, white Gaussian noise of various levels is added to the response signal in the time domain to understand the influence on interply tracking. The signal-to-noise ratio (SNR) is calculated as described in Section 5.4. The errors E^i are plotted in Figure 6-3 for a range of SNR values. Apart from the interplies dominated by the FWE and BWE, the errors E^i for the other interplies are quite acceptable for SNR values higher than 35 dB.

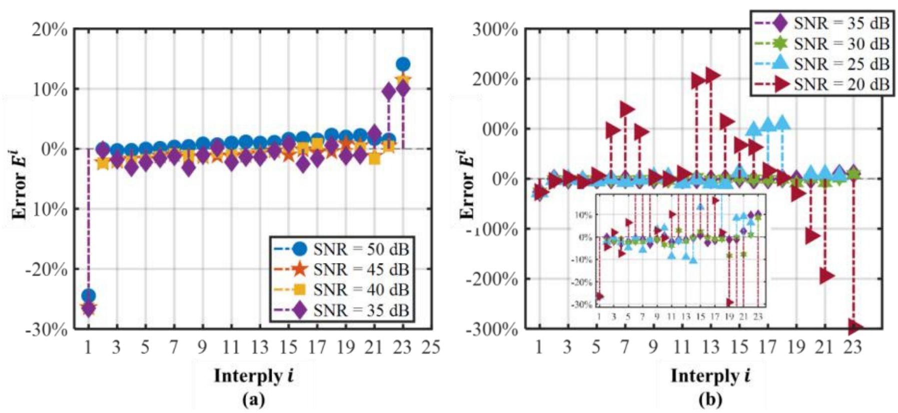

Figure 6-3 Errors E^i of the phase-derived interply tracking corresponding to the SNR of (a) 50–35 dB and (b) 35–20 dB.

However, in reality, it is not always straightforward to achieve a SNR higher than 35 dB. Lowering the SNR below 35 dB yields a clear increase in error E^i of the interply tracking. The negative effect of the added noise is more outspoken in deeper layers due to wave attenuation resulting in a dynamic SNR over depth. Once the SNR drops below 30 dB, the interply tracking procedure deteriorates significantly with errors higher than $\pm 100\%$. Such significant errors mean that the phase-derived interply tracking does not work anymore because the instantaneous phase of the noise dominates the instantaneous phase of the signal (see Figure 6-4). These results clearly indicate that the instantaneous phase does provide a clear metric to track the depth positions of the interplies. However, it is relatively sensitive to the noise level of the signal. Therefore, keeping the SNR as high as possible is crucial, e.g., applying signal averaging or implementing appropriate noise-reduction procedures.

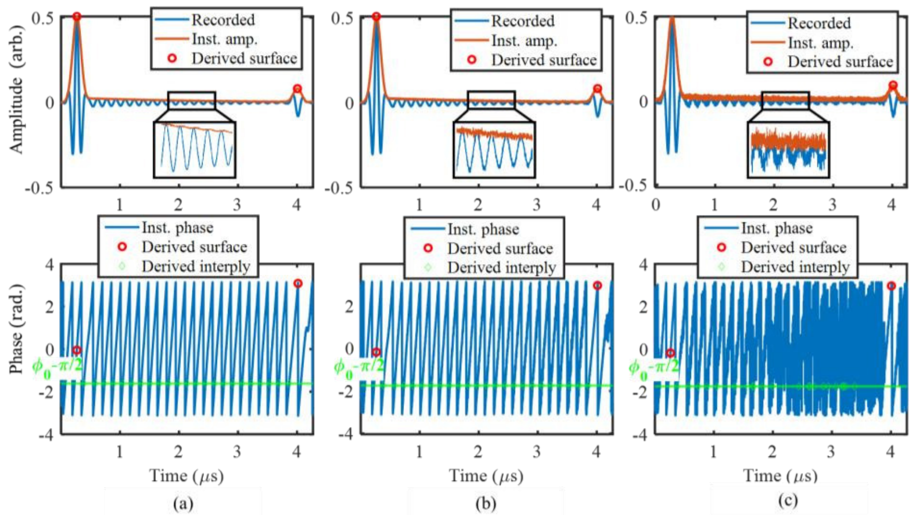

Figure 6-4 Simulated analytic-signals, with their instantaneous amplitudes and instantaneous phases, at various SNR: (a) 50 dB, (b) 35 dB, and (c) 20 dB.

6.3.3 Center frequency

The optimal waveform for the analytic-signal procedure is a pulse with a center frequency equal to the resonance frequency and an appropriate bandwidth close to the center frequency. In Section 5.4, the nominal parameters for frequency and bandwidth were selected as $F_c = 6.5$ MHz and $W = 0.8$. This bandwidth is close to the optimal value. However, selecting a transducer with the optimal center frequency in a real measurement is not straightforward. Therefore, the influence of the center frequency on the interply tracking is studied in this section.

Figure 6-5 shows the influence of the center frequency F_c, considering a bandwidth $W = 0.8$, on the interply tracking errors E^i. Figure 6-6b demonstrates the recorded signal and its analytic-signal response with a center frequency of 6 MHz. A lower F_c (4 MHz in Figure 6-6a) leads to a positive deviation from the true depth position in Figure 6-5a. In terms of a higher F_c (8 MHz in Figure 6-6c), the second-harmonic resonance of a ply could get excited, implying that two $\phi_0 - \pi/2$ positions are possibly tracked in one single-ply. Therefore, a central frequency close to the fundamental resonance frequency corresponding to the ply thickness is crucial for reducing errors. The optimal center frequency is approximately 6.5 MHz in this case. The influence of the center frequency of 6–7 MHz on the errors E^i is shown in Figure 6-5b. It can be seen in Figure 6-5b that a variation of F_c from 6 MHz to 7 MHz, for the considered bandwidth of 0.8, does not cause drastic deviations on the errors E^i. Surprisingly, the errors of the first and last interplies tracking are reduced when F_c equals 6 MHz. This result could be explained by the combined effect of the dominating FWE and BWE and the insufficient center frequency in this case.

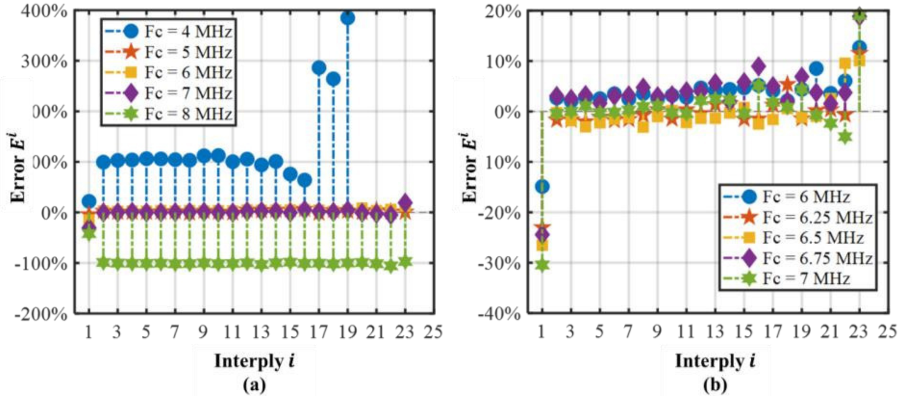

Figure 6-5 Errors E^i on the phase-derived interply tracking corresponding to an input signal with a fixed bandwidth of 0.8 and various center frequencies: (a) 4 MHz to 8 MHz and (b) 6 MHz to 7 MHz.

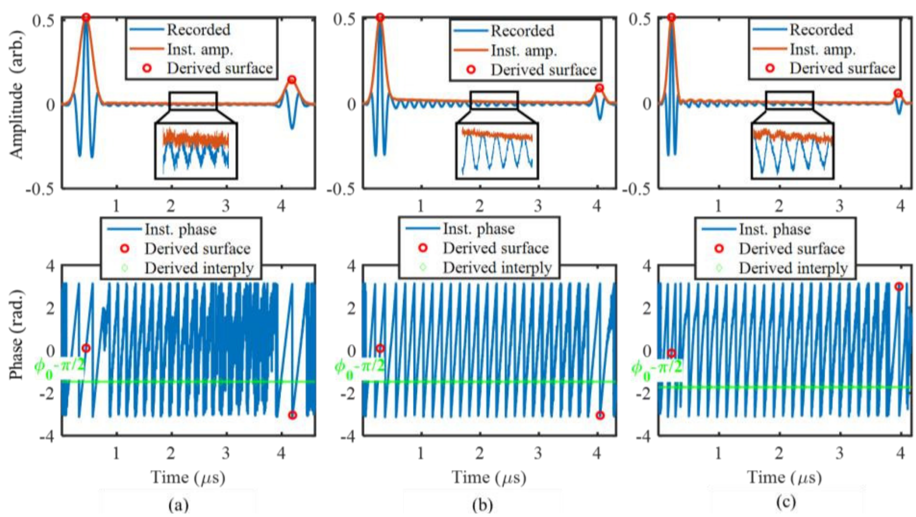

Figure 6-6 Recorded signals and their instantaneous amplitudes and instantaneous phases for an input signal with a fixed bandwidth of 0.8 and various center frequencies: (a) 4 MHz, (b) 6 MHz, and (c) 8 MHz.

6.3.4 Bandwidth

The influence of the bandwidth on the interply tracking is studied in this section. The errors introduced for a range of bandwidth, at the optimal center frequency of $F_c = 6.5$ MHz, are shown in Figure 6-7. For a narrower bandwidth ($W \leq 0.6$), the errors of the interply tracking near the front and back surfaces increase due to a widening of the dominating FWE and BWE (previously discussed in Section 6.3.1). At the bandwidth $W = 0.2$, several tracked interplies near the front- and back surface experience strong errors. The widened FWE and BWE are explicitly demonstrated in Figure 6-8a. Further, a too narrow bandwidth is not desirable in a practical situation, as it cannot cope with variations in ply thickness [1].

On the other hand, a broader bandwidth can cope with variations in ply thickness, but it could excite a strong second-harmonic resonance of a ply [1]. The second-harmonic resonance then results in the wrong positions tracked in one single-ply. The consequence of a strong second-harmonic ply resonance is readily indicated by the orange arrow in Figure 6-8c.

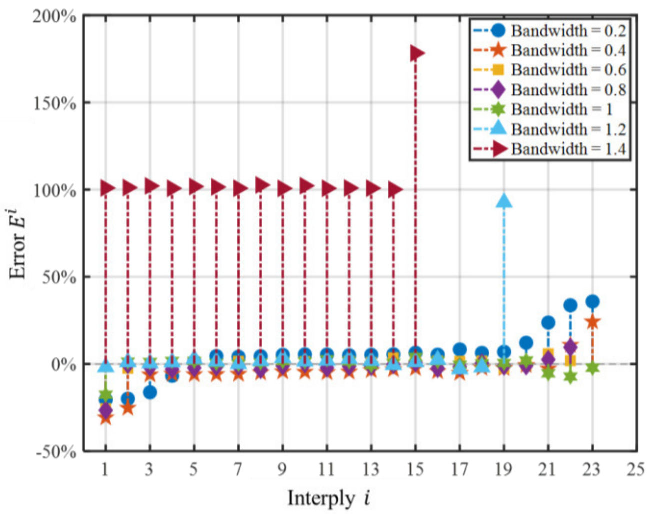

Figure 6-7 Errors E^i on the phase-derived interply tracking for a multi-layer structure with a nominal CFRP ply thickness of 220 μm. An input signal with a center frequency of 6.5 MHz and varying bandwidth was employed.

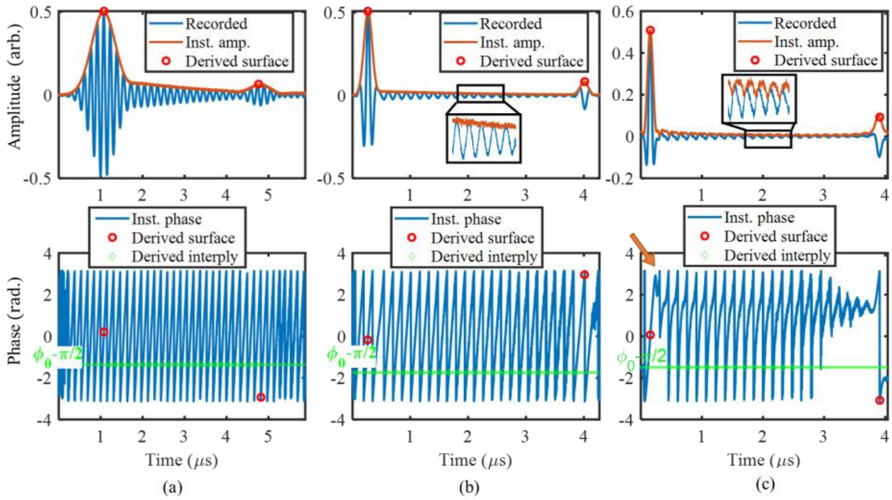

Figure 6-8 Recorded signals and their instantaneous amplitudes and instantaneous phases from a structure with a nominal CFRP ply thickness of 220 μm for an input signal with a bandwidth W of (a) 0.2, (b) 0.8, and (c) 1.4 and a fixed center frequency of 6.5 MHz.

Hence, to test the ability to cope with changes in ply thickness, various ply thicknesses for the CFRP laminate have been considered. The ply thicknesses vary within $\pm$20% of the nominal CFRP ply thickness of 220 μm, and the following CFRP ply thickness sequence is considered: $[260\mu m/220\mu m/180\mu m/220\mu m]_6$. The obtained interply tracking results are reported in Figure 6-9. It is observed that increasing the bandwidth improves the interply tracking significantly. The higher bandwidth of the ultrasonic pulse can better cope with variations in the ply thickness. However, once the bandwidth increases to 1, the second-harmonic ply resonance comes into play, and this obviously leads to erroneous interply tracking results. These observations are consistent with the literature [1].

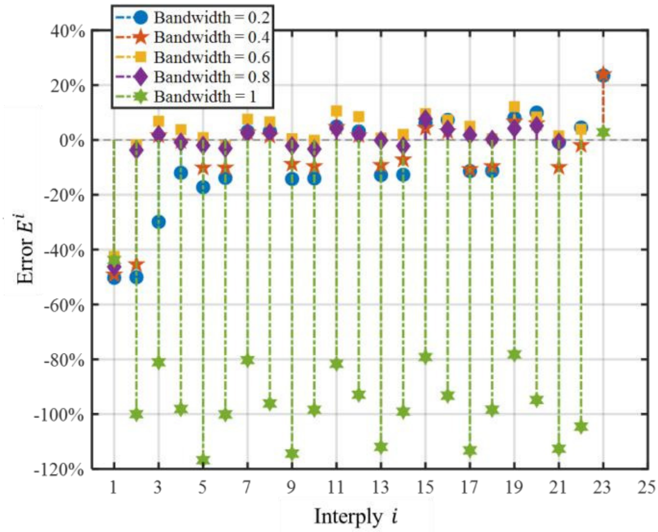

Figure 6-9 Errors E^i on the phase-derived interply tracking for a multi-layer structure with a CFRP ply thickness sequence of $[260\mu m/220\mu m/180\mu m/220\mu m]_6$. An input signal with a center frequency of 6.5 MHz and varying bandwidth was employed.

6.3.5 Sampling rate

The sampling rate influences the sample points of the acquired signal. According to the Nyquist Sampling Theorem, a signal can be sampled and perfectly reconstructed from its sample points if the waveform is adequately sampled. At the same time, acquisition with a high sampling rate records more information about the physical wave and reduces the analog-to-digital quantization error. The main disadvantage of using a high sampling rate is the requirement of ample storage space and high-performance acquisition devices. Furthermore, commercial systems rarely digitize at a higher sampling rate than necessary. The errors of phase-derived interply tracking corresponding to the sampling rate are presented in Figure 6-10. An interpolation procedure is applied to the instantaneous phases to reduce the quantizing errors in all cases. The quantizing error still introduces apparent errors of the interply tracking when the sampling rate decreases to 100 MS/s (see blue dots in Figure 6-10).

It can be seen in Figure 6-11 that the quantizing error of the instantaneous phase increases due to the insufficient sampling rate. The instantaneous phase clearly cannot reach $\pm\pi$ in each 2π phase cycle when the sampling rate is 100 MS/s (see Figure 6-11a). Interleaved sampling could be employed to increase the digitizer's sampling rate, and as such, to reduce the quantizing errors caused by insufficient sampling points. Of course, this procedure complicates the measurement protocol as it requires multiple phase-shifted recordings.

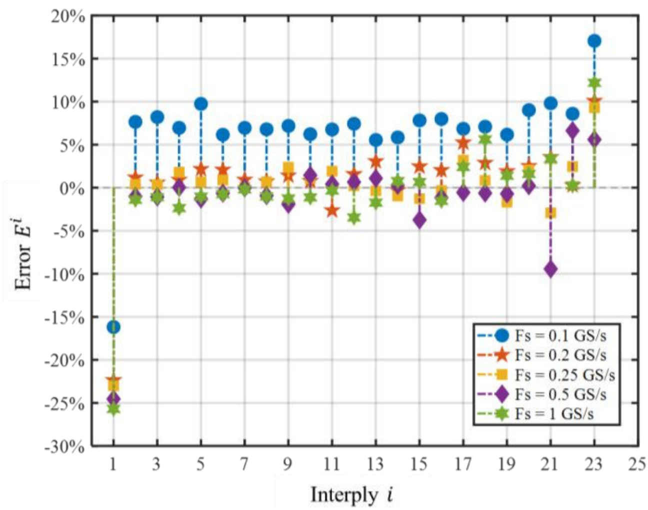

Figure 6-10 Errors E^i of the phase-derived interply tracking corresponding to the sampling rate.

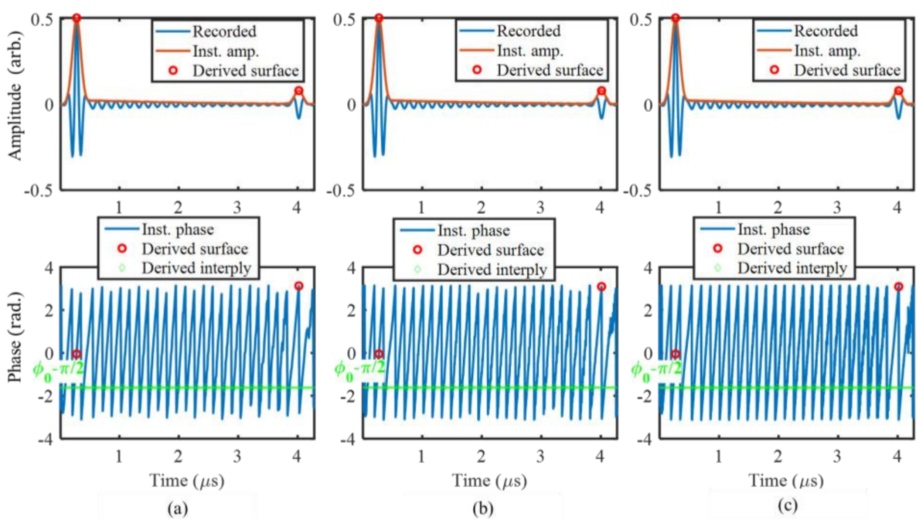

Figure 6-11 Recorded signals and their instantaneous amplitudes and instantaneous phases at a sampling rate of (a) 0.1 GS/s, (b) 0.25 GS/s, and (c) 1 GS/s.

6.3.6 Interply thickness

The two boundaries of the thin polymer interply induce two weak echoes with reversed phases and little time difference. The interaction of these two echoes produces a weak signal with an instantaneous phase close to $-\pi/2$, which is the necessary condition for phase-derived interply tracking. For increasing interply thickness, this condition will be less satisfied. Figure 6-12 demonstrates the errors of interply tracking as a function of the ratio of interply thickness to ply thickness. The nominal situation (CFRP ply thickness of 220 μm and interply thickness of 5 μm) corresponds to the ratio of around 0.025, and it is seen that the errors are minor for all depths. However, once the ratio increases, the results in Figure 6-12 clearly show that the errors increase.

Moreover, the error increases by the depth of the interply. Further, it has been reported that the increased interply thickness results in ultrasonic artefacts deeper in the structure [5]. When the ratio of interply thickness to a ply thickness is more than 0.1, ultrasonic artefacts are caused by phononic band gaps and phase singularities. For the case of the water-immersed laminate in this paper, the effect of phononic band gaps and phase singularities is less prominent compared to the case discussed in the literature [5], where the simulated laminate is immersed in a matched entry. The phase singularity in the signal due to the thicker interplies is indicated in Figure 6-13c. This issue could explain the observed sudden rise in the error for the ratio of 0.1 and 0.15, as indicated with arrows in Figure 6-12. Hence, care is required when applying the instantaneous phase technique for assessing a multi-layer structure in which the plies are bonded by relatively thick adhesive bonds. The thick interply layers formed by particle-toughened resins can occasionally get to 20% of the ply thickness in the extreme. However, in practice, interply layers in real components are unlikely to be thicker than 10% of the ply thickness.

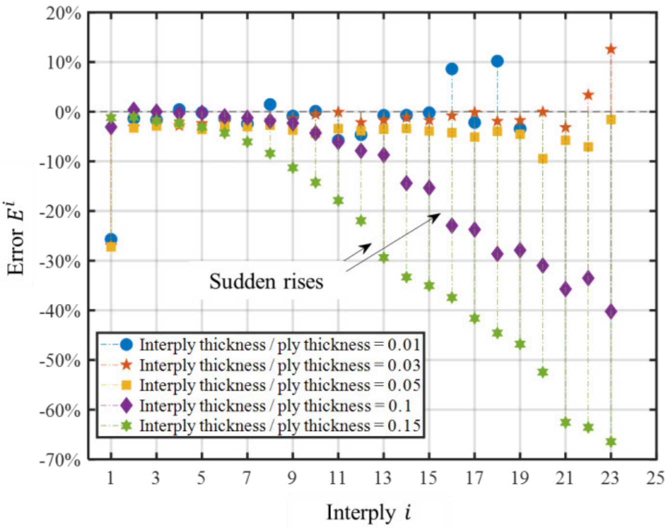

Figure 6-12 Errors E^i on the phase-derived interply tracking corresponding to the interply thickness.

When the interply thickness decreases to 0.01 of the ply thickness, which corresponds to an interply thickness of 2.2 µm for the 220 µm thickness of the CFRP plies, the errors in deep layers increase. This change is attributed to the fact that the echoes amplitudes from the interplies are weakened as the thickness decreases (see Figure 6-13). The reduction in the amplitude is caused by the counteraction of two echoes with reversed phases. Intuitively, an infinitely thin interply produces a perfect instantaneous phase of $-\pi/2$. However, an infinitely thin layer induces a feeble echo that cannot be observed.

Consequently, the SNR decreases when the interply thickness decreases, thus increasing the errors introduced by the noise in deep layers. Hence, there seems to be a lower limit on the interply thickness for stable extraction, especially for deeper interplies. Practically, the minimum interply thickness should be a proportion of the fiber diameter at an interface where fibers change directions (around 2 µm for 7 µm diameter fibers [6]). Furthermore, the realistic minimum usually is about 5 µm.

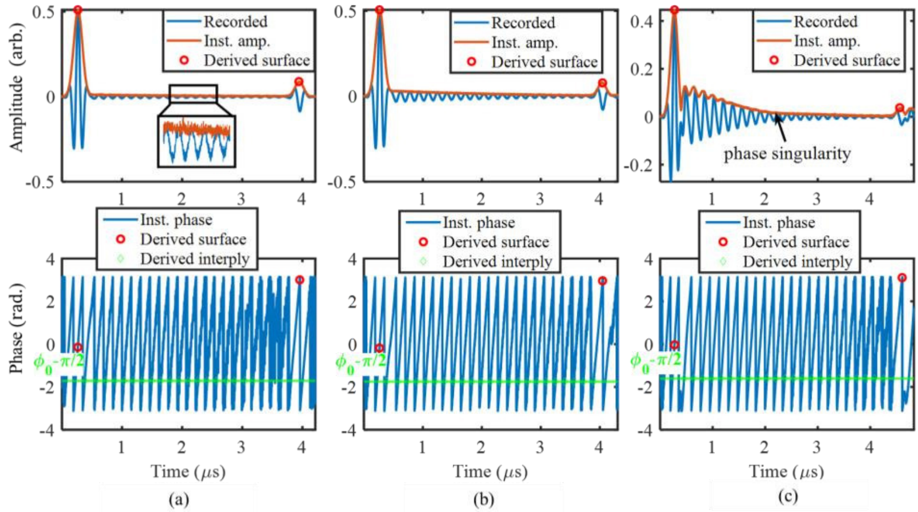

Figure 6-13 Recorded signals and their instantaneous amplitudes and instantaneous phases for various interply thickness to ply thickness ratios: (a) 0.01, (b) 0.03, and (c) 0.15.

6.3.7 Attenuation

The attenuation has a direct influence on the energy in the ultrasonic response signal. The ultrasonic echoes from deeper layers are higher attenuated, which will yield a lower SNR. The influence of both the ply attenuation and the interply attenuation are studied in this section. Frequency-dependent attenuation is considered here. This attenuation includes (amongst others) viscoelastic damping, attenuation due to the presence of voids and porosities [7, 8], and scattering at fiber (bundles) [9, 10]. The nominal ply and interply attenuations are 0.1 and 0.15 dB/mm/MHz, respectively. A variation of the ply attenuation from 0.05 dB/mm/MHz to 0.3 dB/mm/MHz is considered. The errors of the phase-derived interply tracking are shown in Figure 6-14a and b. For relatively low attenuation levels (<0.15 dB/mm/MHz), the induced errors remain at an acceptable level, even for deep plies. Once the ply attenuation rises to 0.15 dB/mm/MHz, the errors in deep layers are over 100%. The noise becomes extremely large when the ply attenuation reaches 0.2 dB/mm/MHz. In that case, no 2π increment can be detected anymore in the deep layers due to noise, resulting in no extracted interply in the deep layers.

The interply attenuation has a minor influence on the interply tracking. Figure 6-14c reveals that even a very high interply attenuation of 2 dB/mm/MHz yields minor errors. This is related to the fact that the interplies in CFRP laminates typically have a small thickness in the order of a few µm, resulting in only limited attenuation of the ultrasonic signal.

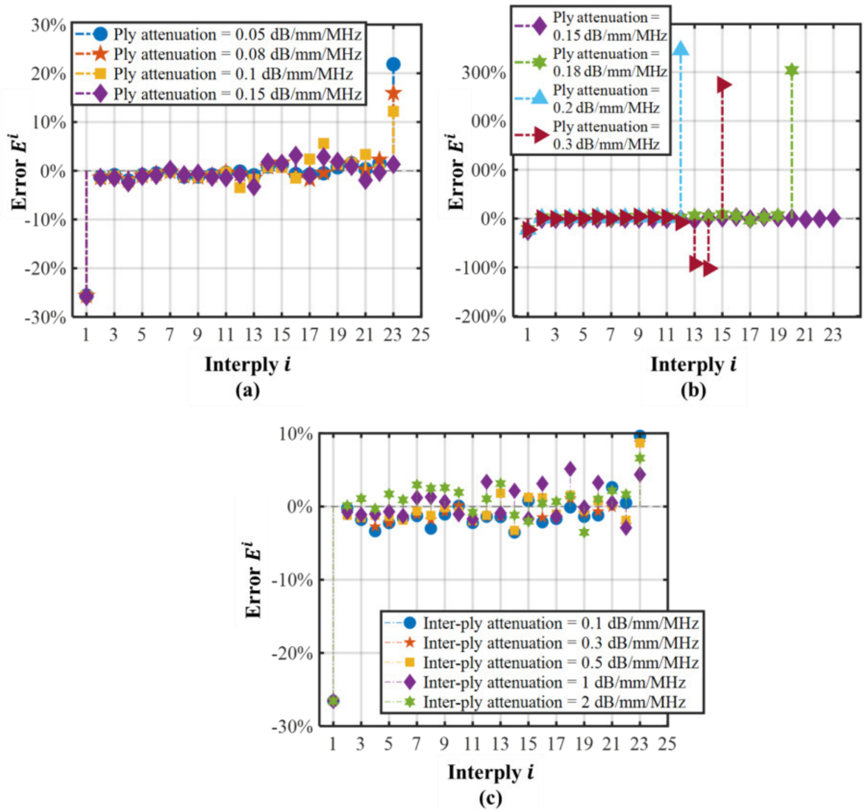

Figure 6-14 Errors E^i of the phase-derived interply tracking corresponding to: (a) ply attenuation in range 0.05–0.0.15 dB/mm/MHz, (b) ply attenuation in range 0.15–0.5 dB/mm/MHz, and (c) interply attenuation in range.

6.3.8 Fiber volume fraction

The fiber volume fraction affects the density and stiffness properties of the ply. Hence, it will influence the impedance mismatch between the ply and the interply and the strength of the interface reflections. It should be noted that the attenuation could also change with the fiber volume fraction because the attenuation in resin is more significant than in fibers. However, it is assumed here that the attenuation does not change with the fiber volume fraction to exclusively study the influence of impedance mismatch on the performance of the interply tracking procedure. The nominal fiber volume fraction is 60%. A variation of the volume fraction from 60% to 30% is considered to study the influence of the fiber volume fraction. Note that the stiffness tensor of the CFRP changes with the fiber volume fraction according to the Chamis formulas, which means the stiffness tensor is calculated again each time the fiber volume fraction changes.

As long as the fiber volume fraction is higher than 40%, the errors of the interply tracking remain stable (see Figure 6-15a). This result can be understood considering that the interply tracking is done by evaluating the instantaneous phase. The varying impedance mismatch changes the amplitudes of the echoes from both boundaries of one interply in the same ratio. Consequently, the instantaneous phases of the echoes from the interplies nearly do not change.

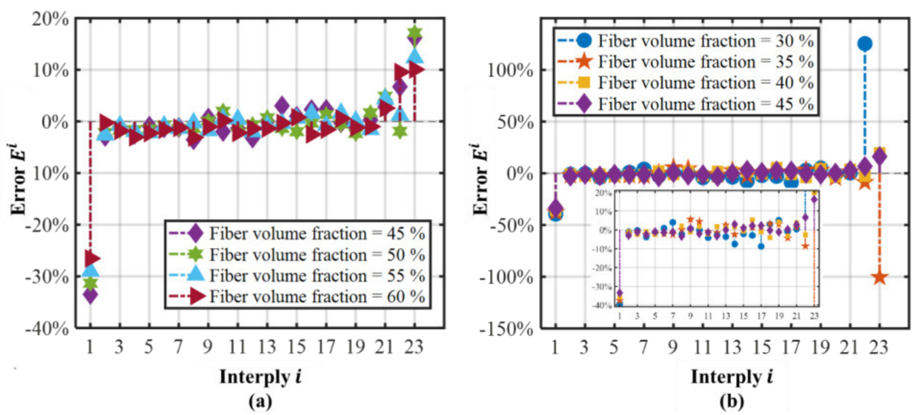

Figure 6-15 Errors E^i of the phase-derived interply tracking corresponding to the fiber volume fraction of (a) 45% to 60% and (b) 30% to 45%.

However, the reduced amplitudes of interply echoes increase the dominating effect of the FWE and BWE, causing more significant errors for the interplies near the surfaces. If the volume fraction becomes lower than 40%, the impedance mismatch between the plies and interplies becomes so small that the echoes from the interplies become very weak. As such, it becomes difficult to extract the instantaneous phase for deep plies in an accurate manner (see Figure 6-15b).

6.4 Improved interply tracking by application of a Log-Gabor Filter

The parametric study in Section 6.3 illustrates that phase-derived interply tracking is sensitive to noise, especially in deep layers where the SNR is low due to the attenuation. Further, the results indicated that it is of utmost importance to select a center frequency close to the resonance frequency of a single ply, together with an optimal bandwidth. Often, ultrasonic transducers do not fulfill these optimal conditions. Therefore, a procedure is proposed based on the log-Gabor filter to decompose the ultrasonic reflection signal in different appropriate time scales. The log-Gabor filter is preferred because it can be constructed with an arbitrary bandwidth and center frequency while maintaining zero gain at the zero-frequency component [11]. It is particularly suited for estimating the instantaneous phase and instantaneous frequency [12]. The log-Gabor filter is defined as follows:

$$G(\omega) = \exp \frac{-\left(\log(\frac{|\omega|}{\omega_0})\right)^2}{2(\log \sigma_0)^2}, \tag{6.3}$$

where ω_0 is the angular center frequency of the passband and σ_0 governs the bandwidth of the passband. The lower bound f_{lower} and the upper bound f_{upper} of the −6 dB bandwidth are

$$f_{lower} = f_0 \exp\left(\sqrt{2\log(2)}\log(\sigma_0)\right), \tag{6.4}$$

$$f_{upper} = f_0 \exp\left(-\sqrt{2\log(2)}\log(\sigma_0)\right), \tag{6.5}$$

where $f_0 = \frac{\omega_0}{2\pi}$ is the center frequency of the filter. And the fractional bandwidth of the filter is

$$W_f = \frac{f_{\text{upper}} - f_{\text{lower}}}{f_0}. \tag{6.6}$$

The filtered reflection spectrum $\widetilde{F_a^R}(\omega)$ is obtained by multiplication of the analytic-signal response $F_a^R(\omega)$ with the log-Gabor filter $G(\omega)$:

$$\widetilde{F_a^R}(\omega) = G(\omega)F_a^R(\omega). \tag{6.7}$$

Finally, the filtered analytic-signal in the time domain is obtained by application of an inverse Fourier transform:

$$\widetilde{s_a^R}(t) = \mathrm{IFT}\big(\widetilde{F_a^R}(\omega)\big), \tag{6.8}$$

It is known from Section 6.3.4 that a too narrow bandwidth cannot cope with widely varying ply thicknesses, while a too wide bandwidth could result in a second-harmonic ply resonance. Considering that the log-Gabor filter puts further restrictions on the bandwidth of the response signal, it is crucial to verify its performance for a multi-layer structure with varying ply thicknesses. Therefore, an additional simulation study is performed for an immersed multi-layer structure with the following CFRP ply thickness sequence: $[260\mu\mathrm{m}/220\mu\mathrm{m}/180\mu\mathrm{m}/220\mu\mathrm{m}]_6$.

Table 6-2 presents the employed parameters for the input signal and data acquisition (chosen according to the available experimental equipment in the NDT lab of UGent-MMS). For the log-Gabor filter, the f_0 equals 6.5 MHz, i.e. the ply resonance frequency for a CFRP ply thickness of 220 μm, while the bandwidth of the passband σ_0 ranges between 0.5 and 0.9 (see Table 6-3). The original signal is displayed in Figure 6-16.

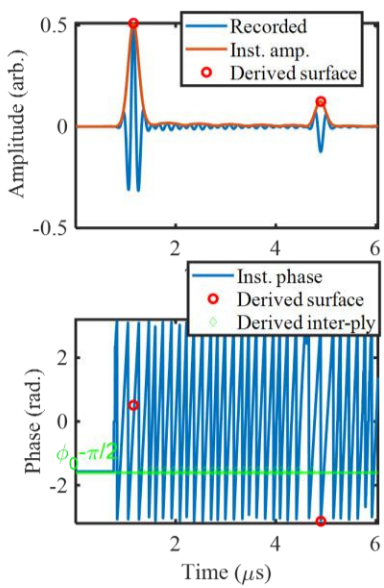

Figure 6-16 Original signals and their instantaneous amplitudes and instantaneous phases with a center frequency of 6.5 MHz.

Table 6-2 The parameters of the input signal and data acquisition for the validation test

Pulse-type	F_c^{val} (MHz)	W^{val}	AW_{dB}^{val} (dB)	Media	SNR^{val} (dB)	Fs^{val} (GS/s)
In-phase	6	0.8	-6	water	35	1

Table 6-3 The considered bandwidths of the log-Gabor filter for the validation test

σ_0	f_{lower} (MHz)	f_{upper} (MHz)	W_f
0.5	2.87	14.70	1.82
0.6	3.56	11.86	1.28
0.7	4.27	9.89	0.86
0.8	5.00	8.45	0.53
0.9	5.74	7.36	0.25

Without the application of the log-Gabor filter, large errors are obtained for the deeper interplies. Application of log-Gabor filter with $\sigma_0 = 0.5$ improves the performance, but still yields large errors for the deepest interplies. The results for $\sigma_0 > 0.5$ indicate good performance with low errors over all plies. However, once the σ_0 increases to 0.9, the results clearly show that the errors increase because of the too narrow fractional bandwidth W_f (see Table 6-3). The filtered signals and their instantaneous amplitudes and instantaneous phases with different σ_0 are displayed in Figure 6-18. Based on these results, a σ_0 of 0.7 ($W_f = 0.86$) seems to be an appropriate choice.

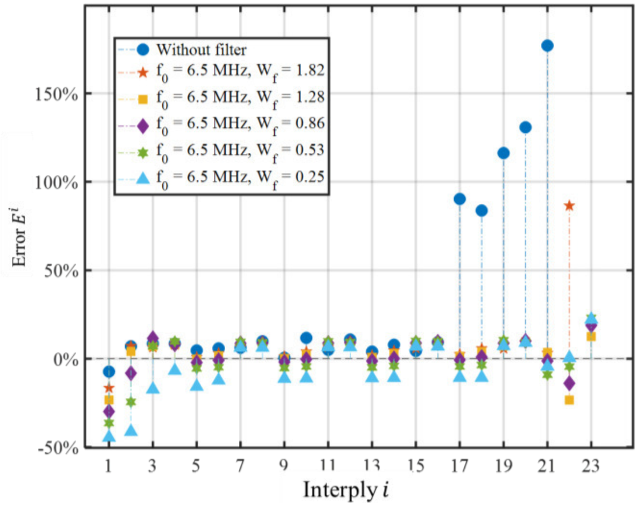

Figure 6-17 Errors E^i on the phase-derived interply tracking for various bandwidths of the log-Gabor filter.

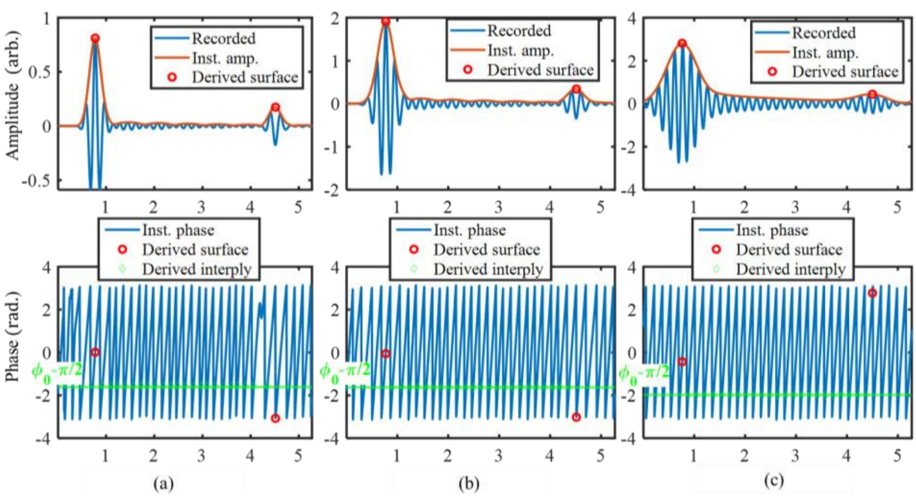

Figure 6-18 Filtered signals and their instantaneous amplitudes and instantaneous phases with a center frequency of 6.5 MHz and various bandwidths for the log-Gabor filter: (a) $\sigma_0 = 0.5$, (b) $\sigma_0 = 0.7$, and (c) $\sigma_0 = 0.9$.

6.5 Experimental Study

An experimental study has been performed on a 24-layer carbon/epoxy laminate with $[0/90]_{6s}$ stacking sequence. The laminate has dimensions of 150 mm × 100 mm and a thickness of 5.55 mm. It has been manufactured by autoclave, and it is assumed to have a uniform ply thickness of around 231 μm.

6.5.1 Experimental setup

The signal is acquired in pulse-echo (PE) mode by a spherically focused immersion transducer (GE H5M) with a nominal central frequency of 5 MHz, a measured −6 dB bandwidth ranging from 2.7 MHz to 6.6 MHz. Thus, the measured center frequency is approximately 4.65 MHz. The transducer has an element diameter of 5 mm and a focal distance of 25.4 mm. The focal point is in the mid-plane of the sample, which is immersed in water. The transducer is excited by an ultrasonic pulser (Tecscan UTPR- CC-50) which provides a spike pulse with a voltage of 120 V (see Figure 6-19). The reflection signal is acquired by a 14-bit digitizer card (NI PXIe-5172) at 250 MS/s. Raster scanning is achieved by a 3-axis Cartesian scanner employing the motion controller card (NI PXI-7350). The scanning area is 20 mm×20 mm. A scanning step size of 0.25 mm is used to scan both x and y directions. The scanning speed in both x and y directions is 20 mm/s.

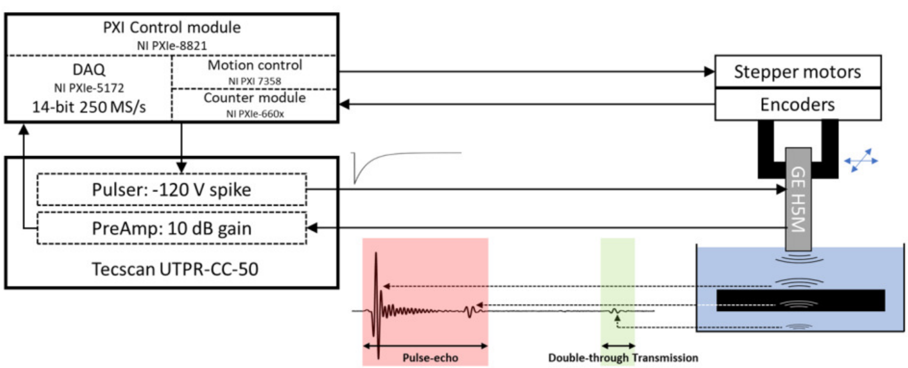

Figure 6-19 Experimental setups of the ultrasonic testing.

6.5.2 Results

The recorded signal and the analytic-signal response are demonstrated in Figure 6-20a for an arbitrary scan point. The depth positions of the interplies are derived from the instantaneous phases. It can be seen in Figure 6-20a that the interply tracking is seriously affected by the noise and the different frequency components in the response signal. In order to improve the interply tracking, a log-Gabor filter is applied. Considering that the TOF between the FWE and BWE corresponds to 3.70 μs, this indicates a ply resonance frequency of 6.49 MHz. Together with the observations in Section 6.4, a log-Gabor filter with a center frequency of 6.5 MHz and a bandwidth of 0.86 ($\sigma_0 = 0.7$) is applied for appropriate scale selection. The SNR of the filtered response signal increases significantly (see Figure 6-20b). More importantly, the interply is tracked in a stable way. Hence, the analytic-signal procedure combined with the optimized log-Gabor filter improves the performance of the phase-derived interply tracking considerably.

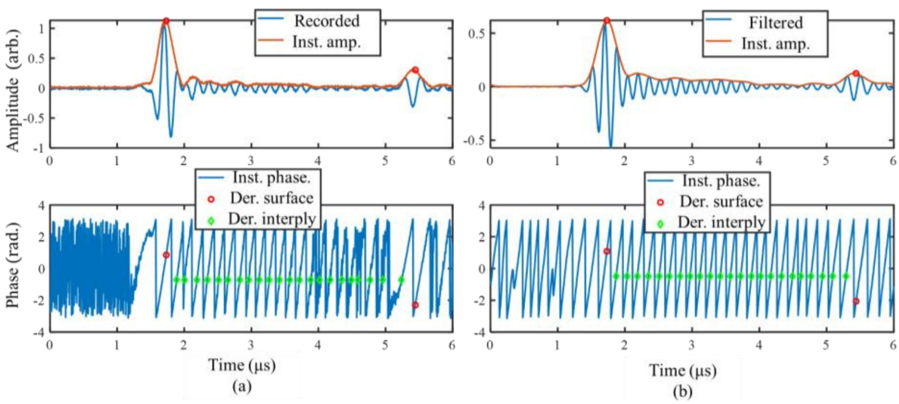

Figure 6-20 Recorded signals and their instantaneous amplitudes and instantaneous phases with (a) no filter, and (b) log-Gabor bandpass filter with a center frequency of 6.5 MHz and a bandwidth of 0.86 ($\sigma_0 = 0.7$).

A cross-sectional view (at $y = 0$ mm) of the interply tracking is presented in Figure 6-21 for both the original and the filtered signals. These results clearly show the added value of the log-Gabor filter for proper scale selection. The derived interply tracks become stable for all layers. The ply thickness (mean value and standard deviation) extracted from the filtered signal is reported in Figure 6-22. The results indicate a range of ply thicknesses from approximately 220 to 240 μm for the 2nd to 22nd plies, which agrees well with the nominal ply thickness of 231 μm (assuming that the plies are uniformly spaced). Note that the standard deviations are pretty minor (in the order of 10 μm) and gradually increase with the depth of the ply. This observation is readily understood in terms of the decreasing SNR with depth. The 1st and the 23rd ply show a higher deviation from the nominal ply thickness, attributed to the dominating effect of the FWE and BWE (see discussion in Section 6.3.1).

Especially for the 23rd ply, it seems reasonable that the echoes from the deepest layers tend to be too weak for observing accurate phases, thus degrading the accuracy of the derived thickness of the deepest plies. Sections 6.3.2 and 6.3.7 illustrate this point clearly.

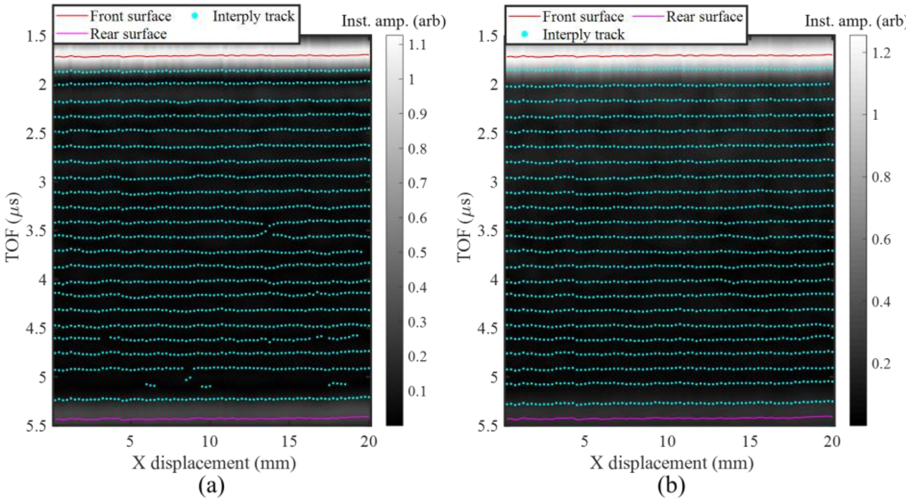

Figure 6-21 Cross-sectional views (at $y = 0$ mm) of the extracted ply tracks for (a) the original signals and (b) the log-Gabor filtered signals.

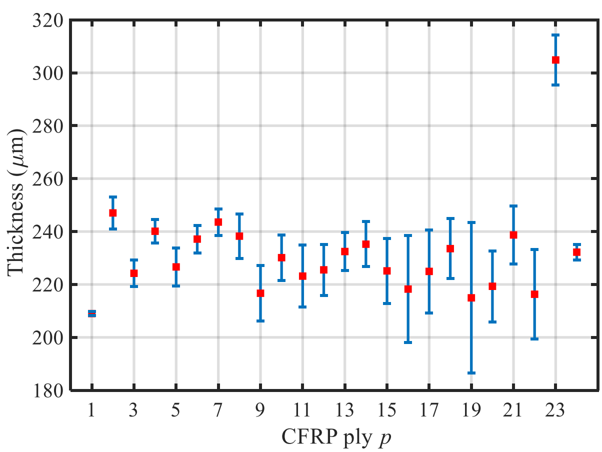

Figure 6-22 Estimated thickness of each ply of the $[0/90]_{6s}$ carbon/epoxy laminate using the instantaneous phase of the log-Gabor filtered response signal. The estimated thickness is represented as mean value$\pm$standard deviation (Error bars represent the standard deviation).

Figure 6-23a and c show the depth profiles of the 5th and the 23rd interply, derived from the original ultrasonic dataset. The result is acceptable for the 5th interply, indicating a depth position mainly between 1.1 mm and 1.25 mm. Nevertheless, for the deep interply, the extracted depth profile is of inferior quality. As is illustrated in the parametric study, the SNR is extremely low in the deep layers resulting in large errors in the determination of the instantaneous phase. Figure 6-23b and d show the depth profiles of the 5th and the 23rd interply, but now for the log-Gabor filtered ultrasonic dataset. The estimated depth profile of the 5th interply becomes more stable. Also, the depth profile of the last interply becomes very stable. It can also be seen that there are structured thickness deviations within a ply that are aligned along the dominating fiber orientations of the cross-ply CFRP laminate.

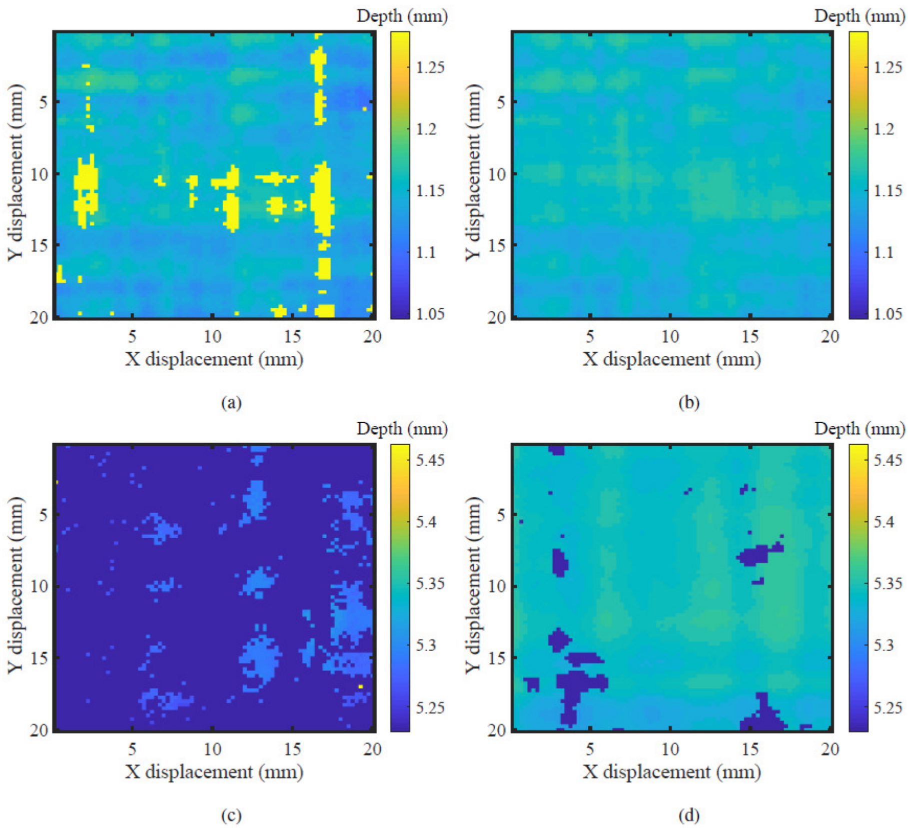

Figure 6-23 Depth of the 5th interply derived from (a) the original and (b) the filtered ultrasonic dataset; The depth of the 23rd interply derived from (c) the original and (d) the filtered ultrasonic dataset.

6.6 Conclusion

A parametric study is presented in order to investigate the performance of the instantaneous phase to track interplies in a CFRP laminate under different conditions. The simulated analytic-signal response from a 24-layer structure representative of a CFRP laminate has been used. The errors of the interply tracking are investigated for a range of material characteristics and ultrasonic parameters. The results provide a view on the conditions for which the analytic-signal technology provides good results for interply tracking. Following observations can be concluded for the here studied multi-layer structure:

- The dominating FWE and BWE for a water-immersed multi-layer structure induce a significant error in the nearby interply tracking. The use of matched media alleviates this error.
- The interply tracking procedure is robust for noise: stable results were obtained for signals with SNR > 30 dB. In the case of a lower SNR, the interply tracking resulted in large errors. The application of a log-Gabor filter can improve the performance for noisy signals.
- The center frequency and the bandwidth of the ultrasonic pulse significantly influence the performance of the interply tracking method. To cope with CFRP with various ply thicknesses ($\pm$20% of the nominal ply thickness), a center frequency close to the nominal ply resonance frequency and a fractional bandwidth of 0.8 are recommended. The application of a log-Gabor filter with the appropriate scale parameters could help in this regard.
- A too low sampling rate (≤100 MS/s) introduces errors in the interply tracking. If a higher sampling frequency cannot be selected due to hardware limitations, interleaved sampling can be considered.
- A very thin interply (≤2.2 µm or ≤1% of nominal ply thickness) leads to weak interply reflections, resulting in large errors in deep layers due to a low SNR. For a thick interply (≥11 µm or ≥5% of nominal ply thickness), the errors increase with depth. A very thick interply (≥22 µm or ≥10% of nominal ply thickness) results in ultrasonic artefacts caused by phononic band gaps and phase singularities.
- The interply tracking errors increase for large attenuation values (>0.15 dB/mm/MHz) as well as for low fiber volume fraction (<40%). This is mainly due to the fact that the SNR drops significantly for the deeper plies.

A $[0/90]_{6s}$ CFRP laminate has been experimentally investigated by raster scanning in PE mode. According to the lessons learned from the parametric study, a log-Gabor filter with appropriate scale parameters was applied to the recorded data. By applying the appropriate log-Gabor filter, the extraction of interply tracks becomes much more stable and robust, especially for the deeper plies. The performance of the analytic-signal procedure combined with a log-Gabor filter is verified by the reconstructed interply tracks in A-scan, B-scan, and C-scan modes. These results demonstrate the added value of the log-Gabor filter for proper scale selection and noise suppression.

References

[1] Smith, R. A., Nelson, L. J., Mienczakowski, M. J., and Wilcox, P. D., "Ultrasonic tracking of ply drops in composite laminates," Proc. AIP Conference Proceedings, AIP Publishing LLC, p. 050006.

[2] Smith, R. A., Nelson, L. J., Mienczakowski, M. J., and Wilcox, P. D., 2017, "Ultrasonic analytic-signal responses from polymer-matrix composite laminates," IEEE transactions on ultrasonics, ferroelectrics, and frequency control, 65(2), pp. 231-243.

[3] Nelson, L., Smith, R., and Mienczakowski, M., 2018, "Ply-orientation measurements in composites using structure-tensor analysis of volumetric ultrasonic data," Composites Part A: Applied Science and Manufacturing, 104, pp. 108-119.

[4] Yang, X., Verboven, E., Ju, B.-f., and Kersemans, M., 2021, "Parametric study on interply tracking in multilayer composites by analytic-signal technology," Ultrasonics, 111, p. 106315.

[5] Smith, R. A., Nelson, L. J., and Mienczakowski, M. J., 2018, "Phononic Band Gaps and Phase Singularities in The Ultrasonic Response from Toughened Composites," Aip Conf Proc, 1949.

[6] Smith, R. A., 2010, "Use of 3D ultrasound data sets to map the localised properties of fibre-reinforced composites," University of Nottingham, Nottingham.

[7] Jeong, H., 1997, "Effects of voids on the mechanical strength and ultrasonic attenuation of laminated composites," Journal of composite materials, 31(3), pp. 276-292.

[8] Jeong, H., and Hsu, D. K., 1995, "Experimental analysis of porosity-induced ultrasonic attenuation and velocity change in carbon composites," Ultrasonics, 33(3), pp. 195-203.

[9] Biwa, S., Watanabe, Y., and Ohno, N., 2003, "Analysis of wave attenuation in unidirectional viscoelastic composites by a differential scheme," Compos Sci Technol, 63(2), pp. 237-247.

[10] Biwa, S., 2001, "Independent scattering and wave attenuation in viscoelastic composites," Mechanics of materials, 33(11), pp. 635-647.

[11] Boukerroui, D., Noble, J. A., and Brady, M., 2004, "On the choice of band-pass quadrature filters," J Math Imaging Vis, 21(1), pp. 53-80.

[12] Granlund, G. H., and Knutsson, H., 2013, Signal processing for computer vision, Springer Science & Business Media.

Chapter 7 Comparative Study of Ultrasonic Techniques for Interply Tracking

7.1 Introduction

High-frequency ultrasound can be utilized to characterize sub-surface damage with a high spatial and temporal resolution [1-3]. As the thickness and the number of plies increase, the attenuation of high-frequency ultrasound becomes a concern, especially for high damping fiber reinforced polymers (FRPs) [4]. A recent study has reported an impacted carbon fiber reinforced polymer (CFRP) laminate inspection using 50 MHz ultrasound and demonstrated a depth probing as deep as 2–2.5 mm [2]. Alternatively, one could lower the ultrasound frequency in order to increase the dynamic depth range, but this is at the expense of the depth resolution. Therefore, researchers have employed various signal processing steps to improve the temporal resolution of the ultrasonic response signal.

A simple approach concerns the application of a low-pass (LP) filter to reduce the high-frequency noise [5, 6]. Another common signal processing step is the deconvolution technique to estimate the impulse response from the recorded signal in the presence of noise. Some studies have compared various deconvolution techniques and found that Wiener filtering-based techniques yield good results for online applications [7, 8]. However, a major problem with the Wiener filter is that it produces a deconvolved signal with a narrowband spectrum. Naturally, the signal with a narrowband spectrum has a decreased temporal resolution. Therefore, it was proposed to additionally use an autoregressive (AR) spectral extrapolation [9-11]. In the application of the AR spectral extrapolation, the deconvolved spectrum with a high signal-to-noise ratio (SNR) is modeled as an AR process, which is then used to extrapolate the low SNR part of the signal spectrum. Combining the Wiener deconvolution and AR spectral extrapolation improves temporal resolution and SNR further [12]. This method, however, suffers from the fact that the optimized parameters need to be found through trial and error [10, 12].

Further, the Wiener deconvolution is not valid when the input signal and the system are unknown [13]. Hence, because the input signal typically has a sparse distribution, it has been proposed to find a deconvolution filter whose output distribution is as sparse as possible [14, 15]. Several blind deconvolution methods have been developed to improve the temporal resolution of the ultrasonic signal [16-18]. However, note that such blind deconvolution is seldom considered in ultrasonic testing (UT) because the impulse response function of an employed ultrasonic system is often well known (or can be easily measured).

As introduced in 0 and 0, the instantaneous phase-derived ply tracking method is based on the condition of ply resonance, which for typical CFRP laminates, happens at low frequencies in the 6–7 MHz range. The instantaneous phase of the analytic-signal becomes locked to the interfaces between plies. As such, this approach yields a high probing depth in multi-layer CFRP laminates. Furthermore, the application of a log-Gabor filter has been presented to make the phase-derived interply tracking more stable and robust [19].

This chapter compares the performance of different ultrasonic approaches for extracting the ply-by-ply structure of CFRP laminates:

- Method 1: 50 MHz, 15 MHz, and 5 MHz ultrasound with LP filtering, using analysis of the instantaneous amplitude,
- Method 2: 15 MHz ultrasound with Wiener deconvolution and autoregressive (AR) spectral extrapolation, using analysis of the instantaneous amplitude,
- Method 3: 5 MHz ultrasound with LP or log-Gabor filtering, using analysis of the instantaneous phase.

Note that the 5 MHz is a frequency commonly used in industry for inspections of aerospace components. Hence, Method 3 can be directly transferred to such an inspection environment without changing any hardware or scanning the parts multiple times.

This chapter is organized as follows. Section 7.2 describes the theoretical framework of the signal processing techniques, including the LP filtering, the deconvolution technique, and the analytic-signal technique. Sections 7.3.1 and 7.3.2 introduce the used parameters in the simulation, and the proposed quantitative evaluation metrics are proposed. Sections 7.3.3 and 7.3.4 investigate the performance of the different techniques for the synthetic data with different SNR. The experimental results are discussed in Section 7.4. Finally, Section 7.5 presents the conclusions.

7.2 Ultrasonic processing methods

7.2.1 Low-pass filter

Finite impulse response (FIR) filters are widely used for LP filtering due to their inherent stability when implemented in non-recursive form and simple extensibility to multi-rate cases. In this study, a FIR LP filter is applied as a pre-processing step to the recorded signals in order to reduce noise features [6]. The cutoff frequency of the FIR LP filter is twice the center frequency of the employed ultrasonic pulse. The transition band steepness is 0.8, and the stopband attenuation is 60 dB.

7.2.2 Wiener deconvolution with spectral extrapolation

In a linear time-invariant (LTI) system, the response signal $y(t)$ can be modeled as the convolution of the input signal $h(t)$ with the reflection sequence of sample $x(t)$, plus the addition of noise $n(t)$ (see Figure 7-1):

$$y(t) = x(t) * h(t) + n(t), \tag{7.1}$$

where $*$ denotes the convolution operator. Eq. (7.1) can be expressed in the frequency domain as follows:

$$Y(\omega) = X(\omega)H(\omega) + N(\omega), \tag{7.2}$$

where $Y(\omega)$, $X(\omega)$, $H(\omega)$, and $N(\omega)$ represent the Fourier transforms of $y(t)$, $x(t)$, $h(t)$, and $n(t)$ respectively.

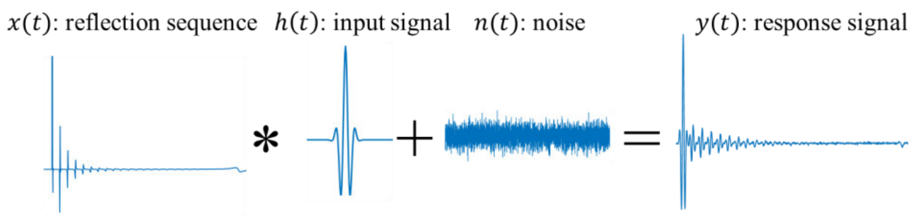

Figure 7-1 Response signal $y(t)$ from the LTI testing system as the convolution of the input signal $h(t)$ with the reflection sequence of the 24-layer structure $x(t)$ plus the addition of noise $n(t)$. The input signal $h(t)$ has a center frequency of 15 MHz and a fractional bandwidth (-6 dB) of 0.8. The scaling of these waveforms is different both in horizontal (time) and vertical (amplitude) directions.

Considering that $y(t)$ is measured and $h(t)$ is known, a deconvolution procedure can be performed to obtain the deconvolved signal $x_e(t)$ in the presence of noise $n(t)$. A Wiener filtering in the frequency domain can be applied to reduce noise. A common approach of the Wiener deconvolution can be formulated as [8]

$$X_e(\omega) = \frac{Y(\omega)H^*(\omega)}{|H(\omega)|^2 + Q^2}, \tag{7.3}$$

where $X_e(\omega)$ represents the Fourier transforms of $x_e(t)$ and Q is the noise desensitizing factor. A commonly recommended value for Q^2 is applied in this study [8, 20]:

$$Q^2 = 10^{-2}|H(\omega)|^2_{max}, \tag{7.4}$$

where $|H(\omega)|^2_{max}$ is the maximum amplitude of $|H(\omega)|$. The final stage is to employ the inverse Fourier transform to obtain the deconvolved signal in the time domain:

$$x_e(t) = \mathrm{IFT}\big(X_e(\omega)\big), \tag{7.5}$$

where $\mathrm{IFT}(\cdot)$ denotes the inverse Fourier transform.

To improve the temporal resolution further, AR spectral extrapolation can be applied to the reflection spectrum $X_e(\omega)$ obtained by Wiener filtering. First, a certain bandwidth of the measured reflection spectrum with a high SNR should be selected, whose lower and upper bounds are f_1 and f_2 respectively. The maximum-entropy algorithm of Burg [21] is then used to calculate the AR coefficients from the selected frequency window. Based on the high SNR reflection spectrum, the lower and upper parts of the reflection spectrum are extrapolated as follows:

$$\widehat{X_e}(m) = -\sum_{k=1}^{p_{ar}} a_k X_e(m+k) \quad m = 1,2,\cdots,\frac{Nf_1}{f_s} - 1, \tag{7.6}$$

$$\widehat{X_e}(n) = -\sum_{k=1}^{p_{ar}} a_k^* X_e(n-k) \quad n = \frac{Nf_2}{f_s} + 1,\cdots,\frac{N}{2}, \tag{7.7}$$

where $\widehat{X_e}(m)$ and $\widehat{X_e}(n)$ are the lower and upper parts of the extrapolated spectrum respectively, N is the sampling points, f_s is the sampling rate, a_k and a_k^* are the AR coefficients and their complex conjugates, respectively, and p_{ar} is the order of the AR model.

It has been proposed that the extrapolated signals obtained from different frequency windows could improve the robustness of this technique [10]. Hence, the extrapolated spectra from various frequency windows are averaged prior to performing the inverse Fourier transform for converting the signal into the time domain. The 3dB to 10 dB drop frequency windows recommended in the literature [10] are applied. Following the selection of the frequency window, the following equation is used to select the optimal order p_{opt} for performing the AR spectral extrapolation (with Burg as the fitting method) [22]:

$$p_{opt} = 0.014SNR + 0.21, \tag{7.8}$$

where SNR is expressed in decibel. Finally, the inverse Fourier transform can be employed on the extrapolated spectrum to obtain the extrapolated signal in the time domain:

$$\widehat{x_e}(t) = \text{IFT}\left(\widehat{X_e}(\omega)\right). \tag{7.9}$$

7.2.3 Analytic-signal with log-Gabor filter

The instantaneous amplitude and instantaneous phase are evaluated following the analytic-signal derivation in Section 5.2 and the interply tracking procedure in Section 6.2. These metrics can be used to derive the positions of the interplies in a CFRP laminate on the condition that the center frequency of the ultrasonic input signal approximately corresponds to the fundamental ply-resonance frequency. The instantaneous amplitude is analyzed to derive the time-of-flight (TOF) of the front-wall echo (FWE) and back-wall echo (BWE). The instantaneous phase is analyzed to derive the depth of the interplies. Note that the instantaneous amplitude can be alternatively used to estimate the locations for the resin-rich interplies (as effectively done for the other methods). As validated in Sections 6.4 and 6.5, the log-Gabor filter decomposes the analytic-signal in different appropriate scales and provides better estimates for the instantaneous phase and instantaneous frequency.

7.3 Simulation study

7.3.1 Simulation parameters

Note that we intend to evaluate the performance of the three ultrasonic techniques for interply tracking in this chapter. The evaluation requires a quantitative investigation of their noise resistance. Therefore, a nominal SNR of 25 dB is used for the simulation data. Considering that the plies in a CFRP laminate do not necessarily have a uniform thickness due to resin flow effects before the polymerisation in the autoclave [23, 24], it is crucial to understand how the three ultrasonic techniques can cope with ply thickness variations. Hence, a combination of 3 different ply thickness sequences is applied for the simulated data as follows: (i) a uniform ply thickness of 220 μm, (ii) a ply thickness sequence of $[220\mu m/210\mu m/230\mu m]_8$, and (iii) a ply thickness sequence of $[220\mu m/230\mu m/210\mu m]_8$. It is worth noting that the varying ply thickness is more challenging for the analysis of the instantaneous phase due to the fact that it requires a center frequency close to the ply-resonance frequency. Table 7-1 displays the used properties of the interply, the ply, and the immersion liquid. Table 7-2 provides the parameters concerning the input signal and data acquisition.

Table 7-1 The properties of the interply, the ply, and the immersion liquid

Name	Materials	Density (kg/m^3)	Thickness (μm)	Wave velocity (m/s)	Attenuation (dB/mm/MHz)
Interply	epoxy	1270 [25]	10	2499 [26]	0.15 [25]
CFRP ply	Mixture of fibers and epoxy matrix	1588	(i) 220 (ii) $[220/210/230]_8$ (iii) $[220/230/210]_8$	2906	0.1 [27]
Immersion water	1000	1480	-	-	-

Table 7-2 Parameters of the input signal and data acquisition

Center Frequency (MHz)	−6 dB fractional bandwidth	Bonding media	Nominal SNR (dB)	Sampling rate (MS/s)
5, 15, 50	0.8	water	25	250

7.3.2 Evaluation Metrics

A quantitative approach is used to investigate the performance of the three different ultrasonic techniques. The LP filtered signal is obtained by applying the LP filter to the original signal. And then, the TOF of the interplies is estimated from the local maxima in the instantaneous amplitude (see Figure 7-2a). The deconvolved signal equals $x_e(t)$ in Eq. (7.5) (or $\widehat{x_e}(t)$ in Eq. (7.9) when considering spectral extrapolation), and the TOF of the interplies is estimated from the local maxima in the instantaneous amplitude (see Figure 7-2a). The analytic-signal equals $s_a^R(t)$ in Eq. (5.7) (or $\widetilde{s_a^R}(t)$ in Eq. (6.8) when considering a log-Gabor filter), and the TOF of the interplies is estimated from the instantaneous phase (see Figure 7-2b). The detailed procedure for estimating the TOF of the interplies is given in the flowcharts in Figure 7-3.

The measurement error E^i of each interply i is calculated as

$$E^i = \frac{\varepsilon^i}{TOF^{ply}} \times 100[\%], \tag{7.10}$$

where TOF^{ply} is the true TOF of a single ply, ε^i is the absolute error (see also Figure 7-2). For each ply thickness sequence, each simulation procedure is repeated 100 times. The statistical information is extracted from the 300 runs in total.

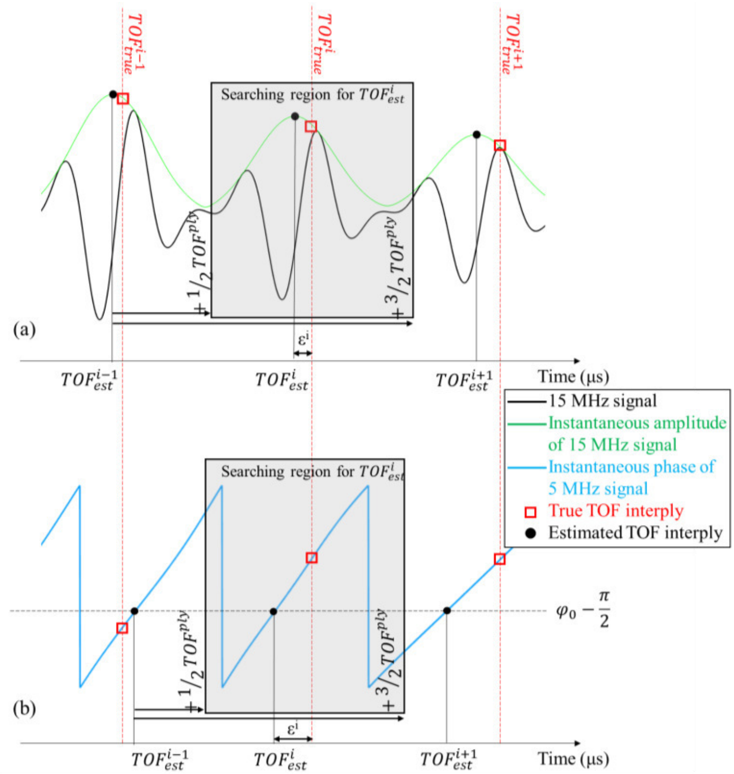

Figure 7-2 Schematic illustration of TOF estimation of the interplies based on (a) the instantaneous amplitude of a 15 MHz signal and (b) the instantaneous phase of a 5 MHz signal. Note: the graphs are only for illustration purposes and do not correspond to real signals.

The mean measurement errors (ME^i) and the standard deviations of the measurement errors ($STDE^i$) are evaluated:

$$ME^i = \frac{\sum_{j=1}^{N_s} E_j^i}{N_s}, \tag{7.11}$$

$$STDE^i = \sqrt{\frac{\sum_{j=1}^{N_s}\left(E_j^i - \overline{E_j^i}\right)^2}{N_s}}, \tag{7.12}$$

where E_j^i is the measurement error E^i in the ith layer and the jth repeat, and N_s is the number of signals considered.

In general, the ME^i and the $STDE^i$ indicate the accuracy and the robustness for estimating the TOF of the ith interply, respectively. Therefore, the error bars representing the ME^i and the $STDE^i$ can provide a comprehensive evaluation of the performance visually. However, the SNR of the signal is occasionally not high enough for properly distinguishing the interply reflections. In case the TOF_{est}^i is randomly distributed (over the 300 runs) in the searching region, and the true TOF of the interply is located in the middle of the searching region, this would result in a ME^i of 0% and an $STDE^i$ of 28.9%, which means the sensitivity to the variations of the ply thickness is wholly lost. Hence, to determine whether the interply reflections are distinguishable, a threshold of the $STDE^i$ is set at 22%. The lower the $STDE^i$, the better the interply reflections are distinguishable.

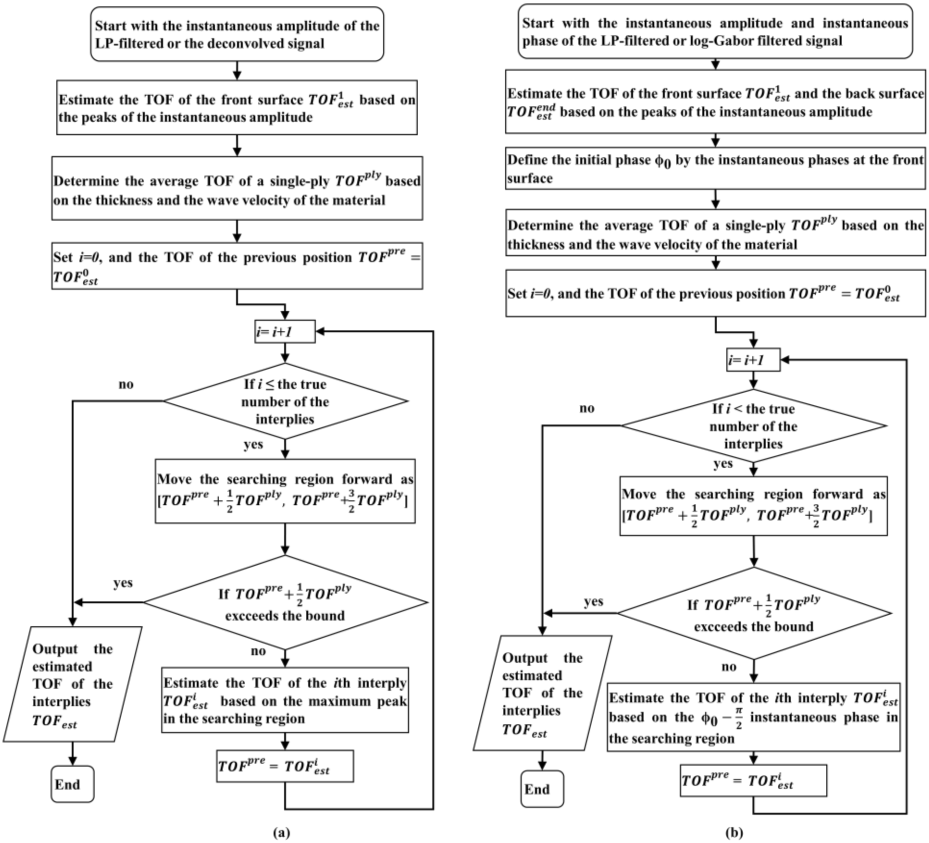

Figure 7-3 Flowcharts for estimating the TOF of the interplies by using (a) the instantaneous amplitude (Methods 1 and 2) and (b) the instantaneous phase (Method 3).

7.3.3 Results

7.3.3.1 Low-pass filtered signal using instantaneous amplitude (50 MHz; 15 MHz; 5 MHz)

The resolution and dynamic depth range of an ultrasonic signal are directly linked to its frequency. Figure 7-4 displays the simulation results for an input signal with center frequencies of 5 MHz, 15 MHz, and 50 MHz, respectively. The instantaneous amplitudes of the response signals have been extracted by using the Hilbert transform. From the instantaneous amplitudes, the positions of the interplies are estimated according to the procedure defined in Section 7.3.2. The true TOF of the interplies are indicated with the vertical red dashed lines. From Figure 7-4, it becomes clear that a higher center frequency produces sharper peaks at the positions of the interplies but at the same time experiences severe attenuation. The ME^i and the $STDE^i$ of the estimated interplies are presented in Figure 7-5. The front-surface and back-surface interplies are indicated with F and B respectively. The interplies i are indicated by their depth position, starting from $i = 1$ for the first interply until $i = 23$ for the last interply. If the $STDE^i$ becomes larger than 22% (= interply i could not be distinguished in a proper way), the value for interply i is greyed out.

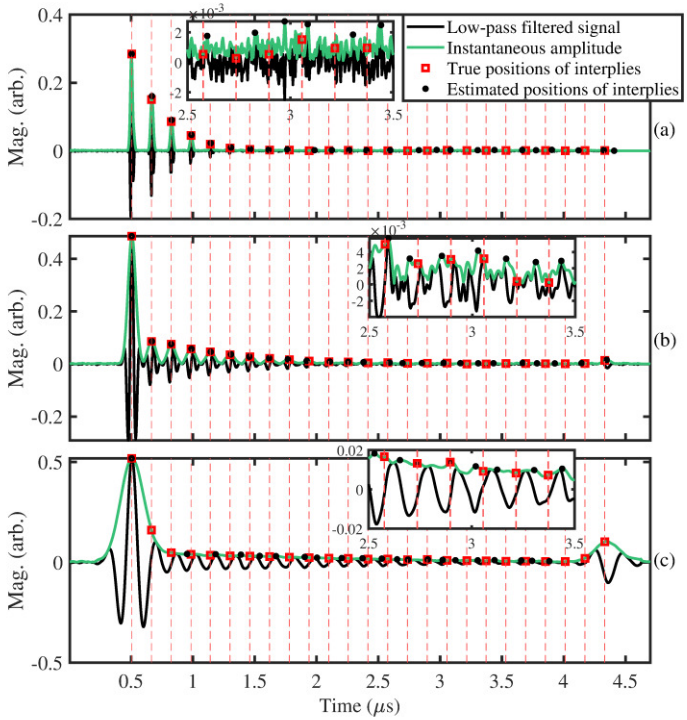

Figure 7-4 LP filtered signals with center frequencies of (a) 50 MHz, (b) 15 MHz, and (c) 5 MHz, respectively, including the instantaneous amplitude (green trace) and the true and estimated positions of the interplies (red square and black dot respectively).

The 50 MHz LP filtered signal produces sharp and clear peaks for the first 7 interplies, and locates these interplies in an accurate and robust manner. After the 8th interply, there is a sharp rise in the $STDE^i$. It can also be observed in Figure 7-4a that a BWE is not present due to excessive attenuation. Hence, the 50 MHz signal provides high depth resolution in the near-surface plies but becomes impractical due to its low SNR for deeper layers (see the inset in Figure 7-5a).

The 15 MHz LP filtered signal has higher $STDE^i$ for the near-surface plies, but it remains longer stable for deeper layers. The $STDE^i$ remain within 10% for the first 9 interplies. The graph reveals the gradual rise in the $STDE^i$ until it becomes fully unstable for plies deeper than the 14th interply. And an increase in the bias can be seen from the ME^i after the 12th interply. The observed gradual deterioration over depth makes the 15 MHz signal particularly well suited for the deconvolution procedure to increase the depth resolution (see further in Section 7.3.3.2).

The 5 MHz ultrasound efficiently penetrates through the whole structure and produces a well-defined BWE. However, the instantaneous amplitude of the 5 MHz LP filtered signal is clearly not valid for extracting the interply locations (see Figure 7-4c). The amplitude near the surfaces is completely affected by the strong surface echoes. Consequently, no peak of instantaneous amplitude is tracked for the 1st interply (see Figure 7-5c).

It can also be seen that the ME^i is very large and $STDE^i$ exceeds the value of 22% instantly. Hence, it is expected that the application of deconvolution will not provide any significant improvement for the 5 MHz signal. Instead, the 5 MHz signal will be coupled to the analytic-signal analysis, and the instantaneous phase will be used for estimating the positions of the interplies (see further in Section 7.3.3.3).

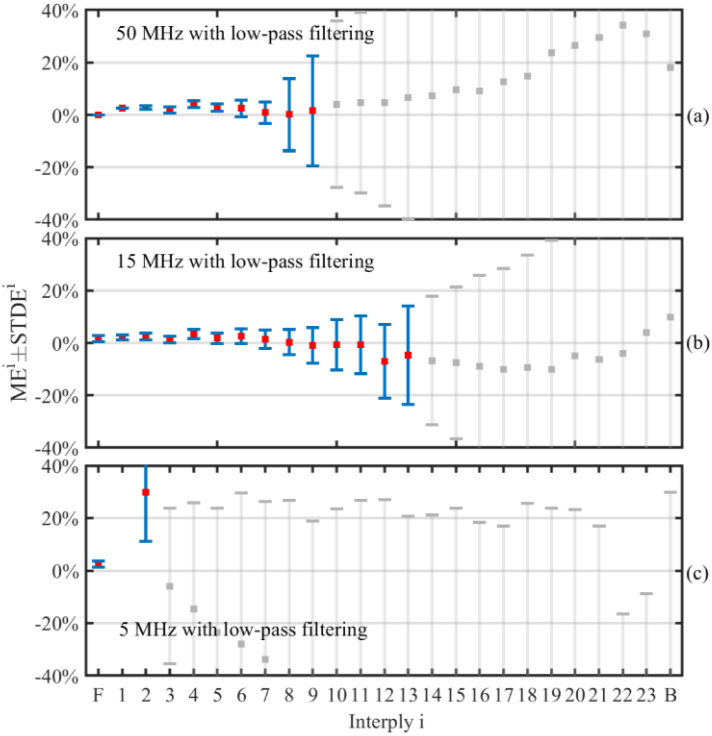

Figure 7-5 Error bars representing the ME^i and the $STDE^i$ of the estimated interplies from the instantaneous amplitudes of the LP filtered signals with center frequencies of (a) 50 MHz, (b) 15 MHz, and (c) 5 MHz, respectively. The data is represented as $ME^i \pm STDE^i$.

7.3.3.2 Deconvolved signal using instantaneous amplitude (15 MHz)

Based on the response signals in the previous section (see Figure 7-4 and Figure 7-5), it is anticipated that the application of deconvolution is a practical way to improve the depth resolution for the 15 MHz signal. Figure 7-6 displays the deconvolved signals with a center frequency of 15 MHz.

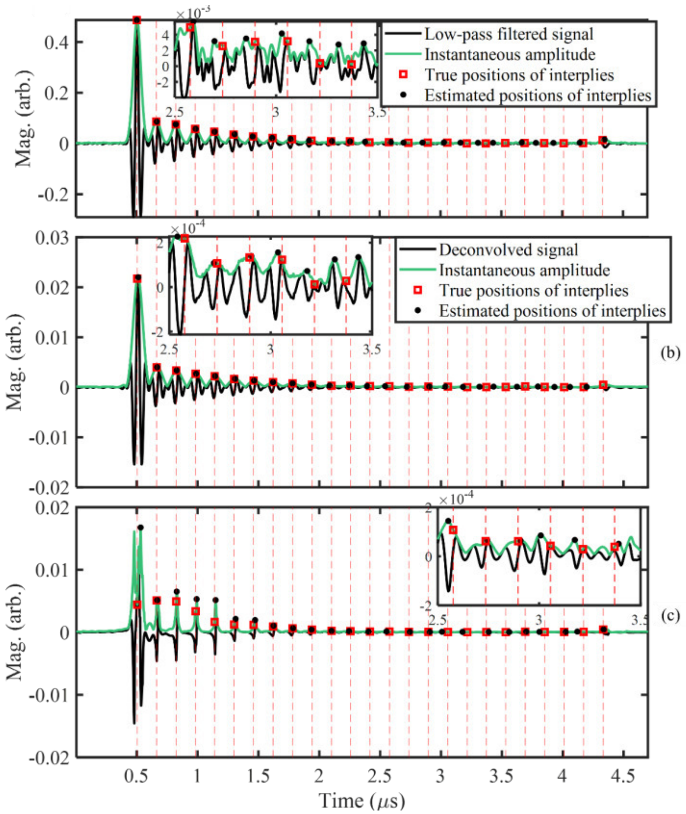

Figure 7-6 (a) LP filtered 15 MHz signal and deconvolved 15 MHz signals by (b) Wiener deconvolution and (c) Wiener deconvolution combined with AR spectral extrapolation. The instantaneous amplitude (green trace) and the true and estimated positions of the interplies (red square and black dot, respectively) are also visualized.

The input pulse with the nominal SNR of 25 dB is used as the deconvolution kernel. **Error! Not a valid bookmark self-reference.** lists the 3 dB to 10 dB drop frequency windows for multiple frequency windows AR spectral extrapolation. The optimal order p_{opt} of the AR process is chosen according to Eq. (7.8) for each window. The instantaneous amplitudes of the deconvolved signals have been extracted by Hilbert transform, from which the positions of the interplies are estimated according to the previously defined procedure (see Section 7.3.2).

Table 7-3 The frequency windows and the optimal orders considered for multiple frequency windows AR spectral extrapolation

Drop (dB)	Frequency range (MHz)	Data points	p_{opt}
-3	10.8–19.2	88–158	39
-4	10.1–19.9	83–163	45
-5	9.5–20.5	78–168	50
-6	9.0–21.0	74–172	55
-7	8.5–21.5	70–176	59
-8	8.1–21.9	66–180	64
-9	7.7–22.3	63–183	67
-10	7.3–22.7	59–186	71

From Figure 7-6 it can be seen that the deconvolution techniques significantly improve the temporal resolution and SNR compared to the LP filtered signal. The ME^i and the $STDE^i$ of the estimated interplies from the LP filtered and the deconvolved signals are compared in Figure 7-7. Compared to the LP filtered signal, the Wiener deconvolution has a minor effect on the ME^i, but reduces the $STDE^i$ significantly. Hence, this indicates that the extraction of interply locations is more stable and robust. Still, for very deep layers (>17th interply), the $STDE^i$ rapidly converges again to values above 22%, indicating completely random TOF estimation.

Contrary to the expectation, the Wiener deconvolved signal combined with AR spectral extrapolation shows the worst performance of the Method 2 approaches. This is possibly due to the fact that the AR process is quite sensitive to noise [28]. Further, some spurious spikes have been reported to be observed in the deconvolved ultrasonic signal by optimized AR spectral extrapolation [22]. These spurious spikes could be large in amplitude and could become comparable to the actual signal. This report is especially valid for the current situation because the reflection signal from the interplies is weak. Hence, the Wiener deconvolution combined with AR spectral extrapolation is not a suitable approach for the here considered case.

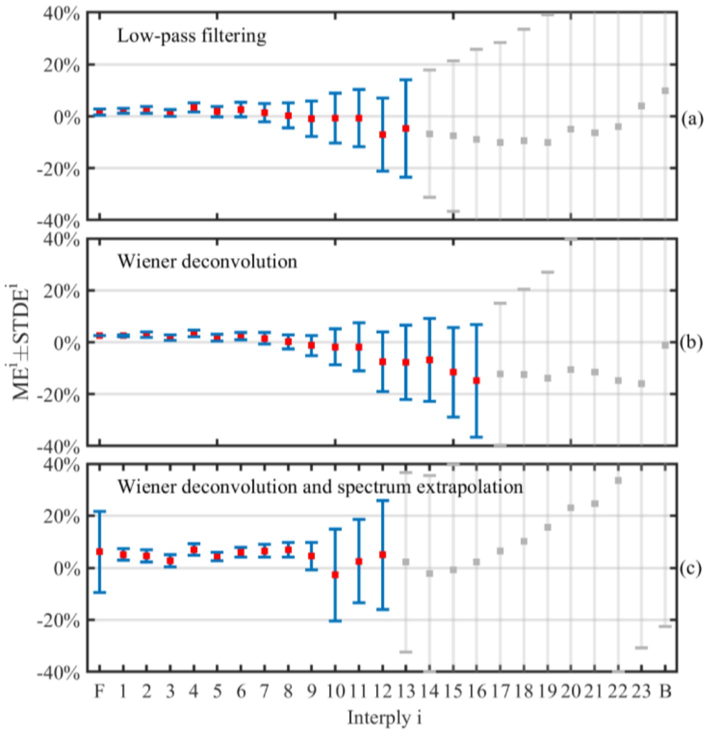

Figure 7-7 Error bars representing the ME^i and the $STDE^i$ of the estimated interplies from the instantaneous amplitudes of (a) the 15 MHz LP filtered signal, (b) the 15 MHz Wiener deconvolved signal, and (c) the 15 MHz Wiener deconvolved signals combined with AR spectral extrapolation. The data are represented as $ME^i \pm STDE^i$.

7.3.3.3 Analytic-signal using instantaneous phase (5 MHz)

From the analysis presented in Section 7.3.3.1, it became clear that the instantaneous amplitude of the 5 MHz LP filtered signal could not be used for estimating the positions of the interplies. Considering that the frequency of 5 MHz is close to the ply-resonance frequency, the instantaneous phase could offer an effective way of estimating the positions of the interplies (see Section 6.2).

Figure 7-8a displays the instantaneous amplitude, instantaneous phase, and instantaneous frequency of the 5 MHz LP filtered analytic-signal. The instantaneous frequency in Figure 7-8 indicates a ply-resonance frequency of approximately 6.3 MHz. As long as the bandwidth in the 5 MHz pulse is sufficiently broad to excite the 6.3 MHz ply-resonance in an efficient manner, the instantaneous phase-derived interply tracking procedure should work. In order to match the input signal better to the ply resonance, a log-Gabor filter is applied for optimal scale selection. The center frequency and σ_0 for the log-Gabor filter are chosen as 6.3 MHz and 0.7, respectively.

Figure 7-8b displays the instantaneous amplitude, instantaneous phase, and instantaneous frequency of the 5 MHz analytic-signal with the application of the log-Gabor filter. One can readily see the filter's effect on the quality of the signals, especially on the instantaneous frequency. Compared to the LP filtered analytic-signal in Figure 7-8a, the log-Gabor filtered analytic-signal shows a steadier instantaneous frequency around the fundamental ply-resonance frequency in Figure 7-8b. The ME^i and the $STDE^i$ obtained from the 5 MHz signals are compared in Figure 7-9.

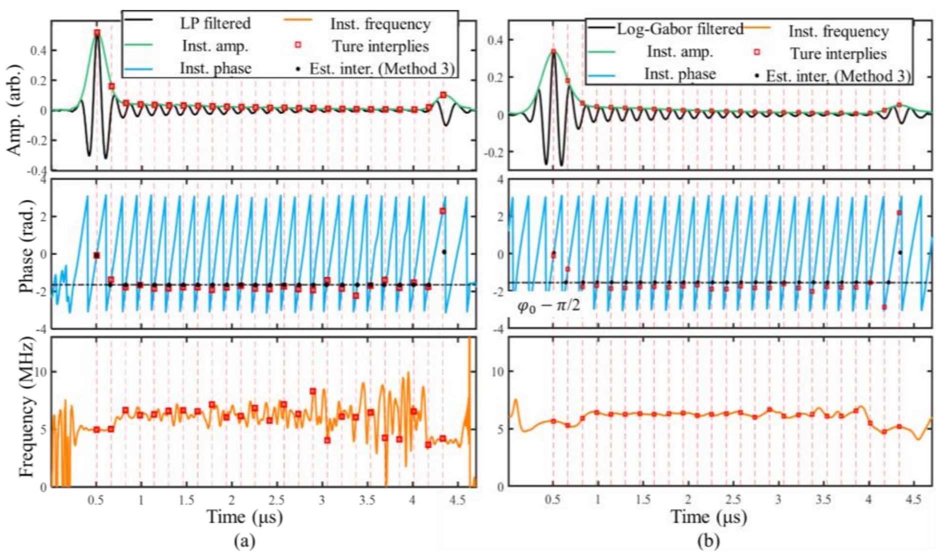

Figure 7-8 5 MHz analytic-signals (a) with LP filtering and (b) log-Gabor filtering, including the instantaneous amplitude (green trace), the instantaneous phase (blue trace), the instantaneous frequency (orange trace). The true and estimated positions of the interplies are indicated by red squares and black dots, respectively.

While the instantaneous amplitude does not indicate the positions of the interplies, the instantaneous phase provides steady results for all interplies. It is worth noting that the $STDE^i$ is significantly improved by the application of the log-Gabor filter. However, the estimated TOF of the interplies near the surfaces shows large ME^i (around -15% for the 1st interply and $+28\%$ for the

23rd interply) due to the dominating effect of the FWE and BWE. Compared to the analytic-signal with LP filtering in Figure 7-9b, the log-Gabor filter reduces the random errors considerably, but magnifies the ME^i in the 1st and the last plies. The $STDE^i$ steadily increases with depth, but remains below 5% by application of the log-Gabor filter, indicating the high robustness of the TOF estimation. The log-Gabor filter is suggested as a better choice because of its high robustness.

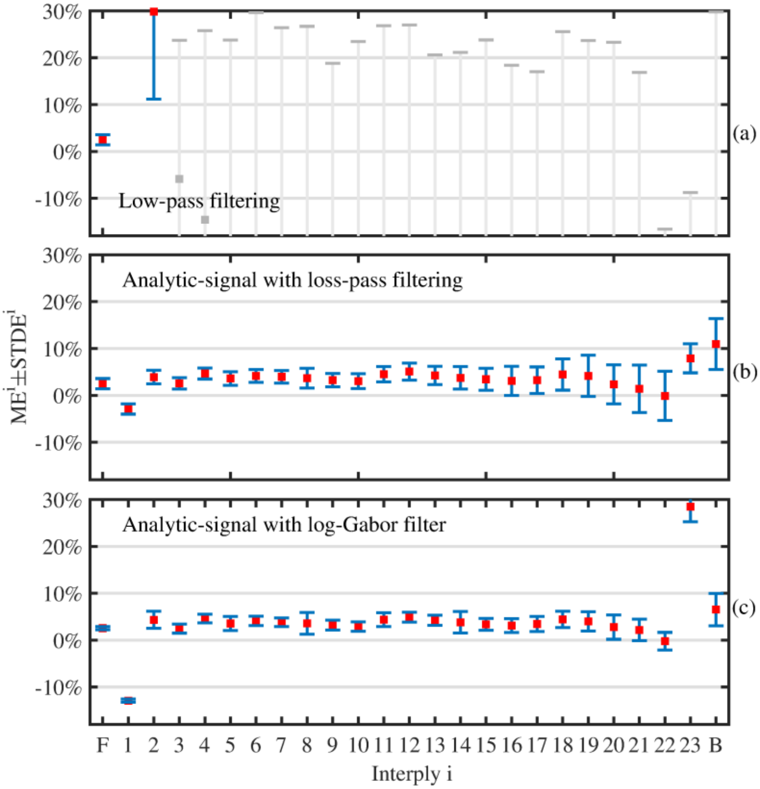

Figure 7-9 Error bars representing the ME^i and the $STDE^i$ of the estimated interplies from (a) the instantaneous amplitude of the 5 MHz LP filtered signal, and the instantaneous phase of the 5 MHz (b) LP filtered, and (c) log-Gabor filtered signals. The data is represented as $ME^i \pm STDE^i$.

7.3.4 Comparative Analysis for Different Noise Levels

The performance of the various techniques for different noise levels is investigated in this section. The results for 3 SNRs (25 dB, 20 dB, and 15 dB) are simulated and analyzed. Figure 7-10 shows the response signal for the various levels of SNR. The ME^i and the $STDE^i$ obtained from the signals for various levels for SNR are compared in Figure 7-11.

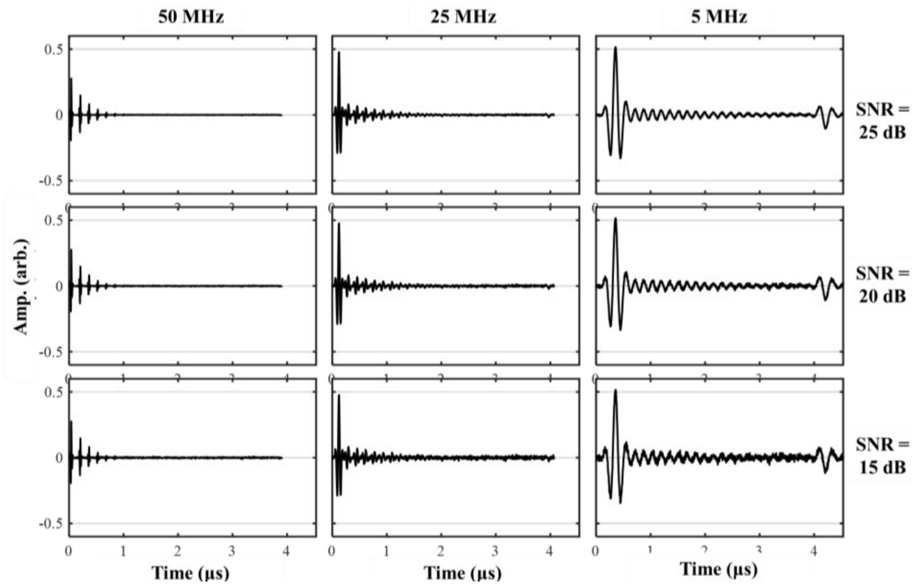

Figure 7-10 Response signals with frequencies of 50 MHz (first column), 15 MHz (second column), and 5 MHz (third column). Results are obtained for different SNRs: 25 dB (first row), 20 dB (second row), and 15 dB (third row).

From Figure 7-11, it is clear that the 50 MHz ultrasound coupled to the LP filtering is not a good approach for extracting deep interply locations. For the SNR of 15 dB, this method already yields unexpected results from the 7th interply on. On the other hand, it keeps a very high resolution and good stability for the near-surface plies under all the considered noise levels.

In a similar way, the 15 MHz ultrasound with Wiener deconvolution becomes more unstable for lower SNR. The $STDE^i$ increases with the decreasing SNR, and for the lowest SNR of 15 dB, the performance of this approach dropped significantly.

In contrast, the 5 MHz ultrasound coupled with analytic-signal analysis with log-Gabor filter performs well for all considered noise levels. However, it can be noted that the ME^i of Interply 1 and Interply 23 is high, while their $STDE^i$ is very small. This indicates a systematic error in the extraction of the location of these two interplies through the instantaneous phase. For the lowest SNR, the ME^i remains relatively stable over all interplies, although the $STDE^i$ increases to some extent. The excellent performance for all considered SNR levels can be attributed to the use of a log-Gabor filter. Indeed, apart from providing an appropriate scale selection, it also suppresses noise features in an efficient manner.

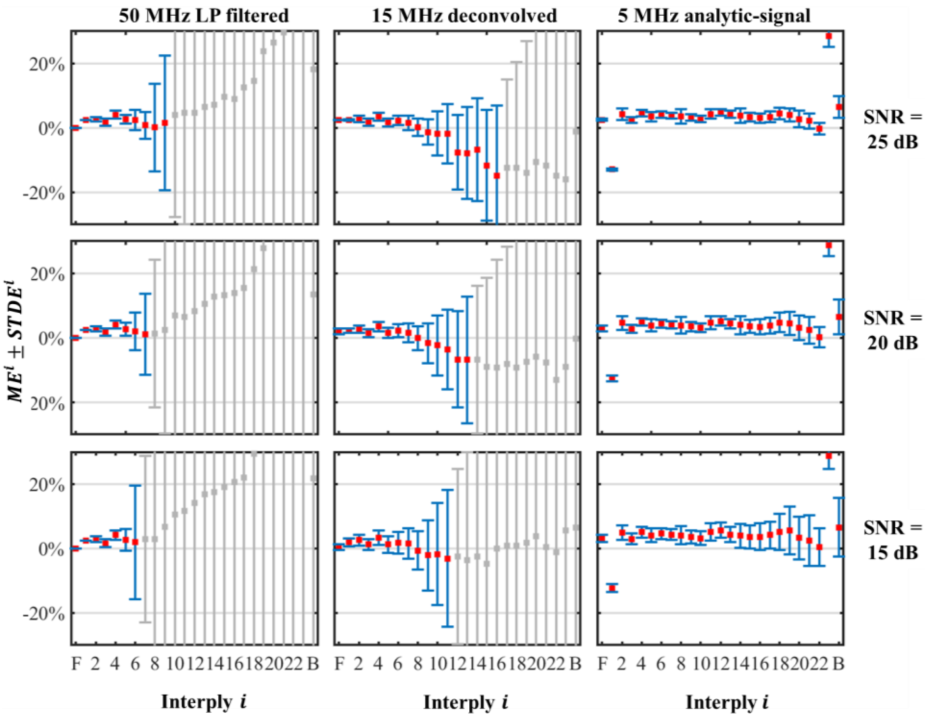

Figure 7-11 Error bars representing the ME^i and the $STDE^i$ of the estimated interplies from: the instantaneous amplitude of the 50 MHz LP filtered signal (first column), the instantaneous amplitude of the 15 MHz signal with Wiener deconvolution (second column), and the instantaneous phase of the 5 MHz analytic-signal with log-Gabor filter (third column). Results are obtained for different SNRs: 25 dB (first row), 20 dB (second row), and 15 dB (third row). The data is represented as $ME^i \pm STDE^i$.

7.4 Experimental Results

7.4.1 Materials and methods

A CFRP laminate (autoclave manufactured) with dimensions 150 mm×100 mm and a thickness of 5.52 mm is studied. It consists of 24 unidirectional plies and has a stacking sequence $[45/0/-45/90]_{3S}$. Each ply is assumed to have a constant and uniform thickness.

Three different spherically focused immersion transducers (center frequency of 5 MHz, 15 MHz, and 50 MHz) are employed. Table 7-4 presents the properties of the transducers applied in this experimental study. Reference signals reflected from a thick steel plate are acquired to calculate the SNR and the bandwidth (at −6 dB) of different transducers. The reference signal of the 15 MHz transducer is used as the deconvolution kernel for the Wiener deconvolution. The transducers are excited by an ultrasonic pulser (Tecscan UTPR-CC-50). The exciting pulse is a negative square wave with a pulse width of 30–500 ns (according to the setting), a rise time below 5 ns, and a fall time below 20 ns. The employed settings for the pulser, including the voltage, capacity, and damping, are also presented in Table 7-4. A 3-axis Cartesian scanner is used to achieve the raster scanning, which is controlled using a motion controller card (NI PXI-7350). The scanning steps in both x and y directions are 0.5 mm, and the scanning area is X×Y=50 mm×50 mm (100×100 data points). The scanning procedure and excitation/acquisition sequence have been programmed in a custom-made LabVIEW® program. The reflected signals from the CFRP laminate for the different employed transducers are displayed in A-scan mode in Figure 7-12.

Table 7-4 The properties of the employed transducers and the corresponding settings for the pulser

Properties of transducers							Settings for pulser		
Man.	Cod.	Freq. (MHz)	−6 dB band. (MHz)	Ele. d. (mm)	Foc. d. (mm)	SNR (dB)	Vol. (V)	Cap. (pF)	Dam. (Ohm)
GE	H5M	5	2.43–6.61	6.35	25.4	39.42	120	1070	45
Olym.	V313	15	10.84–23.08	6.35	25.4	28.20	120	920	78
Olym.	V390	50	26.31–61.85	6.35	12.7	26.84	120	450	500

After collecting the data by the raster scanning, the 3D data matrix is sent to Matlab® in order to reconstruct the positions of the interplies using the flow chart presented in Section 7.3.2. According to the instantaneous amplitude of the 5 MHz LP filtered signals, the TOF between the FWE and BWE is approximately 3.67 µs, which indicates an approximate ply-resonance frequency of 6.5 MHz. Thus, the center frequency and σ_0 of the log-Gabor filter applied on the 5 MHz signals are chosen as 6.5 MHz and 0.7, respectively.

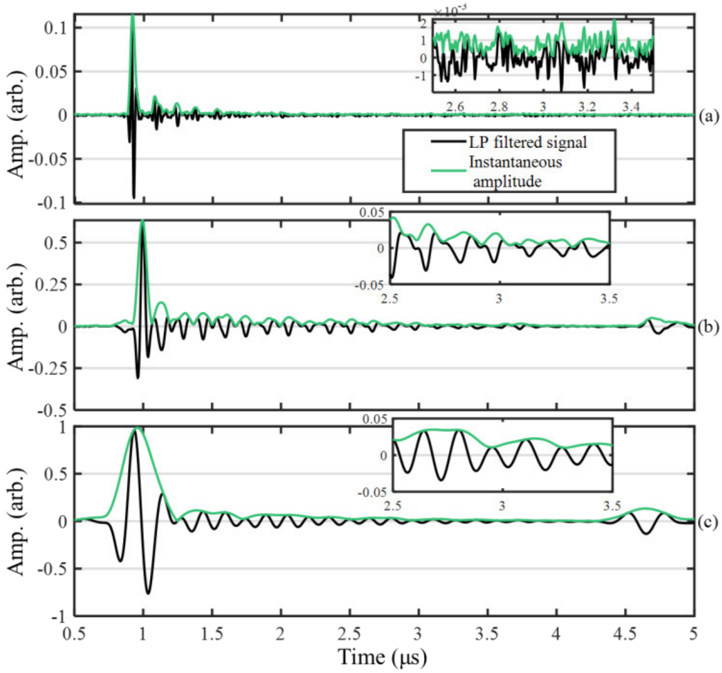

Figure 7-12 LP filtered signal, including the instantaneous amplitude (green trace), from the CFRP laminate for different employed transducers with center frequency (a) 50 MHz, (b) 15 MHz, and (c) 5 MHz.

7.4.2 Comparison and discussion

Figure 7-13 displays the B-scan representation at $y = 25$ mm of the instantaneous amplitude from the 50 MHz LP filtered signals, the 15 MHz Wiener deconvolved signals, and the 5 MHz log-Gabor filtered signals. Three optimal techniques are here applied to estimate positions of the interplies as follows:

- Method 1: The 50 MHz LP filtered signal using analysis of the instantaneous amplitude,
- Method 2: the 15 MHz Wiener deconvolved signal using analysis of the instantaneous amplitude, and
- Method 3: the 5 MHz log-Gabor filtered analytic-signal using analysis of the instantaneous phase.

The estimated positions of the interplies (cyan-colored dots) and uniformly-spaced positions of the interplies (gray-colored dots) are superimposed on these B-scan images. The difference in the quality to extract the interply locations can be readily seen in Figure 7-13. In order to quantify this, the thicknesses of the plies are estimated from the estimated positions of the interplies in each data point. The mean estimated thickness MT^p and the standard deviations of the estimated thickness $STDT^p$ of the pth ply are calculated as:

$$MT^p = \frac{\sum_{j=1}^{m_d} T_j^p}{m}, \tag{7.13}$$

$$STDT^p = \sqrt{\frac{\sum_{j=1}^{m_d}\left(T_j^p - \overline{T_j^p}\right)^2}{m_d}}. \tag{7.14}$$

where T_j^p is the estimated thickness of the pth ply from the A-scan in the jth data point, and m_d is the number of the data points in the scanning area (100×100=10000).

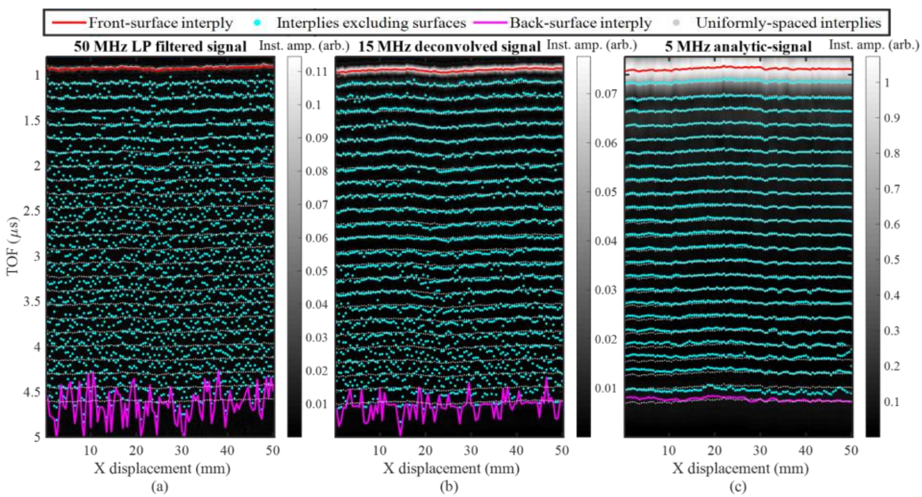

Figure 7-13 B-scan ultrasound images (at y = 25 mm) of the instantaneous amplitude from (a) 50 MHz LP filtered signals, (b) 15 MHz signals with Wiener deconvolution, and (c) 5 MHz analytic-signals with log-Gabor filter. Superimposed are the estimated positions of the interplies (cyan dots) and the uniformly-spaced positions of the interplies (gray dots).

Note that care has to be taken when interpreting these metrics because they include the variation of the actual thickness in each single ply. Figure 7-14 displays the obtained MT^p and $STDT^p$ for the three considered cases. From the total thickness of the sample (5.52 mm) and the number of plies (24 plies), the nominal thickness of a single ply is calculated as $5.52/24 = 0.23$ mm (see the dashed line in Figure 7-14). The calculation is, of course, under the assumption that the autoclave manufacturing process yields a uniformly-spaced ply thickness (T^{us}) over depth and over the CFRP sample. Similarly as for the numerical case, if the $STDT^p$ becomes higher than 22% of the T^{us}, the extracted results are assumed to be random and are therefore greyed out in the graph.

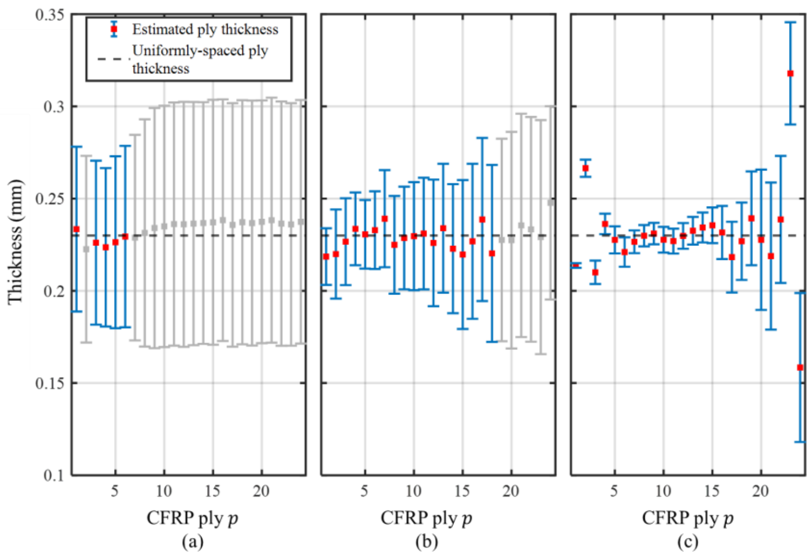

Figure 7-14 Error bars representing the MT^p and the $STDT^p$ of the plies from (a) 50 MHz LP filtered signals, (b) 15 MHz signals with Wiener deconvolution, and (c) 5 MHz analytic-signals with log-Gabor filter. The data is represented as $MT^p \pm STDT^p$.

The 50 MHz signals show a very uniform MT^p over the entire depth (see Figure 7-14a). However, the evaluation of $STDT^p$ tells a different story and indicates the randomness of the estimated ply thickness for deeper plies. The result can also be verified in Figure 7-13a. Hence, this clearly indicates the poor performance and robustness of this method to resolve the ply structure of the CFRP. The 15 MHz signals with Wiener deconvolution provide better probing depth and robustness (see Figure 7-14b). Nearly 18 plies can be distinguished, but the $STDT^{p}$ increases significantly with depth. This can also be verified in Figure 7-13b.

The 5 MHz analytic-signal with log-Gabor filter provides the best results and is able to extract all 24 plies in a stable and robust way (see Figure 7-14c). The result can also be verified in Figure 7-13c. However, one of the issues that emerge from these results is significant systematic errors in the most shallow and deepest plies. The estimated thicknesses of those plies show significant deviations from the T^{us} (see Figure 7-14c). A similar observation has been made in the simulation study (see Figure 7-9c), and this systematic deviation has been attributed to the dominating effect of the FWE and BWE (see the analysis in 0).

Figure 7-15 provides a C-scan representation of the estimated depth of several interplies by considering the three techniques mentioned above. The images of the depth profiles reconstructed by the 50 MHz LP filtered signals are evidently very noisy. One could say that the profile of the 5th interply can be extracted, though with low quality. The 15 MHz signals with Wiener deconvolution can reconstruct the profiles of the 5th and 15th interplies with higher quality but yield fully unstable results for the 22nd ply. The 5 MHz analytic-signals with log-Gabor filter successfully reconstruct the depth profile of all the interplies with high quality. Although, it is clear that the depth profile of the 22nd interply becomes more unsteady and less accurate.

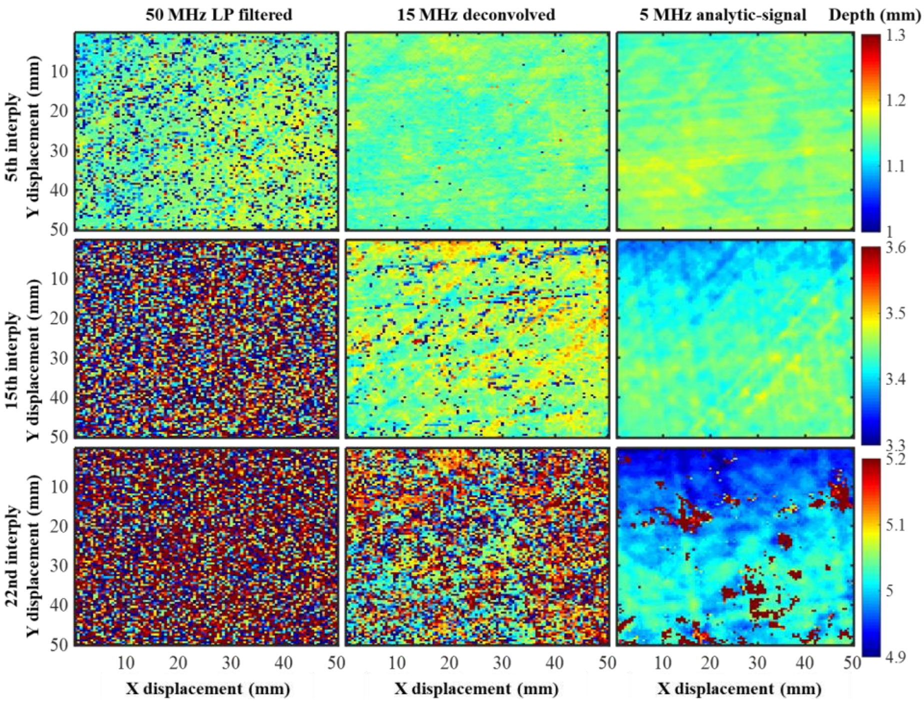

Figure 7-15 C-scan profiles estimated for the 5th (first row), the 15th (second row), and the 22nd (third row) interply. The interplies are estimated from the 50 MHz LP filtered signal (first column), the 15 MHz LP filtered and Wiener deconvolved signal (second column), and the 5 MHz analytic-signal coupled to log-Gabor filtering (third column).

It is essential to note an intrinsic difference in the noise level between the different transducers (see Table 7-4). The higher frequency transducer intrinsically produces more noise due to the electrical power loss and mechanical power loss [29]. Therefore, low-frequency signals tend to be naturally more stable than high-frequency signals. The fact also contributes to the worse performance of the 50 MHz and the 15 MHz signals in the experiments. Another potential problem of high-frequency ultrasound is that it could be sensitive to fiber tows inside the plies [30]. There is an apparent difficulty in reconstructing the positions of the interplies because the echoes from the fiber tows could be mistaken for echoes from the interplies.

7.5 Conclusion

A comparative study is performed between several ultrasonic techniques, operating in different frequency ranges, for reconstructing the multi-layer structure of CFRP laminates. The performance of the different ultrasonic techniques is investigated on synthetic ultrasonic data, with various noise levels, the representative for a 24 layer CFRP laminate immersed in water. It is revealed that the 50 MHz ultrasound with LP filtering, coupled to the analysis of the instantaneous amplitude, can only effectively distinguish the near-surface interplies with good robustness. The 15 MHz ultrasound has better probing depth and yields reasonably stable estimation, especially when coupled to Wiener deconvolution. Though, for the deeper interplies the results become unstable, and their locations could not be extracted in a robust manner. Finally, the 5 MHz ultrasound coupled to analytic-signal analysis provides the best robustness and probing depth under all noise levels. This approach uses the ply-resonance (around 6.5 MHz for the here considered multi-layer structures) and evaluates the instantaneous phase to estimate the depth of the interplies. This approach yields promising results over the full depth of the considered multi-layer structure, especially when coupled to a log-Gabor filter for optimal scaling of the signals. However, the analytic-signal results also indicate a systematic deviation in the depth estimation of the two interplies closest to the front- and back surfaces. This is attributed to the dominating effect of the FWE and BWE, which locally distorts the instantaneous phase profile.

Also, an experimental study on a $[45/0/-45/90]_{3S}$ CFRP sample with 24 plies is reported. The CFRP sample has been raster-scanned in pulse-echo (PE) mode with several transducers operating in different frequency ranges. The estimated positions of the interplies are displayed in B-scan mode, and the extracted ply thicknesses are compared with the nominal ply thickness. The profiles of the estimated interplies at several depths are displayed in C-scan mode. The obtained experimental results demonstrate the high performance of the 5MHz analytic-signal coupled to log-Gabor filter for reconstructing the ply thicknesses by analyzing the instantaneous phase. This is in line with the observations and results obtained from the simulation study.

The comparative analysis of this research provides deeper insights into the performance of the ultrasonic techniques operating in different frequency ranges. It could serve as a base for selecting the appropriate ultrasonic techniques for reconstructing the multi-layer structure of CFRP.

References

[1] Bai, X., Sun, Z., Sun, A., Chen, J., and Ju, B.-F., 2014, "Determination of the multiple local properties of thin layer with high lateral resolution by scanning acoustic microscopy," Review of Scientific Instruments, 85(9), p. 094901.

[2] Morokov, E., Levin, V., Chernov, A., and Shanygin, A., 2021, "High resolution ply-by-ply ultrasound imaging of impact damage in thick CFRP laminates by high-frequency acoustic microscopy," Compos Struct, 256, p. 113102.

[3] Wang, D., He, X., Xu, Z., Jiao, W., Yang, F., Jiang, L., Li, L., Liu, W., and Wang, R., 2017, "Study on damage evaluation and machinability of UD-CFRP for the orthogonal cutting operation using scanning acoustic microscopy and the finite element method," Materials, 10(2), p. 204.

[4] Ono, K., 2020, "A comprehensive report on ultrasonic attenuation of engineering materials, including metals, ceramics, polymers, fiber-reinforced composites, wood, and rocks," Applied Sciences, 10(7), p. 2230.

[5] Burrows, S. E., Fan, Y., and Dixon, S., 2014, "High temperature thickness measurements of stainless steel and low carbon steel using electromagnetic acoustic transducers," Ndt&E Int, 68, pp. 73-77.

[6] Losada, R. A., 2004, "Practical FIR filter design in MATLAB," The Math Works inc. Revision, 1, pp. 5-26.

[7] Sin, S.-K., and Chen, C.-H., 1992, "A comparison of deconvolution techniques for the ultrasonic nondestructive evaluation of materials," IEEE Transactions on Image processing, 1(1), pp. 3-10.

[8] Neal, S. P., Speckman, P. L., and Enright, M., 1993, "Flaw signature estimation in ultrasonic nondestructive evaluation using the Wiener filter with limited prior information," IEEE transactions on ultrasonics, ferroelectrics, and frequency control, 40(4), pp. 347-353.

[9] Zala, C., Barrodale, I., and McRae, K., 1988, "High resolution deconvolution of ultrasonic traces," Signal Processing and Pattern Recognition in Nondestructive Evaluation of Materials, Springer, pp. 101-108.

[10] Honarvar, F., Sheikhzadeh, H., Moles, M., and Sinclair, A. N., 2004, "Improving the time-resolution and signal-to-noise ratio of ultrasonic NDE signals," Ultrasonics, 41(9), pp. 755-763.

[11] Miyashita, T., Schwetlick, H., and Kessel, W., 1985, "Recovery of ultrasonic impulse response by spectral extrapolation," Acoustical Imaging, Springer, pp. 247-257.

[12] Karslı, H., 2006, "Further improvement of temporal resolution of seismic data by autoregressive (AR) spectral extrapolation," Journal of Applied Geophysics, 59(4), pp. 324-336.
[13] Wei, L., Huang, Z.-y., and Que, P.-w., 2009, "Sparse deconvolution method for improving the time-resolution of ultrasonic NDE signals," Ndt&E Int, 42(5), pp. 430-434.
[14] Lee, J.-Y., and Nandi, A., 2000, "Extraction of impacting signals using blind deconvolution," J Sound Vib, 232(5), pp. 945-962.
[15] Wiggins, R. A., 1978, "Minimum entropy deconvolution," Geoexploration, 16(1-2), pp. 21-35.
[16] Chang, Y., Zi, Y., Zhao, J., Yang, Z., He, W., and Sun, H., 2017, "An adaptive sparse deconvolution method for distinguishing the overlapping echoes of ultrasonic guided waves for pipeline crack inspection," Meas Sci Technol, 28(3), p. 035002.
[17] Nandi, A. K., Mampel, D., and Roscher, B., 1997, "Blind deconvolution of ultrasonic signals in nondestructive testing applications," IEEE transactions on signal processing, 45(5), pp. 1382-1390.
[18] Boßmann, F., Plonka, G., Peter, T., Nemitz, O., and Schmitte, T., 2012, "Sparse deconvolution methods for ultrasonic NDT," Journal of Nondestructive Evaluation, 31(3), pp. 225-244.
[19] Yang, X., Verboven, E., Ju, B.-f., and Kersemans, M., 2021, "Parametric study on interply tracking in multilayer composites by analytic-signal technology," Ultrasonics, 111, p. 106315.
[20] Neal, S. P., and Thompson, D. O., 1989, "A prior knowledge based optimal Wiener filtering approach to ultrasonic scattering amplitude estimation," The Journal of the Acoustical Society of America, 86(S1), pp. S94-S94.
[21] Ulrych, T. J., and Bishop, T. N., 1975, "Maximum Entropy Spectral Analysis and Autoregressive Decomposition," Reviews of Geophysics, 13(1), pp. 183-200.
[22] Shakibi, B., 2011, "Resolution Enhancement of Ultrasonic Signals Using Autoregressive Spectral Extrapolation," University of Toronto, Canada
[23] Collombet, F., Mulle, M., Grunevald, Y.-H., and Zitoune, R., 2006, "Contribution of embedded optical fiber with bragg grating in composite structures for tests-simulations dialogue," Mechanics of Advanced Materials and Structures, 13(5), pp. 429-439.
[24] Davila, Y., Crouzeix, L., Douchin, B., Collombet, F., and Grunevald, Y. H., 2017, "Spatial Evolution of the Thickness Variations over a CFRP Laminated Structure," Appl Compos Mater, 24(5), pp. 1201-1215.

[25] Smith, R. A., 2010, "Use of 3D ultrasound data sets to map the localised properties of fibre-reinforced composites," University of Nottingham Nottingham, UK.
[26] Sevenois, R. D. B., Garoz, D., Verboven, E., Spronk, S. W. F., Gilabert, F. A., Kersemans, M., Pyl, L., and Van Paepegem, W., 2018, "Multiscale approach for identification of transverse isotropic carbon fibre properties and prediction of woven elastic properties using ultrasonic identification," Compos Sci Technol, 168, pp. 160-169.
[27] Jeong, H., and Hsu, D. K., 1995, "Experimental-Analysis of Porosity-Induced Ultrasonic-Attenuation and Velocity Change in Carbon Composites," Ultrasonics, 33(3), pp. 195-203.
[28] Shakibi, B., Honarvar, F., Moles, M., Caldwell, J., and Sinclair, A. N., 2012, "Resolution enhancement of ultrasonic defect signals for crack sizing," Ndt&E Int, 52, pp. 37-50.
[29] Karafi, M. R., and Khorasani, F., 2019, "Evaluation of mechanical and electric power losses in a typical piezoelectric ultrasonic transducer," Sensors and Actuators A: Physical, 288, pp. 156-164.
[30] Moon, M., Yun, Y., Yoo, M., Song, J., and Oh, J., 2019, "Carbon fiber manufacturing and applications as a benchmark for nanotube superfiber development," Nanotube Superfiber Materials, Elsevier, pp. 879-896.

Chapter 8 Estimation of Out-of-plane Ply Orientation using Structure Tensor Method

8.1 Introduction

The manufacturing of carbon fiber reinforced polymer (CFRP) laminates often involves manual work, making it crucial to evaluate the final manufacturing quality in a proper way. For example, in compression moulding, there is a clear risk to induce out-of-plane ply wrinkles having a considerable impact on the structural performance of the final composite part [1]. Also, the varying quality in prepreg (uncured single ply) could lead, after curing in an autoclave, to local distortions of the intended ply structure [2]. Following the research [3, 4] for the non-destructive quantification of out-of-plane fiber wrinkling, this chapter couples the instantaneous phase analysis to a structure tensor process. The structure tensor process is introduced in Section 8.2. In Section 8.3, the results for the experimental ultrasonic datasets with different features are discussed and analyzed. The discussion is given in Section 8.4. Section 8.5 gathers the conclusion.

8.2 Structure Tensor Process

The structure tensor process is a flexible and robust method for determining structure orientations in a smoothly varying field [5]. In this study, the structure tensor process is applied to the instantaneous phase of the analytic signal. For the function $\phi_{inst}(\mathrm{x}, \mathrm{y}, t)$, the structure tensor is defined as [6]

$$S_G(p) = \int G_\tau(r) S_0(p-r)\mathrm{d}r, \tag{8.1}$$

with $p = (x, y, t)$ and $r \in R^3$. $G_\tau(r)$ is a 3D Gaussian smoothing kernel according to

$$G_\tau(r) = \frac{1}{(\sqrt{2\pi}\tau)^3}\exp(-\frac{|r|^2}{2\tau^2}), \tag{8.2}$$

with τ the standard deviation. $S_0(p)$ corresponds to

$$S_0(p) = \begin{bmatrix} (\phi_x(p))^2 & \phi_x(p)\phi_y(p) & \phi_x(p)\phi_t(p) \\ \phi_x(p)\phi_y(p) & (\phi_y(p))^2 & \phi_y(p)\phi_t(p) \\ \phi_x(p)\phi_t(p) & \phi_y(p)\phi_t(p) & (\phi_t(p))^2 \end{bmatrix}, \tag{8.3}$$

with $\phi_x(p)$, $\phi_y(p)$, $\phi_t(p)$ representing the three partial derivatives of $\phi_{inst}(\mathrm{x}, \mathrm{y}, t)$. The partial derivatives are obtained as follows [4]

$$\phi_x(p) = \cos\phi_{inst}(\mathrm{p})\frac{\partial \sin\phi_{inst}(\mathrm{p})}{\partial x} - \sin\phi_{inst}(\mathrm{p})\frac{\partial \cos\phi_{inst}(\mathrm{p})}{\partial x} \tag{8.4}$$

$$\phi_y(p) = \cos\phi_{inst}(\mathrm{p})\frac{\partial \sin\phi_{inst}(\mathrm{p})}{\partial \mathrm{y}} - \sin\phi_{inst}(\mathrm{p})\frac{\partial \cos\phi_{inst}(\mathrm{p})}{\partial \mathrm{y}} \tag{8.5}$$

$$\phi_t(p) = \cos\phi_{inst}(\mathrm{p})\frac{\partial \sin\phi_{inst}(\mathrm{p})}{\partial \mathrm{t}} - \sin\phi_{inst}(\mathrm{p})\frac{\partial \cos\phi_{inst}(\mathrm{p})}{\partial \mathrm{t}} \tag{8.6}$$

where the central-difference kernels are applied to the trigonometric function values of the instantaneous phase. The gradients of the unwrapped instantaneous phase are obtained according to Eqs (8.4), (8.5), and (8.6).

An additional 3D Gaussian kernel smoothes the trigonometric function values of the instantaneous phase G_σ before the derivation of the phase gradients. The kernels G_τ and G_σ have standard deviations of τ, and σ respectively. Finally, the eigenvectors $\boldsymbol{v}$ and eigenvalues λ_v of the tensor $S_G(p)$ are obtained which hold information about the structure's orientation at point p:

$$S_G(p)\boldsymbol{v} = \lambda_v \boldsymbol{v}, \tag{8.7}$$

From this, the local out-of-plane ply angle can be extracted by evaluating the principal eigenvector, as shown in Figure 8-1.

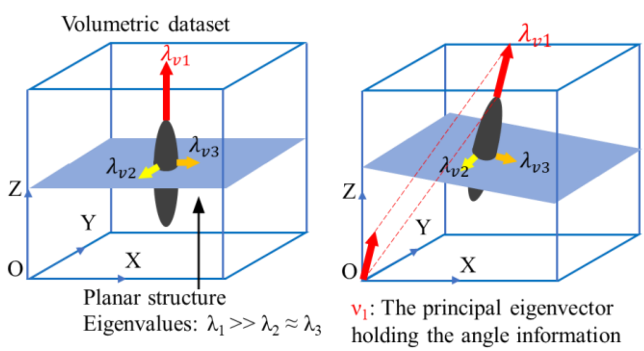

Figure 8-1 Illustration of extracting the principal direction of planar structures in volumetric dataset using structure tensor process.

8.3 Experimental Study

In this section, the structure tensor process introduced in Section 8.2 is applied to different ultrasonic datasets to extract the out-of-plane ply orientation. The front and back surfaces are extracted by analyzing the instantaneous amplitude introduced in Section 7.3.2 before applying the structure tensor process. The methods have been implemented in Matlab® R2019a in a 64-bit operating system. The procedures of the ultrasonic testing (UT) are the same as those in Section 7.4. Table 8-1 presents the parameters of the employed transducer, the settings of the scanner, and the samples used in these experiments.

Table 8-1 The parameters of the transducer, the scanner, and the samples

Features Type	Properties of transducers			Settings for scanner			Sample	
	Freq. (MHz)	Focal d. (mm)	Elem. d. (mm)	Area (mm×mm)	X step (mm)	Y step (mm)	Layer	Spacing (μm)
Ply Wrinkling	7.5 [4]	38 [4]	12.5 [4]	64×17 [7]	0.2 [7]	0.2 [7]	24 [4]	189 [4]
Manufact.distortions	5	12.7	6.35	150×40	0.2	0.2	24	183

8.3.1 Online dataset of CFRP laminate with Ply Wrinkling

The ultrasonic dataset with ply wrinkling features is obtained from an online database [7]. The experimental parameters were found online [4, 7] and are shown in the 1st row in Table 8-1. The sampling rate is 125 MS/s. An X-CT cross-section of the CFRP sample is shown in Figure 8-2a, a B-scan presentation of the instantaneous amplitude and instantaneous phase is displayed in Figure 8-2b and c.

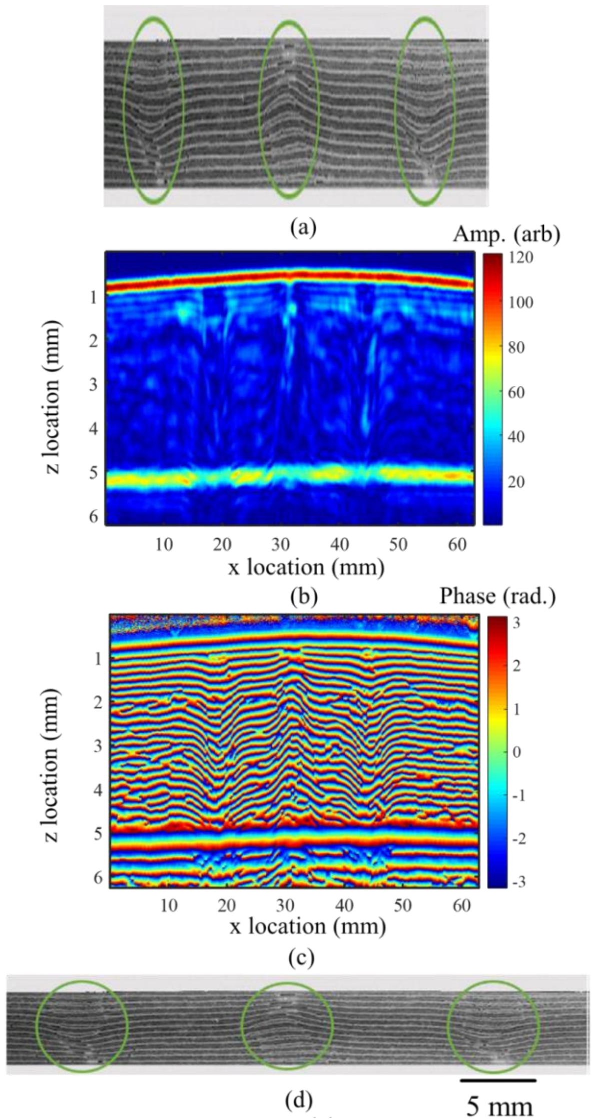

Figure 8-2 Cross-section of the studied CFRP laminate: (a) rescaled X-CT image (Picture adapted from Reference [4]) and B-scan images of (b) instantaneous amplitude and (c) instantaneous phase. Note that the X-CT image in the original scale is shown in (d).

The out-of-plane ply angle map is obtained by applying the structure tensor method on the instantaneous phase (see Figure 8-3a). The standard deviations of G_τ and G_σ are chosen as 3 and 1.5 respectively. Considering the fundamental ply-resonance frequency of 7.9 MHz for the 189 μm thick plies, a log-Gabor filter with a center frequency of 7.9 MHz and a bandwidth of 0.86 ($\sigma_0 = 0.7$) is additionally applied on the ultrasonic dataset. The out-of-plane ply angle map obtained from the log-Gabor filtered dataset is displayed in Figure 8-3b. The result in Figure 8-3b shows the added value of the log-Gabor filter for noise filtering. In accordance with the earlier study in [4], the ply wrinkling has been completely resolved from the ultrasonic dataset.

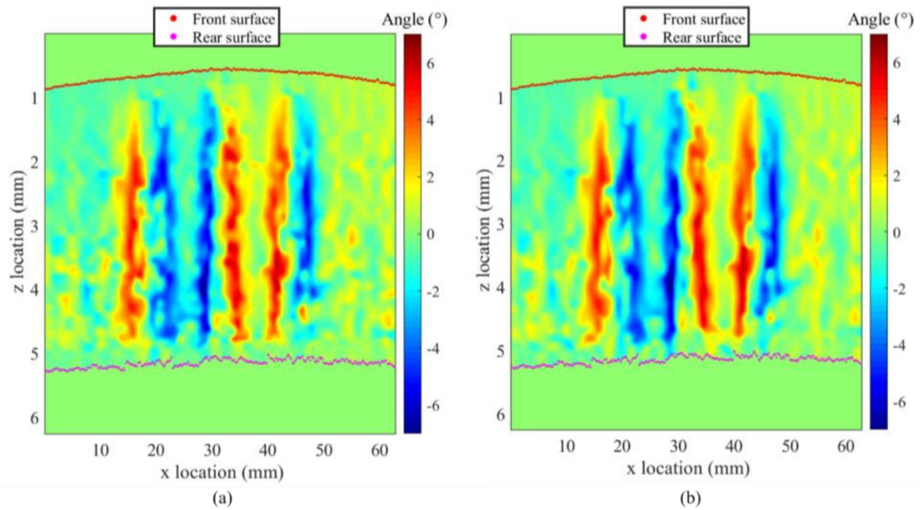

Figure 8-3 Out-of-plane ply angle map in the xz plane measured from the ultrasonic dataset [7] with ply wrinkling features: (a) without and (b) with the application of the log-Gabor filter.

8.3.2 CFRP laminate with Manufacturing Distortions

The studied 24-layer $[0/90]_{3S}$ CFRP laminates have been manufactured by compression moulding. There are 2 samples manufactured: one with optimal processing conditions and another with non-optimal processing conditions. For the latter case, the CFRP laminate shows evident ply distortions that could be seen visually on the surface. Figure 8-2a shows a photograph of the surface of the CFRP laminate, on which vertical line patterns can be observed, which suggest the presence of deviations in the layer structure. Figure 8-2b displays a cross-section of this poorly manufactured CFRP laminate, in which the solid and chaotic out-of-plane ply wrinkling can be readily observed.

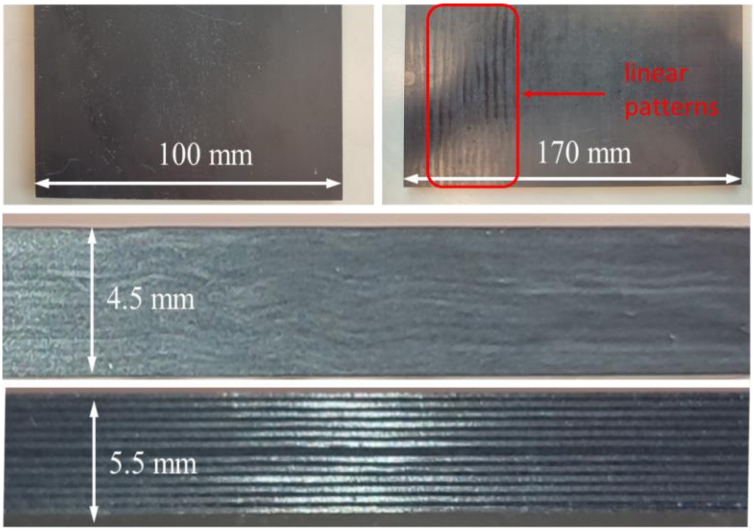

Figure 8-4 Compression moulded CFRP laminates with (a-b) non-optimal manufacturing conditions, and (c-d) optimal manufacturing conditions. Photograph of (left) top surface, and (right) cross-section along xz-plane.

The parameters of the transducer, the scanner, and the sample are shown in the 2nd row in Table 8-1. The transducer is excited by an ultrasonic pulser (Tecscan UTPR-CC-50) with a negative square wave. The voltage, capacity, and damping for the pulser are set at 120 V, 1070 pF, and 45 Ohm, respectively. The signal is pre-amplified with a gain of 11 dB. The signal is then sampled by a 14-bit digitizer card (NI PXIe-5172) at a sampling rate of 250 MS/s. In total, 1300 time samples are stored for each A-scan signal. In order to increase the signal-to-noise ratio (SNR), averaging has been applied (4 averages per scan point). In order to make optimal use of the fundamental ply-resonance frequency of this sample, a log-Gabor filter with a center frequency of 7.7 MHz and a bandwidth of 0.86 ($\sigma_0 = 0.7$) has additionally applied.

The out-of-plane ply angle maps at a slice in the xz plane and in the yz-plane are displayed in Figure 8-6 for the manufactured CFRP laminates with optimal processing conditions. For the CFRP laminate manufactured with optimal parameters, the results in Figure 8-5 indicate some minor deviations in the out-of-plane ply orientation (< 2 degrees), corresponding to natural variability in compression moulding. For the sample with non-optimal manufacturing condition, a very chaotic distortion of the out-of-plane ply orientation is obtained (see Figure 8-6). The internal distortions close to the surface are consistent with the observed vertical lines observed at the surface of the CFRP laminate (see Figure 8-4a). The obtained out-of-plane ply orientation results in this poorly manufactured CFRP laminate clearly confirm the chaotic cross-sectional photograph presented in Figure 8-4b.

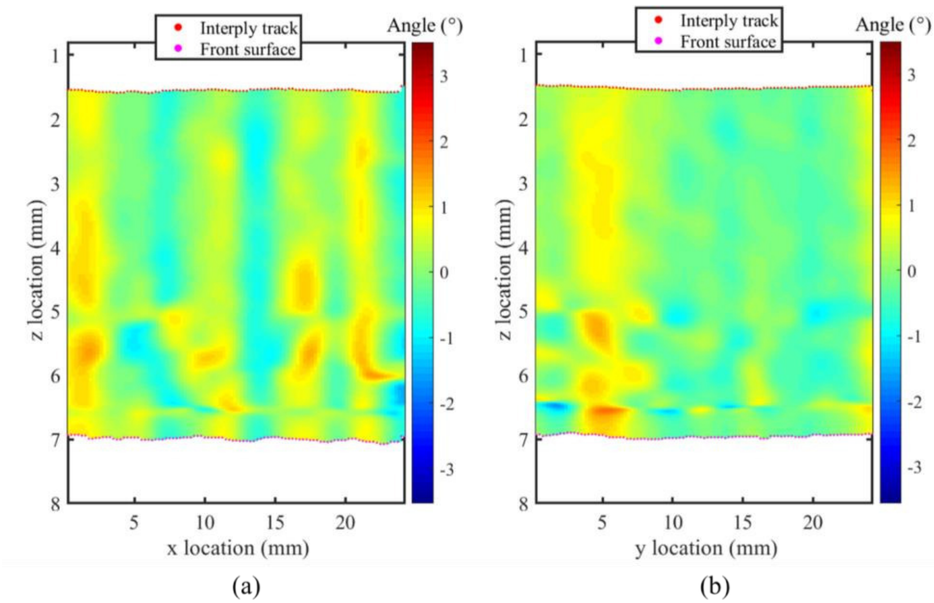

Figure 8-5 Out-of-plane ply angle maps in (a) the xz plane and (b) the yz plane for compression moulded CFRP laminate with optimal manufacturing conditions.

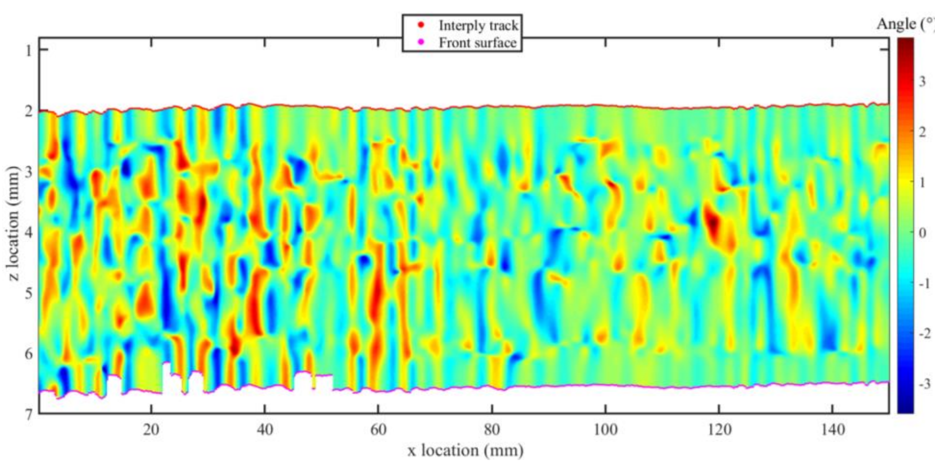

Figure 8-6 Out-of-plane ply angle maps in the xz plane or compression moulded CFRP laminate with non-optimal manufacturing conditions.

8.4 Discussion

It is worth pointing out that the standard deviations of the Gaussian kernels G_τ and G_σ are could be tuned. Interestingly, it has been reported in the literature that by changing the standard deviations of the kernels, one could improve the spatial fidelity of the orientation measurement [4]. As the ply orientation changes within the smoothing kernel G_σ , the ply-angle deviation from horizontal would be underestimated. And the amount of the underestimation is affected by the value of the standard deviation for G_σ. On the other hand, the standard deviation of the kernel G_τ determines the size of the region over which local gradient products are assessed, and as such, affects the sensitivity of the angular measurements to local noise. A G_τ with a small standard deviation can resolve small local features in the data but lead to larger errors induced by noise. Increasing the standard deviation of G_τ increases bias and systematic errors, resulting in a larger amount of underestimation of the ply-angle deviation. Hence, it is crucial to optimize the Gaussian kernels' standard deviations to balance the noise resistance and the underestimation of the ply-angle deviation.

To illustrate this, a range of standard deviations have been considered and applied on the online dataset [7] of the CFRP laminate with wrinkling. Figure 8-7 shows the results for a G_σ standard deviation of 2, 3, and 4 respectively, with a fixed G_τ standard deviation of 3. It can be readily seen that the amount of the underestimation of ply-angle deviations increase significantly with the G_σ standard deviation.

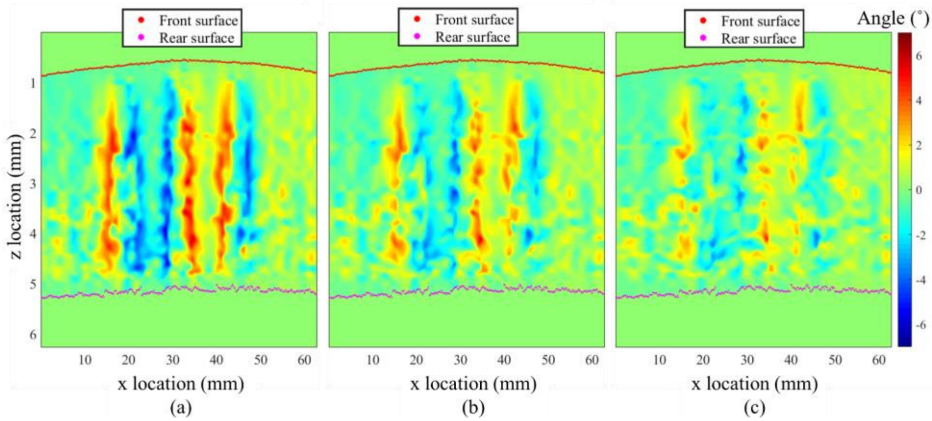

Figure 8-7 Out-of-plane ply angle map in the xz plane measured from the ultrasonic dataset [7] with ply wrinkling features for a G_{σ} standard deviation of (a) 2, (b) 3, and (c) 4 respectively, with a fixed G_{τ} standard deviation of 3.

Figure 8-8 shows the results for a G_{τ} standard deviation of 2, 3, and 4 respectively with a fixed G_{σ} standard deviation of 3. It can be seen from Figure 8-8 that the amount of the underestimation of ply-angle deviations also increase with the G_{τ} standard deviation slightly. Compared to the influence of G_{σ}, an increased G_{τ} standard deviation provides an obvious smoothing effect (see Figure 8-8c and Figure 8-7c). Although a decreased G_{τ} standard deviation is capable of resolving small local ply-angle deviations, the results deteriorate due to the sensitivity to local noise.

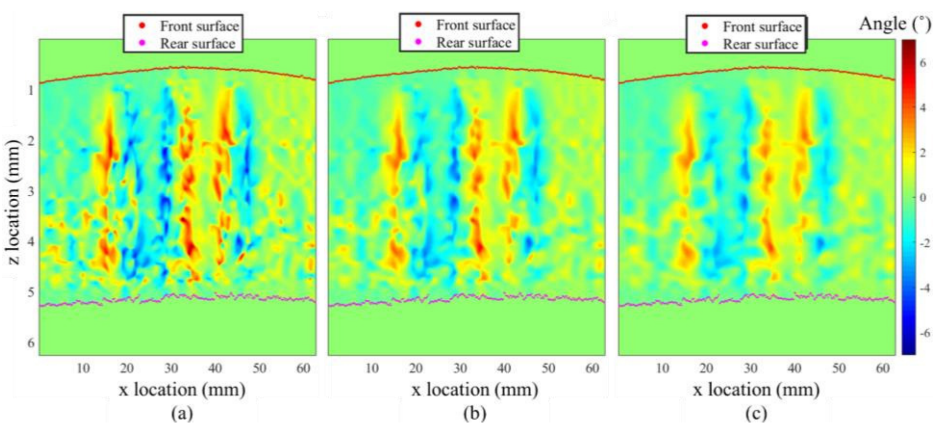

Figure 8-8 Out-of-plane ply angle map in the xz plane measured from the ultrasonic dataset [7] with ply wrinkling features for a G_{τ} standard deviation of (a) 2, (b) 3, and (c) 4 respectively, with a fixed G_{σ} standard deviation of 3.

Following the discussions, we would suggest that a small G_σ standard deviation and a relatively larger G_τ standard deviation in this case in order to balance the sensitivity to local ply-angle deviations and local noise. Without any prior knowledge of the dataset, more ideally, a procedure should be devised to obtain the optimal standard deviations.

8.5 Conclusion

A structure tensor process for the reconstruction of out-of-plane ply orientation of multi-layer CFRP laminates is introduced. The procedure is applied to the instantaneous phase of log-Gabor filtered ultrasound data. The method is experimentally demonstrated on a benchmark ultrasonic dataset from literature and an internally generated ultrasonic dataset. Both ultrasonic datasets were representative for CFRP laminates with various levels of out-of-plane fiber wrinkling. The experimental results indicate the excellent performance of the structure tensor process for reconstructing out-of-plane ply orientations. Further, it is shown that the value of the standard deviations of the Gaussian kernels G_τ and G_σ in the structure tensor method could be optimized in view of balancing the noise resistance with the bias in the out-of-plane ply-angle estimation.

References

[1] Thor, M., Sause, M. G., and Hinterhölzl, R. M., 2020, "Mechanisms of origin and classification of out-of-plane fiber waviness in composite materials—a review," Journal of Composites Science, 4(3), p. 130.

[2] Amann, C., Kreissl, S., Grass, H., and Meinhardt, J., 2017, "A review on process-induced distortions of carbon fiber reinforced thermosets for large-scale production," Prod Eng-Res Dev, 11(6), pp. 665-675.

[3] Larrañaga-Valsero, B., Smith, R. A., Tayong, R. B., Fernández-López, A., and Güemes, A., 2018, "Wrinkle measurement in glass-carbon hybrid laminates comparing ultrasonic techniques: A case study," Composites Part A: Applied Science and Manufacturing, 114, pp. 225-240.

[4] Nelson, L., Smith, R., and Mienczakowski, M., 2018, "Ply-orientation measurements in composites using structure-tensor analysis of volumetric ultrasonic data," Composites Part A: Applied Science and Manufacturing, 104, pp. 108-119.

[5] Pinter, P., Dietrich, S., Bertram, B., Kehrer, L., Elsner, P., and Weidenmann, K. A., 2018, "Comparison and error estimation of 3D fibre orientation analysis of computed tomography image data for fibre reinforced composites," Ndt&E Int, 95, pp. 26-35.

[6] Khan, A. R., Cornea, A., Leigland, L. A., Kohama, S. G., Jespersen, S. N., and Kroenke, C. D., 2015, "3D structure tensor analysis of light microscopy data for validating diffusion MRI," Neuroimage, 111, pp. 192-203.
[7] Fraij, C., Hughes, R., Mienczakowski, M., Boumda, R., Xie, N., Nelson, L., Smith, R., Mhlanga, S., 2017, "Data for Ply-orientation measurements in composites using structure-tensor analysis."

Chapter 9 Estimation of In-plane fiber Orientation using Gabor-filter based Information Diagram

9.1 Introduction

Apart from out-of-plane ply deviations, as discussed in the previous chapter, carbon fiber reinforced polymer (CFRP) laminates could also experience in-plane fiber deviations, e.g., in-plane fiber waviness or stacking errors [1]. Even a minor deviation from the desired orientation can seriously reduce the structural stiffness/strength in specific directions [2]. Thus, there is an increasing interest in measuring the in-plane fiber orientation of multi-layer CFRP in a non-destructive manner [3-5].

Recent studies demonstrated the in-plane fiber measurement of a unidirectional CFRP by means of eddy current testing (ECT) [6-10]. These studies showed promising results, but the eddy current method is only applicable to electrically conductive materials [11]. Further, all layers under the probe contribute to the response signal, but their contribution strongly decays with their depth. Although some attempts have been made to distinguish between depths [10], it remains a challenging problem. Thus, the technique is mainly limited to estimating near-surface orientation, and is less suited for extracting the fiber orientation through depth in multi-layer CFRP.

The use of X-CT for reconstructing the local fiber architecture has already been demonstrated in a multitude of studies [3, 12-16]. Under specific conditions, X-CT can provide detailed imaging results and even track single fibers in fiber reinforced polymer (FRP) [17]. However, the imaging contrast is quite limited for CFRP because of the similar X-ray attenuation characteristic of polymer and carbon fibers. Further, the resolution of X-CT is limited by the physical size of the investigated composite part [18]. Hence, reconstruction of local fiber orientation is typically done on tiny parts (order of mm) [19]. Determining the local fiber orientation for CFRP with significant dimensions (e. g. dimensions 75 mm×75 mm×5 mm) is not possible with current X-CT technology.

UT has also been proposed to extract local fiber orientations in multi-layer CFRP [20-22]. The lateral resolution is directly related to the employed ultrasound wavelength. At 50–200 MHz operation frequencies, the resolution is in the range of a few tens of microns: 10–50 μm. In that regard, high-frequency ultrasound has been used to extract fiber orientations by visualizing individual fiber tows [23]. The downside of such high-frequency ultrasound is its excessive attenuation due to acoustic absorption and scattering processes, which strongly limits its probing depth range [24]. Lowering the ultrasonic frequency allows to inspect materials deeper, but the wavelength becomes too large for visualizing individual fiber tows. As a result, there is a trade-off between signal-to-noise ratio (SNR) and lateral resolution with the choice of frequency. At shallow depths, it is possible to reach a satisfactory resolution to image fiber tows and adequate SNR. However, it is harder to reach an acceptable resolution together with adequate SNR in deep structures.

In the case that individual fiber tows cannot be imaged, the fiber orientation should instead be computed based on features [14]. For this purpose, many texture analysis and pattern recognition methods have been proposed and implemented, such as 2D fast Fourier transform [8, 20, 25-27], image gradient (structure tensor) methods [28-30], rotated periodic filters [31-33], and Radon transform (RT) [34, 35].

Some studies have thoroughly compared various reconstruction methods for determining the fiber orientation of multi-layer CFRP using 3D ultrasonic data [22, 35]. It has been reported that the RT and the Gabor filter methods are appropriate for extracting the fiber orientation and that the RT method produces more consistent and stable results [34]. However, those studies mainly focused on the extraction of the global stacking sequence of the CFRP by using fixed kernel sizes rather than the local fiber orientation. While a large kernel size is a powerful tool to determine the dominant orientation in noisy images, it underestimates the maximum deviation in a small-scale region. Recently, rectangular kernels with changeable size have been employed in the RT method, showing improved performance for woven samples [36]. The Gabor filter method is based on filters with a certain wavelength and therefore has difficulty dealing with multi-scale local variations.

To tackle the abovementioned challenge in reconstructing multi-scale features, this chapter proposes using a Gabor filter-based method coupled to an Information Diagram to reconstruct the local fiber orientation of a multi-layer CFRP from a 3D ultrasonic pulse-echo (PE) dataset. Instead of implementing a rotated filter in which a fixed wavelength for the Gabor kernel is chosen, the concept of Information Diagram brings the analysis to a multi-scale level [37-39]. The GF-ID method automatically yields optimal local Gabor filter parameters, i.e., wavelength and rotation, allowing better reconstructing local variations in features and orientations.

The structure of the paper is as follows. The concepts of RT and GF-ID methods are introduced in Section 9.2. Sections 10.3, 10.4, 0, and 10.6 discuss and analyze the results for synthetic texture images and experimental ultrasonic datasets. Section 9.7 gathers the conclusion.

9.2 Feature Orientation Extraction Methods

9.2.1 Radon transform RT

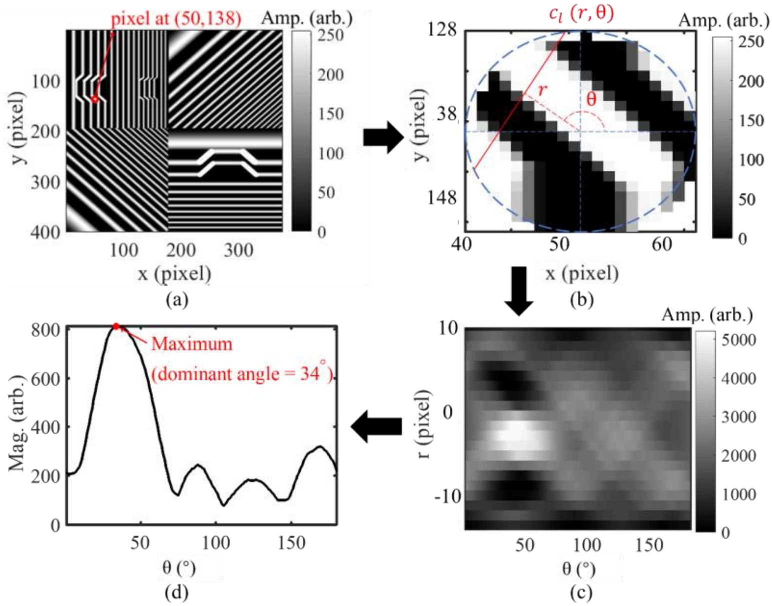

Figure 9-1 Schematic of the procedure of the RT method: (a) the original image $I(x, y)$, (b) the circular kernel around the pixel at (50, 138), (c) the sinogram image formed from the projections, and (d) the 1D angular distribution calculated from the sinogram.

To determine the local orientation at one pixel in the original image $I(x, y)$ in Figure 9-1a, a circular kernel with a specific radius (10 pixels in this case) is first extracted, shown in Figure 9-1b. The RT is the projection of $I(x, y)$ along the straight lines $c_l(r, \theta)$ according to:

$$R\{I\}(r, \theta) = \int_{(x,y) \text{ on } c_l(r,\theta)} I(x, y)\ \mathrm{d}x\, \mathrm{d}y, \tag{9.1}$$

where x and y are the spatial coordinates, r is the distance from the line to the origin, and θ is the angle between the normal of the line and the x-axis [38]. This procedure results in a sinogram (see Figure 9-1c), which is subsequently reduced to a 1D angular distribution (see Figure 9-1d) by summing the absolute gradients for each projection [40]

$$AD\{I\}(\theta) = \int_r \left| \frac{\mathrm{d}R\{I\}(r,\theta)}{\mathrm{d}r} \right| \mathrm{d}r, \tag{9.2}$$

Prior to calculating the gradients using a central-difference kernel, each projection (pixel in the sinogram) is divided by the number of pixels from which it is formed to remove the projection bias of the RT. Finally, the location of the maximum amplitude of the 1D angular distribution (see the indicator in Figure 9-1d) is associated with the dominant fiber angle at that specific pixel. It should be noted that the maximum amplitude also yields information on the confidence of the reconstructed orientation. If there is a clear maximum, the orientation is determined with high confidence, and vice versa. Therefore, if the maximum amplitude is less than the mean value plus the standard deviation of the $AD\{I\}(\theta)$ in that circular kernel, the reconstructed orientation is considered to be undetermined. This procedure is repeated for each pixel in the original image, which yields a representation of the local orientation.

The methods have been implemented in Matlab® R2019a in a 64-bit operating system.

9.2.2 Gabor Filter Information Diagram GF-ID

The GF-ID automatically constructs a spatial 2D Gabor filter with optimal orientation and wavelength in order to estimate the local fiber direction. A 2D Gabor filter $h(x,y)$ with arbitrary orientation θ is given by [41]

$$h(x,y) = \exp\left[-\left(\frac{x'^2}{2\sigma_x^2} + \frac{y'^2}{2\sigma_y^2}\right)\right] \times \exp\left[\mathrm{i}\left(2\pi\frac{x'}{\lambda_s} + \phi_s\right)\right], \tag{9.3}$$

$$x' = x\cos\theta - y\sin\theta\,, \tag{9.4}$$

$$y' = x\sin\theta + y\cos\theta\,, \tag{9.5}$$

where x and y are the spatial coordinates, λ_s and ϕ_s are the wavelength and phase of the sinusoidal plane wave. The parameters σ_x and σ_y determine the space constants of the Gaussian envelope along the x- and y-axes, respectively:

$$\sigma_x = \frac{\lambda_s}{\pi}\sqrt{\frac{\ln 2}{2}} \times \frac{2^b + 1}{2^b - 1}, \tag{9.6}$$

$$\sigma_y = \frac{\lambda_s}{\gamma\pi}\sqrt{\frac{\ln 2}{2}} \times \frac{2^b + 1}{2^b - 1}, \tag{9.7}$$

where b and γ are the spatial frequency bandwidth and the spatial aspect ratio, respectively, which together control the kernel shape. These parameters could be optimized to fit particular features better. In this chapter, however, they are fixed and have the values $b = 1$ and $\gamma = 0.7$.

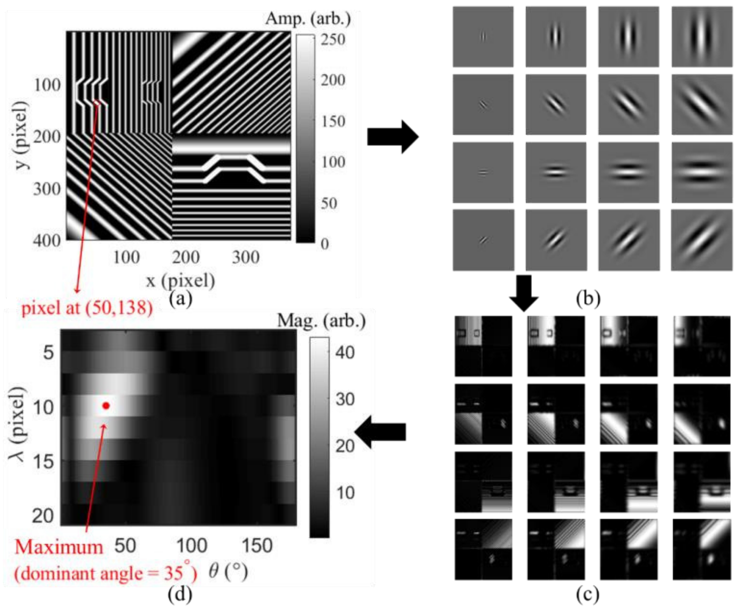

Figure 9-2 Schematic of the procedure of the GF-ID method: (a) the original image $I(x, y)$, (b) the Gabor filter bank with various wavelengths (horizontal) and orientations (vertical), (c) the magnitudes of the Gabor responses of the original image, and (d) the ID of the pixel at (50, 138).

A 2D Gabor filter is applied on an image $I(x, y)$ (see Figure 9-2a). The normalized Gabor response $r^n_{\theta,\lambda_s}(x, y)$ is then obtained as follows [38]:

$$r^n_{\theta,\lambda_s}(x, y) = \frac{1}{2\pi\sigma_x\sigma_y} h(x, y) * I(x, y), \tag{9.8}$$

where $*$ denotes the convolution operator. As shown in Figure 9-2b, a 2D Gabor filter bank with various wavelengths and orientations is applied to $I(x, y)$. For illustration purposes, a very large increment in wavelength (5, 10, 15, and 20) and orientation (0°, 45°, 90°, and 135°) is chosen in Figure 9-2b and Figure 9-2c. In reality, a much smaller increment is considered for both the wavelength and the orientation in order to be able to resolve minor deviations. The resulting $r^n_{\theta,\lambda_s}(x, y)$ are presented in Figure 9-2c. Considering that the Information

Diagram method becomes unstable when the noise features fit one of the wavelengths, an additional 2D Gaussian kernel could be applied to $r^n_{\theta_0,\lambda}(x,y)$ in Figure 9-2c:

$$G(x,y) = \frac{2}{\pi K^2 {\lambda_s}^2} \exp\left(-\frac{2(x^2+y^2)}{K^2 {\lambda_s}^2}\right), \tag{9.9}$$

where K governs the smoothness of the kernel. The K-value is selected as 0.5 in this chapter in order to balance the sensitivity to local variations and to noise.

Application of the filter kernel $G(x,y)$ to $r^n_{\theta,\lambda_s}(x,y)$ finally yields the filtered normalized Gabor response $\tilde{r}^n_{\theta,\lambda_s}(x,y)$:

$$\tilde{r}^n_{\theta,\lambda_s}(x,y) = G(x,y) * r^n_{\theta,\lambda_s}(x,y), \tag{9.10}$$

The magnitude of the filtered normalized Gabor response $\tilde{r}^n_{\theta,\lambda_s}(x,y)$ as a function of the 2D Gabor filter orientation and wavelength parameters forms the $ID_{x,y}(\theta,\lambda_s)$ (see Figure 9-2d). The maximum in the $ID_{x,y}(\theta,\lambda_s)$ is adopted to determine the local fiber orientation at a certain pixel (x,y). The maximum amplitude also yields information on the confidence of the reconstructed orientation. Similarly to Section 9.2.1, if the maximum amplitude is less than the mean value plus the standard deviation of the $ID_{x,y}(\theta,\lambda_s)$, the reconstructed orientation is considered to be undetermined. Applying this procedure for each pixel in the original image then yields a representation of the local in-plane fiber orientation.

The methods have been implemented in Matlab® R2019a in a 64-bit operating system.

9.3 Synthetic 2D Texture Image

In this section, the RT and the GF-ID methods are applied to a 2D synthetic multi-scale texture image with local variations.

The synthetic 2D texture image is shown in Figure 9-3a. To evaluate the noise-resistance, noise with probability density function equal to Gaussian distribution with zero-mean and variance of 25.5 (0.1 of the maximum amplitude) is added to each pixel in the original image (see Figure 9-3b) to simulate sensor and electronic noise. The actual local orientation of the synthetic texture image is also displayed in Figure 9-3c. These images do not represent the typical textures found in ultrasonic data obtained for a CFRP laminate. However, these images allow us to clearly illustrate and demonstrate the added value of the proposed GF-ID method for multi-resolution texture.

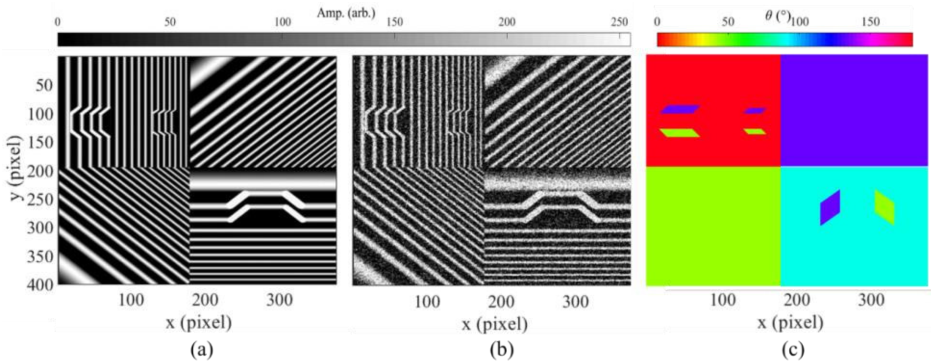

Figure 9-3 The synthetic texture images (a) without noise and (b) with Gaussian noise, respectively, and (c) the actual local orientation map.

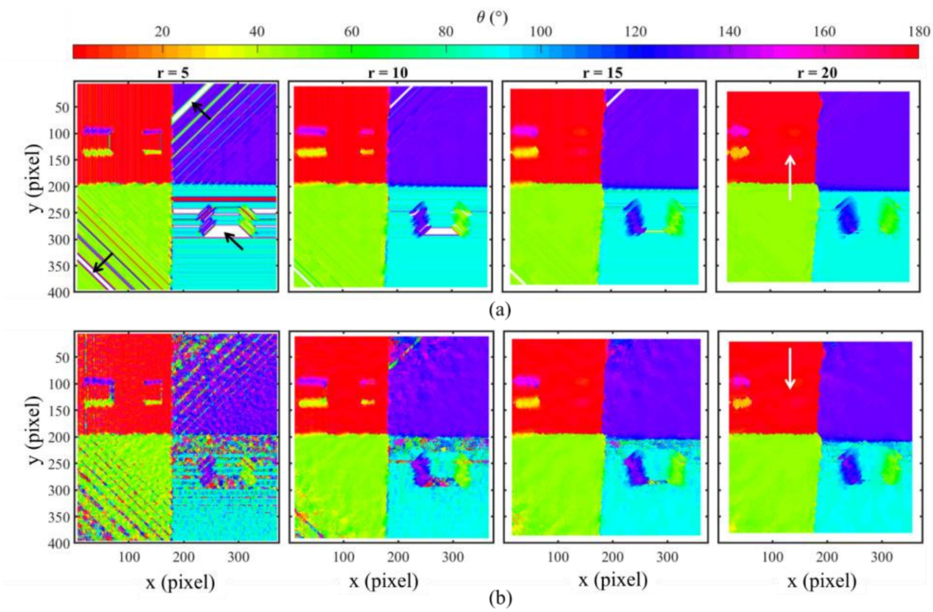

Figure 9-4 Local orientation map reconstructed by the RT method for the synthetic texture image (a) without noise and (b) with Gaussian noise. The radiuses for the circular kernel are respectively 5, 10, 15, and 20 pixels from left to right.

The RT method described in Section 9.2.1 is applied to extract the local orientations from these 2D images. The angle θ of the projections composing the RT image ranges from 1° to 180° with a spacing of 1°. Different radii of 5, 10, 15, 20 pixels for the circular kernel are applied. Pixels closer to the edges than the considered radius are not considered.

The obtained results are displayed in Figure 9-4. It can be observed that the RT with a small radius can resolve small local features, but it has low noise resistance. Further, the result indicates that large features, i.e., scale > radius, cannot be reconstructed in a proper manner (see the black arrows in Figure 9-4 for the results obtained with a radius of 5). Increasing the radius of the circular kernel makes the method much more noise resistant and provides a view on large features. However, the small local features cannot be resolved anymore (see the white arrows in Figure 9-4 for the results obtained with a radius of 20). Hence, it is crucial for the RT method to optimize the radius to balance its noise resistance and sensitivity to local variations. An acceptable choice for this particular input data seems to be a radius of 10 pixels.

The GF-ID method described in Section 9.2.2 is applied to extract the local orientations from the synthetic 2D texture images. The Gabor filter bank consists of filters with wavelengths ranging from 4 to 20 pixels with a spacing of 2 pixels and orientations ranging from 1° to 180° with a spacing of 1°. Similar to the RT method, pixels closer to the edges than half of the maximum wavelength are not considered.

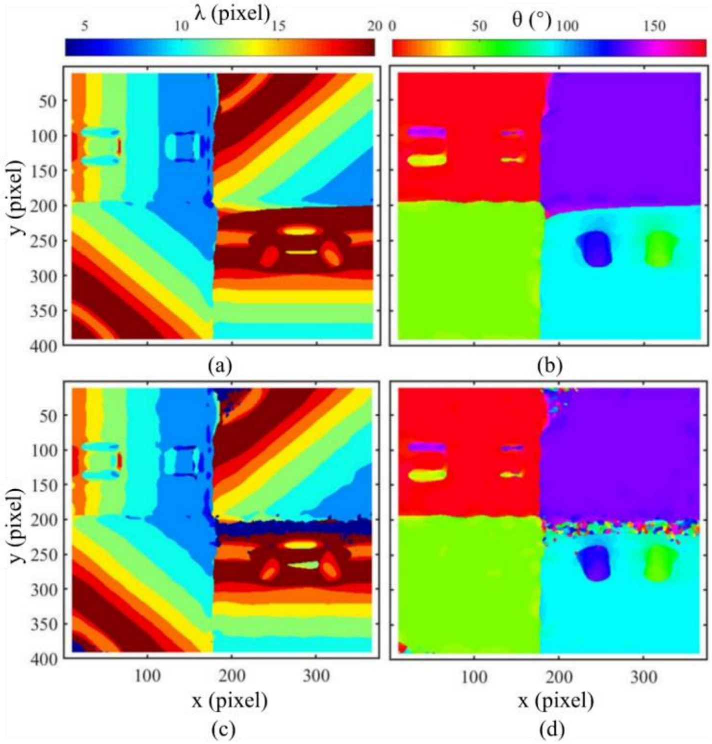

Figure 9-5 Local scale and local orientation maps reconstructed by the GF-ID method for the synthetic texture image (a-b) without noise and (c-d) with Gaussian noise.

The results obtained from the GF-ID method are displayed in Figure 9-5. The GF-ID provides both the local scale and local orientation of features, but our primary interest is reconstructing the local orientation (Figure 9-5b and d). It can be seen that the GF-ID method provides an accurate estimation of the local orientations of both small and large features. Further, Figure 9-5d shows the good noise resistance of the GF-ID method. Still, the noise is not completely eliminated. An increased K -value could resolve this, but this is not recommended because it will lower the sensitivity to small features.

9.4 Synthetic Image with Fiber Waviness features

To evaluate the performance of the proposed GF-ID method for a more realistic case, a synthetic in-plane waviness pattern with structural noise features (i.e., variation in angles and fiber tow widths) is simulated, see Figure 9-6. The same procedures and parameters mentioned in Section 9.3, i.e., wavelengths ranging from 4 to 20 pixels with a spacing of 2 pixels and orientations ranging from 1° to 180° with a spacing of 1°, are employed.

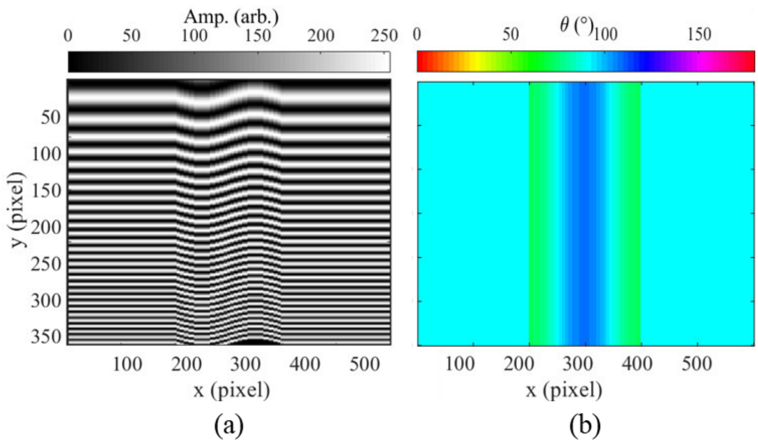

Figure 9-6 (a) Synthetic in-plane waviness image and (b) the actual local orientation map.

The results obtained from the RT and the GF-ID methods are displayed in Figure 9-7 and Figure 9-8, respectively. It can be observed that both methods suffer bias from underestimating the angular deviations in waviness. The amount of the underestimation of the RT method increase with the radius of the circular kernel (see Figure 9-7). Note that the GF-ID method automatically constructs local Gabor filters with optimal wavelength and orientation, resulting in a dynamic bias. It can be observed from the local scale and orientation maps in Figure 9-8 that the amount of the underestimation increases with the kernel size (wavelength).

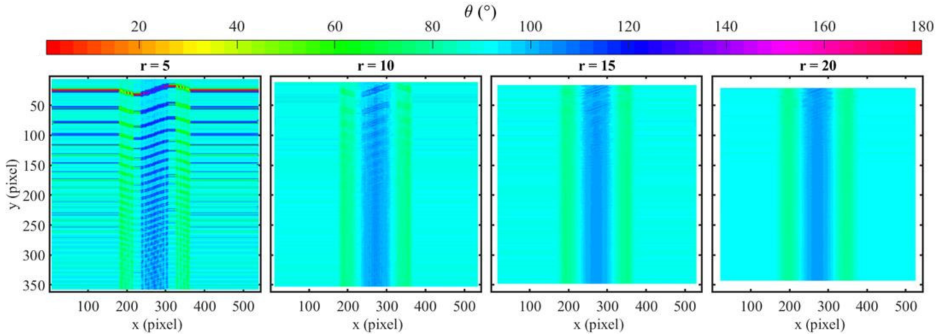

Figure 9-7 Local orientation maps obtained by the RT method for the synthetic in-plane waviness image. The radii for the circular kernel are respectively 5, 10, 15, and 20 pixels from left to right.

Also, the GF-ID method shows good resistance to structural noise, which should be attributed to the application of the additional 2D Gaussian kernel. The radius needs to be optimized for the RT method to cope with the variable fiber tow widths.

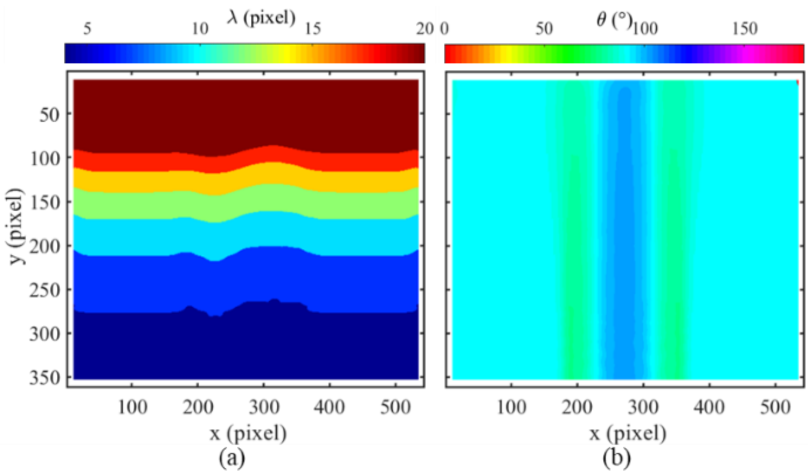

Figure 9-8 Local scale and local orientation maps obtained by the GF-ID method for the synthetic in-plane waviness image.

9.5 Ultrasonic Dataset from 8-layer thin CFRP laminate with Fiber Waviness Feature

In this section, the performance of the RT and the GF-ID methods are evaluated on an ultrasonic dataset with in-plane fiber waviness features. The ultrasonic dataset is obtained from an 8-layer CFRP laminate with a stacking sequence $[0/90]_{2S}$ and a total thickness of 2.0 mm. The sample was made from prepreg material, and has been cured in an autoclave. In an attempt to create in-plane fiber waviness, the 3rd prepreg layer has been contaminated with acetone to dissolve the epoxy. Then, by applying a manual shear force to this prepreg lamina, a deviation in its in-plane fiber orientation is induced (see Figure 9-9b).

A 15 MHz spherically focused immersion transducer with a focal distance of 25.4 mm (Olympus V313) is employed in the PE mode for raster scanning. This transducer is specifically chosen because it provides sufficient lateral resolution and good SNR through the whole depth for the inspected laminate. The aperture diameter is 6.35 mm. The essential requirements for the lateral resolution are: (a) −6 dB pulse-echo focal beam width as small as possible to detect features in the fiber spread, and (b) −6 dB pulse-echo range of focus higher than the thickness of the laminate [42]. The −6 dB focal beam width w_f and range of focus z_r in the pulse-echo mode can be theoretically estimated as follows [42]:

$$w_f = 1.032\lambda_{\mathrm{w}} F/D, \tag{9.11}$$

$$z_r = 6\lambda_{\mathrm{w}}(F/D)^2, \tag{9.12}$$

where λ_{w} is the wavelength in the water, F is the focal distance, and D is the aperture diameter. Thus, the used transducer has a w_f of 0.41 mm and a z_r of 9.6 mm.

The focal point was put in the middle of the CFRP laminate. The ultrasonic response is recorded using a 14-bit acquisition card (PXIe-5172) at a sampling frequency of 250 MS/s. The scanning steps in both x and y directions are 0.2 mm, and the total scan area is 110 mm× 70 mm (550 pixels× 350 pixels). The instantaneous amplitude is extracted from the recorded ultrasonic dataset by applying the Hilbert transform and evaluating the magnitude. The time-of-flight (TOF) corresponding to the front and back surfaces are determined according to the peak instantaneous amplitudes in the waveform. These values extract x-y slices throughout the laminate, which are thus aligned with the outer surfaces. The RT and the GF-ID methods are applied on a multitude of such x-y slices.

Following the discussion in Section 9.3, a radius of 10 pixels is chosen for the RT method in order to balance the sensitivity to local variations and the noise resistance. For the GF-ID method, the same parameters as those in Section 9.3, i.e., wavelengths ranging from 4 to 20 pixels with a spacing of 2 pixels and orientations ranging from 1° to 180° with a spacing of 1°, are employed in order to provide an identical sensitivity to the local variations. Unlike the RT method, which considers a kernel with a fixed radius, the GF-ID method constructs local Gabor filters with optimal wavelength and orientation. The x-y slices of the instantaneous amplitude dataset at the middle of the 3rd and 6th plies are extracted and displayed in Figure 9-9c. According to the stacking sequence of the CFRP laminate, those laminae should have a fiber orientation of 90°. It is observed that for deeper plies, the contrast and SNR are lower due to the attenuation of the ultrasonic signal.

The results obtained by using the RT and GF-ID methods are displayed in Figure 9-9d and e, respectively. Both methods resolve the global fiber direction in the 6th ply and the distorted local in-plane fiber direction in the 3rd ply. However, it is difficult to quantify the reconstruction quality of the RT and GF-ID methods for the fiber waviness due to the flawed and uncontrolled manufacturing process. Further, it can be observed that the images show apparent noise, which can be expected considering the poor quality of the prepreg and intrusive operation during manufacturing. However, the result for the 6th ply reveals the higher noise resistance of the GF-ID method.

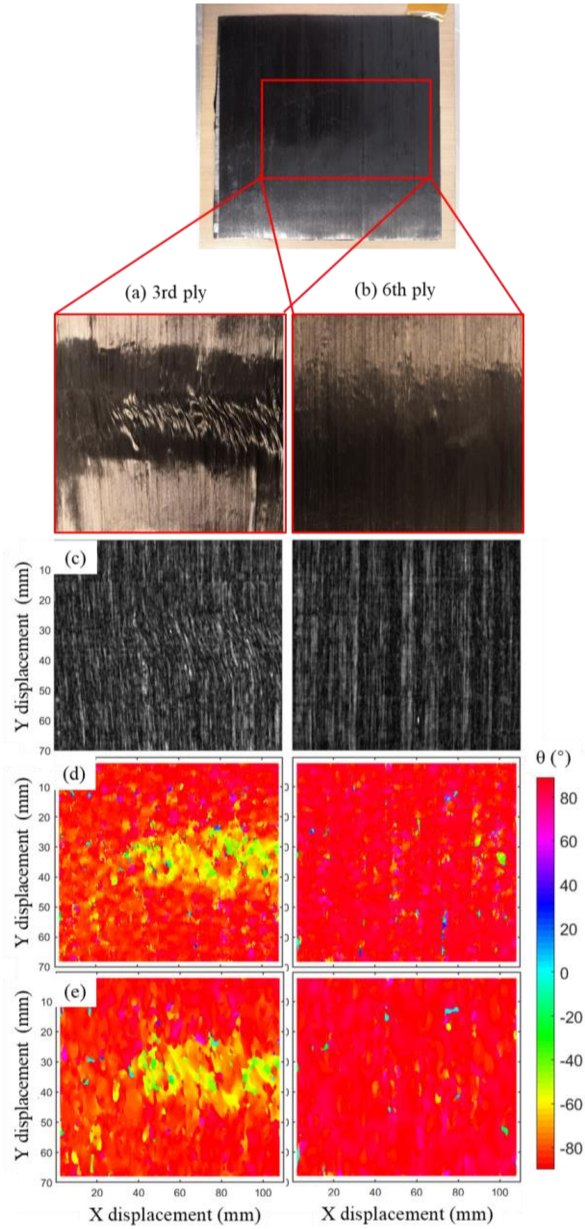

Figure 9-9 8-layer CFRP laminate with artificial fiber waviness; the prepregs of (a) the 3rd prepreg ply and (b) the 6th prepreg ply with artificial fiber waviness; (c) the x-y slices of the instantaneous amplitude dataset at the middle of the 3rd and 6th plies respectively; The fiber angle maps extracted from the 3rd and 6th plies by (d) RT (10 pixels) and (e) GF-ID methods ($K = 0.5$).

9.6 Ultrasonic Dataset from 24-layer thick CFRP Laminate

The performance of the RT and the GF-ID methods are also evaluated on low-contrast 3D ultrasonic data. The ultrasonic dataset is obtained from a 24-layer CFRP laminate with a total thickness of 5.5 mm. The sample is made from high-quality prepreg with a stacking sequence of $[45/0/-45/90]_{3S}$, and was cured using the recommended autoclave cycle. As such, it is expected that the manufactured CFRP laminate has high quality, and that the fiber orientations are close to the intended stacking sequence. The main challenge for this sample is its high thickness, making the extraction of the in-plane fiber orientation for the deep layers a challenging task.

The same transducer, scanning system, and settings as those in Section 9.5 are employed except for the scanning steps and area. The scanning steps in both x and y directions are 0.25 mm, and the total scan area is 75 mm×75 mm (300 pixels×300 pixels). The dataset is also processed in the same way as that in 0. The x-y slices of the instantaneous amplitude dataset at the middle of the 3rd, 11th, and 22nd plies are extracted and displayed in Figure 9-10a, b, and c. According to the stacking sequence of the CFRP laminate, they should all have a fiber orientation of −45°. It is observed that for deeper plies, the contrast and SNR are lower due to the attenuation of the ultrasonic signal.

The local fiber orientation maps reconstructed by applying the RT and GF-ID methods are presented in Figure 9-10d and f. In order to quantify the reconstruction results, the normalized histogram of the observed distributions of the fiber angles are displayed below the orientation maps (see Figure 9-10e and g). It can be seen from Figure 9-10d and e that the RT method suffers quite a lot from noise features, especially for the deeper layers. On the other hand, the GF-ID method introduces several more significant regions of a single erroneous angle due to leakage of the adjacent plies (0° and 90° angles).

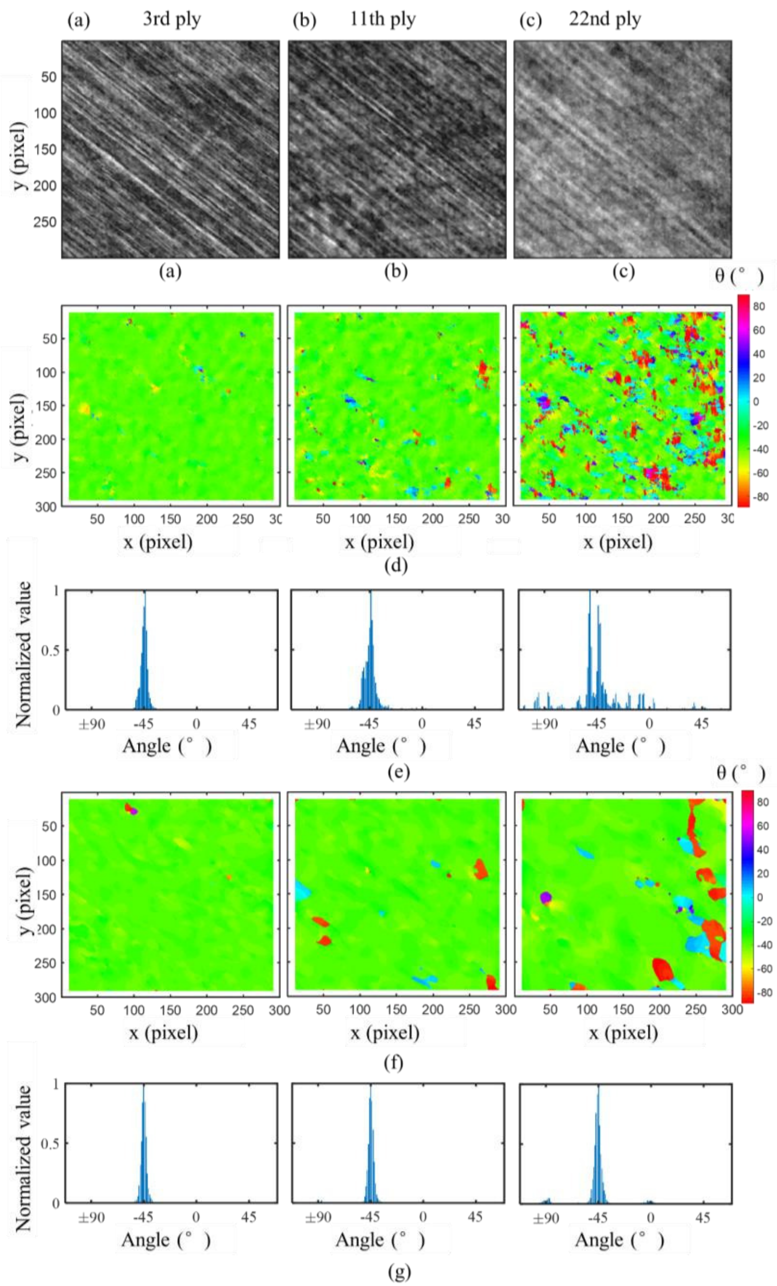

Figure 9-10 X-y slices of the instantaneous amplitude dataset at the middle of the (a) 3rd, (b) 11th, and (c) 22nd plies. The corresponding in-plane fiber orientation maps and -distributions are measured by (d–e) the RT and (f–g) the GF-ID methods.

The analysis has been extended by applying the reconstruction procedure for each time instance of the recorded ultrasonic dataset. Figure 9-11a displays the instantaneous amplitude of the 3D dataset along with different orthogonal slices. The reconstructed volumetric in-plane fiber orientation maps are displayed in Figure 9-11b and c for the RT and the GF-ID methods, respectively. It can be observed that the GF-ID results are less affected by noise features, especially for the deeper plies in the CFRP laminate. The observed distributions of the in-plane fiber angles are reported for each ply of the CFRP laminate in Figure 9-12. Care must be taken when interpreting these results because the CFRP laminate has slight deviations from its nominal stacking (due to manufacturing variability). The visual comparison reveals the more robust and stable reconstruction results of the GF-ID method, especially for the deep plies. It is worth noting that besides the principal distributions, the fiber angles also follow a summation of several sparse distributions associated with the impression of the angular features of the plies above and below, especially in deep plies (see Figure 9-12). In view of this, researchers have proposed to average multiple slices of instantaneous amplitude in the targeted ply prior to the reconstruction. It was found that this could lead to more stable angle measurement and could suppress the effects of adjacent plies [35].

In terms of computational efficiency, the RT method outperforms the GF-ID method. For the volumetric reconstruction of the fiber orientations in the 24-layer CFRP laminate, the RT and GF-ID methods resulted in a calculation time of 69.4 min and 149.1 min, respectively on a computer with an Intel® Xeon® Gold 6146 CPU, of which 12 CPU cores are used, and 256 GB RAM. The result is not surprising because although the angular resolution is equal for both methods, the GF-ID method employs a filter bank with variable kernel size. In contrast, the RT method employs a circular kernel with a fixed radius. Finally, note that currently a search in the 2D parameter space $ID_{x,y}(\theta, \lambda_s)$ is performed to determine the dominant in-plane fiber orientation. However, the GF-ID can also be implemented in 4D parameter space $(\theta, \lambda_s, b, \gamma)$ by including the parameters b and γ. Especially for cases with significant local changes in noise and features, this would be beneficial. On the other hand, such a 4D approach will increase the computational time significantly.

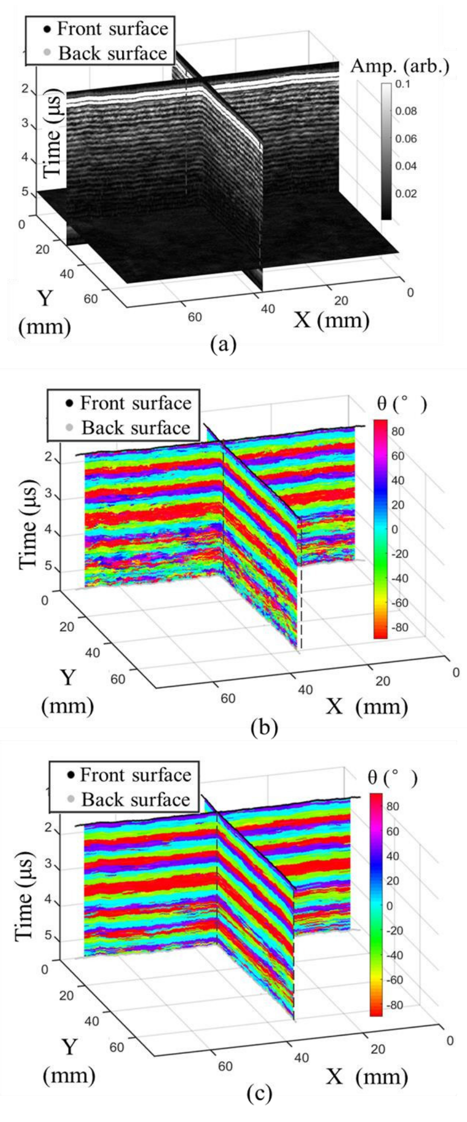

Figure 9-11 Orthogonal slices of (a) the instantaneous amplitude of the ultrasonic dataset and reconstruction of in-plane fiber orientation using the (b) RT method and (c) GF-ID method.

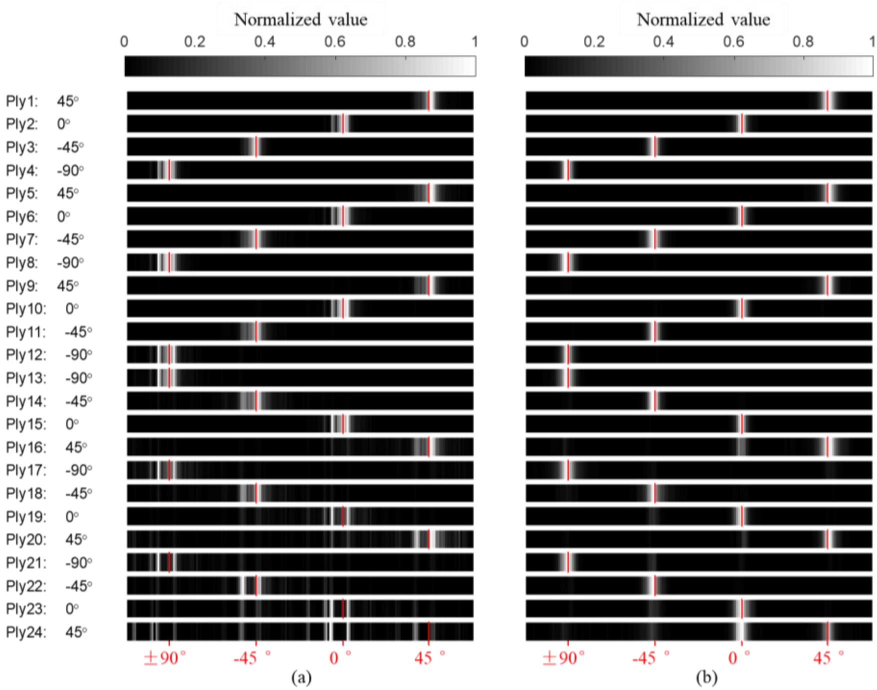

Figure 9-12 Normalized gray-scale maps representing the observed distributions of the in-plane fiber angles of each ply of the CFRP laminate obtained by the (a) RT method and (b) GF-ID method. Red vertical lines indicate the nominal in-plane fiber angles of the manufactured CFRP laminate.

9.7 Conclusion

A processing method for ultrasonic tomographic reconstruction of in-plane local fiber orientations of CFRP is developed. The procedure is based on the Gabor filter coupled to the concept of Information Diagram (GF-ID), and is demonstrated on synthetic images having texture and waviness. It is shown that by extending the fixed Gabor kernel to multi-scale Gabor kernels, the GF-ID reconstruction method can handle data which contains features at different scales and orientations. Also, its high resistance to random noise is demonstrated by applying an additional smoothing 2D Gaussian kernel. Like other known reconstruction approaches, the GF-ID method suffers bias from underestimating angular deviations in waviness and observed leakage from adjacent plies.

The developed GF-ID method is also applied on experimental 3D ultrasonic datasets obtained for an 8-layer CFRP laminate with fiber waviness features and a stacking sequence $[0/90]_{2S}$, and a high-quality 24-layer CFRP laminate with a stacking sequence $[45/0/-45/90]_{3S}$. A comparative analysis with the classical RT method demonstrates the performance of the GF-ID method for a more robust reconstruction of local fiber orientations from ultrasonic datasets.

References

[1] Potter, K., Khan, B., Wisnom, M., Bell, T., and Stevens, J., 2008, "Variability, fibre waviness and misalignment in the determination of the properties of composite materials and structures," Compos Part a-Appl S, 39(9), pp. 1343-1354.
[2] Wagih, A., Maimi, P., Blanco, N., Garcia-Rodriguez, S. M., Guillamet, G., Issac, R. P., Turon, A., and Costa, J., 2019, "Improving damage resistance and load capacity of thin-ply laminates using ply clustering and small mismatch angles," Compos Part a-Appl S, 117, pp. 76-91.
[3] Emerson, M. J., Jespersen, K. M., Dahl, A. B., Conradsen, K., and Mikkelsen, L. P., 2017, "Individual fibre segmentation from 3D X-ray computed tomography for characterising the fibre orientation in unidirectional composite materials," Compos Part a-Appl S, 97, pp. 83-92.
[4] Shen, H. B., Nutt, S., and Hull, D., 2004, "Direct observation and measurement of fiber architecture in short fiber-polymer composite foam through micro-CT imaging," Compos Sci Technol, 64(13-14), pp. 2113-2120.
[5] Smith, R. A., Nelson, L. J., Xie, N., Fraij, C., and Hallett, S. R., 2015, "Progress in 3D characterisation and modelling of monolithic carbon-fibre composites," Insight, 57(3), pp. 131-139.
[6] Mizukami, K., Mizutani, Y., Kimura, K., Sato, A., Todoroki, A., and Suzuki, Y., 2016, "Detection of in-plane fiber waviness in cross-ply CFRP laminates using layer selectable eddy current method," Compos Part a-Appl S, 82, pp. 108-118.
[7] Mizukami, K., Mizutani, Y., Todoroki, A., and Suzuki, Y., 2016, "Detection of in-plane and out-of-plane fiber waviness in unidirectional carbon fiber reinforced composites using eddy current testing," Compos Part B-Eng, 86, pp. 84-94.
[8] Bardl, G., Nocke, A., Cherif, C., Pooch, M., Schulze, M., Heuer, H., Schiller, M., Kupke, R., and Klein, M., 2016, "Automated detection of yarn orientation in 3D-draped carbon fiber fabrics and preforms from eddy current data," Compos Part B-Eng, 96, pp. 312-324.
[9] Bouloudenine, A., Feliachi, M., and Latreche, M. E., 2017, "Development of circular arrayed eddy current sensor for detecting fibers orientation and in-plane fiber waviness in unidirectional CFRP," Ndt&E Int, 92, pp. 30-37.

[10] Hughes, R. R., Drinkwater, B. W., and Smith, R. A., 2018, "Characterisation of carbon fibre-reinforced polymer composites through radon-transform analysis of complex eddy-current data," Compos Part B-Eng, 148, pp. 252-259.
[11] Cheng, J., Wang, B. Y., Xu, D. Z., Qiu, J. H., and Takagi, T., 2021, "Resistive loss considerations in the finite element analysis of eddy current attenuation in anisotropic conductive composites," Ndt&E Int, 119, p. 102403.
[12] Auenhammer, R. M., Mikkelsen, L. P., Asp, L. E., and Blinzler, B. J., 2021, "Automated X-ray computer tomography segmentation method for finite element analysis of non-crimp fabric reinforced composites," Compos Struct, 256, p. 113136.
[13] Elberfeld, T., De Beenhouwer, J., den Dekker, A. J., Heinzl, C., and Sijbers, J., 2018, "Parametric Reconstruction of Glass Fiber-reinforced Polymer Composites from X-ray Projection Data-A Simulation Study," Journal of Nondestructive Evaluation, 37(3), pp. 1-11.
[14] Pinter, P., Dietrich, S., Bertram, B., Kehrer, L., Elsner, P., and Weidenmann, K. A., 2018, "Comparison and error estimation of 3D fibre orientation analysis of computed tomography image data for fibre reinforced composites," Ndt&E Int, 95, pp. 26-35.
[15] Schöttl, L., Dörr, D., Pinter, P., Weidenmann, K. A., Elsner, P., and Kärger, L., 2020, "A novel approach for segmenting and mapping of local fiber orientation of continuous fiber-reinforced composite laminates based on volumetric images," Ndt&E Int, 110, p. 102194.
[16] Sinchuk, Y., Kibleur, P., Aelterman, J., Boone, M. N., and Van Paepegem, W., 2020, "Variational and Deep Learning Segmentation of Very-Low-Contrast X-ray Computed Tomography Images of Carbon/Epoxy Woven Composites," Materials, 13(4), p. 936.
[17] Kastner, J., Plank, B., Reh, A., Salaberger, D., and Heinzl, C., "Advanced X-ray tomographic methods for quantitative characterisation of carbon fibre reinforced polymers," Proc. Proceedings of the 4th International Symposium on NDT in Aerospace, Citeseer, pp. 1-9.
[18] Ali, M. A., Umer, R., Khan, K. A., and Cantwell, W. J., 2019, "Application of X-ray computed tomography for the virtual permeability prediction of fiber reinforcements for liquid composite molding processes: A review," Compos Sci Technol, 184, p. 107828.
[19] Garcea, S., Wang, Y., and Withers, P., 2018, "X-ray computed tomography of polymer composites," Compos Sci Technol, 156, pp. 305-319.
[20] Hsu, D. K., Fei, D., and Liu, Z., 2002, "Ultrasonically mapping the ply layup of composite laminates," Mater Eval, 60(9), pp. 1099-1106.

[21] Smith, R. A., and Clarke, B., 1994, "Ultrasonic C-Scan Determination of Ply Stacking-Sequence in Carbon-Fiber Composites," Insight, 36(10), pp. 741-747.
[22] Nelson, L. J., and Smith, R. A., "Three-dimensional fibre-orientation characterisation in monolithic carbon-fibre composites," Proc. Proc. European Conference on NDT.
[23] Morokov, E., Levin, V., Chernov, A., and Shanygin, A., 2021, "High resolution ply-by-ply ultrasound imaging of impact damage in thick CFRP laminates by high-frequency acoustic microscopy," Compos Struct, 256, p. 113102.
[24] Morokov, E., and Levin, V., 2019, "Spatial resolution of acoustic microscopy in the visualization of interfaces inside a solid," Acoustical Physics, 65(2), pp. 165-170.
[25] Brandley, E., Greenhalgh, E. S., Shaffer, M. S., and Li, Q., 2018, "Mapping carbon nanotube orientation by fast fourier transform of scanning electron micrographs," Carbon, 137, pp. 78-87.
[26] Smith, R. A., and Nelson, L. J., 2014, "Composite evaluation," US Patents.
[27] Smith, R. A., Nelson, L. J., Mienczakowski, M. J., and Challis, R. E., 2009, "Automated analysis and advanced defect characterisation from ultrasonic scans of composites," Insight-Non-Destructive Testing and Condition Monitoring, 51(2), pp. 82-87.
[28] Karamov, R., Martulli, L. M., Kerschbaum, M., Sergeichev, I., Swolfs, Y., and Lomov, S. V., 2020, "Micro-CT based structure tensor analysis of fibre orientation in random fibre composites versus high-fidelity fibre identification methods," Compos Struct, 235, p.111818.
[29] Nelson, L., Smith, R., and Mienczakowski, M., 2018, "Ply-orientation measurements in composites using structure-tensor analysis of volumetric ultrasonic data," Composites Part A: Applied Science and Manufacturing, 104, pp. 108-119.
[30] Zhu, E., Yin, J., Hu, C., and Zhang, G., 2006, "A systematic method for fingerprint ridge orientation estimation and image segmentation," Pattern recognition, 39(8), pp. 1452-1472.
[31] Kokare, M., Biswas, P. K., and Chatterji, B. N., 2007, "Texture image retrieval using rotated wavelet filters," Pattern recognition letters, 28(10), pp. 1240-1249.
[32] Sampo, J. A., Takalo, J. J., Siltanen, S., Miettinen, A., Lassas, M., and Timonen, J., 2014, "Curvelet-based method for orientation estimation of particles from optical images," Optical engineering, 53(3), p. 033109.

[33] Tzanis, A., 2017, "A versatile tuneable curvelet-like directional filter with application to fracture detection in two-dimensional GPR data," Signal Process, 132, pp. 243-260.
[34] Nelson, L., and Smith, R., 2019, "Fibre direction and stacking sequence measurement in carbon fibre composites using Radon transforms of ultrasonic data," Composites Part A: Applied Science and Manufacturing, 118, pp. 1-8.
[35] Smith, R., Nelson, L., Xie, N., Fraij, C., and Hallett, S., 2015, "Progress in 3D characterisation and modelling of monolithic carbon-fibre composites," Insight-Non-Destructive Testing and Condition Monitoring, 57(3), pp. 131-139.
[36] Maybury, L., 2020, "Advanced 3D ultrasonic characterisation of 2D woven composites," University of the West of England.
[37] Daugman, J. G., 1985, "Uncertainty relation for resolution in space, spatial frequency, and orientation optimized by two-dimensional visual cortical filters," JOSA A, 2(7), pp. 1160-1169.
[38] Kamarainen, J., Kyrki, V., and Kalviainen, H., "Fundamental frequency Gabor filters for object recognition," Proc. Object recognition supported by user interaction for service robots, IEEE, pp. 628-631.
[39] Moreno, P., Bernardino, A., and Santos-Victor, J., "Gabor parameter selection for local feature detection," Proc. Iberian conference on pattern recognition and image analysis, Springer, pp. 11-19.
[40] van Ginkel, M., Hendriks, C. L., and van Vliet, L. J., 2004, "A short introduction to the Radon and Hough transforms and how they relate to each other," Delft University of Technology.
[41] Kruizinga, P., and Petkov, N., 1999, "Nonlinear operator for oriented texture," IEEE Transactions on image processing, 8(10), pp. 1395-1407.
[42] 1992, "ASM Handbook," Nondestructive Evaluation and Quality ControlMaterials Park, Ohio, pp. 231-277.

Chapter 10 A Planar Ultrasound Computed Tomography Method for Reconstruction of Fiber Architecture in CFRP Laminates

10.1 Introduction

0 and 0 have demonstrated the high performance of the analytic-signal procedure coupled to log-Gabor filter for robust interply tracking in carbon fiber reinforced polymer (CFRP) laminates. Following the analytic-signal analysis, the out-of-plane ply orientation is extracted by applying the structure tensor method to the instantaneous phase (see 0). Besides, the in-plane fiber orientation is extracted by applying the Gabor filter-based Information Diagram (GF-ID) method to the instantaneous amplitude (see Chapter 9). As a result, the application of the analytic-signal technique coupled with different advanced analysis tools has been successful in extracting information on the local fiber architecture. Furthermore, these analysis tools are all based on the pulse-echo (PE) ultrasound dataset and thus can be combined and integrated into a data processing pipeline. Combining these analysis tools, the data processing pipeline yields critical information, including ply thickness, out-of-plane ply orientation, and in-plane fiber orientation, thus reproducing the entire fiber architecture. This data processing pipeline is named “planar ultrasound computed tomography (pU-CT)”.

The extraction of the fiber architecture is helpful for the inspection of manufacturing quality. It is also essential to estimate load-induced changes in the fiber structure, of which particular interest is the low-velocity impact (LVI) induced damages. LVI events are well-known to pose a severe threat to structural integrity [1] and typically induce barely visible impact damage (BVID), a complex damage phenomenon consisting of fiber breakage, delaminations, matrix cracking, and plastic deformations [2, 3]. The BVID significantly jeopardizes the structural performance of the CFRP. For example, a highly reduced compression-after-impact strength has been reported in the literature [4, 5]. The reduction in strength is mainly attributed to the presence of delaminations, promoted by matrix cracks, stiffness mismatch, ply clustering, the laminate deflection [6], and the out-of-plane plastic deformation coming along with local buckling [7]. Of particular concern is that the BVID can rarely be detected by visual inspection and grow upon other loadings [8]. Thus, pU-CT for reconstructing fiber architecture of impacted CFRP could draw research attention.

The pU-CT technique mainly consists of three steps. The first step is a hybrid analytic-signal analysis to determine the surfaces, interplies, and delaminations robustly and efficiently. Step 2 makes use of a structure tensor process for the extraction of the local out-of-plane ply orientation. In step 3, the GF-ID method is employed to extract the local in-plane fiber direction robustly. The developed pU-CT technique is demonstrated on a 24-layer quasi-isotropic CFRP laminate which suffered an LVI event with an energy of 5.3 J.

This chapter is organized as follows. The pU-CT technique is introduced in Section 10.2. The impacted CFRP laminate and the experimental methodology are described in Section 10.3. The obtained results and discussions are given in Section 10.4. Finally, the conclusion is presented in Section 10.5.

10.2 Planar Ultrasound Computed Tomography pU-CT methodology

The underlying assumption made in the pU-CT approach is that the excitation signal is sufficiently broadband. Both the fundamental ply-resonance and the 2nd-harmonic ply-resonance are excited with sufficient energy. The pU-CT method consists of three steps; each step extracts a specific metric from the structure of the CFRP (see Figure 10-1). The three steps are detailed in the following subsections.

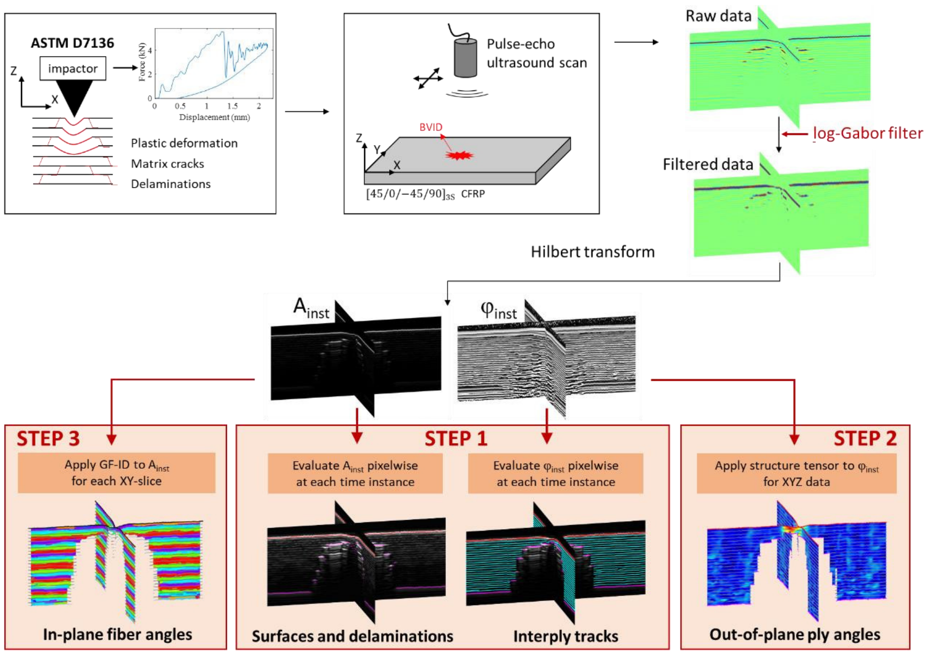

Figure 10-1 Conceptual overview of the pU-CT method.

10.2.1 Step 1: Interface mapping via hybrid analytic-signal analysis

A hybrid analytic-signal analysis is employed in order to distinguish between the ultrasonic reflections from different interfaces, i.e., front- and back surfaces, delaminations, and interplies. The filtered analytic-signal $\widetilde{s_a^R}(t)$ is obtained as introduced in Section 6.4. The instantaneous amplitude $A_{inst}(t)$ and instantaneous phase $\phi_{inst}(t)$ are then derived

$$A_{inst}(t) = \sqrt{[\mathrm{Re}(\widetilde{s_a^R}(t))]^2 + [\mathrm{Im}(\widetilde{s_a^R}(t))]^2}, \tag{10.1}$$

$$\phi_{inst}(t) = \arctan\frac{\mathrm{Im}(\widetilde{s_a^R}(t))}{\mathrm{Re}(\widetilde{s_a^R}(t))} + \pi \times \mathrm{sgn}(\mathrm{Im}(\widetilde{s_a^R}(t))). \tag{10.2}$$

The instantaneous amplitude is first evaluated to derive the time-of-flight (TOF) of the front-wall echo (FWE), back-wall echo (BWE), and delamination echo (see Figure 10-2). The first peak amplitude exceeding typical magnitudes is defined as the FWE. In order to determine the delamination echo and BWE appropriately, a dynamic amplitude correction is performed for compensating the ultrasonic attenuation through depth. Here, the echo with an amplitude A_b

exceeding the dynamic reference amplitude is determined as the echo corresponding to the back-wall or delamination as follows:

$$A_b > 0.5A_f \times \exp\left(-\alpha_{DAC}\left(TOF_b - TOF_f\right)\right), \tag{10.3}$$

where A_f and TOF_f are the amplitude and the TOF of the FWE respectively, TOF_b is the TOF of the echo A_b (which can correspond to a delamination echo or the BWE), and α_{DAC} is a compensation factor set as 0.75 /µs. This specific value is chosen based on the amplitude and TOF of both the FWE and BWE.

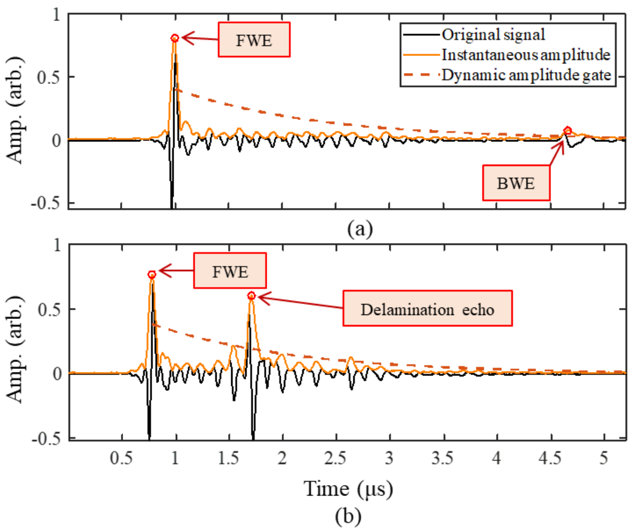

Figure 10-2 (a) Healthy and (b) delaminated A-scan signals from the impacted CFRP laminate with the indication of the dynamic amplitude gate.

The instantaneous phase associated with the FWE is set to ϕ_0 as reference. The instantaneous phase at the fundamental ply-resonance is used for basic interply tracking [9]. Practically, the interpolated $\phi_0 - \pi/2$ position in each 2π phase cycle is tracked, and the corresponding TOF indicates the depth positions of the interplies. Though, the dominating nature of the FWE, BWE, and delamination echo makes the extraction of nearby interplies problematic [9-11]. In order to reduce this dominating effect, the instantaneous phase at the 2nd-harmonic ply-resonance is analyzed to derive these nearby interplies (see Figure 10-3b). Practically, the interpolated $\phi_0 - \pi/2$ positions in the second and the second-to-last 2π phase cycles are tracked, and the corresponding TOF indicate then the depth positions of the first and the last interplies. Hence, we analyze the instantaneous phase at fundamental ply-resonance for stable interply tracking, and take advantage of the 2nd-harmonic ply-resonance to reduce the dominating effect of the wall echoes (see Figure 10-3b and c). Two log-Gabor filters are applied to optimally decompose the ultrasonic reflection signal to obtain specific ply-resonance frequencies for this hybrid instantaneous phase analysis. However, this improved analysis requires that the input signal is sufficiently broadband so that the decomposition can be done in a stable and robust manner.

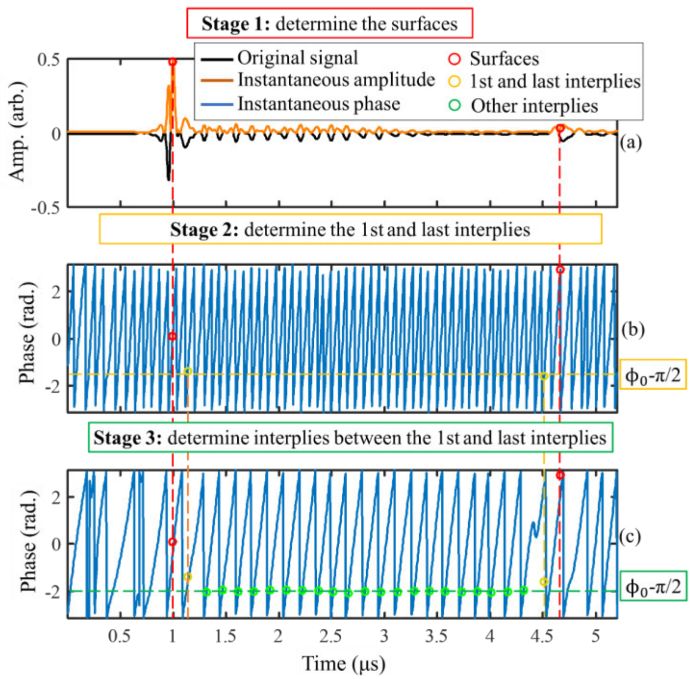

Figure 10-3 Illustration of the hybrid analytic-signal analysis on a healthy A-scan signal: (a) Extraction of surface echoes by the instantaneous amplitude of the original signal, (b) extraction of the first and the last interplies using the instantaneous phase of the filtered signal at the 2nd-harmonic ply-resonance, and (c) extraction of other interplies using the instantaneous phase of the filtered signal at the fundamental ply-resonance.

10.2.2 Step 2: Out-of-plane ply angle via structure tensor process

The structure tensor process described in 0 is applied to the instantaneous phase. The instantaneous phase at the 2nd-harmonic ply-resonance (obtained in Section 10.2.1) is employed since it is close to the center frequency of the used transducer, resulting in a high signal-to-noise ratio (SNR). Further, the 2nd-harmonic ply-resonance is well-locked to the interply tracks, leading to stable results. The focus here is the out-of-plane ply angle relative to the principal direction of the planar structure and the z-axis. The standard deviations of the Gaussian kernels G_τ and G_σ are both set as the constant of 3 in this study.

10.2.3 Step 3: In-plane fiber angle via Gabor filter-based Information Diagram

The GF-ID method described in Chapter 9 is applied to the instantaneous amplitude of the filtered signal. This step does not require the necessity to operate at the fundamental or the 2nd harmonic ply-resonance. Though, to improve the signal quality, a log-Gabor filter around the center frequency of the transducer is applied for noise filtering in the time domain. To avoid the presence of edge artifacts, a 2D Gabor kernel surpassing the bounds of the scan area is not considered in the construction of the $ID_{x,y}(\theta, \lambda_s)$. The 2D Gabor filter bank has wavelengths ranging from 4 to 16 pixels with a spacing of 1 pixel and angles ranging from 1° to 180° with a spacing of 1°.

10.3 Materials and methods

10.3.1 Material preparation

The studied CFRP laminate has a stacking sequence according to $[45/0/-45/90]_{3S}$. The material is a combination of polyacrylonitrile (PAN) based carbon fibers in PYROFIL #360 resin which has a density of 1200 $\mathrm{kg/m^3}$ and a glass transition temperature of 170 °C [12]. This resin is modified to allow curing in under 5 min, with a gel time of 200 sec at 130 ℃. The laminate is produced in an autoclave using compression molding for 7 min at 140 °C and a pressure of 8 MPa. The fiber volume fraction of the specimen is close to 60%. Finally, the specimen is cut to dimensions of 150 mm by 100 mm using a waterjet and conditioned to reduce the effect of moisture on the results. The same ultrasonic testing (UT) as described in Section 9.6 is applied to the impacted sample.

10.3.2 Low-velocity impact

The ASTM D7136 test standard is considered for impact testing [13]. A gravity-operated drop tower with a 7.72 kg impactor is used to perform the test. It drops the impactor from a height of 0.1 m onto the CFRP laminate, and prevents it from impacting again after the rebound. In the large-mass impact, the typical test duration is much longer than the required time for the stress waves to reach the boundaries [14]. The impactor is equipped with an Endevco Isotron 23-1 load cell holding a 16 mm diameter hemispherical hardened solid steel impact tip. It measures the compression force during the LVI. A line pattern is attached to the impactor to allow optical tracking of the vertical position using a Photron Fastcam SA-4 high-speed camera. The data acquisition is performed using an HBM GEN5i digital oscilloscope at a sampling rate of 1 MS/s. Based on the force signal, the oscilloscope sends a trigger signal to the camera to start recording the frames. The specimen temperature during the test is 29.74 ℃, which is recorded using a laser thermometer. The recorded force-displacement diagram is given in Figure 10-4, where the initial position before the impact is set at 0 mm. The actual impact energy was measured to be 5.3 J.

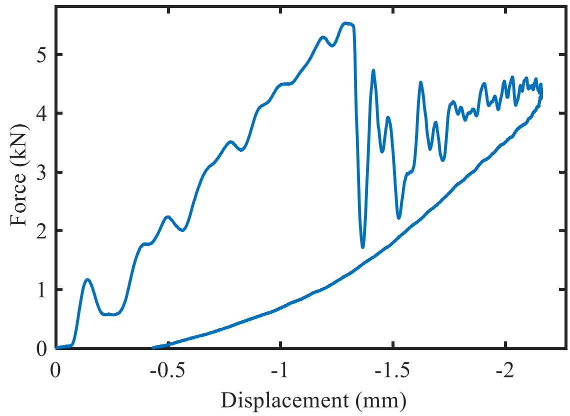

Figure 10-4 Force-displacement diagram of the LVI test from a height of 0.1 m on the CFRP laminate. The force is registered by the load cell, and the displacement is obtained from the optical tracking.

10.3.3 Optical microscopy

The impacted surface of the CFRP laminate has been investigated by a digital microscopy (VHX-7000 Keyence), having a lens with a magnification factor of x200. A 3D stitching procedure is employed to image an area of 20 mm×25 mm in which the focus depth is dynamically adapted. This procedure allows to visualize the 3D indentation profile, i.e., plastic deformation at the top surface, due to the impact event.

10.4 Results and discussions

The acquired ultrasonic pulse-echo (PE) data is processed in Matlab® R2019a. The computed A_{inst} and ϕ_{inst} of the ultrasonic response signals are displayed in Figure 10-5a and b, respectively, for two orthogonal planes at the center of the impact area.

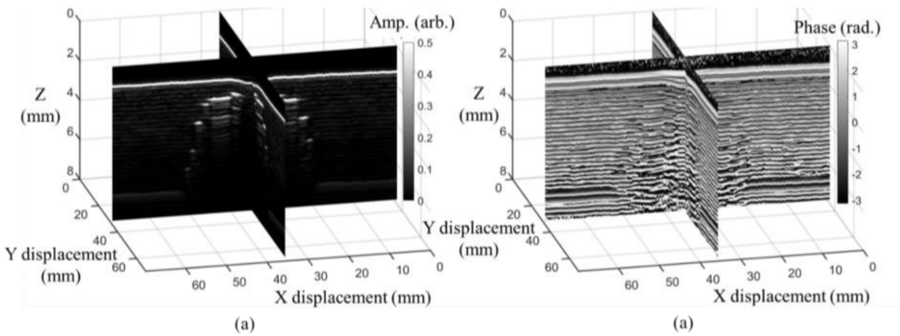

Figure 10-5 Orthogonal slices representing (a) the instantaneous amplitude and (b) the instantaneous phase of the recorded ultrasonic dataset

10.4.1 STEP 1: Structural interfaces

Based on the analysis of the instantaneous amplitude (see Section 10.2.1), the FWE, BWE, and delamination echo are extracted for each scanning instance. Figure 10-6a presents a projected visualization of the delamination cluster, clearly reflecting the quasi-isotropic stacking sequence of the impacted CFRP. The depth information of the damage can be obtained by multiplying the longitudinal wave velocity in the thickness direction with the TOF between the FWE and the delamination echo. Figure 10-6b combines both the instantaneous amplitude and the depth information in order to obtain a 3D visualization of the internal delamination features due to the impact event. It can be readily seen that the impact-induced delamination cluster resembles a pine-tree pattern, which accords with earlier studies [15, 16]. Note that due to shadowing effects, overlapping delaminations cannot be imaged.

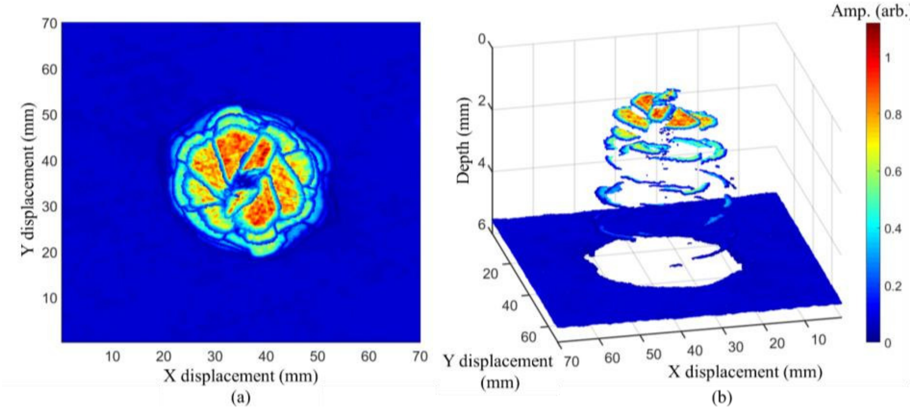

Figure 10-6 Visualization of BVID: (a) top view and (b) 3D perspective view.

Table 10-1 The parameters of the applied log-Gabor filters

Function	f_0 (MHz)	σ_0	−6 dB bandwidth (MHz)
Fundamental ply-resonance	6	0.7	3.94–9.13
2nd-harmonic ply-resonance	12.5	0.8	9.61–16.26
Noise filtering	15	0.7	9.86–22.83

The hybrid instantaneous phase analysis introduced in Section 10.2.1 is applied for extracting the interply tracks. The parameters of the applied Gabor filters are shown in the 1st and 2nd rows of Table 10-1. The center frequency f_0 is determined based on the ply-resonance, the σ_0 is chosen according to previous investigation in 0[10]. The extracted positions of surfaces, delaminations, and interplies are superimposed on the instantaneous amplitude dataset in Figure 10-7. The global interply tracks appear relatively continuous and smooth, demonstrating nearly uniform-spaced positions of the interplies throughout the laminate. This result indicates the high-quality manufacturing process of the CFRP laminate. Another interesting aspect of this hybrid instantaneous phase analysis is that information of the interplies near the delamination area is clearly provided. As such, the presumable crack path of progressive interply delamination is revealed, which provides crucial information for damage evolution prognosis. Some local interply tracks show discontinuities, especially for the deep plies, probably due to the sensitivity of the instantaneous phase to noise features. Further, the ply tracks seem slightly distorted at specific (x,y) locations (see the orange indicators on Figure 10-7), which is likely related to the manufacturing process and the quality of the prepreg. Also, there seems to be a local distortion of the front surface, and the sub-surface interply tracks at the zone of impact. The local out-of-plane ply orientation will be discussed in a quantitative manner in the next section.

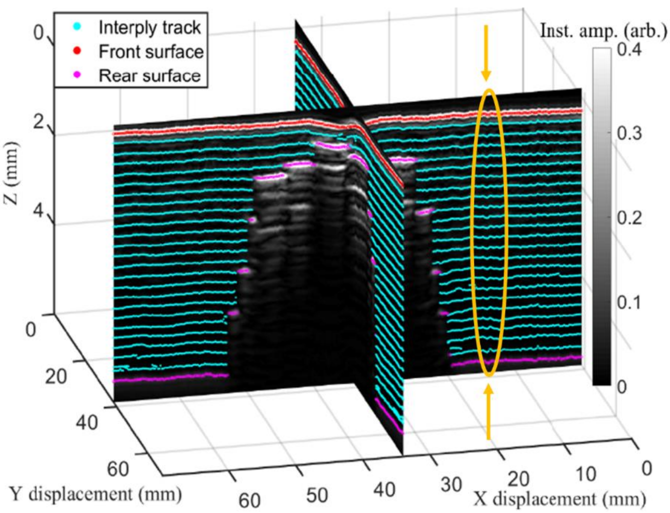

Figure 10-7 Orthographic projection slices through the instantaneous amplitude dataset. Superimposed are the front surface (red lines), back surface and delaminations (magenta lines), and interply tracks (green lines) obtained by the hybrid analytic-signal analysis.

10.4.2 STEP 2: Out-of-plane ply angles $\boldsymbol{\alpha}$

Out-of-plane ply orientation features in the bulk of the CFRP sample are extracted by applying the structure tensor process (see Section 10.2.2) to the instantaneous phase dataset. Figure 10-8 shows the measured out-of-plane ply angle map relative to the principal direction of the planar structure and the z-axis. The scan region away from the impact shows minor deviations from the nominal out-of-plane ply angle of 0°, indicating the high manufacturing quality of the CFRP laminate. However, in certain areas small deviations in the out-of-plane fiber orientation can be observed (see the orange indicators in Figure 10-8), having a typical angle of around 1–1.5°, which corresponds to the earlier observation in Figure 10-7.

Interestingly, Figure 10-8 clearly reveals an indent at the impact location due to local plasticity. The front-surface profile measured by optical microscopy is shown in Figure 10-9a. Note that the square patterns in the optical image are not material characteristics but are attributed to the 3D stitching procedure in the microscopic imaging procedure. The front-surface profile is also extracted by the analysis of the ultrasonic FWE (see Figure 10-9b). Both measurements indicate an indentation depth of ~150 μm. Figure 10-10 shows cross-sectional profiles through the indentation area, from which a consistent indentation geometry (width and depth) is observed. The benefit of the ultrasonic inspection is its capability to provide also information about the local plastic deformation inside the bulk of the CFRP laminate. It can be seen from Figure 10-8 that the plastic deformation is mainly concentrated in the top few plies directly beneath the impact location.

Furthermore, the ultrasonic reconstruction indicates that small plastic deformation appears near the delamination edges. The limited plastic deformation is attributed to the fact that the impact energy is mainly absorbed through the thickness direction of the laminate by ply splitting and delamination formation [3]. The latter can be readily seen in Figure 10-6.

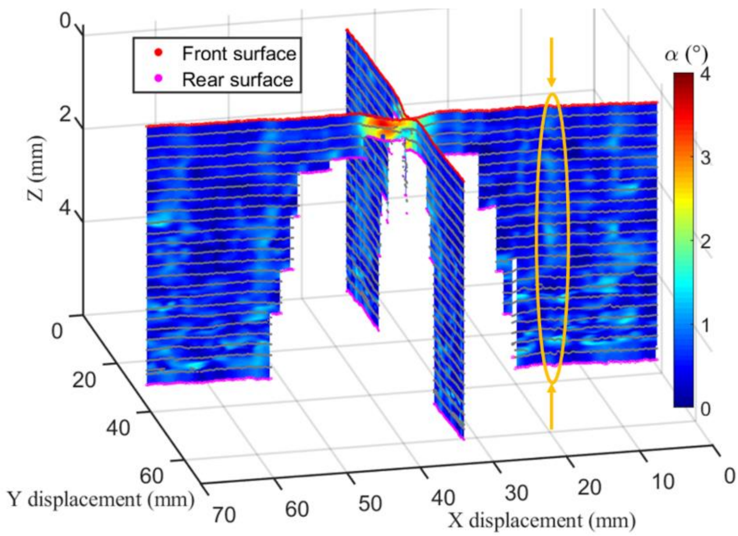

Figure 10-8 Reconstructed out-of-plane ply angle maps relative to the planar structure and the z-axis.

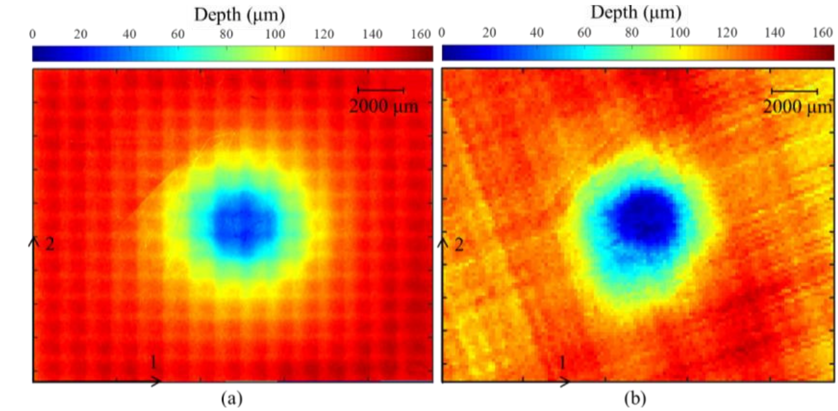

Figure 10-9 Measured front-surface profiles by (a) optical microscopy and (b) ultrasound.

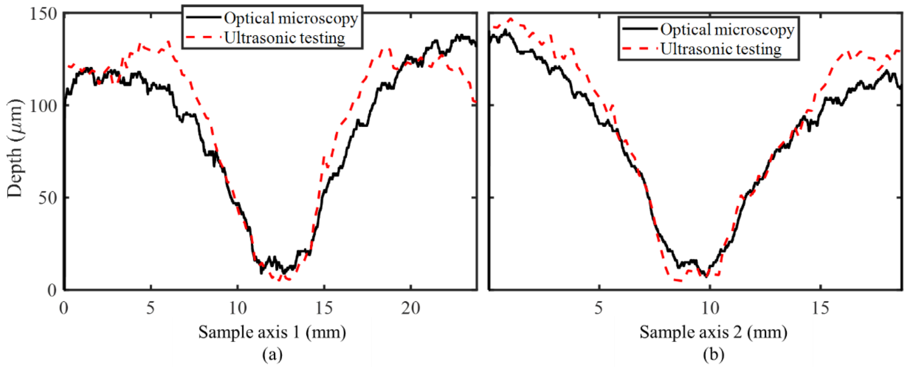

Figure 10-10 Cross-section through the impact position of the measured front-surface profiles along (a) sample axis 1 and (b) sample axis 2.

10.4.3 STEP 3: In-plane fiber angles $\boldsymbol{\theta}$

The GF-ID method (see Section 10.2.3) is applied to multiple slices of the instantaneous amplitude in view of extracting the in-plane fiber angles. The employed parameters of the log-Gabor filter are listed in the 3rd row of Table 10-1. The slices are taken such that they are parallel to the interply tracks extracted in Section 10.4.1.

Figure 10-11a shows such a slice in the middle of the 7th ply with a nominal fiber angle of $-45°$. The obtained scale map of the GF-ID procedure is presented in Figure 10-11b. More interesting for our application is the map of the identified local direction θ, see Figure 10-11c. Note that the angle of the scanning direction (≈20°) has been compensated in the extraction of the in-plane fiber angles. For this specific slice, the results indicate an in-plane fiber angle of $\theta = -43.5° \pm 7.0°$ (mean $\pm$ std) which is in good accordance with the nominal fiber angle for the 7th ply. Some deviations from the nominal fiber angle can be seen, especially near edge features.

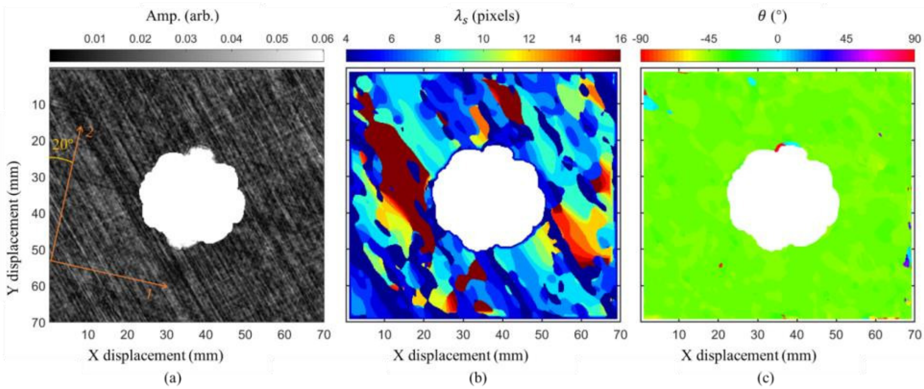

Figure 10-11 (a) Filtered instantaneous amplitude slice at the middle of the 7th ply (nominal angle of $-45°$); representation of the in-plane fiber (b) scale and (c) direction, reconstructed by the GF-ID method.

The procedure has been repeated for 120 slices through depth, and the obtained in-plane fiber directions are represented in Figure 10-12. The extracted global in-plane fiber directions correspond well to the nominal stacking sequence, i.e. $[45/0/-45/90]_{3S}$, of the studied CFRP laminate. However, the measured fiber direction in the 1st and the last plies shows many deviations due to strong front- and back wall echoes. The significant ultrasonic attenuation for deep plies further complicates the stable extraction of the in-plane fiber angles θ.

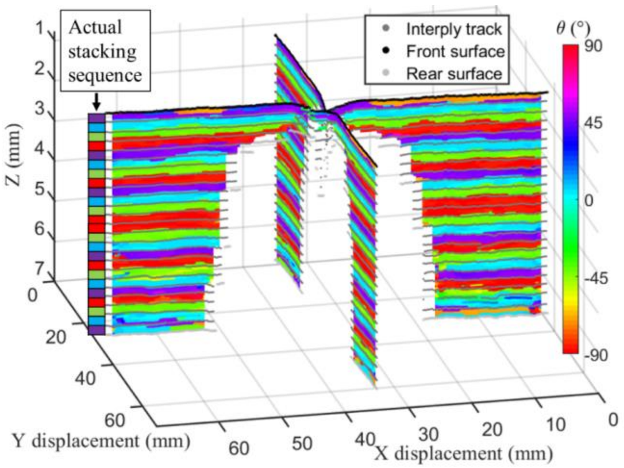

Figure 10-12 Reconstructed in-plane fiber angle maps by means of the GF-ID method. Superimposed in gray are the interply tracks. The actual stacking sequence is given as a reference.

10.5 Conclusion

An ultrasonic PE method, coupled to tomographic reconstruction approaches, has been proposed to extract both damage features and the local ply-fiber architecture of CFRP. This so-called pU-CT technique relies on the use of ply-resonances and involves three main analysis steps:

- Step 1: Mapping ply-interfaces via a hybrid analytic-signal analysis;
- Step 2: Reconstructing the local out-of-plane ply orientation via a structure tensor process;
- Step 3: Extracting the local in-plane fiber direction via a GF-ID.

The proposed pU-CT method has been applied on a 5.5 mm thick CFRP laminate with a stacking sequence $[45/0/-45/90]_{3S}$. The 24-layer CFRP laminate suffered a low-velocity impact of 5.3 J, resulting in BVID. The impact event induced local plasticity, resulting in an indentation profile at the impact location. The indentation profile measured by pU-CT has been validated by 3D optical microscopy. Further, the pU-CT results clearly show the presence of sub-surface plastic deformation, resulting in out-of-plane ply wrinkling. This local plasticity is mainly limited to the first few plies beneath the impact location. The pU-CT also provided a view on the complex delamination cluster that spreads throughout the CFRP laminate depth. The detailed reconstruction of the ply tracks near the delamination edges provides a means to predict the presumable crack propagation path during damage evolution. The reconstructed in-plane fiber angles remained unaffected by the impact event and closely matched the nominal quasi-isotropic stacking sequence of the manufactured CFRP laminate.

The proposed pU-CT seems to offer an alternative/complementary methodology to X-CT for reconstructing the local fiber architecture and complex damage phenomena in CFRP laminates.

References

[1] Sohn, M., Hu, X., Kim, J. K., and Walker, L., 2000, "Impact damage characterisation of carbon fibre/epoxy composites with multi-layer reinforcement," Composites Part B: Engineering, 31(8), pp. 681-691.
[2] Azouaoui, K., Azari, Z., and Pluvinage, G., 2010, "Evaluation of impact fatigue damage in glass/epoxy composite laminate," International journal of Fatigue, 32(2), pp. 443-452.
[3] Chen, D., Luo, Q., Meng, M., Li, Q., and Sun, G., 2019, "Low velocity impact behavior of interlayer hybrid composite laminates with carbon/glass/basalt fibres," Composites Part B: Engineering, 176, p. 107191.
[4] Liv, Y., Guillamet, G., Costa, J., González, E., Marín, L., and Mayugo, J., 2017, "Experimental study into compression after impact strength of laminates with conventional and nonconventional ply orientations," Composites Part B: Engineering, 126, pp. 133-142.
[5] Daelemans, L., Cohades, A., Meireman, T., Beckx, J., Spronk, S., Kersemans, M., De Baere, I., Rahier, H., Michaud, V., Van Paepegem, W., and De Clerck, K., 2018, "Electrospun nanofibrous interleaves for improved low velocity impact resistance of glass fibre reinforced composite laminates," Mater Design, 141, pp. 170-184.
[6] Gonzalez, E. V., Maimi, P., Camanho, P. P., Lopes, C. S., and Blanco, N., 2011, "Effects of ply clustering in laminated composite plates under low-velocity impact loading," Compos Sci Technol, 71(6), pp. 805-817.
[7] Vieille, B., Casado, V. M., and Bouvet, C., 2014, "Influence of matrix toughness and ductility on the compression-after-impact behavior of woven-ply thermoplastic- and thermosetting-composites: A comparative study," Compos Struct, 110, pp. 207-218.
[8] Karakuzu, R., Erbil, E., and Aktas, M., 2010, "Impact characterization of glass/epoxy composite plates: An experimental and numerical study," Composites Part B: Engineering, 41(5), pp. 388-395.
[9] Smith, R. A., Nelson, L. J., Mienczakowski, M. J., and Wilcox, P. D., 2017, "Ultrasonic analytic-signal responses from polymer-matrix composite

laminates," IEEE transactions on ultrasonics, ferroelectrics, and frequency control, 65(2), pp. 231-243.
[10] Yang, X., Verboven, E., Ju, B.-f., and Kersemans, M., 2021, "Parametric study on interply tracking in multilayer composites by analytic-signal technology," Ultrasonics, 111, p. 106315.
[11] Yang, X., Verboven, E., Ju, B.-f., and Kersemans, M., 2021, "Comparative study of ultrasonic techniques for reconstructing the multilayer structure of composites," Ndt&E Int, p. 102460.
[12] Product Data sheet - Quick Cure & High Tg Matrix Resin System PYROFIL #360 / #361. Technical report, Mitsubishi Rayon Co., Ltd., Carbon Fiber and Composite Materials Division, January 2014.
[13] ASTM International. ASTM Standard D7136, 2015, “Measuring the Damage Resistance of a Fiber-Reinforced Polymer Matrix Composite to a Drop-Weight Impact Event”. Technical report, American Society for Testing and Materials, West Conshohocken, PA, 2015.
[14] Spronk, S., Kersemans, M., De Baerdemaeker, J., Gilabert, F., Sevenois, R., Garoz, D., Kassapoglou, C., and Van Paepegem, W., 2018, "Comparing damage from low-velocity impact and quasi-static indentation in automotive carbon/epoxy and glass/polyamide-6 laminates," Polymer Testing, 65, pp. 231-241.
[15] Balakrishnan, V. S., Wartig, K., Tsombanis, N., and Seidlitz, H., 2019, "Influence of processing parameters on the impact behaviour of glass/polyamide-6 composite," Composites Part B: Engineering, 159, pp. 292-299.
[16] De Freitas, M., Silva, A., and Reis, L., 2000, "Numerical evaluation of failure mechanisms on composite specimens subjected to impact loading," Composites Part B: Engineering, 31(3), pp. 199-207.

Chapter 11 Conclusions and Prospects

11.1 General Overview and Conclusions

The overall objective of the work is to develop ultrasonic techniques for the robust extraction of layer parameters from multi-layer composites. For this, different tools have been developed and implemented. In the author's opinion, the research objectives have been achieved. Below is a more detailed description on the achieved results.

Part I focused on isotropic metallic Functionally Graded Materials (FGMs), and its investigation using high-frequency ultrasonic methods (25–75 MHz).

0 starts with the practical double focus technique based on a single depth scanning of a spherically focused immersion transducer. A new multi-mode wave focusing (MMWF) model has been proposed in order to interpret the results of depth scanning on thin layers. This proposed model fully accounts for the phenomenon of mode conversion and additional reflection peaks in the $V(z,t)$ curve. The thickness and multi-mode wave velocities are simultaneously extracted from the thin layer. Besides, a comprehensive interpretation of the measurements is provided, thus contributing to the identification of longitudinal-wave foci in cases of simultaneous measurement on multi-layer materials.

Following the in-depth investigation on the double focus technique, a variable focus technique is proposed in **0** for the acoustic measurement of multi-layer materials with no prior knowledge. A 'Bottom Left' principle is proposed based on the MMWF theory for the purpose of identifying the longitudinal-wave foci from the depth-scanning results. In addition, a phase differentiation theory is proposed to produce more accurate measurement results. The single and multi-layer experiments are successfully performed to validate the proposed technique.

Part II focused on anisotropic Carbon Fiber Reinforced Polymers (CFRP), and its investigation with low-frequency ultrasonic methods (5–15 MHz).

0 serves as a theoretical framework for the analysis of the analytic-signal technique. The analytic-signal response from CFRP laminates is modeled.

In **0**, the errors of phase-derived interply tracking are analytically studied for a wide range of parameters. It provides a guideline on how to improve the performance of the interply tracking procedure in real measurements. In the experimental study, a standard log-Gabor filter is introduced to make the analytic-signal procedure more robust against measurement noise.

In **0**, the performance of different ultrasonic pulse-echo (PE) approaches (low frequency of 5 MHz – mid frequency of 15 MHz – high frequency of 50 MHz) for extracting the ply-by-ply structure of multi-layer CFRP is compared. In the simulation study, the performance of the various techniques is investigated on synthetic data representative for a 24-layer CFRP. The robustness of the techniques is evaluated for different signal-to-noise ratios (SNRs). The various techniques are further investigated on experimental data of a 24-layer cross-ply CFRP. The ply-by-ply structure is extracted, and the thickness of each ply is estimated for quantitative analysis. The results indicate that the 5 MHz ultrasound coupled to log-Gabor filtered analytic-signal analysis shows the best performance.

0 is focused on the implementation of a structure tensor method for the estimation of the out-of-plane ply orientation in multi-layer CFRP. The procedure has been demonstrated and validated on various CFRP laminates with out-of-plane ply wrinkling and manufacturing distortions.

Chapter 9 introduced a Gabor filter-based Information Diagram (GF-ID) method for the tomographic reconstruction of the local in-plane fiber direction in multi-layer CFRP. A 3D ultrasonic dataset is first sliced in-plane successively through depth, and each 2D slice is locally analyzed by the GF-ID method. The performance of the developed GF-ID method is investigated on both synthetic texture images and an experimental ultrasonic dataset obtained from a 24-layer $[45/0/-45/90]_{3S}$ CFRP. Comparison with the classical Radon transform (RT) approach reveals the higher performance of the GF-ID method for ultrasonic reconstruction of the local in-plane fiber orientation in multi-layer CFRP.

0 presents the developed planar ultrasound computed tomography (pU-CT) technique to reconstruct the local 3D fiber architecture of (impacted) CFRP laminates. The proposed pU-CT technique employs a PE scanning modality and the analytic-signal analysis coupled with the processing tools developed in Chapters 6-9. The developed pU-CT technique is experimentally demonstrated on an impacted 24-layer CFRP laminate with a stacking sequence $[45/0/-45/90]_{3S}$. The internal fiber architecture and damage features of the CFRP laminate are reconstructed in great detail. It is anticipated that the pU-CT method could complement/substitute X-ray computed tomography measurements to inspect (damaged) CFRP laminates with sizeable dimensions.

11.2 Future Prospects and Recommendations

A short overview of recommended future work is provided here:

Transferring the pU-CT technique to other inspection modalities

On the merit of the high SNR signal and high resolution of the immersion ultrasonic C-scan in the PE mode, this thesis successfully applies the pU-CT technique to the high-quality dataset. However, the requirement of coupling agents limits the in-line application of ultrasonic testing (UT). Fortunately, we can also obtain datasets through alternative UT approaches, such as air-coupled UT, laser Ultrasonics, and electromagnet UT. Especially, the scanning laser ultrasonic in PE mode could be a promising tool in the in-line NDT of the aerospace CFRP. As such, it would be of high interest to match scanning laser ultrasonic with the developed pU-CT method.

Comparison studies of the pU-CT technique and X-CT

It is anticipated that the pU-CT method could complement the X-CT method for reconstructing the 3D internal structure of (damaged) CFRP laminates and obtaining an improved understanding of complex damage phenomena in composites. A comparative study of the pU-CT technique and X-CT is thus valuable to further explore their opportunities, challenges and limitations. Furthermore, a fusion of the pU-CT and X-CT results will likely lead to a complete and detailed representation of the investigated composite.

Extending the application of the analytic-signal technique to woven fiber composites

Besides the unidirectional CFRP, woven CFRP has also found much application in a variety of industries. The challenge arises for the application of the analytic-signal technique on the woven fiber composites due to the fact of non-uniform ply thicknesses and spatial modulation effects. Fortunately, the presented log-Gabor filter provides an added value of choosing the frequency range, and as such, the different ply thickness ranges could be tackled. A scheme is thus presented to extend the application of the analytic-signal technique to woven FRP.

Curriculum vitae

Personal

Name	Xiaoyu Yang
Gender	Male
Nationality	China
Date of birth	19 November 1993
Place of birth	Wuhan, China

Education

2012-2016	Bachelor in Mechatronic Engineering, ZJU
2016-2021	PhD Student in Mechatronic Engineering, ZJU
2019-2021	PhD Student in Electromechanical Engineering, UGent

Awards

2019	UGent CSC Preference Scholarship
2018	ZJU Excellence Student
2018	Ferrotec Doctoral Scholarship
2017	ZJU Excellence Social Practice Individual Award

Publication list

- **Yang, X**., Ju, B. F., & Kersemans, M. (2022). Assessment of the 3D ply-by-ply fiber structure in impacted CFRP by means of planar Ultrasound Computed Tomography (pU-CT). Composite Structures, 279, 114745.
- **Yang, X**., Verboven, E., Ju, B. F., & Kersemans, M. (2021). Comparative study of ultrasonic techniques for reconstructing the multi-layer structure of composites. NDT & E International, 121, 102460.
- **Yang, X**., Verboven, E., Ju, B. F., & Kersemans, M. (2021). Parametric study on interply tracking in multi-layer composites by analytic-signal technology. Ultrasonics, 111, 106315.
- **Yang, X**., Ju, B. F., & Kersemans, M. (2021). Ultrasonic tomographic reconstruction of local fiber orientation in multi-layer composites by a Gabor Filter-based Information Diagram method. NDT & E International, 124, 102545.
- **Yang, X**., Zhang, C., Sun, A., Ju, B. F., & Shen, Q. (2021). Application of all-optical laser ultrasonics for characterization of sub-mm layers in multi-layer structure. Applied Acoustics, 182, 108284.
- **Yang, X**., Wang, C., Sun, A., & Ju, B. F. (2020). Multi-mode ultrasonic waves focusing in a variable focus technique for simultaneous sound-velocity and thickness measurement. Applied Acoustics, 159, 107090.
- **Yang, X**., Zhang, C., Wang, C., Sun, A., Ju, B. F., & Shen, Q. (2019). Simultaneous ultrasonic parameter estimation of a multi-layer material by the PSO-based least squares algorithm using the reflection spectrum. Ultrasonics, 91, 231-236.
- **Yang, X**., Zhang, C., Sun, A., Bai, X., Ju, B. F., & Shen, Q. (2018). Numerical and experimental analysis of a focused reflected wave in a multi-layer material based on a ray model. Ultrasonics, 86, 41-48.
- **Yang, X**., Sun, A., Ju, B. F., & Xu, S. (2018). A rotary scanning method to evaluate grooves and porosity for nerve guide conduits based on ultrasound microscopy. Review of Scientific Instruments, 89(7), 073705.
- Sevenois, R. D., **Yang, X**., Verboven, E., Kersemans, M., & Van Paepegem, W. (2021). Permanent Deformation and Stiffness Degradation of Open Hole Glass/PA6 UD Thermoplastic Composite in Tension and Compression. Materials, 14(10), 2646.
- Zhang, C., **Yang, X**., Luo, G., Shen, Q., & Zhang, J. (2021). Simultaneous determination of layer thicknesses in graded layer materials by ultrasonic non-destructive method. Insight-Non-Destructive Testing and Condition Monitoring, 63(4), 229-235.
- Chen, C., Ju, B. F., **Yang, X**., Wang, C., Sun, A., Gong, J., & Li, Z. (2021). All-optical laser-ultrasonic technology for width and depth gauging of

rectangular surface-breaking defects. Review of Scientific Instruments, 92(5), 054901.

- Wang, C., Sun, A., **Yang, X**., Ju, B. F., & Pan, Y. (2018). Numerical simulation of the interaction of laser-generated Rayleigh waves with subsurface cracks. Applied Physics A, 124(9), 1-10.
- Wang, C., Sun, A., **Yang, X**., Ju, B. F., & Pan, Y. (2018). Laser-generated Rayleigh wave for width gauging of subsurface lateral rectangular defects. Journal of Applied Physics, 124(6), 065104.

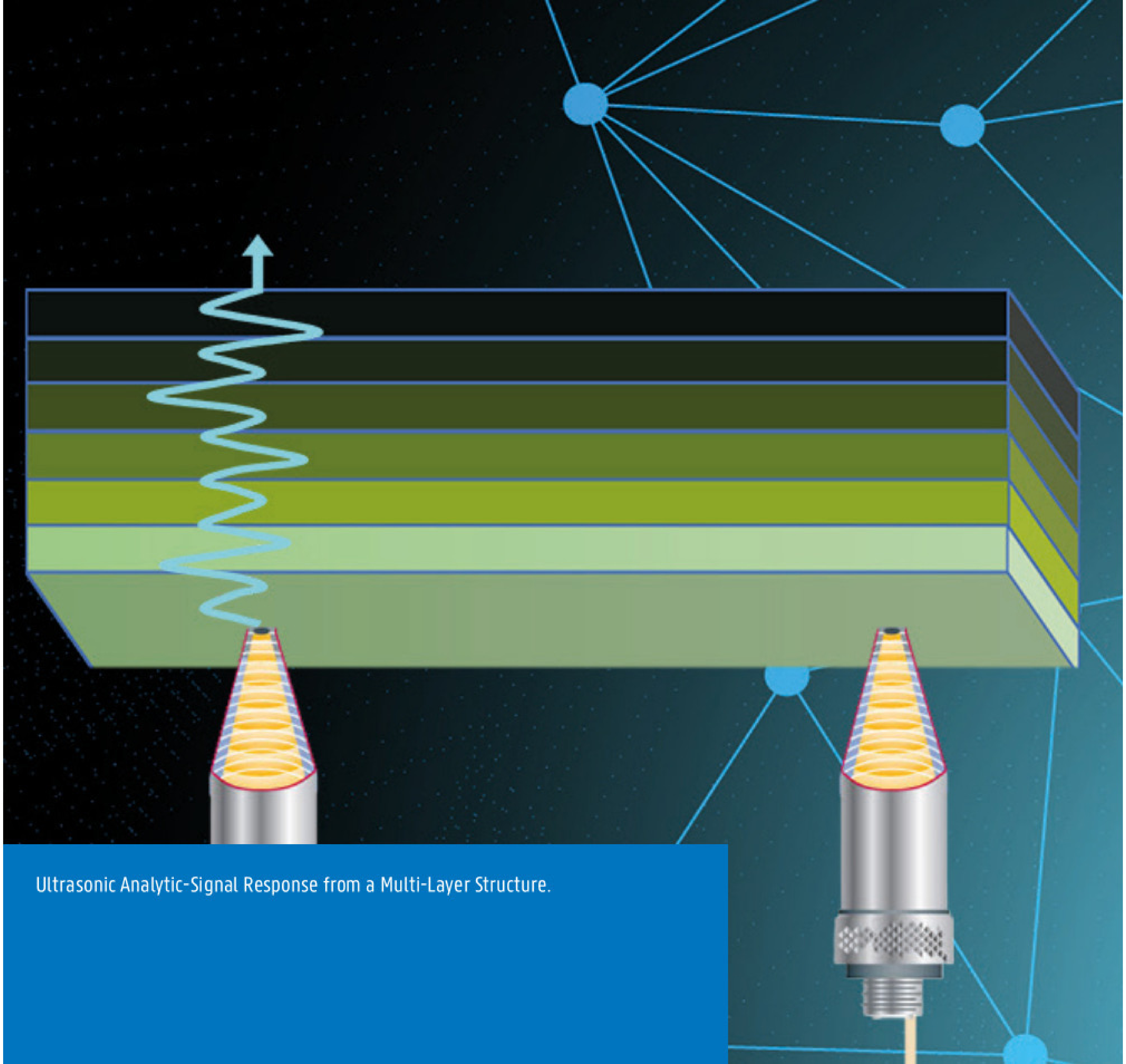
Ultrasonic Analytic-Signal Response from a Multi-Layer Structure.